EFFECTS OF STRUCTURAL NONLINEARITIES ON EFFECTIVE FORCE TESTING

by

Matthew R. Dove

A thesis submitted to Johns Hopkins University in conformity with the requirements for the degree of Master of Science in Engineering

Baltimore, Maryland

May, 2014

Abstract

Effective force testing (EFT) provides an alternative experimental method for the dynamic testing of structures using force controlled hydraulic actuators. Previous experimental EFT research has confirmed limitation in force tracking performance for nonlinear test structures. This thesis presents a parametric study via computational simulation of EFT to investigate the resulting effects of structural nonlinearities. Two configurations for an experimental test structure are identified and implemented into a computational EFT framework using Matlab and Simulink. Force feedback control is employed through loop shaping techniques. Structural behavior is examined for linear elastic, bilinear elastic, bilinear hysteretic, and bilinear hysteretic pinching structural models. Computational simulation of EFT shows that a loop shaping controller is stable for the behavior of each model and the expected force-displacement relations are developed. However, some simulations result in instabilities for bilinear hysteretic pinching behavior. Overall, this study demonstrates that force tracking performance significantly diminishes as the structural models become highly nonlinear. This effect is evident for both test structure configurations in all three nonlinear models.

Advisor: Professor Narutoshi Nakata, Department of Civil Engineering

Acknowledgments

Foremost, I would like to thank Professor Narutoshi Nakata for all of his help and guidance throughout my research and the preparation of this essay.

I would also like to express my gratitude to my peers in Professor Nakata's research group who had any contribution to this project: Matthew Stehman, Mike Lijoi, Richard Erb, and John Boutillier. Utmost appreciation is extended to Mike Lijoi for his design and fabrication of the members in the experimental setup.

Lastly, I want to sincerely thank my parents, Lee and Christine, as well as my Aunt, Patricia Santora. Thank you for your support, insight, and encouragement throughout my entire academic career.

Table of Contents

List of Tables

List of Figures

Chapter 1

Introduction

This thesis further investigates the application of the effective force test method as a means of seismic simulation for structures. Experimental earthquake engineering is an essential area of research for the investigation of structural response to a given seismic hazard. This field has been traditionally rooted in displacement based test methods because of their stability and ease of control when using hydraulic actuators, mechanical devices capable of applying large dynamic force. These methods involve converting ground acceleration data into equivalent displacements. The most widely used experimental method utilizing displacement feedback is shaking table testing. Shake table testing is advantageous because inertial effects of the structure are included in the structural response in real-time; therefore, the response of a test structure strictly resembles how that structure would perform in the field. Despite these advantages, shake table testing has significant limitations due to the scale of the structure tested, and only a small number of large scale shake table facilities exist.

Effective force testing (EFT) offers an alternative test method for researchers in experimental earthquake engineering that is based on force feedback control. Instead of imposing forces at the base of test structures, EFT applies an equivalent earthquake load at the structural nodes. Any structure that can be idealized as a lumped mass system can be subjected to EFT. A primary advantage of EFT is its ability to perform real-time seismic simulation for large scale test structures. EFT is capable of employing smaller

hydraulic actuators than those used in shake table testing since the entire structure does not have to be displaced during implementation.

Challenges for EFT lie within force feedback control. Force feedback measurement is subject to high levels of noise that can lead to significant instabilities in experimental testing. In an effort to ease the challenges in experimental implementation, computational models have been developed to test and refine force feedback controllers before stepping foot in the lab. These developments have provided a valuable starting point for the continued development of EFT in experimental earthquake engineering.

1.1. Purpose and Scope of Research

Previous research has verified force feedback control for single degree-of-freedom linear elastic and nonlinear EFT, both experimentally and computationally (Nakata and Krug, 2013). Nakata and Krug (2013) have identified that force tracking is compromised in the nonlinear range of a structure during EFT implementation. **This thesis aims to quantify the predominant effects of structural nonlinearities on EFT.** A primary objective is to observe any degradation in the performance of a force controller using three nonlinear models. This study utilizes computational system identification techniques for a physical three-dimensional steel frame structure, loop shaping force feedback to account for control-structure interaction, and nonlinear computational simulations to assess EFT performance.

1.2. Organization

The remainder of this thesis is organized in the following manner. Chapter 2, Background and Literature Review, provides fundamental knowledge on the concept of EFT, actuator dynamics, loop shaping control, and research developments in EFT. Chapter 3, Experimental Setup, describes the physical test structure and the free vibration analysis and results. Chapter 4, Computational Simulation of EFT, discusses the existing computational EFT framework, system identification, loop shaping controller design, linear and nonlinear structural models, and EFT evaluation criteria. Chapter 5, Computational EFT Results and Discussion, presents the results from the methodology described in Chapter 4. The results from the system identification, loop shaping controller design, and data analysis are discussed, and significant trends on the effects of structural nonlinearities are observed. Unstable simulations for one nonlinear model are also investigated. Chapter 6, Conclusions, summarizes the pertinent results from this study and looks into future research for the improvement of nonlinear EFT. The Appendices include the complete simulation results for the three nonlinear parametric studies. The Bibliography provides the works read and publications cited throughout this thesis.

Chapter 2

Background and Literature Review

A review of the literature relevant to this study is summarized in this chapter. Specific background information on actuator dynamics and loop shaping control is provided to facilitate further understanding of effective force testing (EFT) and its challenges. The information in this chapter serves as prerequisite knowledge for EFT research.

2.1 Concept of an Effective Force

The concept of an effective force is succinctly described by Chopra (2012) in the following manner. The equation of motion for a linear elastic single degree-of-freedom (SDOF) structure subjected to ground acceleration $\ddot{x}_g(t)$ is

$$m\ddot{x} + c\dot{x} + kx = -m\ddot{x}_g(t) \qquad (2\text{-}1)$$

where *m* is the mass, *c* is the damping, and *k* is the stiffness of the structure, and $\ddot{x}$, $\dot{x}$, and *x* are the acceleration, velocity, and displacement of the structural response, respectively. The relative displacement *x(t)* of the structure due to ground acceleration $\ddot{x}_g(t)$, shown in Figure 2.1, is equivalent to the displacement *x(t)* of the structure with a stationary base subjected to an external force of $-m\ddot{x}_g(t)$, shown in Figure 2.2. The external force, called an effective earthquake force, can replace the ground motion as

$$p_{eff}(t) = -m\ddot{x}_g(t) \qquad (2\text{-}2)$$

2.2 Concept of EFT

As seen in Figure 2.2, EFT applies the effective earthquake force $p_{eff}(t)$ to the lumped structural mass at the structural nodes. If the mass of a test structure can be accurately estimated, the structural response in EFT is theoretically equivalent to shake table testing. EFT is advantageous in that the entire structure does not have to be displaced in order examine the dynamic structural response.

Hydraulic actuators are employed in both test methods to control the applied motion. Shake table testing typically incorporates displacement controlled actuators attached to the base of the structure. In contrast, EFT relies on dynamic force control of the actuators attached to the structure at the structural nodes. This detail of EFT couples the dynamics of the actuator and structure together. Force control of hydraulic actuators in this manner has proved to be problematic, and several researchers have focused on this aspect in EFT development.

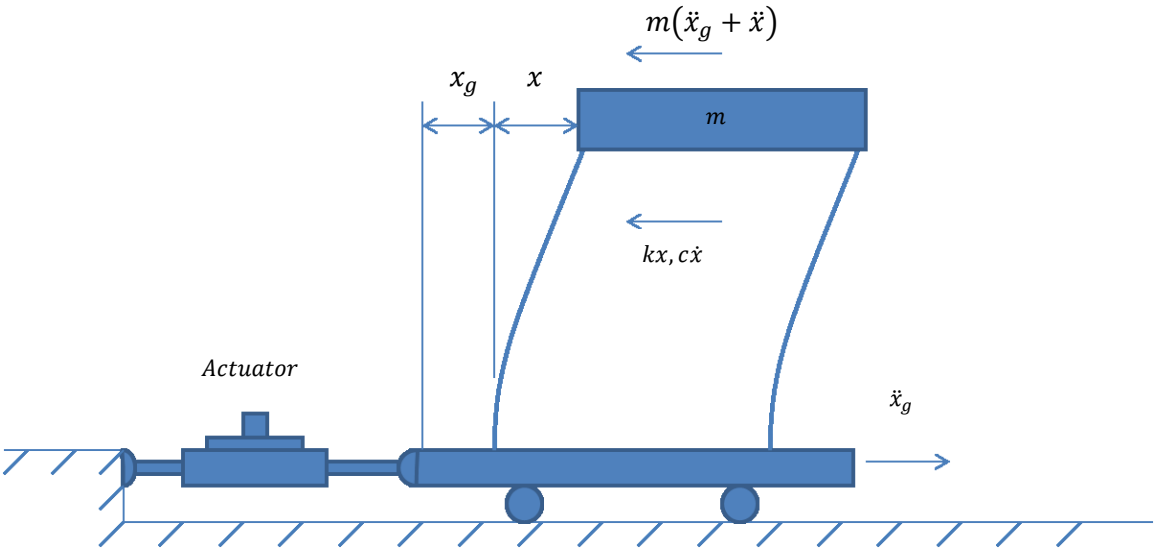

Figure 2.1. Shake table test illustration for SDOF structure.

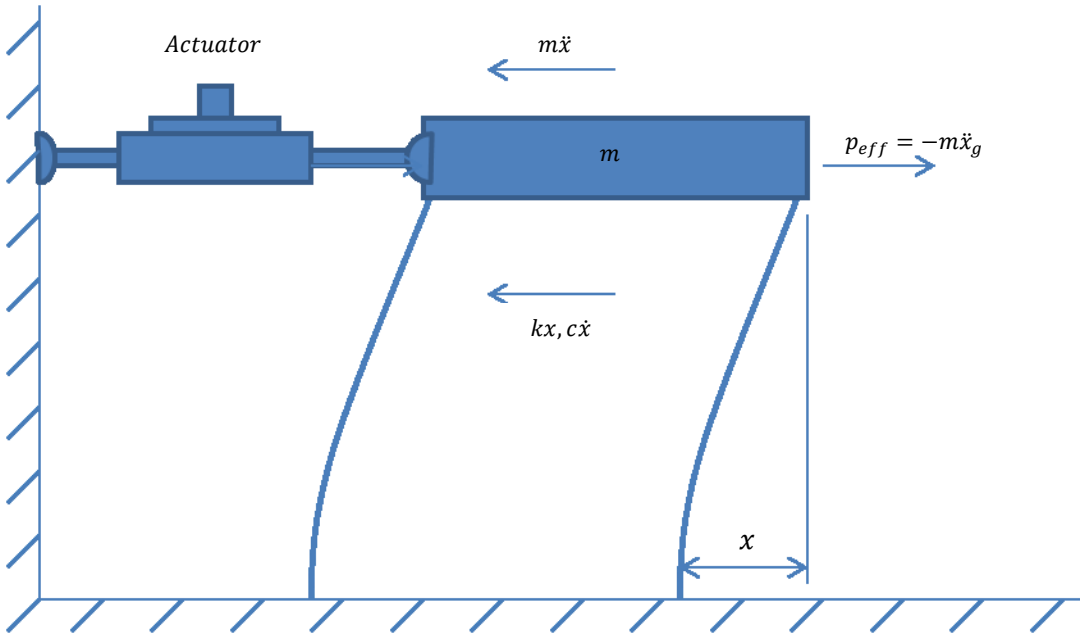

Figure 2.2. EFT illustration for SDOF structure.

2.3 Investigations on EFT

A few proof-of-concept investigations have been performed for the development of linear and nonlinear EFT. During these studies, two separate research groups experimentally verified a main challenge in the implementation of EFT – the presence of control-structure interaction. Control-structure interaction is a result of the dynamic coupling between the actuator and the structure. It limits the ability of the actuator to apply forces at the natural frequency of the structure (Dyke *et al*., 1995). This phenomenon will be further examined in section 2.4 Actuator Dynamics. Various compensation methods have been implemented to overcome its effects.

Dimig *et al*. (1999) first investigated EFT implementation using a linear elastic, SDOF mass-spring-damper cart system. Their work concluded that the addition of a linear velocity feedback loop in the system would adequately compensate the effects of control-

structure interaction. Experimental and computational simulations verified the desired performance which displayed accurate force tracking for the test system subjected to EFT.

Building upon this initial study, Zhao *et al*. (2005) incorporated higher-order servo valve dynamics and a nonlinear flow property into EFT. An experimental EFT study demonstrated that nonlinear velocity feedback compensation outperforms linear velocity feedback in both force command tracking and structural displacement response.

Direct force feedback control for EFT was introduced by Nakata (2013) using a linear elastic SDOF mass-spring system. It was shown through the closed loop system dynamics that it is not possible to fully eliminate control-structure interaction using velocity feedback compensation. Nakata also showed that a proportional-integral-derivative (PID) force controller for EFT was unable to compensate for control-structure interaction. Based on these findings, a loop shaping force feedback controller was proposed for EFT. General background on loop shaping control will be provided in section 2.5 of this chapter. Nakata found that loop shaping force feedback control in EFT provides excellent force tracking and robustness while successfully compensating the effect of control-structure interaction.

2.4 Actuator Dynamics

A review of hydraulic actuator dynamics is needed in order to fully describe the source of control-structure interaction in EFT. Hydraulic actuators are mechanical devices with unique dynamics. They rely on electromagnetic servo valves that control current flow which, in turn, controls the flow of hydraulic oil within the actuator. As a result, the

desired forces, displacements, or accelerations can be achieved depending on the control system used. In EFT, dynamic force control of actuators is needed; therefore, the coupled actuator-structure system dynamics need to be understood.

Figure 2.3 shows a diagram of the underlying dynamics of a hydraulic actuator system with an electromagnetic servo valve (Nakata and Krug, 2013). The dynamics of this servo hydraulic system are outlined by a series of input-output relationships called transfer functions. Transfer function analysis utilizes Laplace transformations in the frequency domain.

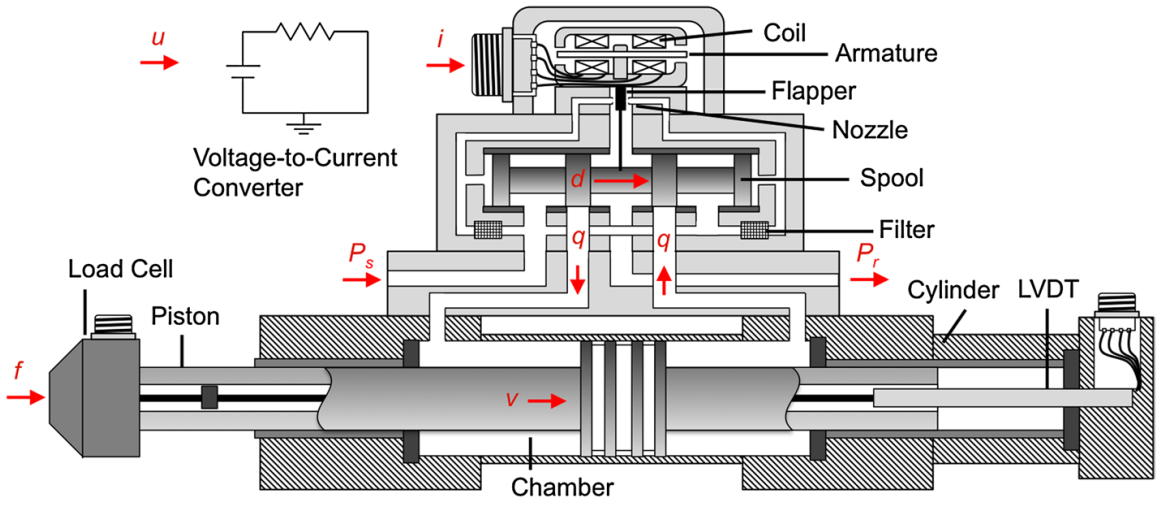

Figure 2.3. Schematic of a servo hydraulic actuator system with linear variable differential transducer (Nakata and Krug, 2013).

In this system, the input valve command *u* is regulated by a controller (i.e. displacement, force, etc.). For a current driven servo valve, a conversion is necessary when the valve command is a voltage. This conversion is described through the following transfer function (Erikson, 1997)

$$H_{iu}(s) = \frac{n_{iu}(s)}{d_{iu}(s)} = \frac{i_{max}}{u_{max}} \frac{1}{1+\tau_c s} \qquad (2\text{-}3)$$

where $H_{iu}(s)$ is the transfer function from voltage to current, i_{max} is the maximum rated current of the converter, u_{max} is the maximum rated voltage of the converter, τ_c is the time constant of the converter, and s is the Laplace variable ($s=i\omega$).

After the conversion to current, the magnetic field of a coil in the servo valve alters the position of a nozzle flapper, which then changes the position of a spool. The following transfer function describes this process (Dyke *et al*., 1995; and Conte and Trombetti, 2000)

$$H_{di}(s) = \frac{n_{di}(s)}{d_{di}(s)} = \frac{d_{max}}{i_{max}} \frac{1}{1+\tau_v s} \qquad (2\text{-}4)$$

where $H_{di}(s)$ is the transfer function from current to spool opening, d_{max} is the maximum opening of the spool, and τ_v is the time constant of the servo valve.

The previous transfer function regulates the opening of a spool which controls the oil flow within the actuator. Merritt (1967) experimentally obtained the following relationship between the spool opening, the pressure drop, and the oil flow within the actuator chamber

$$q = k_q d \sqrt{1 - \frac{d}{|d|} \frac{p}{p_s}} \qquad (2\text{-}5)$$

where q is the oil flow, k_q is the flow gain of the servo valve, d is the opening of the spool, p is the pressure drop across the chamber, and p_s is the supply pressure. For small pressure drops across the actuator chamber, Equation 2-5 shows that the oil flow can be

approximated as the linear relationship $q = k_q d$. The linear oil flow relationship can be represented as

$$H_{qd}(s) = \frac{n_{qd}(s)}{d_{qd}(s)} = k_q \qquad (2\text{-}6)$$

where $H_{qd}(s)$ is the transfer function from spool opening to oil flow.

In addition, the oil flow can be represented as the following flow continuity equation from the actuator piston (Nakata, 2013)

$$q = Av + k_e f + \frac{V}{4\beta A}\dot{f} \qquad (2\text{-}7)$$

where A is the area of the actuator piston, v is the actuator piston velocity, k_e is the flow-force coefficient, f is the actuator force, V is the volume of the actuator chamber, and β is the bulk modulus of the hydraulic oil. The expression $V/4\beta A$ can be represented by the variable k_l, the flow force rate coefficient.

Using Equation 2-7, the oil flow to actuator force transfer function can be represented as (Conte and Trombetti, 2000)

$$H_{fq}(s) = \frac{n_{fq}(s)}{d_{fq}(s)} = \frac{1}{AsH_{xf} + k_e + k_l s} = \frac{d_{xf}}{Asn_{xf} + (k_e + k_l s)d_{xf}} \qquad (2\text{-}8)$$

Where $H_{fq}(s)$ is the oil flow to actuator force transfer function, $H_{xf}(s)$ is the actuator force to piston displacement transfer function, and n_{xf} and d_{xf} are the numerator and denominator polynomials of $H_{xf}(s)$, respectively.

In EFT, the actuators are physically attached to the test structure at the nodes, as seen in Figure 2.2. In consequence, the actuator displacement, x, is equal to the displacement of the test structure. For a SDOF structure, the transfer function $H_{xf}(s)$ is represented by

$$H_{xf}(s) = \frac{n_{xf}(s)}{d_{xf}(s)} = \frac{1}{ms^2+cs+k} \qquad (2\text{-}9)$$

The denominator $d_{xf}(s)$ of the transfer function $H_{xf}(s)$ represents the characteristic equation of the structure. The roots of this polynomial are equal to the natural frequency of the structure. The values of the natural frequency represent the poles of the transfer function which cause the amplification of the structural response at that frequency.

Including the transducer transfer function, $S_f(s)$, from the load cell, the valve command to actuator force relationship is represented by (Nakata, 2013)

$$H_{fu}(s) = S_f(s)H_{fq}(s)H_{qd}(s)H_{di}(s)H_{iu}(s)$$

$$= \frac{n_f}{d_f}\frac{n_{qd}}{d_{qd}}\frac{n_{di}}{d_{di}}\frac{n_{iu}}{d_{iu}}\frac{d_{xf}}{Asn_{xf}+(k_e+k_l s)d_{xf}} \qquad (2\text{-}10)$$

Equation 2-10 shows that the denominator of the structure transfer function is located in the numerator of the valve-to-force relationship. The zeros of the valve-to-force transfer function correspond to the natural frequencies of the structure. This represents how control-structure interaction significantly limits the ability of the hydraulic actuator to apply forces at the natural frequencies of the structure (Dyke *et al*., 1995). Advanced force control methods are able to compensate the effect of control-structure interaction through loop shaping. General loop shaping control will be discussed next.

2.5 Loop Shaping Control

Loop shaping is a frequency domain technique for the design of feedback control systems. It is used when the transfer function of the process is known, so that the desirable closed loop responses are attained (Astrom and Murray (2007); and Kopasakis (2007)). The loop transfer function *L(s)* is a product of the controller *C(s)* and the process *P(s),* resulting in *L(s) = C(s)P(s)*. *L(s)* relates the system input to the system output, as seen in Figure 2.4.

The controller is designed to achieve the shape of the loop transfer function frequency response curve seen in Figure 2.5. The magnitude of *L(s)* should be large for low frequencies to provide good reference tracking, and small at high frequencies to resist amplification of measurement noise (Astrom and Murray, 2007). The gain crossover frequency, ω_{gc} in Figure 2.5, is chosen based on a balance of reducing load disturbances, amplification of measurement noise, and overall robustness (Astrom and Murray, 2007).

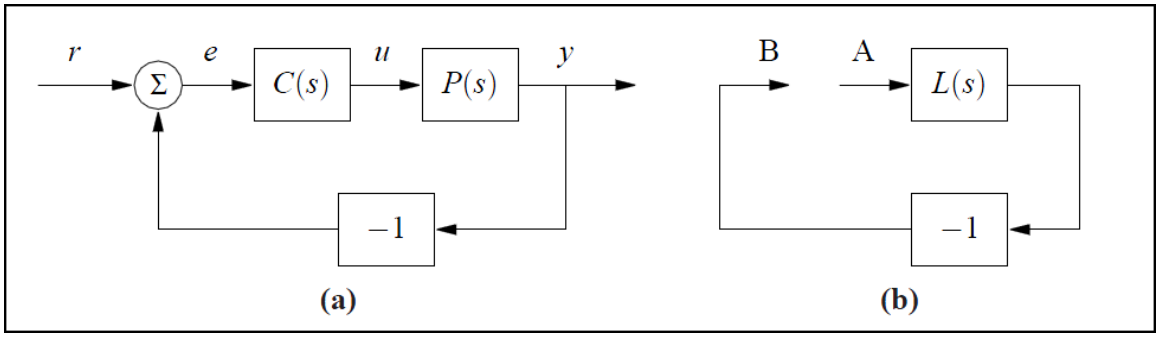

Figure 2.4. Block diagram representation of the loop transfer function (Astrom & Murray, 2007).

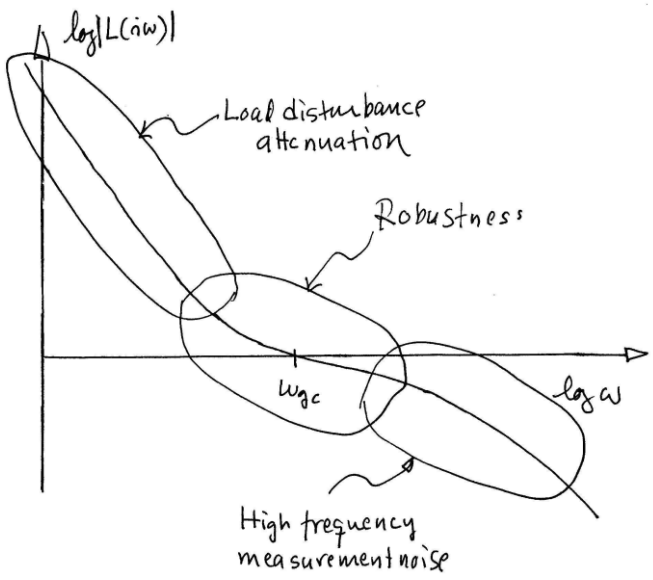

Figure 2.5. Desired frequency response curve for a loop transfer function, *L(s)=C(s)P(s)* (Astrom and Murray, 2007).

2.6 Limitations of Loop Shaping Control in EFT

The Nakata research group has found that loop shaping force feedback control in EFT has generally resulted in good performance, but limitations of this method do exist. In a subsequent experimental study by Nakata and Krug (2013), loop shaping techniques in EFT were extended to a SDOF nonlinear test structure consisting of a 1.2 meter W6x20 steel beam. The findings confirmed that a loop shaping controller provides robustness for nonlinear EFT, and that it can successfully complete testing within the nonlinear range of the structure. However, the limitations of a loop shaping controller were realized as experimental results for nonlinear EFT did not provide adequate force tracking. Figure 2.6 shows time histories taken from Nakata and Krug (2013) for the nonlinear test structure. The measured experimental force becomes significantly less than the reference force as the maximum reference force increases. Errors are greatest at the peaks within

the 5 to 10 second range of the EFT time history. This research serves as an extension of the previous work completed on nonlinear EFT by the Nakata research group.

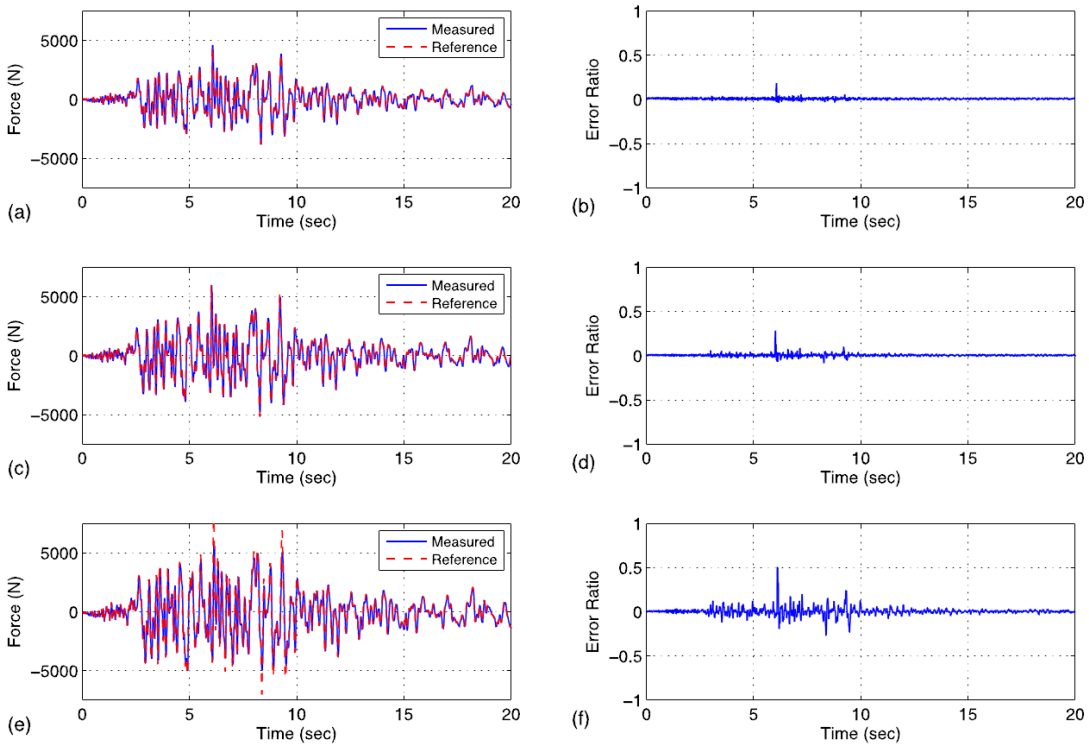

Figure 2.6. Comparison between the reference and measured forces, and force error ratio for the Northridge earthquake: (a) and (b) force time history and force error ratio for the peak excitation of 4448N, respectively; (c) and (d) force time history and force error ratio for the peak excitation of 6672N, respectively; (e) and (f) force time history and force error ratio for the peak excitation of 8007N, respectively. (Nakata and Krug, 2013).

2.7 Summary

This chapter presented background information and a brief overview of the literature on EFT. Previous research shows that loop shaping control in EFT provides robustness and is successful in suppressing control-structure interaction, but limitations are present in the nonlinear range of a structure. This research serves as a continuation of the completed work on nonlinear EFT by the Nakata research group.

Chapter 3

Experimental Setup

This chapter details the experimental setup for a three-dimensional steel frame test structure whose damping and stiffness parameters are defined through free vibration analysis. Along with the structural mass, only these parameters are needed for the implementation of the computational simulation of effective force testing (EFT). All experimental work took place in the Smart Structures and Hybrid Testing (SSHT) Laboratory at Johns Hopkins University (JHU).

3.1 Test Structure Details

The experimental setup in the SSHT Lab consists of a single degree-of-freedom (SDOF), three-dimensional steel frame structure as seen in Figure 3.1. This setup builds upon the literature by extending EFT to a more realistic structural system, as previous studies have limited implementation to simplified SDOF and multi degree-of-freedom (MDOF) proof-of-concept tests.

The three-dimensional steel frame is comprised of ten A36 carbon steel members. Four columns (W4x13) connect to two girders (W6x16) at their top ends, and four beams (W4x13) span perpendicularly between the girders at 16″ on center. All columns, beams, and girders are 49 ¼″ in length, 49″ in length, and 53″ in length, respectively. The W4x13 sections, both columns and beams, are capped at each end with 4 ½″ x 4 ½″ x ½″ thick steel plates which are welded along the perimeter of the W4x13 section. This detail

allows for simplified bolted connections between the members in the structure. Each connection has four ½″ diameter holes that are fastened with $^{3}/_{8}$″ diameter bolts.

The bases of the columns connect to four 9 ¼″ x 4 ½″ x ¾″ thick steel base plates that are bolted to two base beams (W12x65). The base beams are secured to a 12′ x 16′ isolated concrete slab through tie-down threaded holes. This provides a strong floor to attach the frame for any experimental dynamic testing.

Figure 3.2 provides a labeled Google SketchUp rendering of the experimental setup described in this section.

Figure 3.1. Experimental EFT setup in SSHT Lab at JHU.

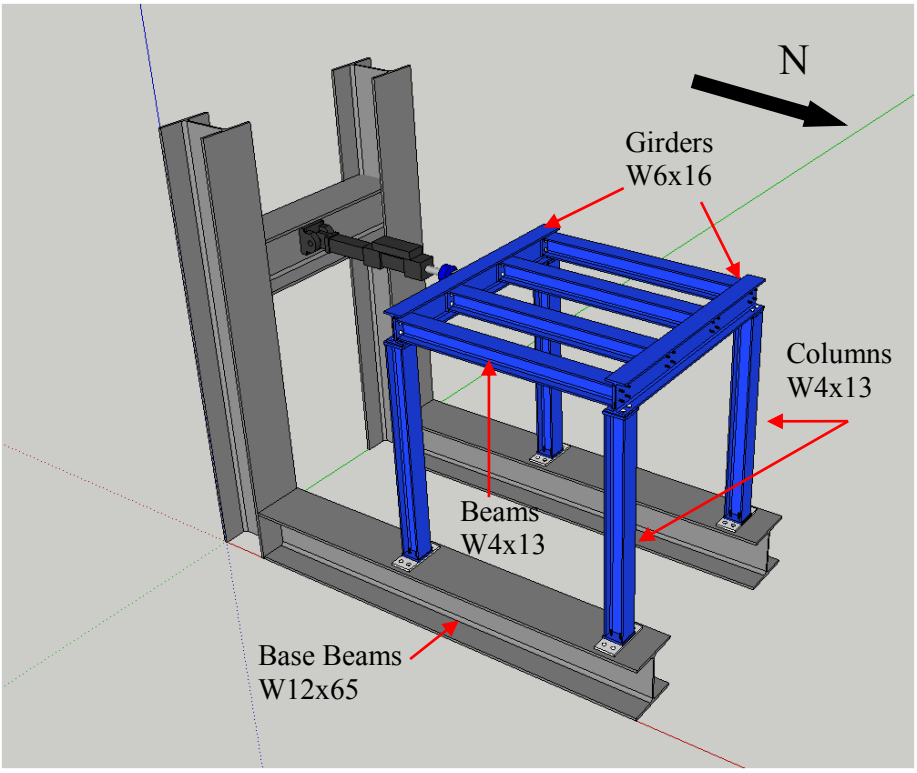

Figure 3.2. Google SketchUp rendering of the experimental EFT setup.

3.1.1 Structure Configurations

Several structure configurations are possible in order to vary the dynamic behavior of the frame. Variability in the structure test setup allows for the implementation of multiple systems for comparison in the computational simulation of EFT. This criterion is best met through two connection schemes located at the bases of the columns. The frame can either be rigidly connected at its base or semi-rigidly connected with 'pins'.

3.1.1.1 Rigid Base

The rigidly connected case sees each column directly secured to the base plates on top of the W12x65 sections. This set up provides the most field-realistic state for the test structure because the base connections are fully fixed. Figure 3.3 displays a typical rigid connection at the column base. It is assumed that this configuration will provide the stiffest structure and, therefore, the highest natural frequency.

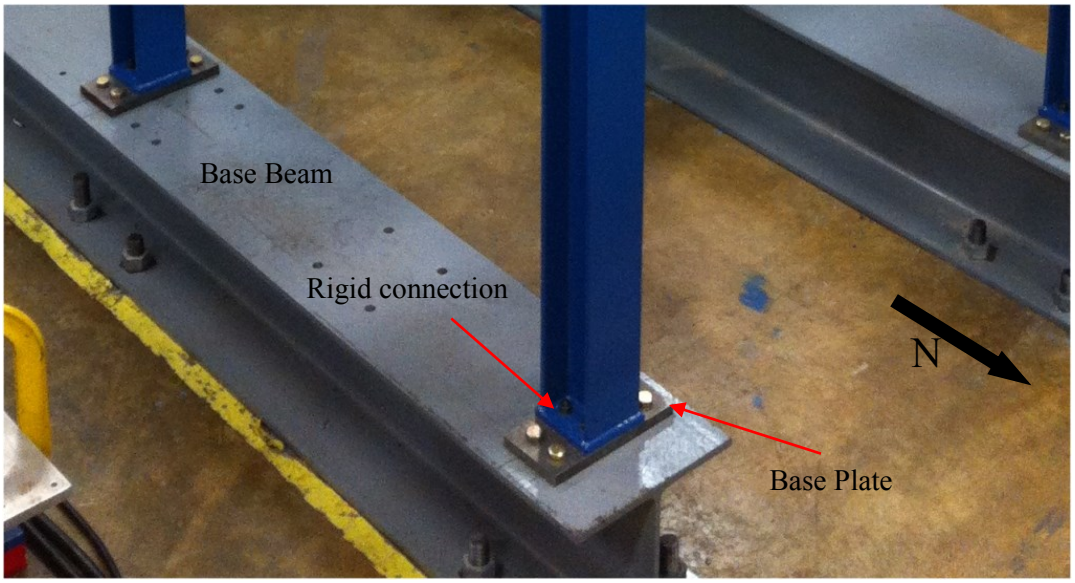

Figure 3.3. Typical rigid connection at column base.

3.1.1.2 Pinned Base

In an effort to decrease the natural frequency of the frame, 5″ long W4x13 sections are added as 'pins' to the bases of the four columns. This allows for a more semi-rigid connection. A typical 'pinned' connection can be seen in Figure 3.4. To ensure that the structure is not too flexible for force control, the pins are rotated 90 degrees with respect

to each other on both East and West sides. The rotation of the pins allows each side to have stiffness contributions from the strong and weak axes of the W4x13 pin sections. This configuration is more clearly seen in Figure 3.5.

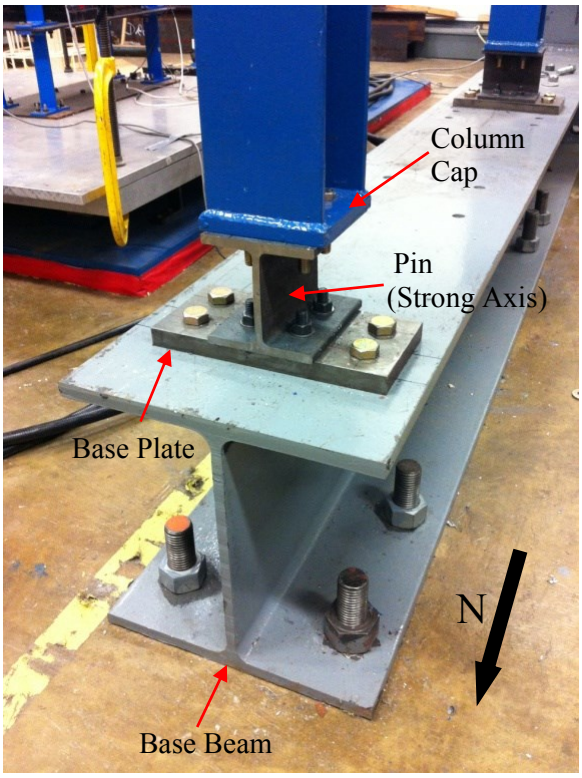

Figure 3.4. Typical pinned connection at column base.

Figure 3.5. Pin orientation at bases of columns (Red circle – strong axis (S), Blue circle – weak axis (W)).

3.2 Instrumentation

Instrumentation for test structures is essential in EFT. Referencing Nakata (2013), the SSHT Lab at JHU incorporates actuators (Shore Western, Inc., Monrovia, California, USA; Model number: 911D) with an embedded direct-current-operated linear variable differential transducer (LVDT) for the measurement of actuator piston displacement. The measurement of actuator force, acceleration, and velocity, uses a 22.2-kN loadcell from (Interface, Inc., Scottsdale, Arizona, USA), 4 g general purpose accelerometers from (Omega, Inc., Stamford, Connecticut, USA), and a 100-mm-stroke electro-magnetic velocity transducer from (Trans-Tek, Inc., Ellington, Connecticut, USA).

A National Instruments (PXI Express, National Instruments Corporation, Austin, Texas, USA) system is employed for an integrated control and data acquisition process. An embedded real-time controller, PXI-8031, allows analog-to-digital and digital-to-analog signal conversions at a sampling rate of 4 kHz. (LabVIEW Real-Time, National Instruments Corporation, Austin, Texas, USA) is used as a software platform for the implementation of controller designs in EFT.

For this research, only the accelerometers are used to measure the free vibration response of each structural system. Acceleration data is collected with the 4 g general purpose accelerometers placed along the top face of the south girder. Acceleration data acquisition is employed through the National Instruments system and LabVIEW Real-Time.

The rigid structure collects data through one accelerometer secured in the middle of the south girder, as seen in the SketchUp rendering in Figure 3.6. An additional accelerometer is added for the testing of the pinned structure to ensure that the orientations of the pin axes do not induce any significant torsional modes of vibration. The accelerometers are placed on the east and west sides of the south girder for this configuration, as shown in Figure 3.7. If both acceleration time histories are in phase, then the data is reliable for free vibration analysis.

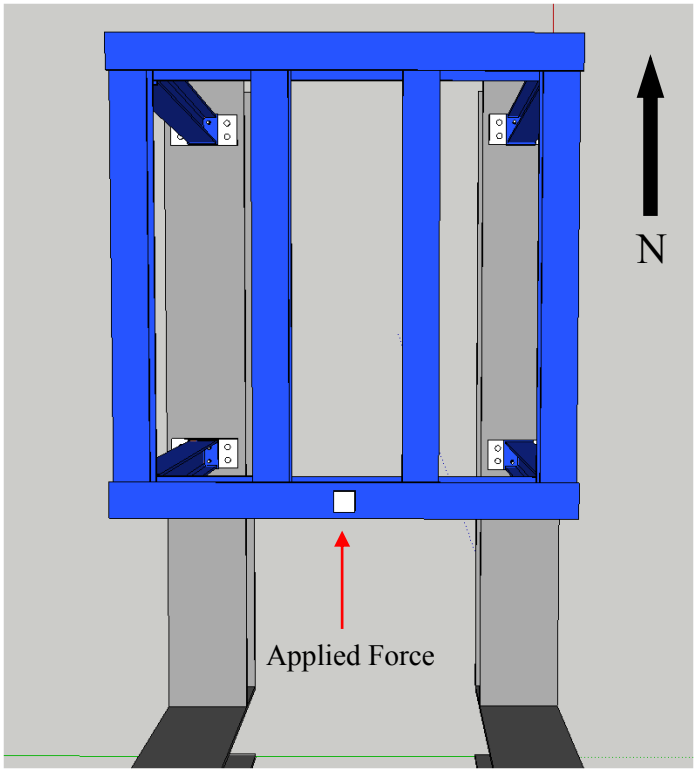

Figure 3.6. Accelerometer placement for rigid case.

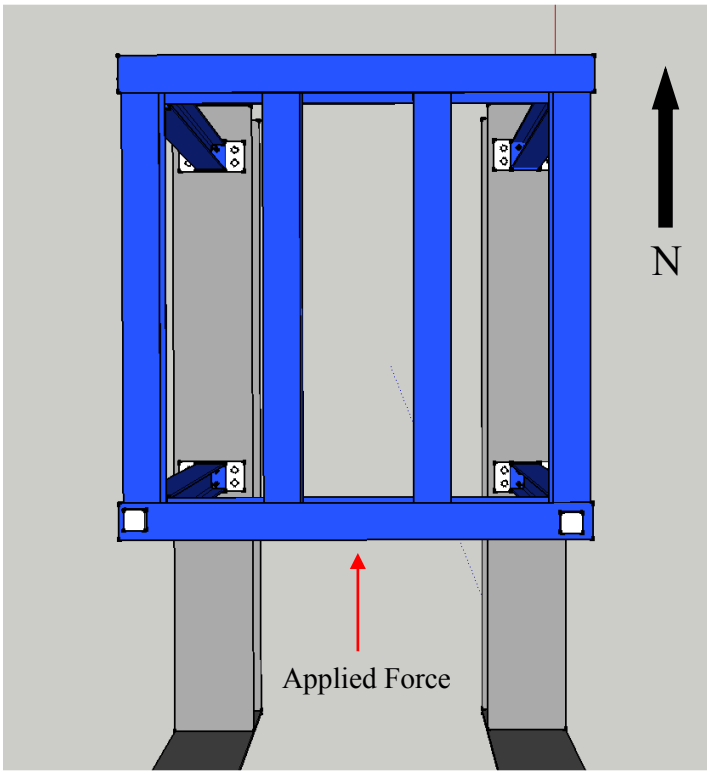

Figure 3.7. Accelerometer placement for pinned case.

3.3 Free Vibration Analysis

Free vibration analysis of the acceleration data is utilized to estimate the natural frequency, damping, and stiffness of the test structure. The calculated natural frequency of the structure is verified through frequency domain methods using the Fast Fourier Transform (FFT) command *fft[]* in Matlab.

A manually applied impulse force to the center of the south girder in the north-south direction serves to capture the first mode of vibration of the structure via translation, as seen in Figures 3.6 and 3.7. The structure is allowed to freely oscillate as the accelerometers record the data into a text file.

The first step in free vibration analysis is to find the period of damped vibration (T_d). This is performed by plotting the acceleration time history and choosing reasonable peaks that fit well within the decaying sinusoidal envelope. Time and acceleration data are recorded over 21 periods of vibration to ensure a thorough average. These are symbolized in the following equations as t_1, $\ddot{x}_1$, t_{21} and $\ddot{x}_{21}$. The period of damped vibration is calculated from the total time elapsed between the two peaks divided by the number of cycles, n

$$T_d = \frac{t_{21} - t_1}{n} \qquad (3\text{-}1)$$

From the period of damped vibration, the damped angular natural frequency (ω_d) is calculated as

$$\omega_d = \frac{2\pi}{T_d} \qquad (3\text{-}2)$$

The damped natural frequency (f_d) is determined from the inverse of the damped natural period

$$f_d = \frac{1}{T_d} = \frac{\omega_d}{2\pi} \quad (3\text{-}3)$$

With the damped characteristics of the structures determined, the logarithmic decrement method is used to estimate the damping ratio (ζ) for each configuration

$$\alpha = \frac{\ln(r)}{2\pi n} = \frac{\zeta}{\sqrt{1-\zeta^2}} \quad (3\text{-}4)$$

where α is a dimensionless parameter and r is the ratio between the two recorded accelerations, $\ddot{x}_1$ and $\ddot{x}_{21}$

$$r = \frac{\ddot{x}}{\ddot{x}}\frac{(t)}{(t+nT_d)} = \frac{\ddot{x}_1}{\ddot{x}_{21}} \quad (3\text{-}5)$$

The damping ratio (ζ) is then calculated by

$$\zeta = \sqrt{\frac{\alpha^2}{1+\alpha^2}} \quad (3\text{-}6)$$

The angular natural frequency (ω_n) and the natural frequency (f_n) of the structure are calculated using the damped natural frequency and the damping ratio

$$\omega_n = \frac{\omega_d}{\sqrt{1-\zeta^2}} \quad (3\text{-}7)$$

$$f_n = \frac{\omega_n}{2\pi} \quad (3\text{-}8)$$

In order to complete the free vibration analysis, the damping coefficient, *c*, and the stiffness, *k*, are calculated using

$$c = 2\zeta\omega_n m \quad (3\text{-}9)$$

$$k = \omega_n^2 m \quad (3\text{-}10)$$

where *m* is the mass of the structure. The total mass is estimated from the member lengths and unit weights of the wide flange sections used.

3.4 Free Vibration Results

The free vibration analysis is completed in Microsoft Excel using Equations 3-1 through 3-10. Table 3.1 displays the results of these calculations.

Table 3.1. Free vibration calculations for the rigid and pinned cases.

	Rigid	Pinned
t_1 (s)	4.3300	3.4860
t_{21} (s)	6.0040	6.3060
n	21.0000	21.0000
$\ddot{x}_1$ (g)	0.1824	0.1593
$\ddot{x}_{21}$ (g)	0.0644	0.0403
T_d (s)	0.0797	0.1343
ω_d (rad/s)	78.8213	46.7897
f_d (Hz)	12.5448	7.4468
r	2.8327	3.9529
α	0.0166	0.0219
ζ	0.0166	0.0219
ω_n (rad/s)	78.8321	46.8009
f_n (Hz)	12.5465	7.4486
m (lb·s²/in)	1.2293	1.2293
c (lb·s/in)	3.2115	2.5164
k (lb/in)	7,639.4688	2,692.5537
m (kg)	215.4560	215.4560
c (N·s/m)	562.8658	441.0460
k (N/m)	1,337,806.6710	471,513.9641

In order to begin the calculations, the free vibration time histories needed to be examined. The free vibration acceleration time history and Fourier spectrum for the rigid configuration are shown in Figure 3.8. These results indicate a stiff structure with low damping as anticipated. In consequence, the natural frequency of the system is calculated at 12.55 Hz. This value correlates well with the peak of the Fourier spectrum of 12.57 Hz. The free vibration acceleration time history and Fourier spectrum for the pinned configuration are shown in Figure 3.9. Both east and west accelerometers are in phase, signifying that no significant torsional modes of vibration are excited. The natural frequency of this system is calculated as 7.45 Hz. The Fourier spectrum verifies the free vibration analysis, peaking at 7.42 Hz.

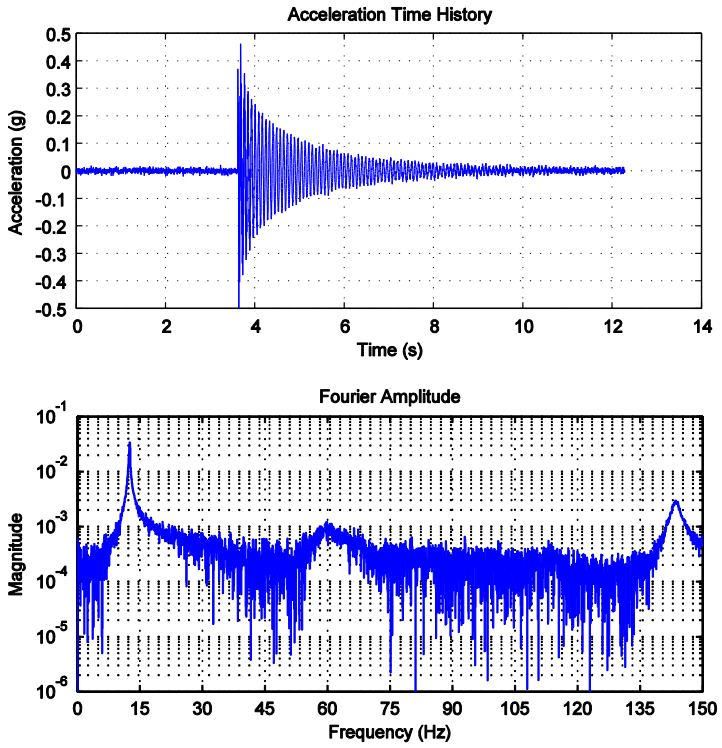

Figure 3.8. Free vibration acceleration time history and frequency domain plots for rigid base.

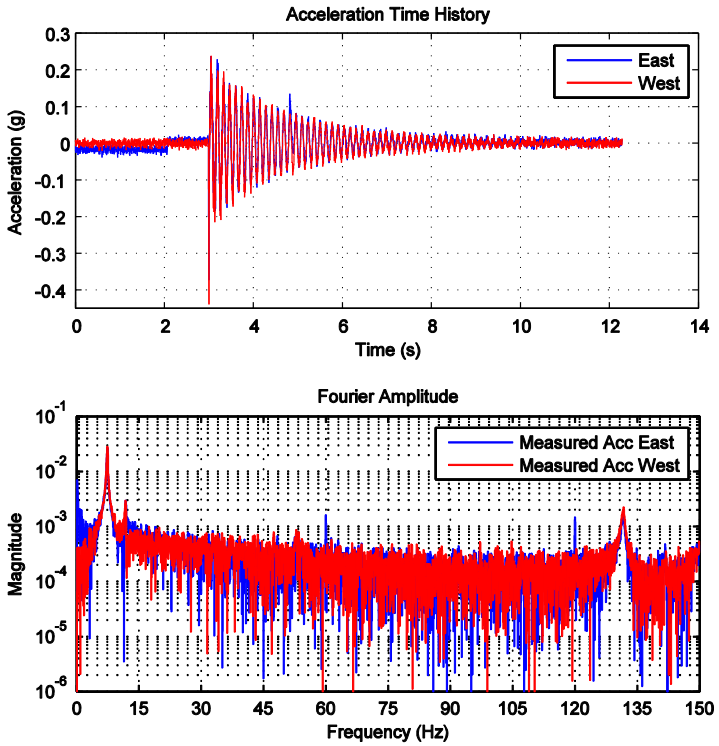

Figure 3.9. Free vibration acceleration time history and frequency domain plots for pinned base.

3.5 Summary

This chapter detailed the experimental setup for the test structure and presented the structural damping and stiffness results for use in the computational simulation of EFT. Computational simulation of EFT is performed using SI units, so the structural damping and stiffness values used in the analyses are 562.9 N·s/m and 1,337,807 N/m for the rigid case, and 441.1 N·s/m and 471,514 N/m for the pinned case. Although not in the scope of this thesis, the author also collaborated in the completion of a full experimental EFT investigation on the same test structure as part of the Nakata research group at JHU.

Chapter 4

Computational Simulation of EFT

Computational EFT is desired for this research because it allows the effects of multiple controlled nonlinear parameters to be investigated without the expense and challenges of experimental implementation. A parametric study is more conducive in obtaining large amounts of data via simulation.

The methods presented in this chapter for the computational simulation of EFT are performed in a computationally equivalent manner as an experimental investigation in the lab. A computational framework developed by Nakata and Krug (2013) provides the basis for the simulations. System identification is performed using a displacement feedback Simulink model that simulates random excitation testing. Force feedback controllers are then designed using loop shaping control and verification of the controllers is carried out through linear elastic simulation. Computational EFT is then extended to three nonlinear structural models: bilinear elastic, bilinear hysteretic, and bilinear hysteretic pinching. Lastly, the EFT evaluation criteria are discussed.

4.1 Computational Framework

Computational tools are a powerful resource in advanced experimental methods such as EFT. Based on the expense and challenge of experimental EFT discussed in Chapter 2, Nakata and Krug (2013) developed a computational framework for EFT in Matlab and Simulink. Figures 4.1 and 4.2 show the Simulink block diagrams for this framework. Figure 4.1 represents the overall force feedback system. The actuator-structure system

block seen in Figure 4.1 is expanded into its own subsystem in Figure 4.2. This subsystem simulates the dynamics between the servo valve and actuator, and inputs the resulting velocity into the structure subsystem. The structure subsystem block, seen in Figure 4.2, can represent any type of modeled structural behavior (i.e. linear, nonlinear). The computational framework includes all equations and transfer function relationships as described in section 2.4 Actuator Dynamics.

Nakata and Krug (2013) validated the computational framework by comparing experimental EFT results with the simulated results for the linear elastic and nonlinear test specimens described in Chapter 2. The verification of this framework makes it a reliable computational tool for EFT research.

Table 4.1 lists the properties of the servo valve and actuator system used in both experimental and computational studies by Nakata and Krug (2013). The values from Table 4.1 are incorporated into the computational simulations discussed in the following sections of this chapter.

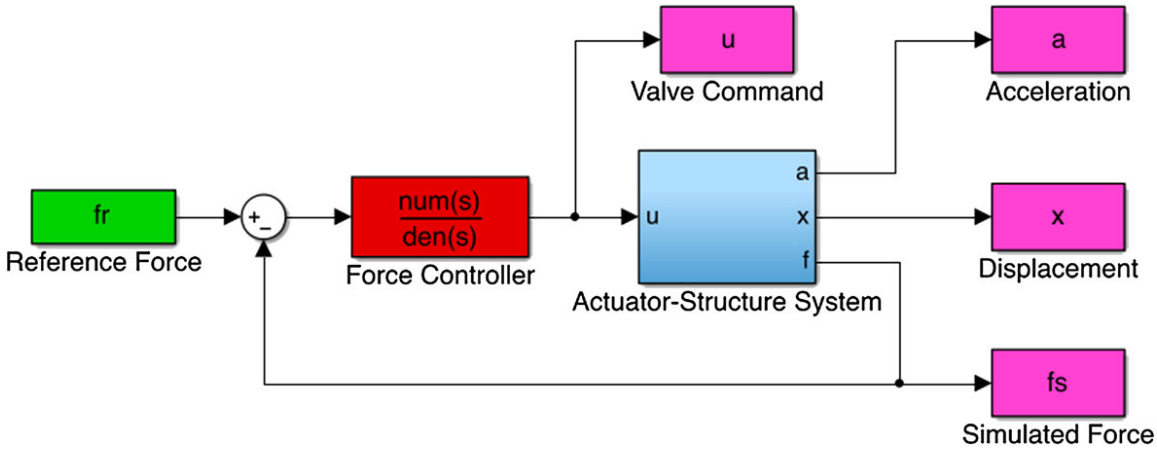

Figure 4.1. Computational framework block diagram for force feedback control (Nakata and Krug, 2013).

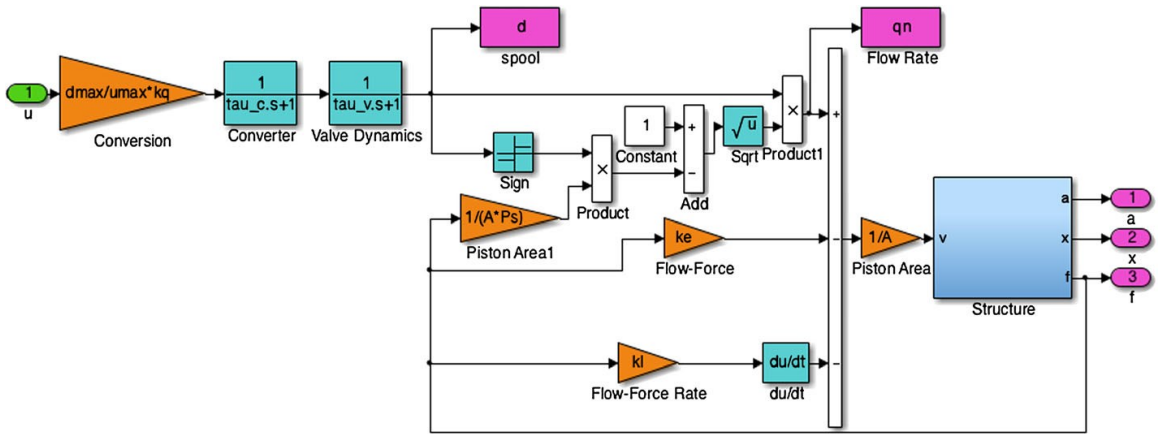

Figure 4.2. Computational framework block diagram for actuator-structure system (Nakata and Krug, 2013).

Table 4.1. Actuator and electrohydraulic servo valve system properties for Smart Structures and Hybrid Testing Lab at JHU (Nakata, 2013; Nakata and Krug, 2013).

	Properties	**Parameters**
$\mathbf{i_{max}}$	Maximum current to the servo valve	20 mA
$\mathbf{u_{max}}$	Maximum voltage from the controller	10 V
$\mathbf{d_{max}}$	Maximum opening of the spool	100 %
A	Piston area	1303 mm^2
$\mathbf{P_s}$	Pressure supply	20.684 MPa
$\mathbf{k_q}$	Flow gain of the servo valve	5.03 x 10^{-6} $m^3/s/\%$
$\mathbf{k_e}$	Flow-force coefficient	3.24 $mm^3/s/N$
$\mathbf{k_l}$	Flow-force rate coefficient	7.89 x 10^{-2} mm^3/N
$\mathbf{\tau_c}$	Time constant of the converter	0.0018 s
$\mathbf{\tau_v}$	Time constant of the spool	0.20

4.2 System Identification

Before implementation of the computational EFT framework, the coupled dynamics of the actuator-structure system need to be identified. Implementing the mass, damping,

and stiffness parameters calculated in Chapter 3 yields the system transfer functions via computational system identification techniques. The following computational process described is equivalent to the experimental process in Nakata (2013).

For the system identification, a displacement feedback model is created in Simulink to simulate band-limited white noise in random excitation testing. The block diagram of this model can be seen in Figure 4.3. Random excitation is generated with the *randn[]* command in Matlab for a time equal to fifty seconds, a comparable value used in experimental band-limited white noise techniques. The input matrix *disp* contains the time vector and random number vector of simulated displacements. Sampling time is 0.002 seconds and the random number vector is converted to millimeters beforehand. This conversion ensures that the simulated displacements will be within the linear elastic range of the structures.

The displacement feedback model outputs the valve command (u), structure acceleration (a), structure displacement (x), and simulated force (f_s). As Figure 4.3 shows, the output displacement x is circulated back through the system and subtracted from the reference displacement (*disp*), thus completing the closed loop system. The actuator-structure block contains dynamics of the actuator-structure subsystem seen in Figure 4.2. A linear elastic structural model is used for the system identification. This computational process yields the valve-to-force and force-to-displacement transfer functions described in section 2.4 Actuator Dynamics.

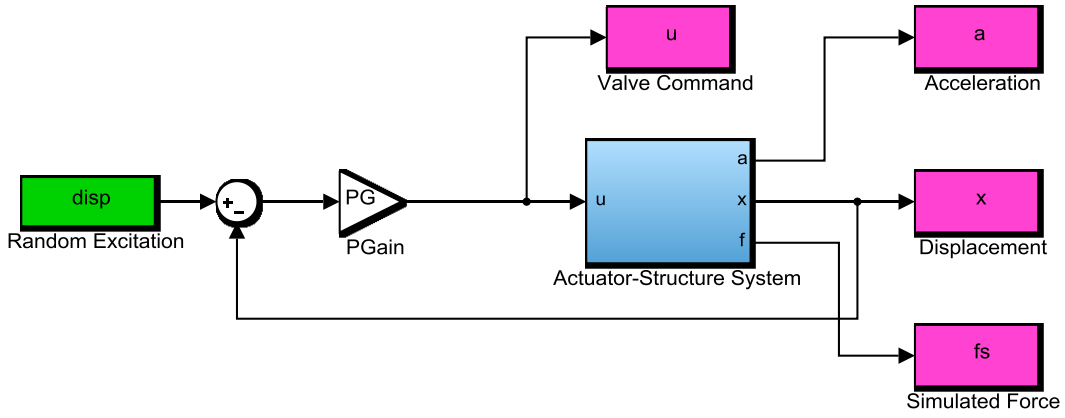

Figure 4.3. Displacement feedback control block diagram.

4.3 Loop Shaping Controller Design

Based on the transfer functions obtained in system identification, loop shaping controllers are designed for both systems. The subsequent material on loop shaping control in EFT is adapted from Nakata (2013). The optimal design of a loop shaping controller in EFT implements the lowest order controller that successfully counters the effect of control-structure interaction. It can be designed using the following equation

$$C_f^{LS} = \frac{\gamma}{d_{xf}} \qquad (4\text{-}1)$$

where γ is the controller gain and d_{xf} is the denominator of the structure transfer function. Using the structure transfer function as the poles of the controller compensates for the effect of control-structure interaction. This process is called pole-zero cancellation. The

poles of the controller *C(s)* will negate the zeros of the process *P(s)* by amplifying the overall response of the loop transfer function *L(s)=C(s)P(s)*.

4.4 Structural Models

Once the loop shaping controllers are designed, they can be implemented in the computational EFT framework described in section 4.1. The framework is developed in a modular fashion so that any type of structural response can be modeled. Each structural model follows the same system hierarchy in the computational framework.

The differences in the models lie within the structure subsystem itself. Unlike the linear elastic case, the structural stiffness will change along with the loading history for each nonlinear model. The nonlinear models simulate these changes through prescribed yield displacements (X_y), prescribed yield strengths (Y_y), the original stiffness of the system (k_0), and the post-yield stiffness of the system (k_1). These parameters are varied before each simulation in order to observe their respective effects on the force tracking capabilities of the controller and the overall structural response. A ± 10 volt saturation for the valve command is added to all models to simulate the experimental conditions in the lab.

4.4.1 Linear Elastic Model

The first simulation for each system implements a linear elastic structural model. Successful linear elastic simulations serve as verification of the controller designs since they are designed for the linear elastic range of the structure. This model will provide a base case in the evaluation of each nonlinear model. The structure block diagram for a

linear elastic model is shown in Figure 4.4, and Figure 4.5 shows an example of the force-displacement relationship in linear elastic response. The restoring force in the linear elastic model will be unchanged throughout the entire time history ($R = k_0 * x$).

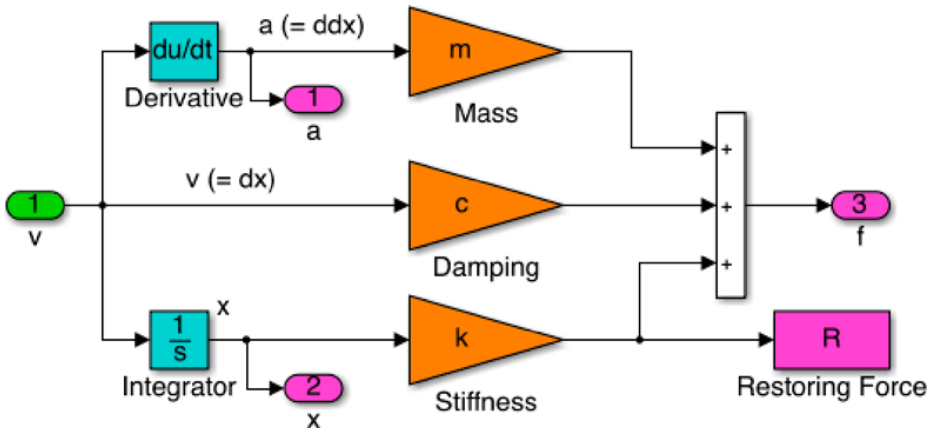

Figure 4.4. Structure block diagram for linear elastic model.

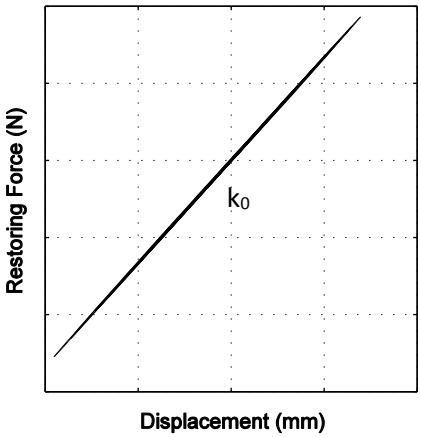

Figure 4.5. Example of linear elastic behavior.

4.4.2 Bilinear Elastic Model

The bilinear elastic structural model, as seen in Figure 4.6, changes the structural stiffness once the response reaches a prescribed yield displacement (X_y). If the absolute value of the structural displacement (x) is less than the yield displacement, the system maintains linear elastic behavior ($R = k_0 * x$). However, when the displacement of the structure exceeds the yield displacement, the restoring force includes post-yield stiffness effects ($R = [k_1 * (x - X_y) + k_0 * X_y]$). This model produces elastic unloading, an example of which is seen the force-displacement relationship in Figure 4.7.

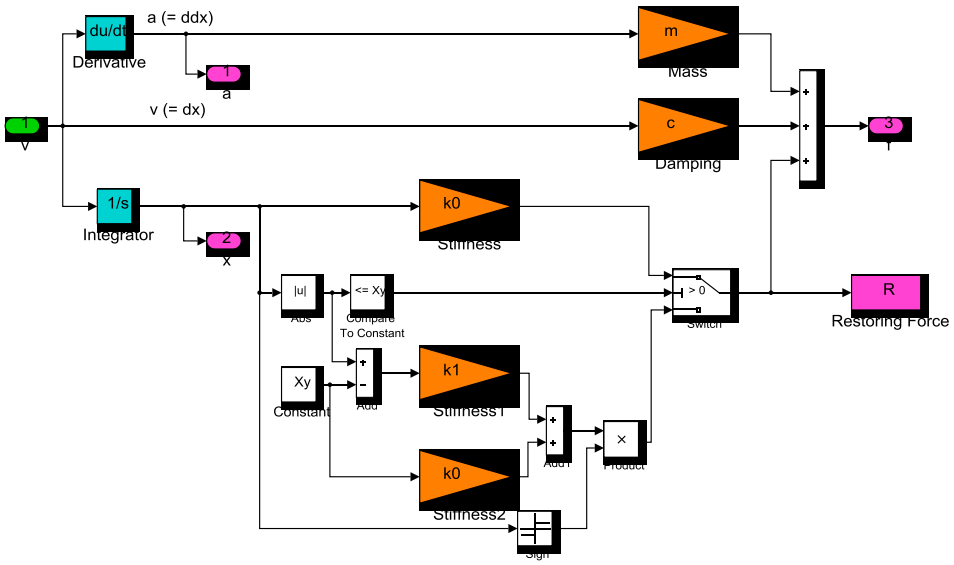

Figure 4.6. Structure block diagram for bilinear elastic model.

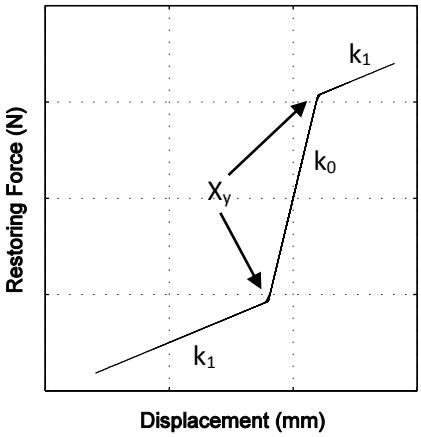

Figure 4.7. Example of bilinear elastic behavior.

4.4.3 Bilinear Hysteretic Model

Figure 4.8 shows the bilinear hysteretic structure subsystem. Unlike the bilinear elastic model, the restoring forces developed here are based upon yield strength (Y_y) and post-yield stiffness (k_1). The structural displacement is compared to a constant of $Y_y/(k_0-k_1)$, which represents an equivalent yield displacement of the system. The restoring force follows a linear elastic ($R = k_0*x$) response when the absolute value of displacement is less than the constant, otherwise, the restoring force includes the post-yielding effects ($R = Y_y + k_1*x$). This model produces inelastic unloading, an example of which is seen in the restoring force-displacement relationship in Figure 4.9. The hysteresis is produced by energy dissipation in the system which is equal to the total area under the hysteresis curve.

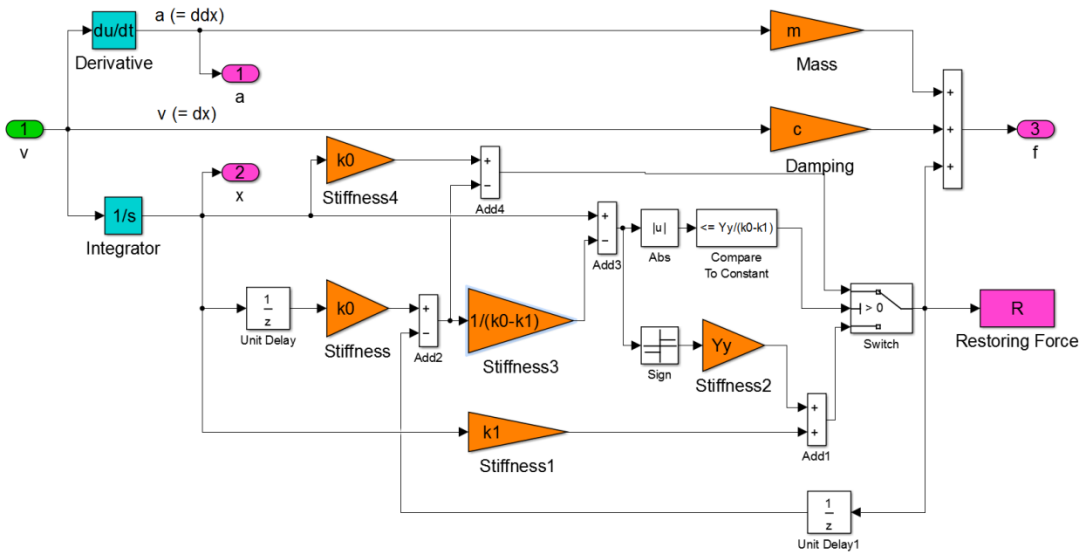

Figure 4.8. Structure block diagram for bilinear hysteretic model.

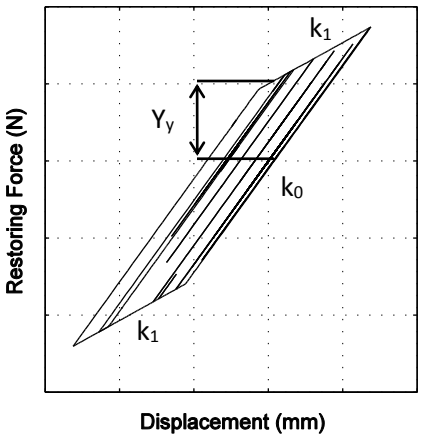

Figure 4.9. Example of bilinear hysteretic behavior.

4.4.4 Bilinear Hysteretic Pinching Model

The bilinear hysteretic pinching model can be seen in Figure 4.10. The nonlinear restoring forces developed in this model depend upon yield strength (Y_y) and post-yield stiffness (k_1). Its behavior is similar to the bilinear hysteretic model, except the pinching action adds an additional criterion to the restoring force after yielding. An example of a

bilinear hysteresis with a pinching effect is shown in Figure 4.11. The controlling constant for this model is $Y_y/[2*(k_0-k_1)]$. Linear elastic behavior results for displacements below this constant value ($R = k_0*x$). Restoring forces vary above this threshold into two different cases. The first is continuation of the loading, dependent on the post-yield stiffness and yield strength ($R = Yy + k_1*x$), and the second only depends on the post-yield stiffness ($R = k_1*x$) for the unloading. In the same manner as the bilinear hysteretic model, the hysteresis forms due to dissipation of energy within the structure. An example of a structural system with this nonlinear behavior is a shear wall with fastener pull through response.

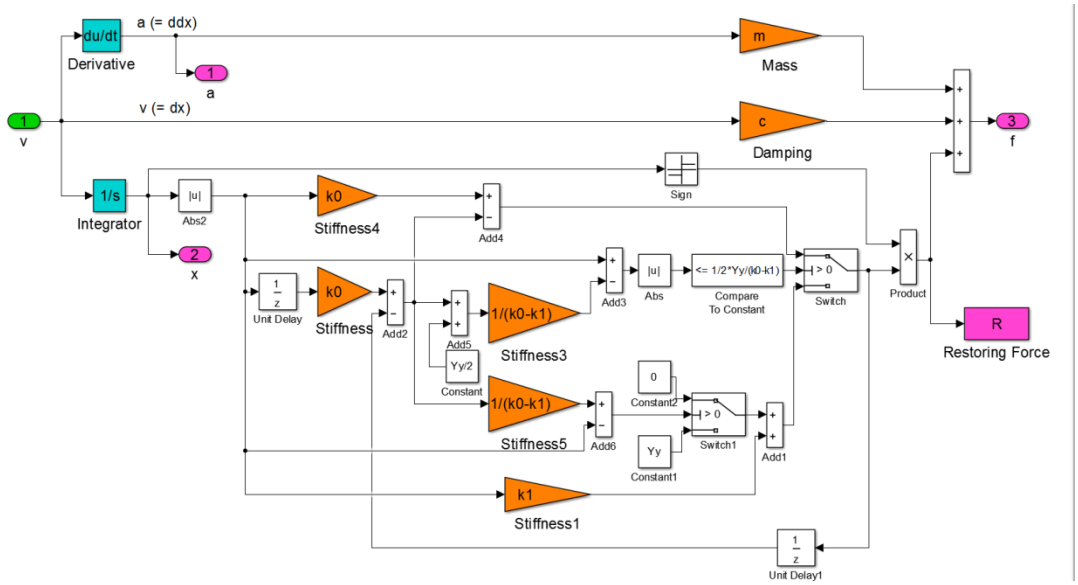

Figure 4.10. Structure block diagram for bilinear hysteretic pinching model.

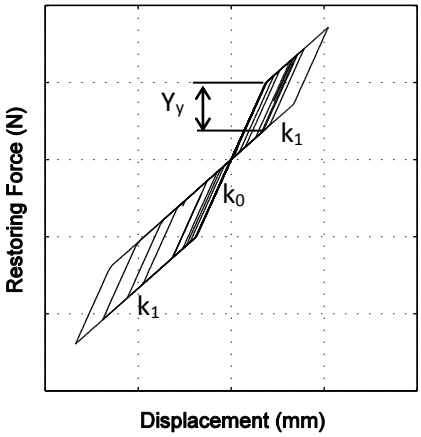

Figure 4.11. Example of bilinear hysteretic behavior with pinching.

4.5 EFT Evaluation Criteria

The 1995 Kobe earthquake acceleration record was chosen for all computational simulations. This record provides well-defined peak forces that are desirable in evaluating the performance of the force controllers in EFT. Accurate tracking of the reference force over the entire time history is a primary focus in the EFT results and data analysis. The inherent time delays of the controllers are adjusted before applying the following methods of data analysis.

Root mean square error and maximum positive and negative peak-to-peak ratios are used to measure correlation between the reference and simulated forces. Force error ratios are also examined in each individual analysis. These error ratios are calculated from the respective force errors normalized by the maximum value of the reference force.

4.5.1 Time History Data

Individual time history results include: reference vs. simulated force, force error ratio, structural displacement, and valve command. They provide a qualitative means of examination for all linear elastic and nonlinear simulations. Appendices A – C contain the complete simulation results for the bilinear elastic, bilinear hysteretic, and bilinear hysteretic pinching models, respectively.

4.5.2 Root Mean Square Error

Root mean square error (RMSE) provides a measure of deviation between the simulated force and reference force. For these analyses, it is calculated by

$$RMSE = \sqrt{\frac{\sum_{i=1}^{n}(f_{ri}-f_{si})^2}{n}} \qquad (4\text{-}2)$$

where f_{ri} is the reference force at time step i, f_{si} is the simulated force at time step i, and n is the total number of time steps in the Kobe earthquake force-time history. RMSE will give a performance metric in a global sense.

4.5.3 Peak-to-Peak Ratio

Peak-to-peak ratios show the how well the maximum positive and maximum negative magnitudes of the simulated force compare with the expected values of the reference force. In this analysis, the maximum positive peak is the largest force in the positive range of the time history, and the maximum negative peak is the largest force in the negative range of the time history. This is an important aspect in gauging the force

tracking capabilities of EFT, especially as the structure moves into the nonlinear range. Peak effective forces must be able to be accurately reproduced in order to fully capture the structural response of any tested structural system. This is important because they represent the maximum forces that the structure will see. The maximum positive and negative peak-to-peak ratios, respectively, are calculated as such

$$P2P_{Pos} = \frac{f_{s(pos)}}{f_{r(pos)}} \qquad (4\text{-}3)$$

$$P2P_{Neg} = \frac{f_{s(neg)}}{f_{r(neg)}} \qquad (4\text{-}4)$$

For the Kobe record used in the computational simulations, the maximum positive peak force occurs during the interval 5.4 to 5.6 seconds, and the maximum negative peak force occurs during the interval 3.0 to 3.3 seconds. Peak-to-peak ratios will provide a performance metric in a local sense.

4.6 Summary

This chapter examined the published computational framework and extended it to full computational simulation of EFT. The computational simulation of EFT presented in this chapter is equivalent to the experimental implementation of EFT. Four structural models were introduced for computational EFT analysis in the next chapter: linear elastic, bilinear elastic, bilinear hysteretic, and bilinear hysteretic pinching. Evaluation criteria were discussed for the simulation results, and the 1995 Kobe acceleration record was chosen for all simulations.

Chapter 5

Computational EFT Results and Discussion

This chapter presents the results from the computational simulation of effective force testing (EFT) with linear elastic and nonlinear structural models. First, the system frequency response and loop shaping force controllers are defined for each structure. Next, the results from a representative time history for each model are examined, and root mean square error (RMSE) and peak-to-peak ratios are investigated against the post-yield stiffness. Overall trends on the performance of EFT due to the nonlinear structural parameters are then summarized.

5.1 System Identification

The transfer functions of the rigid and pinned structures are obtained through simulation of the displacement feedback model. Figures 5.1 and 5.2 display the computational system identification results for the rigid and pinned structural configurations, respectively. These figures show the frequency response curves and phase angles for the valve command to the actuator force (H_{fu}) and actuator force to actuator displacement (H_{xf}) relationships. They represent the open-loop dynamics of the coupled actuator-structure systems. The blue curves represent the frequency response of the computational system identification. In order to capture the frequency response of this simulation, analytical models are developed using a curve fitting technique. The analytical models are needed for the subsequent design of the loop shaping controllers. It is seen that analytical models, shown as a dashed red curve, fully capture the computational response.

The frequency responses for both structures have distinct peaks in magnitude that occur at their natural frequencies. A pronounced drop in magnitude is noticeable in the valve-to-force response curves at the same frequencies. This behavior is indicative of control-structure interaction, which verifies the inability of the actuator to successfully apply forces at the natural frequency of the structures. This is why a significant decrease in magnitude is observed. A successful force feedback controller design will compensate for this phenomenon.

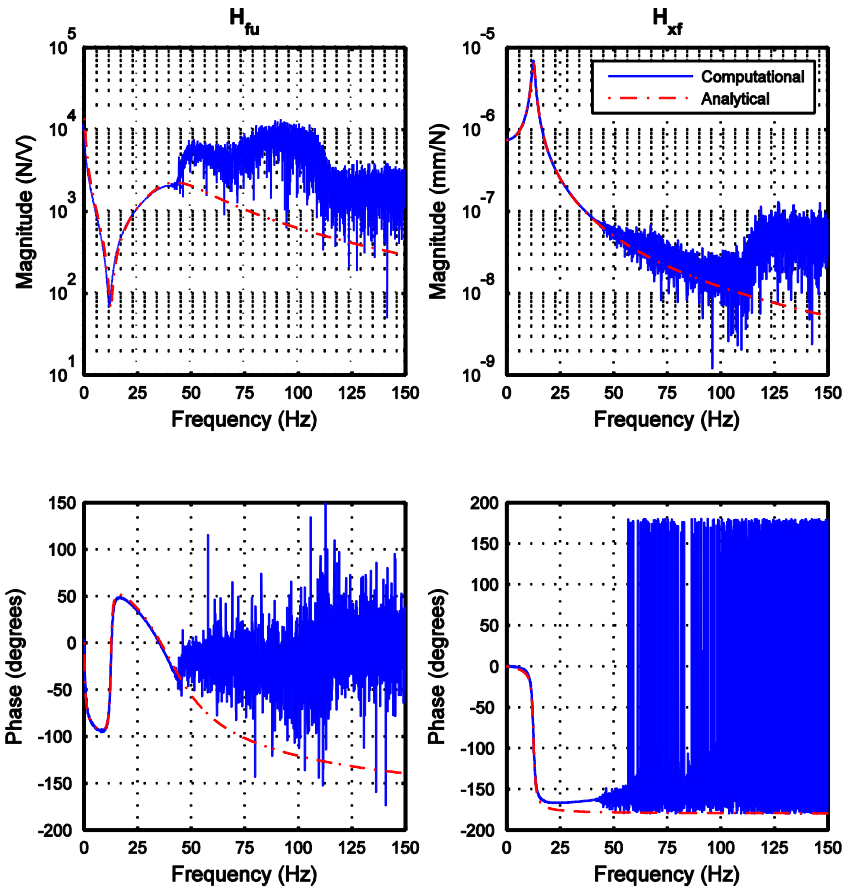

Figure 5.1. Frequency response curves and phase curves for rigid base configuration. Valve command to actuator force, H_{fu} (left), and actuator force to actuator displacement, H_{xf} (right).

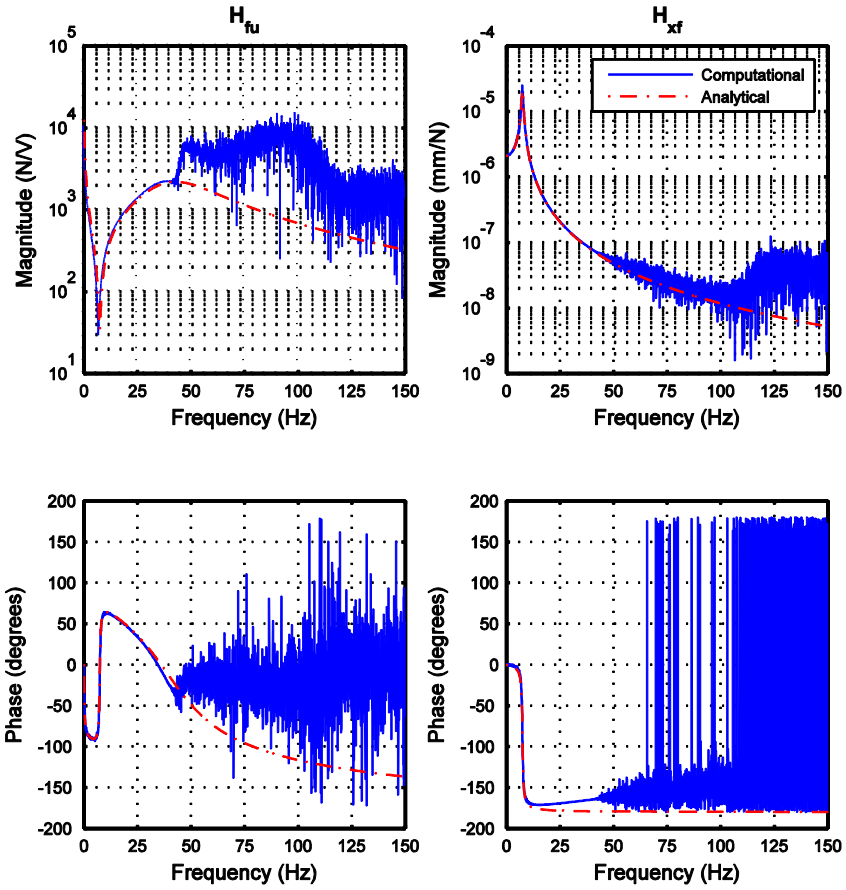

Figure 5.2. Frequency response curves and phase curves for pinned base configuration. Valve command to actuator force, H_{fu} (left), and actuator force to actuator displacement, H_{xf} (right).

5.2 Loop Shaping Controller Design

The frequency response curves seen in the previous section are representative of the linear elastic structure. This means the force feedback controllers will be designed for the linear elastic range in the implementation of computational EFT for both linear elastic and nonlinear models.

The following loop shaping force feedback controllers are designed to compensate the effect of control-structure interaction

Rigid base: $C_f^{LS} = \frac{8}{s^2+8s+6116}$

Pinned base: $C_f^{LS} = \frac{8}{s^2+4.2s+2167}$

where s is the Laplace variable ($s=i\omega$). Denominators polynomials in the controllers are taken from the analytical force-to-displacement transfer functions obtained in the previous section.

Figures 5.3 through 5.6 show the frequency response characteristics for both controllers. As seen in Figures 5.3a and 5.5a, the controller transfer functions peak at the respective natural frequency of the structures. The amplification of these transfer functions will compensate for the drop in magnitude recognized in the valve-to-force relationships.

The loop transfer functions for both controllers are shown in Figures 5.3b and 5.5b. Both loop transfer functions exhibit the desired performance characteristics; high gain in the low frequency range and low gain in the high frequency range. Crossover frequencies occur around 10 Hz for both systems, which is a result of the gain $\gamma=8$.

Performance of the controllers is analyzed through the closed loop system dynamics ($CL(s)=L(s)/[1+L(s)]$) as seen in Figures 5.4 and 5.6. Both controllers have good performance in the low frequency range (0-5 Hz), and then slowly trail off into the high frequency range, thus demonstrating robustness.

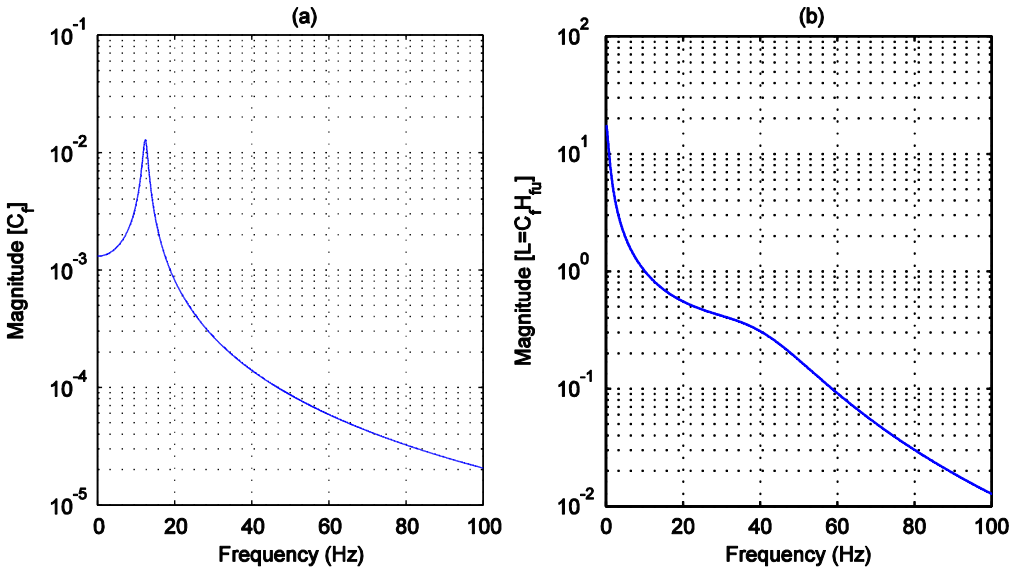

Figure 5.3. Rigid base a) controller transfer function b) loop transfer function.

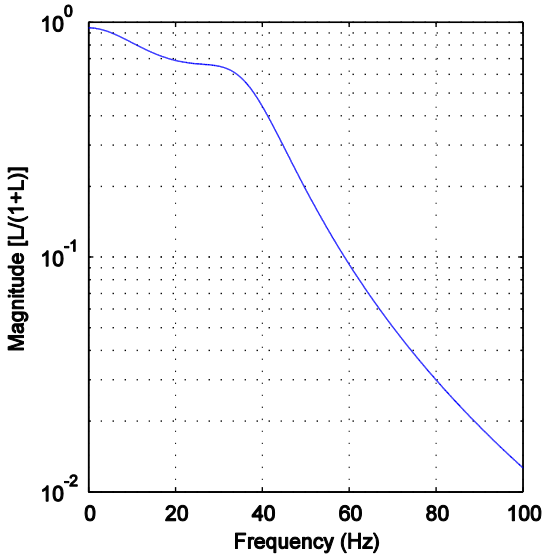

Figure 5.4. Rigid base closed loop force feedback transfer function.

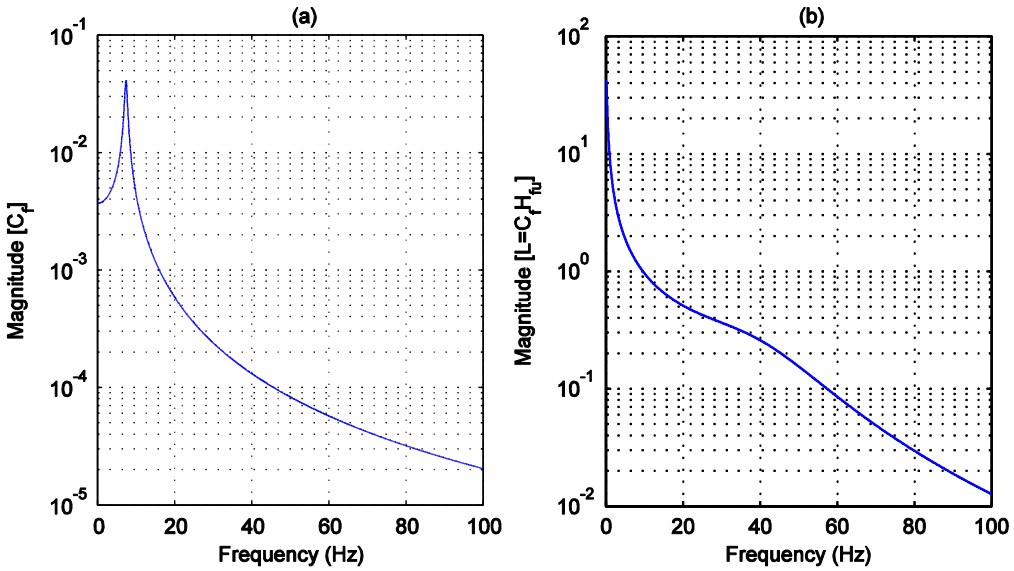

Figure 5.5. Pinned base a) controller transfer function b) loop transfer function.

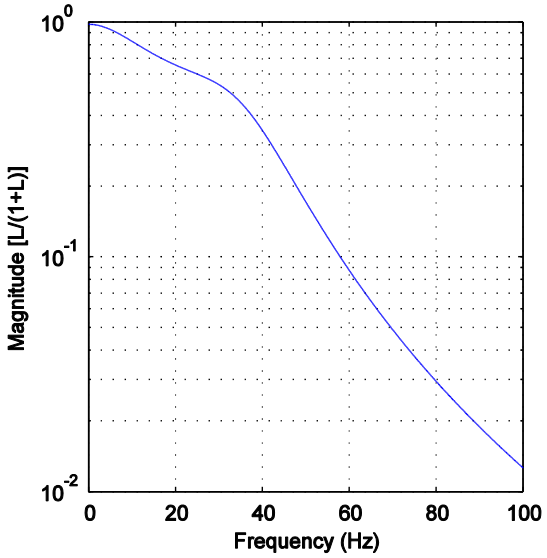

Figure 5.6. Pinned base force feedback closed loop transfer function.

5.3 Results for Computational Simulation of EFT

Next, the loop shaping force feedback controllers are implemented into the computational EFT framework. The linear elastic model is simulated first, and then the nonlinear models are analyzed through a parametric study.

5.3.1 Linear Elastic Model

Performance verification of the designed loop shaping force feedback controllers is carried out through linear elastic simulation. Since the controllers were designed in the linear range of the structure, optimal performance should be achieved using this model. Figures 5.7 and 5.8 display the time histories for the a) force, b) error ratio, c) structure displacement, and d) servo valve command, as well as the e) restoring force-displacement relationship for the rigid and pinned cases, respectively.

It is observed that the simulated forces match up well with the reference forces, thus representing the desired global force tracking capability. Errors between the two forces are generally small with greater local concentrations at the peaks. Table 5.1 contains the resultant values of the EFT evaluation criteria for each structure. These values will be used as a basis for comparison to the results of the nonlinear models.

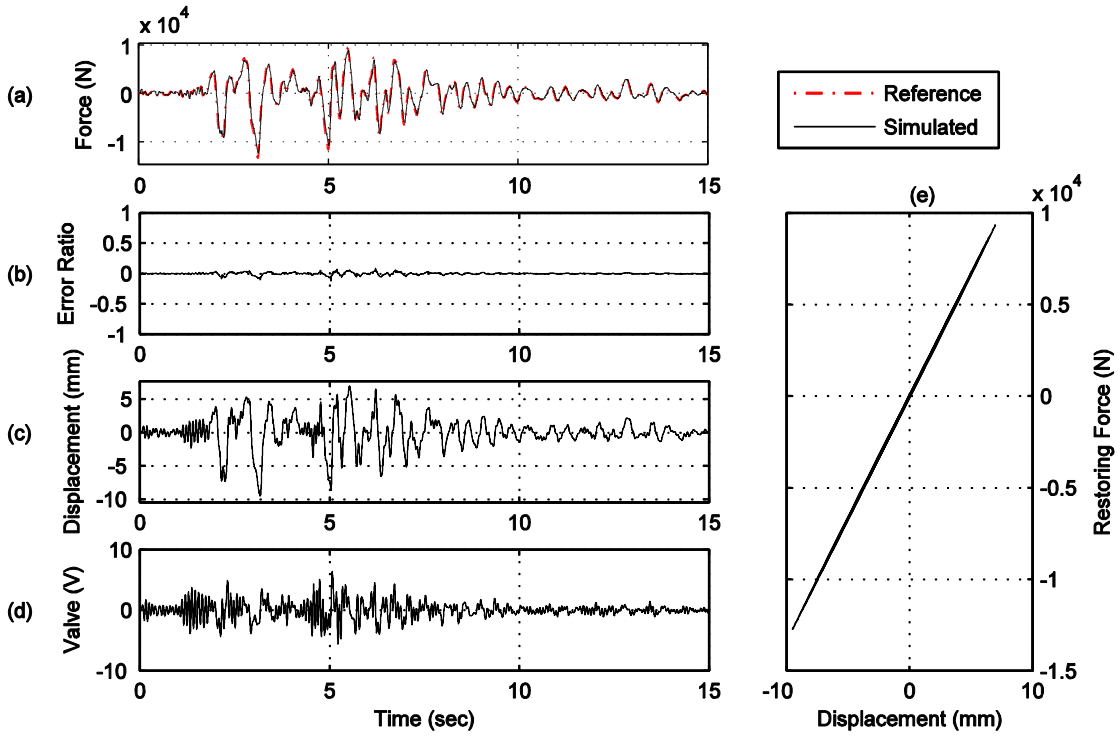

Figure 5.7. Rigid base linear elastic simulation results.

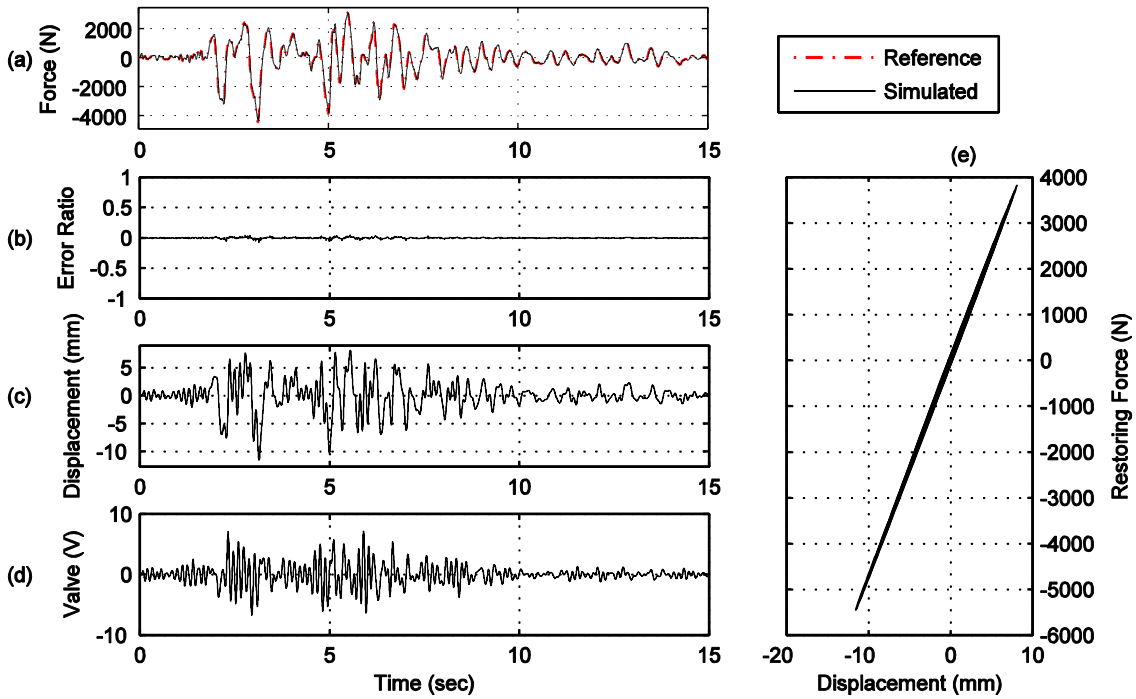

Figure 5.8. Pinned base linear elastic simulation results.

Table 5.1. RMSE, maximum positive peak-to-peak ratio, and maximum negative peak-to-peak ratio for both systems.

	RMSE (N)	Max Pos (f_s/f_r)	Max Neg (f_s/f_r)
Rigid	237.45	0.934	0.923
Pinned	40.43	0.978	0.976

Creating a ratio of the RMSE in Table 5.1 to the maximum value of the reference force reveals that the simulated force for the rigid case can deviate by 1.8%, and the simulated force for the pinned case can deviate by 0.9%. The low percentages reinforce the general good performance of the loop shaping controllers. The slight differences in the evaluation criteria for linear elastic simulation can be traced back to the closed loop responses for each controller, seen in Figures 5.4 and 5.6. Complete unity (10^0) between the reference force input and simulated output could not be entirely achieved during the controller design, so there will always be some error for a stable simulation.

5.3.2 Bilinear Elastic Model

Bilinear elastic analysis involves simulations that vary the prescribed structure yield displacement (X_y) and post-yield stiffness (k_1). In the simulations, yield displacements are increased in 0.002 meter (m) increments; from 0.002 m to 0.008 m for the rigid case and 0.002 m to 0.010 m for the pinned case. Post-yield stiffness is incrementally decreased by 10%, from $0.9*k_0$, to $0.1*k_0$, for each yield displacement. These variations intend to create a breadth of simulations for the parametric study which enables comparison of highly nonlinear response to linear elastic like behavior. In total, 36 simulations are performed for the rigid structure and 45 simulations are performed for the pinned structure.

For this model, the reference forces had to be scaled to ensure portions of the displacement time histories exceed the yield displacements. The maximum reference force for the rigid structure was scaled to 13,344 N (3 kips) and the maximum reference force for the pinned structure was scaled to 4,448 N (1 kip). In order to stay consistent between structural models, the scaling is unchanged throughout all linear and nonlinear simulations.

An example of a time history plot for the bilinear elastic model is shown in Figure 5.9. The figure shows results for the rigid structure with a 0.004 m yield displacement and a $0.2*k_0$ post-yield stiffness. This simulation is chosen to show a representative case of bilinear elastic behavior in the computational simulation of EFT.

First, the results verify that a loop shaping controller can successfully perform EFT for structures with bilinear elastic behavior because the simulation is stable. The simulation also captures the nonlinear phenomenon of the bilinear elastic model as seen in the force-displacement relationship. These observations can allow the bilinear elastic model to be incorporated into the computational EFT framework. Structural systems exhibiting bilinear elastic behavior should also be able to successfully complete experimental EFT.

Despite the validity of the model, simulations with a low yield displacement and low post-yield stiffness exhibit error at the peaks in the nonlinear range of the structure. Comparing the error ratio with the linear elastic simulation reveals much greater inaccuracy in the force tracking. This is probably caused by the complex behavior of the structural nonlinearity. Also, valve command saturation is captured as it would be in

experimental EFT, reaching its limit just after 5 seconds. Complete simulation results for the bilinear elastic parametric study are located in Appendix A.

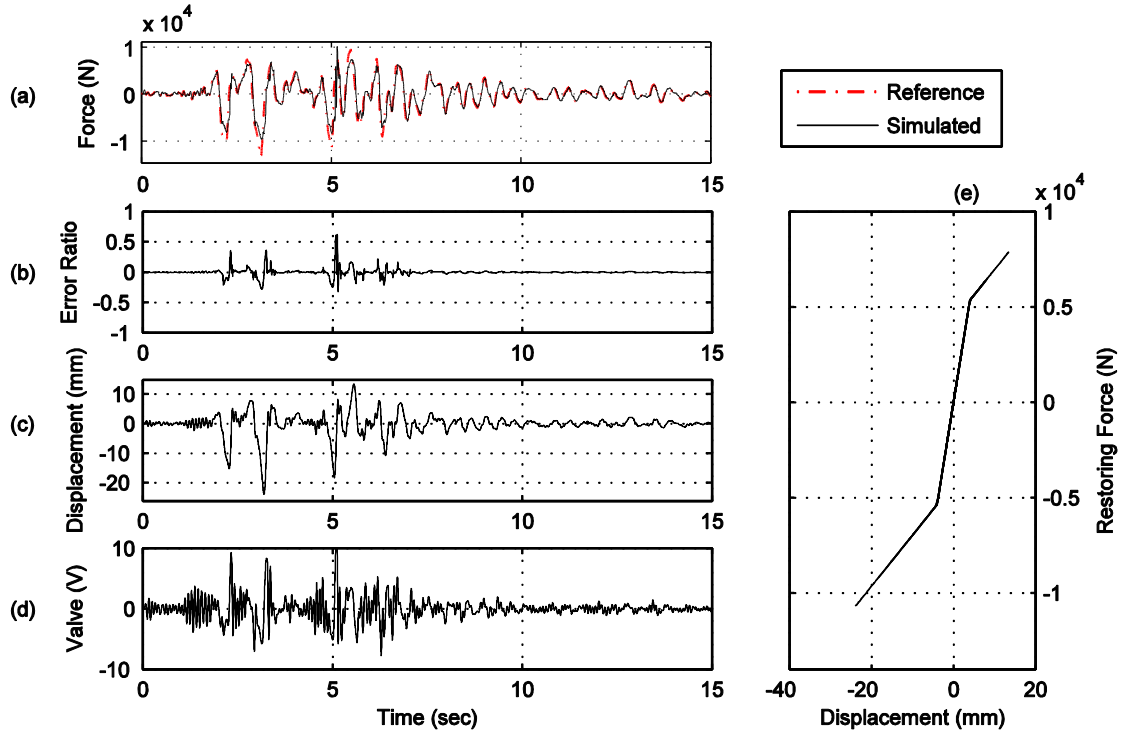

Figure 5.9. Bilinear elastic simulation for rigid structure, Yield displacement X_y = 0.004m, post-yield stiffness $k_1 = 0.2*k_0$.

Figures 5.10 and 5.11 show RMSE and maximum positive and negative peak-to-peak ratios plotted against the post-yield stiffness for the rigid and pinned structures, respectively. It is evident that decreasing the post-yield stiffness of the structure has an adverse effect on the force tracking capabilities in EFT with the bilinear elastic model. This trend is apparent for all RMSE and peak-to-peak ratios. For a low yield displacement, the values grow (RMSE) or decline (Peak-to-peak) exponentially with decreasing post-yield stiffness. Both figures clearly show that this trend is independent

of the individual dynamics of the respective structural system being tested. The maximum RMSE for the rigid structure is about 7 times greater than the linear elastic case, and the peak-to-peak ratios are approximately 40% less. For the pinned structure, the RMSE is about 16 times greater than linear elastic simulation, and peak-to-peak ratios are approximately 40 % less. In contrast, as the yield displacement increases, this effect becomes less significant. A higher yield displacement is not surpassed as often in the displacement history of the structure which signifies that the majority of the structural response is within the linear elastic controllable range.

The figures show that, typically, the maximum negative peak-to-peak ratios are slightly lower than the maximum positive peak-to-peak ratios. For the 1995 Kobe record, the maximum negative peak force is approximately 1.4 times greater than the maximum positive peak force. The controller cannot match the maximum negative peak force as easily since it is the maximum force seen in the nonlinear range of the structure.

In general, the results indicate that as the post-yield stiffness and yield displacement get smaller, the error in the force tracking becomes larger.

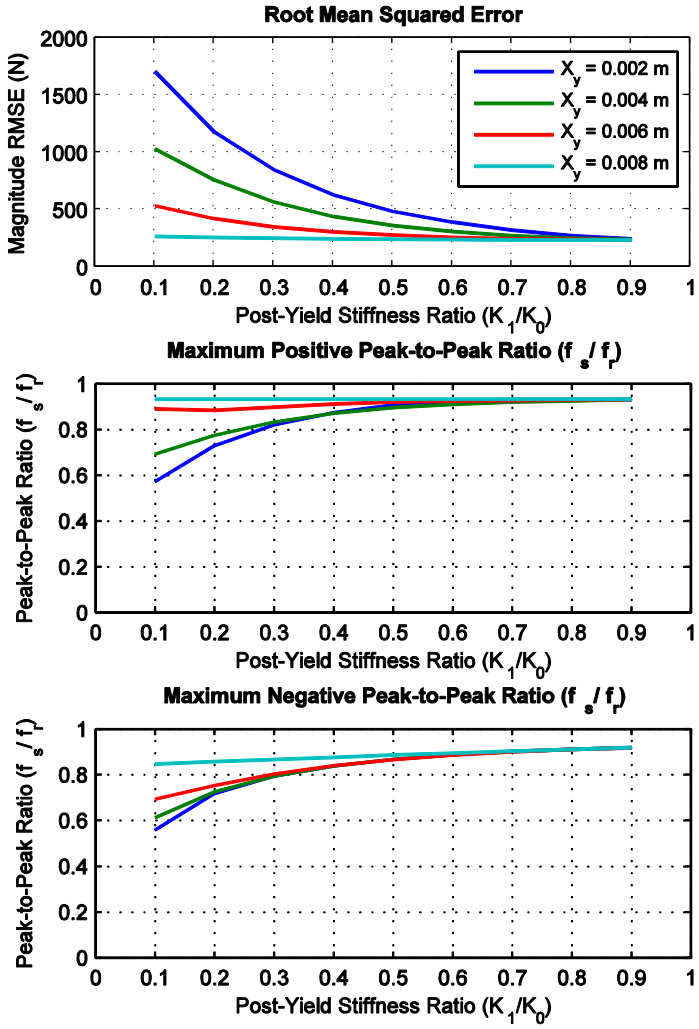

Figure 5.10. Rigid base bilinear elastic results with reference force normalized to 13,344 N (3 kips). RMSE, maximum positive peak-to-peak ratio, and maximum negative peak-to-peak ratio with varying post-yield stiffness.

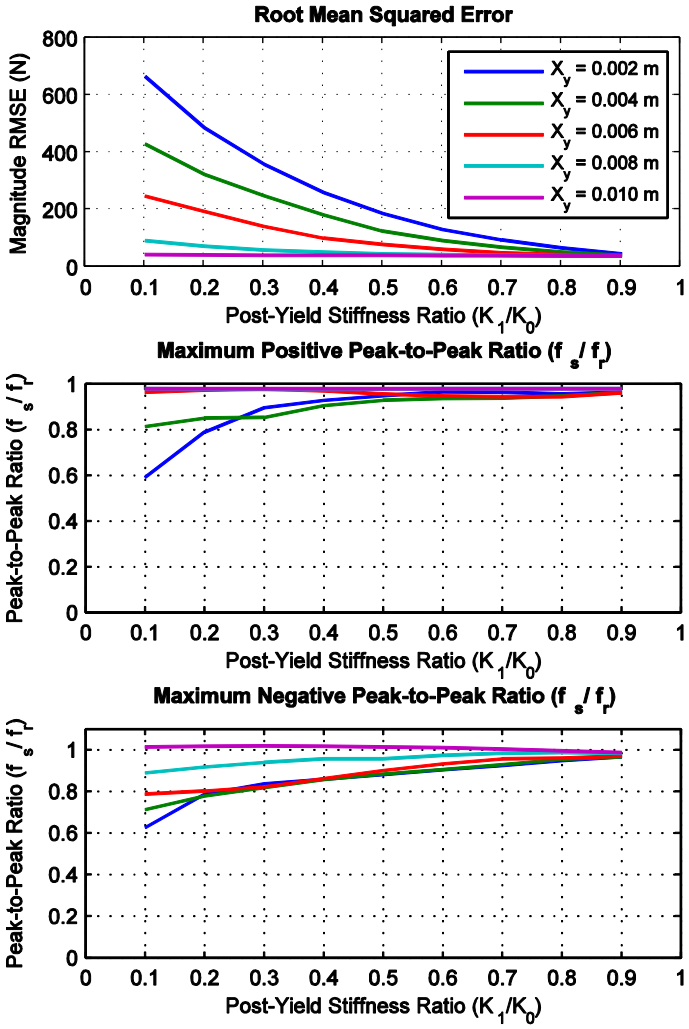

Figure 5.11. Pinned base bilinear elastic results with reference force normalized to 4,448 N (1 kip). RMSE, maximum positive peak-to-peak ratio, and maximum negative peak-to-peak ratio with varying post yield stiffness.

5.3.3 Bilinear Hysteretic Model

The bilinear hysteretic model bases its analysis on prescribed yield strength (Y_y) and post-yield stiffness (k_1). Yield strengths are incrementally increased by 2,000 N for the rigid structure (from 1,000 N to 11,000 N) and by 500 N for the pinned structure (1,000 N to 3,500 N). The post-yield stiffness is incrementally decreased by 10%, from 0.9*k_0 to

$0.1*k_0$. Overall, 54 bilinear hysteretic simulations are performed for each structure in the parametric study.

A representative case for the bilinear hysteretic simulations is shown in Figure 5.12. The figure shows results for the rigid structure with 5,000 N yield strength and $0.1*k_0$ post-yield stiffness. The results verify that a loop shaping controller is stable for bilinear hysteretic behavior. Force control is successfully performed in this simulation. As expected, the force-displacement relationship verifies the validity of the computational model. In consequence, the bilinear hysteretic model can be successfully incorporated into the computational EFT framework. Structures with idealized bilinear hysteretic behavior should be able to successfully complete nonlinear experimental EFT.

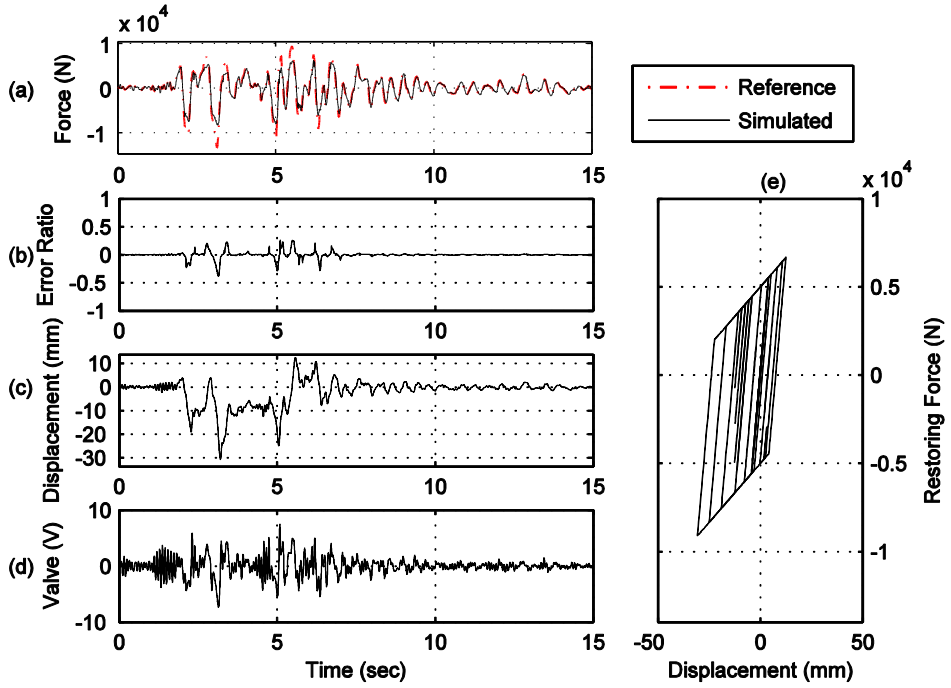

Figure 5.12. Bilinear hysteretic simulation for rigid structure, Yield strength Y_y = 5,000 N, post-yield stiffness $k_1 = 0.1*k_0$.

In contrast, a limitation is seen in the performance of the reference force tracking. The simulated force is diminished at the peaks after the yield strength of the structure is surpassed. The error ratio is significantly greater when compared against the linear elastic results. Complete simulation results for the bilinear hysteretic parametric study are found in Appendix B.

Figures 5.13 and 5.14 display RMSE and peak-to-peak ratios for the rigid and pinned structures, respectively. The RMSE and peak-to-peak ratio values adhere to a similar trend observed in the results from the bilinear elastic model. RMSE significantly increases with decreasing post-yield stiffness for low yield strengths; about 8 and 11 times greater than the linear elastic simulation for the rigid and pinned structures, respectively. Maximum positive and negative peak-to-peak ratios follow in a similar manner with significant reductions as the post-yield stiffness decreases. Peak-to-peak ratios deviate from linear elastic behavior by 43% for the rigid case and by 40% for the pinned case. The simulations begin to converge near linear elastic behavior as the yield strength increases due to its infrequent exceedance in the force time histories.

In general, decreasing the yield strength and post-yield stiffness induce considerable force tracking error in this model.

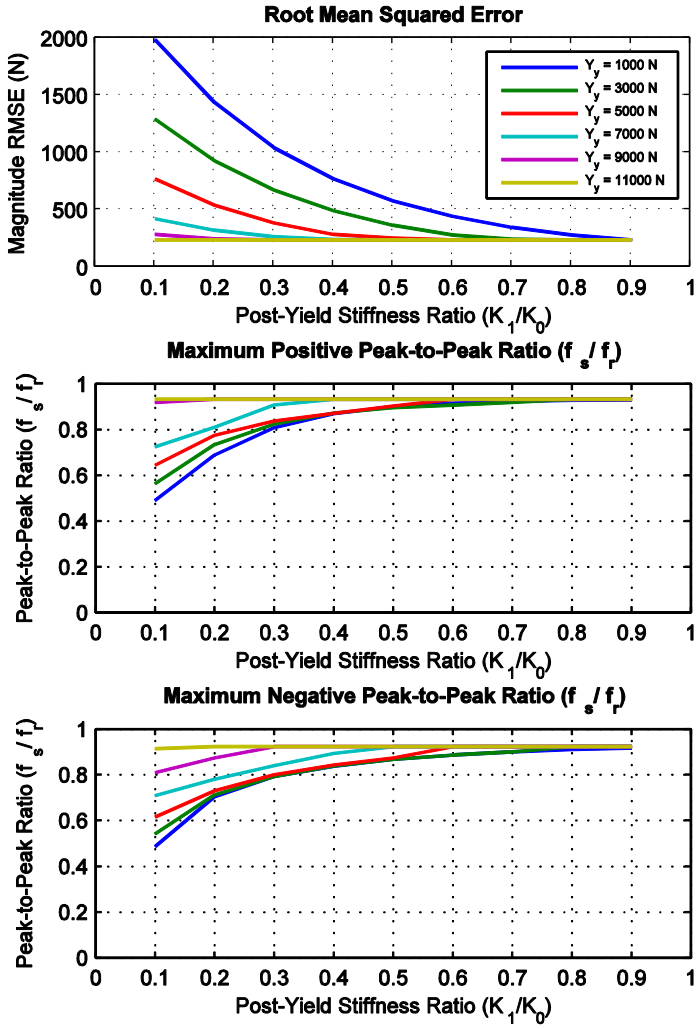

Figure 5.13. Rigid base bilinear hysteretic results with reference force normalized to 13,344 N (3 kips). RMSE, maximum positive peak-to-peak ratio, and maximum negative peak-to-peak ratio with varying post-yield stiffness.

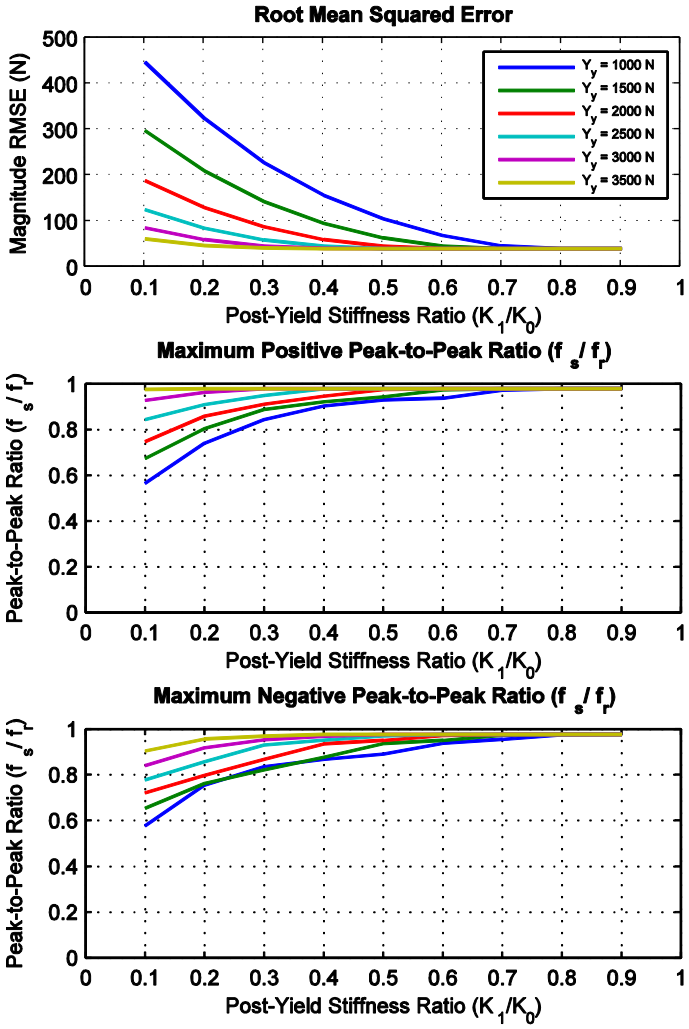

Figure 5.14. Pinned base bilinear hysteretic results with reference force normalized to 4,448 N (1 kip). RMSE, maximum positive peak-to-peak ratio, and maximum negative peak-to-peak ratio with varying post-yield stiffness.

5.3.4 Bilinear Hysteretic Pinching Model

The bilinear hysteretic pinching model also performs its analysis based on prescribed yield strength (Y_y) and post-yield stiffness (k_1). In the same scheme used for the bilinear hysteretic simulations, the yield strengths for the rigid and pinned structures are incrementally increased by 2,000 N and 500 N, respectively, and the post-yield stiffness

is incrementally decreased by 10%. Altogether, 54 computational simulations are completed for each structure in this parametric study.

Figure 5.15 shows results for a typical stable bilinear hysteretic pinching simulation. The results are from the rigid structure with 5,000 N yield strength and $0.1*k_0$ post-yield stiffness. This simulation shows that a loop shaping controller is stable for bilinear hysteretic pinching behavior and that the expected force-displacement relation is verified through the model. As a result, the computational EFT framework can successfully incorporate the bilinear hysteretic pinching model.

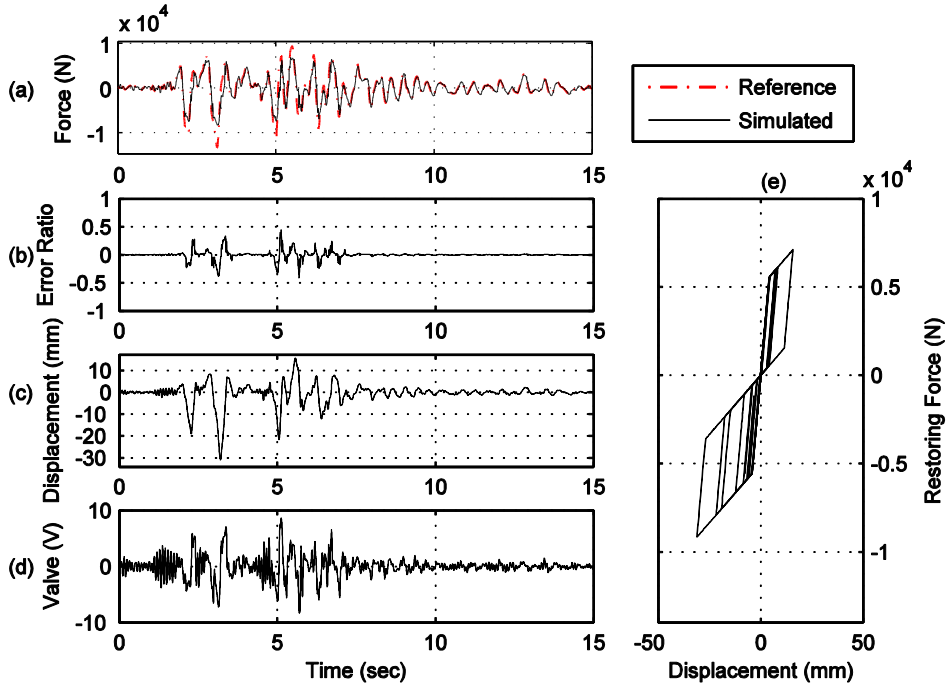

Figure 5.15. Bilinear hysteretic pinching simulation for rigid structure, Yield strength Y_y =5,000 N, post-yield stiffness $k_1 = 0.1*k_0$.

Similar performance trends are noted in the results of this model. There is much greater error in the force tracking when compared to linear elastic simulation. Error ratios almost reach 50% at the peak forces in the time history which further demonstrates the worsened performance. After the yield strength is surpassed, the simulated forces lose their ability to track the reference force accurately. Complete simulation results for the bilinear hysteretic pinching parametric study are located in Appendix C.

In some cases, instabilities arise in this model. Table 5.2 provides a summary of the unstable bilinear hysteretic pinching simulations. As a consequence, test structures exhibiting bilinear hysteretic pinching behavior may prove to be unstable for implementation in experimental EFT.

Table 5.2. Summary of unstable simulations for bilinear hysteretic pinching model.

	Yield Strength (Y_y), N	Post-Yield Stiffness (k_1)
Rigid	3,000	$0.9*k_0$
	3,000	$0.8*k_0$
	5,000	$0.6*k_0$
	5,000	$0.5*k_0$
	7,000	$0.5*k_0$
	9,000	$0.9*k_0$
	9,000	$0.8*k_0$
	11,000	$0.6*k_0$
	11,000	$0.2*k_0$
Pinned	2,000	$0.3*k_0$
	3,000	$0.1*k_0$

Figures 5.16 and 5.17 display the resulting EFT performance criteria for the rigid and pinned structures. The figures clearly show the effect of the unstable simulations, most notably in Figure 5.16 for the rigid structure. A closer investigation of these simulations will be discussed in the next section.

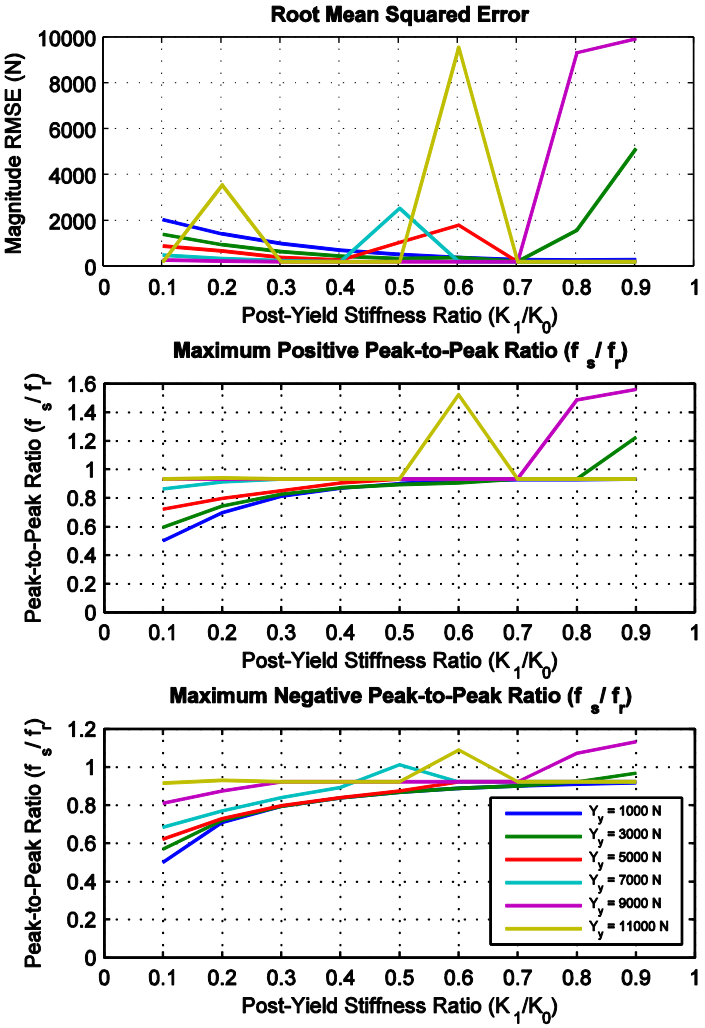

Figure 5.16. Rigid base bilinear hysteretic pinching results with reference force normalized to 13,344 N (3 kips). RMSE, maximum positive peak-to-peak ratio, and maximum negative peak-to-peak ratio with varying post-yield stiffness.

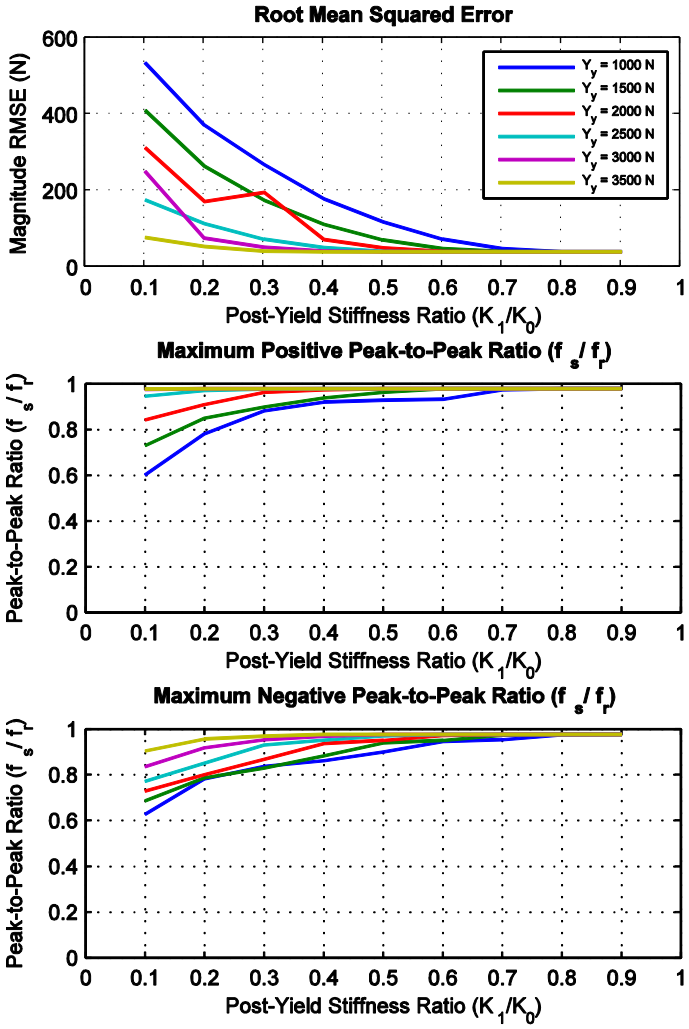

Figure 5.17. Pinned base bilinear hysteretic pinching results with reference force normalized to 4,448 N (1 kip). RMSE, maximum positive peak-to-peak ratio, and maximum negative peak-to-peak ratio with varying post-yield stiffness.

Figures 5.18 and 5.19 show the results for the two unstable simulations for the pinned structure. Although these two simulations see some amplification at the very beginning of the time history, the force tracking smoothes out after the first 2-3 seconds and stable performance is attained for the remainder of the simulation. In contrast, the rigid simulations are unstable for the entire length of the time histories and show instances of high frequency vibration.

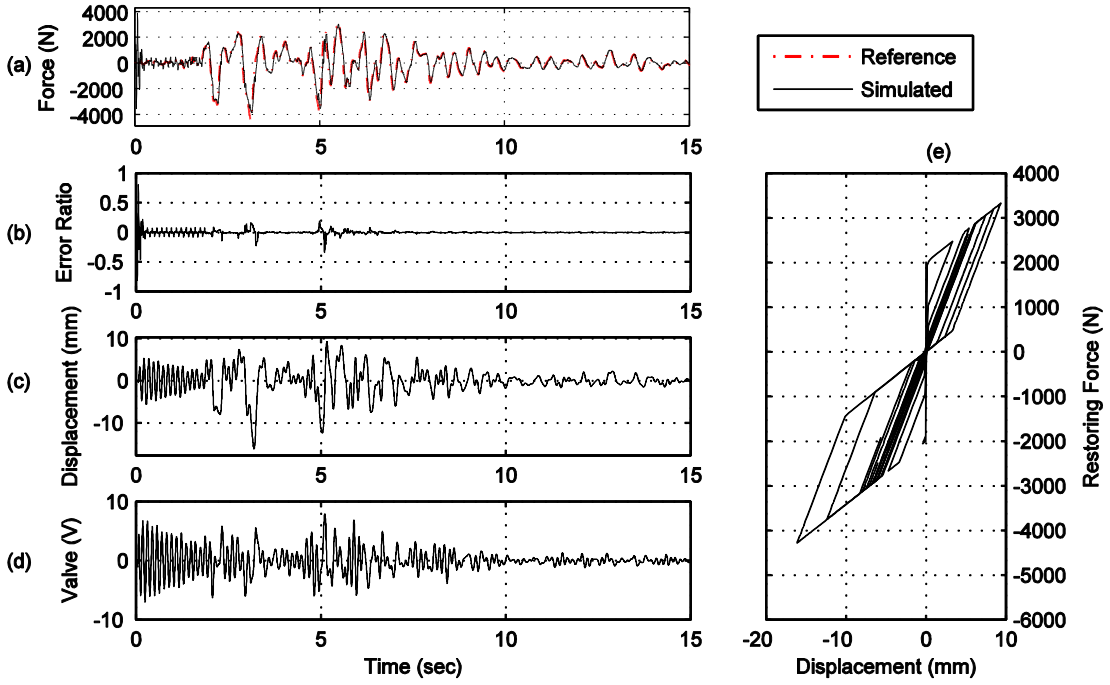

Figure 5.18. Pinned base results for Y_y = 2,000 N and $k_1 = 0.3*k_0$.

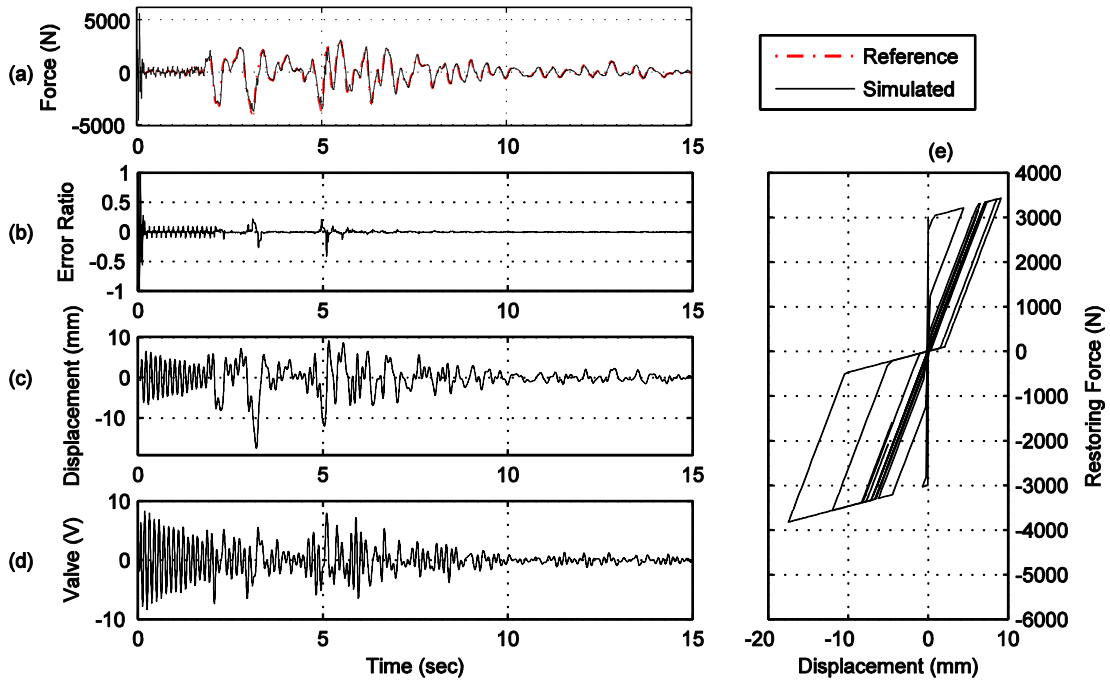

Figure 5.19. Pinned base results for Y_y = 3,000 N and $k_1 = 0.1*k_0$.

Excluding the unstable cases, a similar trend in the EFT performance criteria is noticed in Figures 5.16 and 5.17. Values of RMSE and peak-to-peak ratios worsen as the post-yield stiffness and yield strength decrease. The simulations also verify that some cases reach the valve command capacity for this model.

Overall, the stable simulations see considerable limitation in reference force tracking as the yield strength and post-yield stiffness decrease. The unstable simulations show that structural systems characterized by bilinear hysteretic pinching behavior should be approached with caution in EFT implementation.

5.3.4.1 Redesign of Loop Shaping Controller

Further analysis of the unstable bilinear hysteretic pinching simulations for the rigid structure reveals that the response histories are excited around the natural frequency of the structure and high frequency vibrations occur in the 35-40 Hz range. Instability at the natural frequency indicates that the loop shaping controller could be over amplifying the system response when compensating for control-structure interaction. Figure 5.20 shows the sensitivity function ($S(s)=1/[1+L(s)]$) for the current loop shaping controller used for the rigid structure. This function indicates over-amplification of the system response, primarily in the 20-40 Hz range.

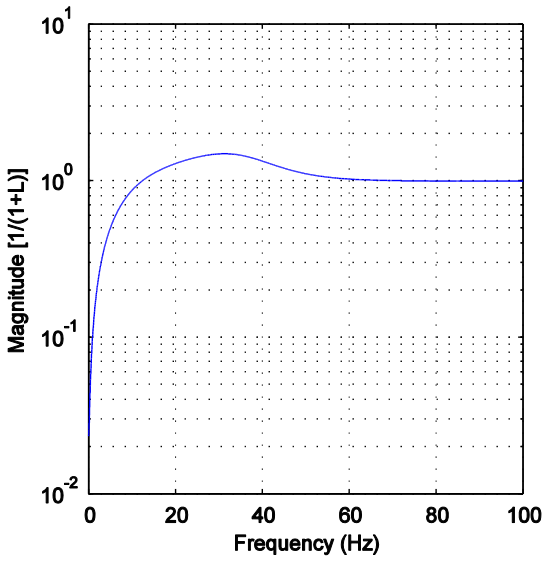

Figure 5.20. Sensitivity function for rigid structure force feedback controller.

In an attempt to mitigate these effects, a more conservative loop shaping controller is designed for use in this model, as seen below

$$C_f^{LS} = \frac{5}{s^2 + 400s + 46100}$$

A decrease in gain and an increase in damping are applied in the new controller design. Figure 5.21 shows the original result for the 9,000 N yield strength and 0.9*k_0 post-yield stiffness simulation. Figure 5.22 shows result of the same simulation using the redesigned controller. The figures indicate that increasing the damping and decreasing the controller gain allows for more stable force tracking, even if the performance of the controller is intentionally sacrificed. However, the displacement results for this simulation do not follow the expected behavior. A ±0.1 mm displacement range is very small in comparison to the stable simulations. These observations indicate that the

instabilities could be a result of computational errors within the bilinear hysteretic pinching structural model.

These results demonstrate that structural models with more complex nonlinearity can affect the stability of EFT. Stability issues that arise are dependent on the design of the loop shaping controller. The instabilities can be partially compensated with a more conservative controller design, although overall performance will be worsened. It is interesting to note that the unstable simulations are scattered throughout the full range of yield strength and post-yield stiffness combinations, and that they are prevalent in the rigid configuration.

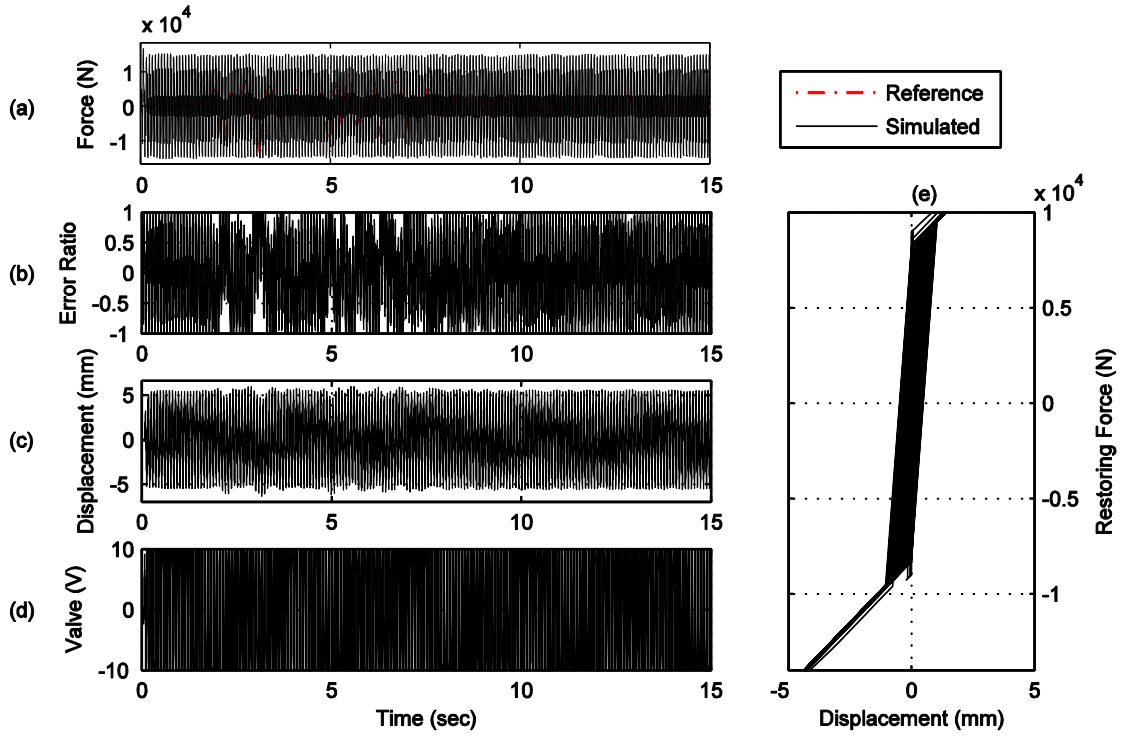

Figure 5.21. Rigid base results for Y_y = 9,000 N and $k_1 = 0.9*k_0$.

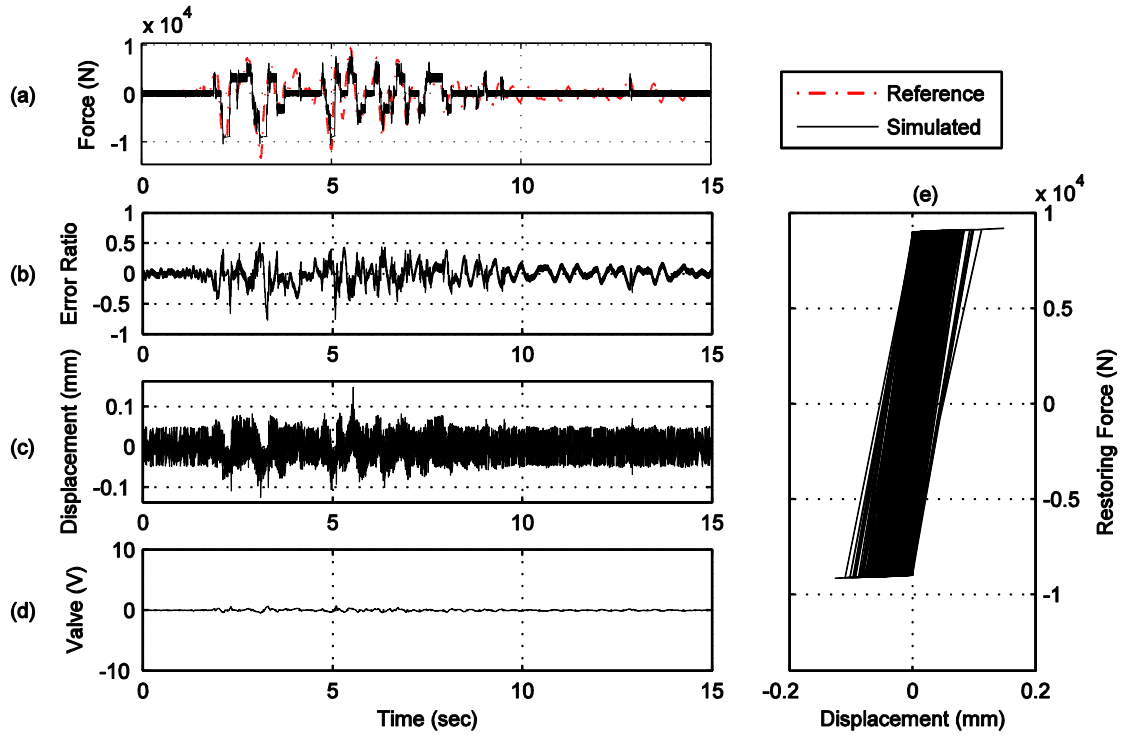

Figure 5.22. Redesigned controller rigid base results for Y_y = 9,000 N and $k_1 = 0.9*k_0$.

5.4 Summary of Nonlinear EFT Performance

Overall, if a structure exhibits high nonlinearity, the performance of EFT is greatly affected. Highly nonlinear structures possessing the lowest post-yield stiffness and yield displacement/strength have a significant impact on the force tracking performance in EFT. These combinations see peak simulated forces of only 49% to 81% of the reference force, and a RMSE to maximum reference force ratio of 8% to 16% deviation. Tables 5.3 - 5.5 outline the results of the low yield displacement/strength simulations for RMSE to maximum reference force ratio, maximum positive peak-to-peak ratio, and maximum negative peak-to-peak ratio. The highlighted values indicate simulations in which the valve command saturation is captured. Excluding the unstable simulations in bilinear

hysteretic pinching behavior, valve command saturation seems to correlate with highly nonlinear cases in EFT due to the large changes in force.

Table 5.3. RMSE to maximum reference force ratio results for the nonlinear simulations.

Model	Yield Disp./Yield Strength	k_1=0.1*k_o	k_1=0.2*k_o	k_1=0.3*k_o	k_1=0.4*k_o	k_1=0.5*k_o	k_1=0.6*k_o	k_1=0.7*k_o	k_1=0.8*k_o	k_1=0.9*k_o
Bilinear Elastic - Rigid	0.002m	0.13	0.09	0.06	0.05	0.04	0.03	0.02	0.02	0.02
	0.004m	0.08	0.06	0.04	0.03	0.03	0.02	0.02	0.02	0.02
Bilinear Elastic - Pinned	0.002m	0.15	0.11	0.08	0.06	0.04	0.03	0.02	0.02	0.01
	0.004m	0.10	0.07	0.06	0.04	0.03	0.02	0.02	0.01	0.01
Bilinear Hysteretic - Rigid	1000 N	0.15	0.11	0.08	0.06	0.04	0.03	0.03	0.02	0.02
	3000 N	0.10	0.07	0.05	0.04	0.03	0.02	0.02	0.02	0.02
Bilinear Hysteretic - Pinned	1000 N	0.10	0.07	0.05	0.04	0.02	0.02	0.01	0.01	0.01
	1500 N	0.07	0.05	0.03	0.02	0.01	0.01	0.01	0.01	0.01
Bilinear Hysteretic Pinch- Rigid	1000 N	0.16	0.11	0.08	0.06	0.04	0.03	0.02	0.02	0.02
	3000 N	0.11	0.07	0.05	0.04	0.03	0.03	0.02	0.12	0.39
Bilinear Hysteretic Pinch - Pinned	1000 N	0.12	0.08	0.06	0.04	0.03	0.02	0.01	0.01	0.01
	1500 N	0.09	0.06	0.04	0.03	0.02	0.01	0.01	0.01	0.01

Table 5.4. Maximum positive peak-to-peak ratios for the nonlinear simulations.

Model	Yield Disp./Yield Strength	k_1=0.1*k_o	k_1=0.2*k_o	k_1=0.3*k_o	k_1=0.4*k_o	k_1=0.5*k_o	k_1=0.6*k_o	k_1=0.7*k_o	k_1=0.8*k_o	k_1=0.9*k_o
Bilinear Elastic - Rigid	0.002m	0.57	0.73	0.82	0.88	0.91	0.93	0.93	0.93	0.93
	0.004m	0.69	0.77	0.83	0.87	0.90	0.91	0.92	0.93	0.93
Bilinear Elastic - Pinned	0.002m	0.59	0.79	0.90	0.93	0.95	0.96	0.96	0.96	0.96
	0.004m	0.81	0.85	0.85	0.91	0.93	0.94	0.94	0.95	0.96
Bilinear Hysteretic - Rigid	1000 N	0.49	0.69	0.81	0.87	0.90	0.92	0.92	0.93	0.93
	3000 N	0.56	0.73	0.82	0.87	0.90	0.91	0.92	0.93	0.93
Bilinear Hysteretic - Pinned	1000 N	0.57	0.74	0.84	0.90	0.93	0.94	0.97	0.98	0.98
	1500 N	0.67	0.80	0.89	0.92	0.94	0.97	0.98	0.98	0.98
Bilinear Hysteretic Pinch- Rigid	1000 N	0.50	0.70	0.81	0.87	0.90	0.92	0.93	0.93	0.93
	3000 N	0.59	0.75	0.83	0.87	0.90	0.91	0.93	0.93	1.23
Bilinear Hysteretic Pinch - Pinned	1000 N	0.60	0.78	0.88	0.92	0.93	0.93	0.97	0.98	0.98
	1500 N	0.73	0.85	0.90	0.94	0.96	0.98	0.98	0.98	0.98

Table 5.5. Maximum negative peak-to-peak ratios for the nonlinear simulations.

Model	Yield Disp./Yield Strength	k_1=0.1*k_o	k_1=0.2*k_o	k_1=0.3*k_o	k_1=0.4*k_o	k_1=0.5*k_o	k_1=0.6*k_o	k_1=0.7*k_o	k_1=0.8*k_o	k_1=0.9*k_o
Bilinear Elastic - Rigid	0.002m	0.56	0.72	0.79	0.84	0.87	0.89	0.90	0.91	0.92
	0.004m	0.61	0.73	0.80	0.84	0.87	0.89	0.90	0.91	0.92
Bilinear Elastic - Pinned	0.002m	0.62	0.79	0.84	0.86	0.88	0.90	0.93	0.95	0.97
	0.004m	0.71	0.78	0.82	0.86	0.88	0.91	0.93	0.95	0.97
Bilinear Hysteretic - Rigid	1000 N	0.49	0.71	0.79	0.84	0.87	0.89	0.90	0.91	0.92
	3000 N	0.54	0.71	0.79	0.84	0.87	0.89	0.90	0.92	0.92
Bilinear Hysteretic - Pinned	1000 N	0.58	0.75	0.84	0.87	0.89	0.94	0.96	0.97	0.98
	1500 N	0.65	0.76	0.82	0.88	0.94	0.95	0.97	0.98	0.98
Bilinear Hysteretic Pinch- Rigid	1000 N	0.50	0.71	0.79	0.84	0.87	0.89	0.90	0.91	0.92
	3000 N	0.57	0.72	0.80	0.84	0.87	0.89	0.90	0.92	0.97
Bilinear Hysteretic Pinch - Pinned	1000 N	0.63	0.78	0.84	0.86	0.90	0.94	0.95	0.97	0.98
	1500 N	0.69	0.79	0.83	0.88	0.94	0.95	0.97	0.98	0.98

Chapter 6

Conclusions

This thesis presented an extensive parametric study on the effects of structural nonlinearities on effective force testing (EFT). Structural characteristics for an experimental test structure were identified for two test structure configurations. Computational EFT framework for linear and nonlinear EFT was employed for a breadth of simulations that focused on the influence of the following nonlinear parameters: yield displacement, yield strength, and post-yield stiffness. Computational simulations demonstrated that:

1. A loop shaping force feedback controller is stable and allows for successful completion of EFT for all structural models, but highly nonlinear cases have inevitable errors.
2. Force tracking performance in EFT significantly degrades as the structure becomes highly nonlinear; this effect is independent of the test structure and how the nonlinearities are modeled (i.e. bilinear elastic, bilinear hysteretic, bilinear hysteretic pinching).
3. Computational simulation of EFT verifies that some nonlinear simulations reach the servo valve command capacity.
4. Computational simulation of EFT is useful as a preliminary study for experimental EFT implementation.

Experimental EFT is challenging, and this effort serves as a basis for understanding the effects of structural nonlinearities in the continued development of EFT. Loop shaping

control provides a great start, but there is space for improvement in nonlinear EFT. In order to achieve more accurate reference force tracking, further advances in force feedback control are needed. A possible area for future exploration could be the use of adaptive force control for the nonlinear range. Supplemental investigations on nonlinear EFT using the computational framework would best serve this area of development. Additional experimental investigations are also needed in nonlinear EFT for more complex structural systems.

Appendix A

Computational EFT Results for Bilinear Elastic Model

Rigid Base

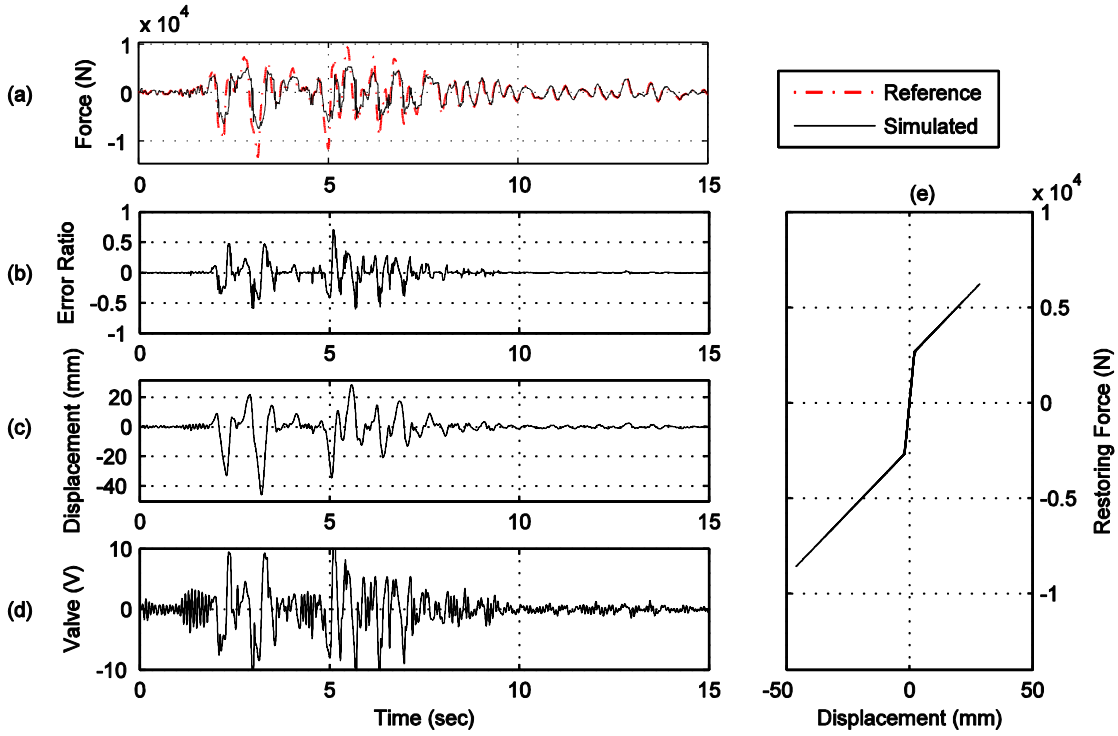

Figure A.1. Yield displacement X_y = 0.002m, post-yield stiffness $k_1 = 0.1*k_0$.

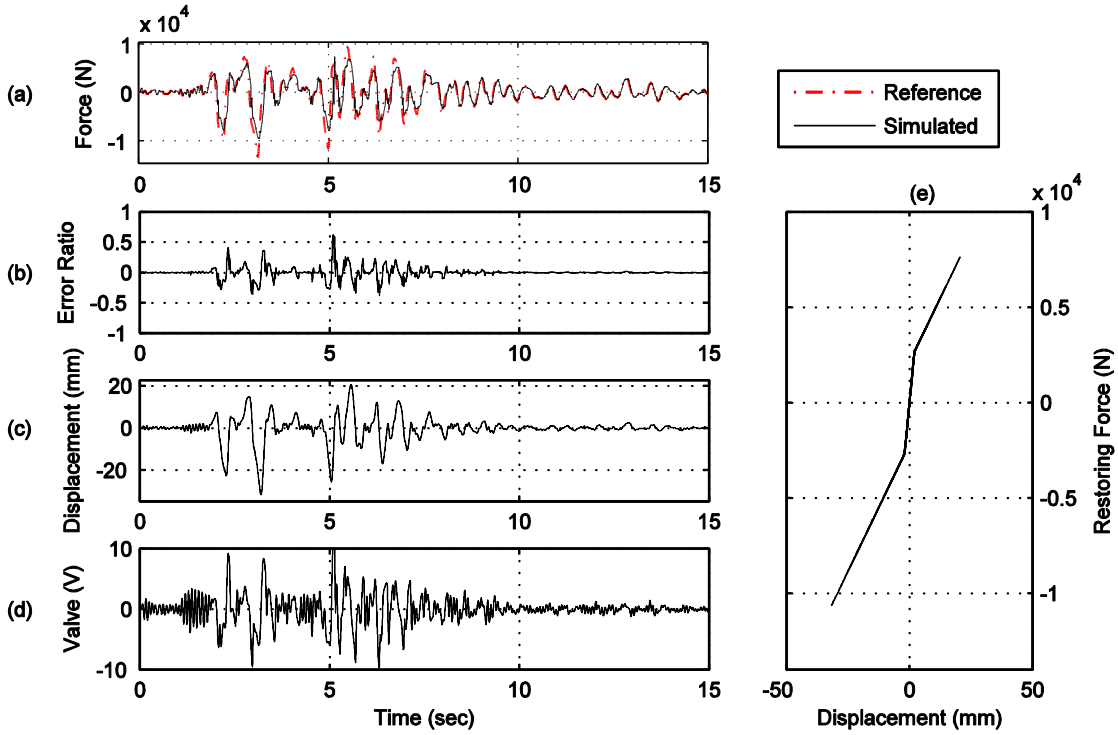

Figure A.2. Yield displacement X_y = 0.002m, post-yield stiffness $k_1 = 0.2*k_0$.

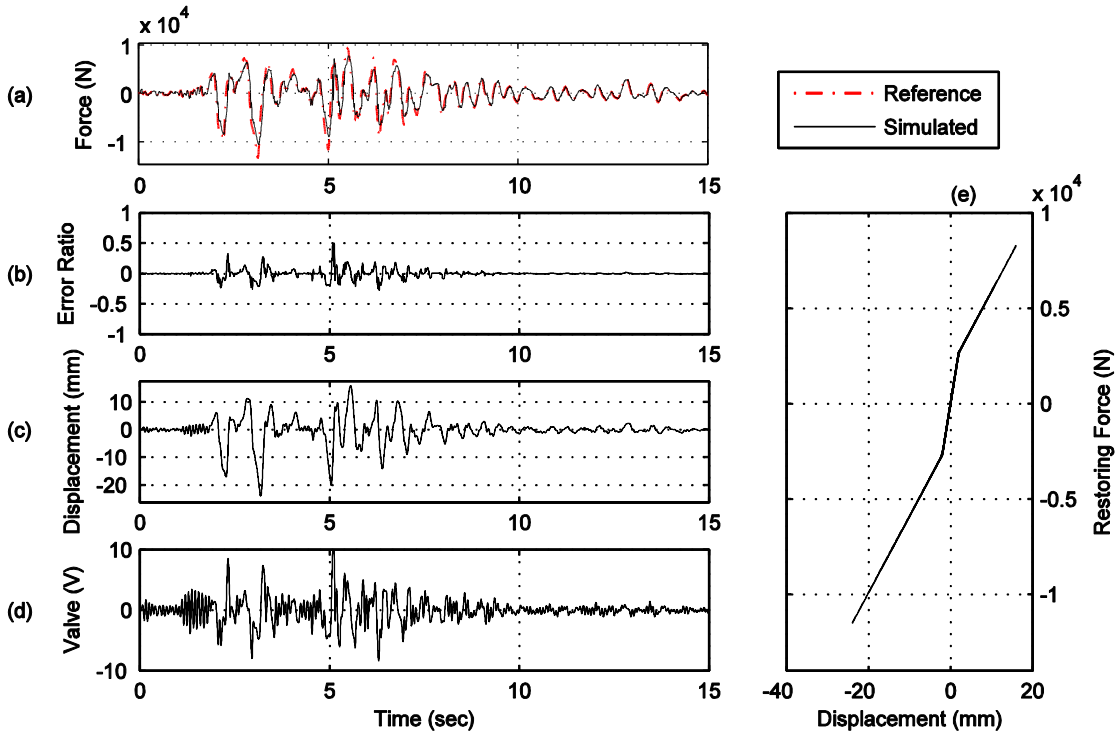

Figure A.3. Yield displacement X_y = 0.002m, post-yield stiffness $k_1 = 0.3*k_0$.

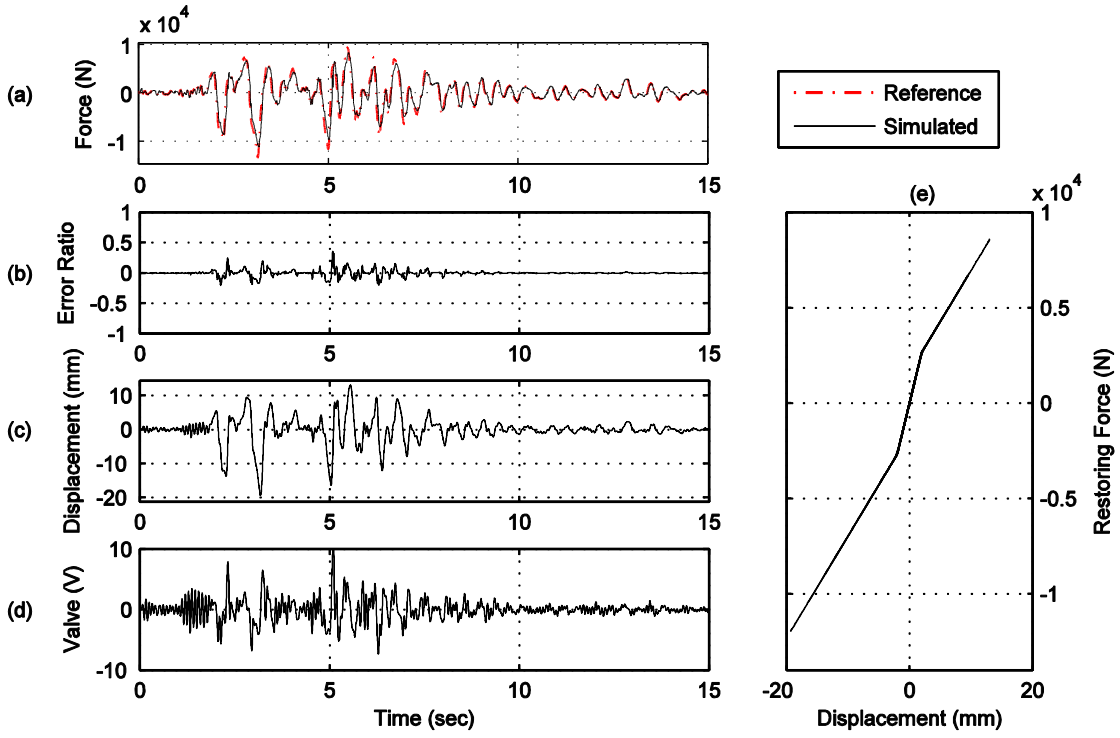

Figure A.4. Yield displacement X_y = 0.002m, post-yield stiffness $k_1 = 0.4*k_0$.

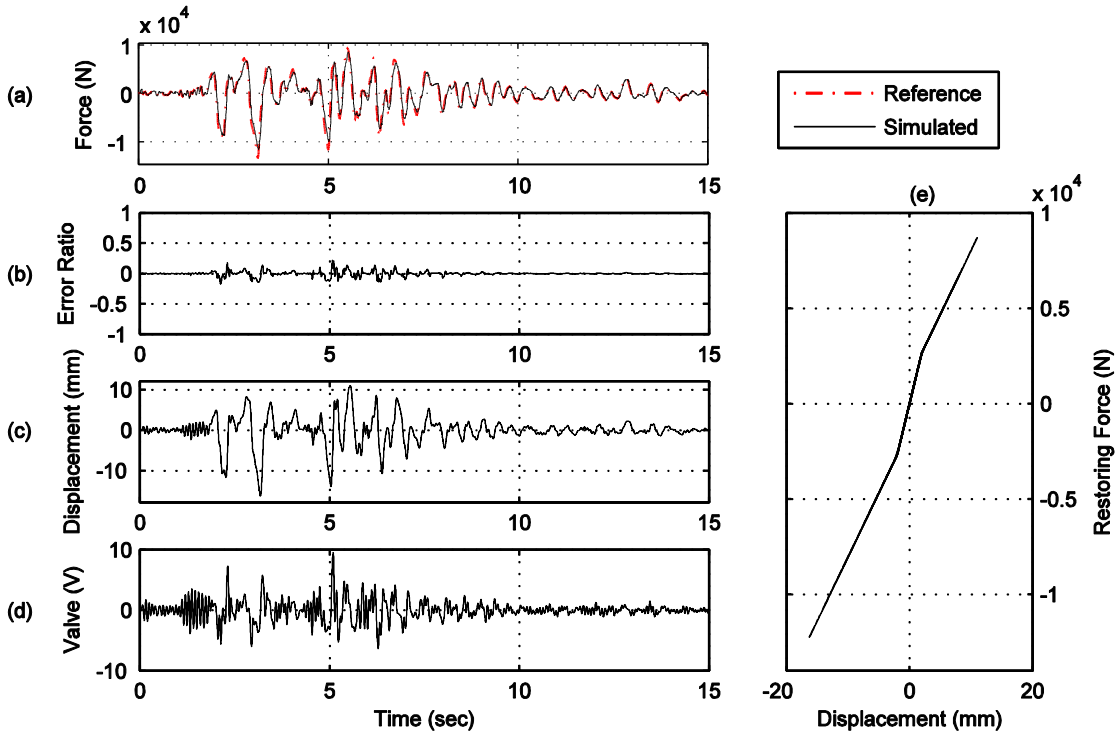

Figure A.5. Yield displacement X_y = 0.002m, post-yield stiffness $k_1 = 0.5*k_0$.

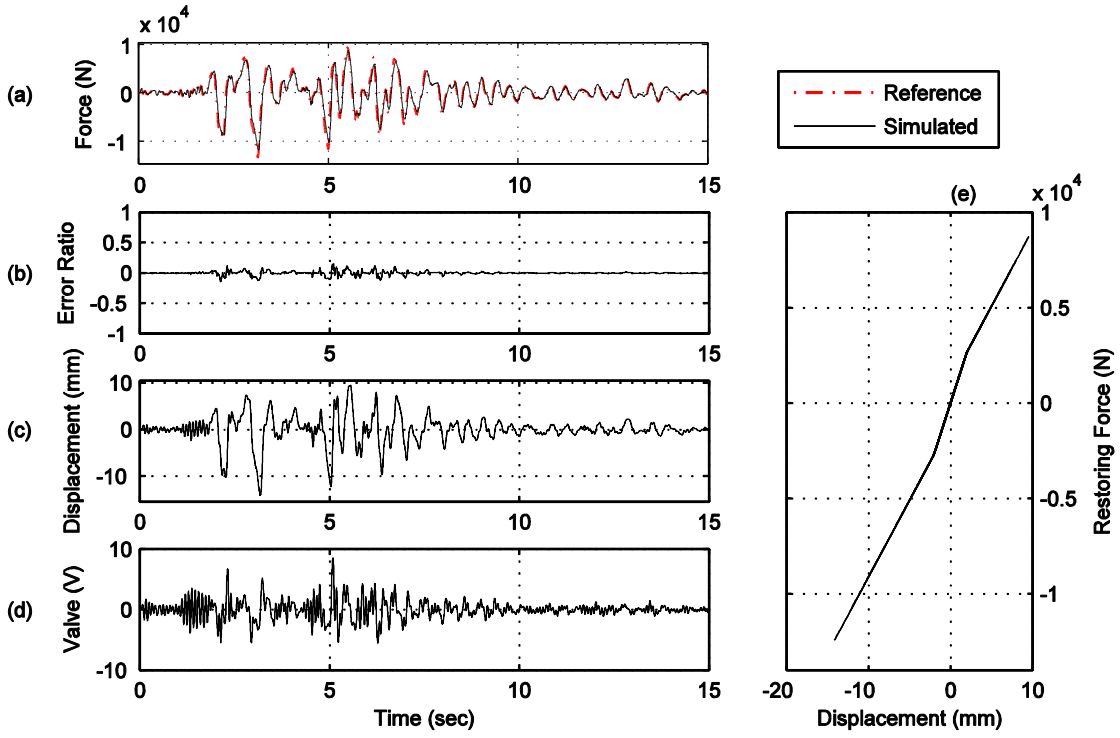

Figure A.6. Yield displacement X_y = 0.002m, post-yield stiffness $k_1 = 0.6*k_0$.

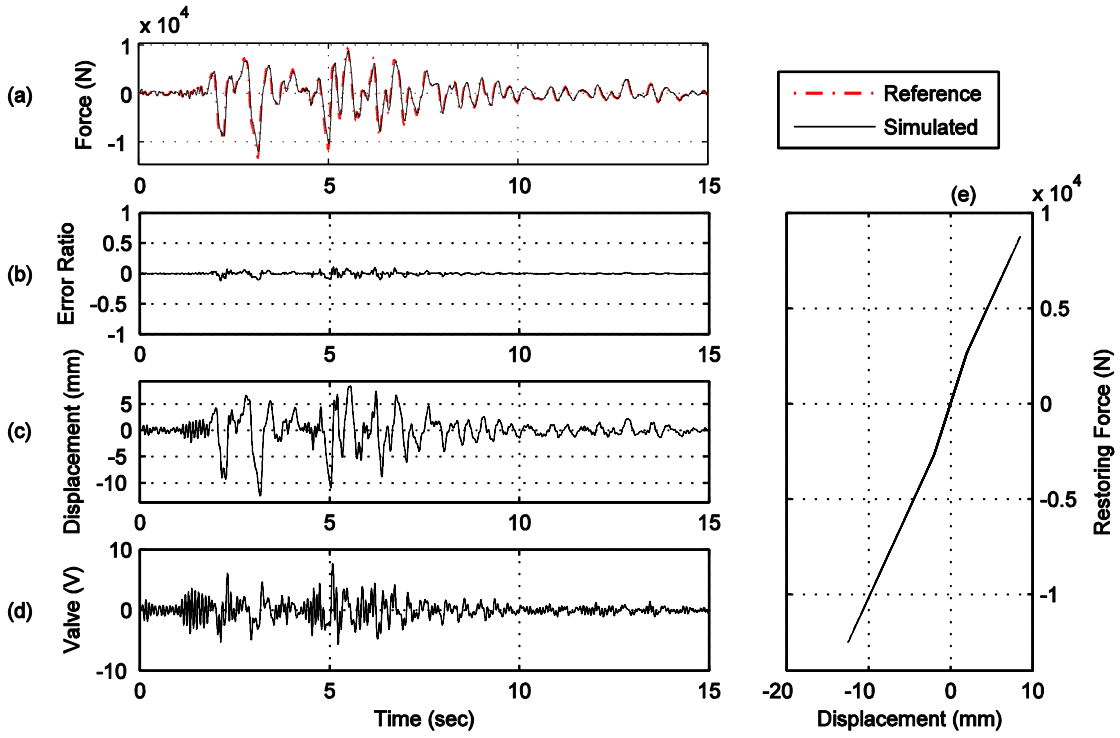

Figure A.7. Yield displacement X_y = 0.002m, post-yield stiffness $k_1 = 0.7*k_0$.

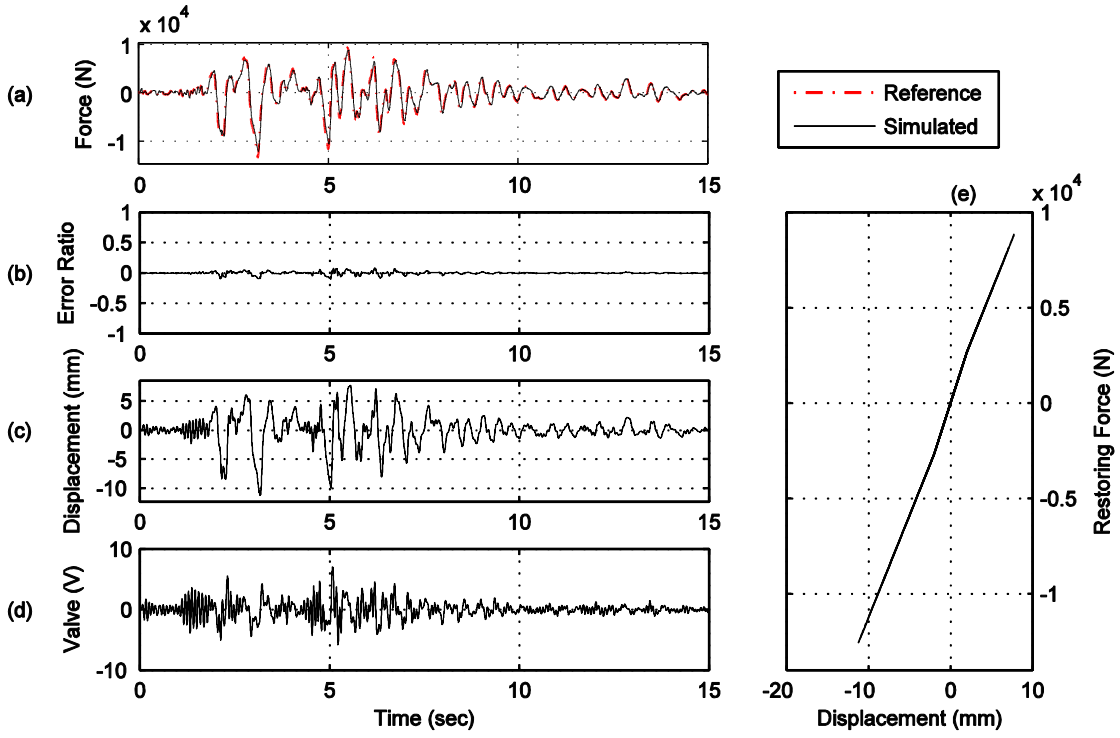

Figure A.8. Yield displacement X_y = 0.002m, post-yield stiffness $k_1 = 0.8*k_0$.

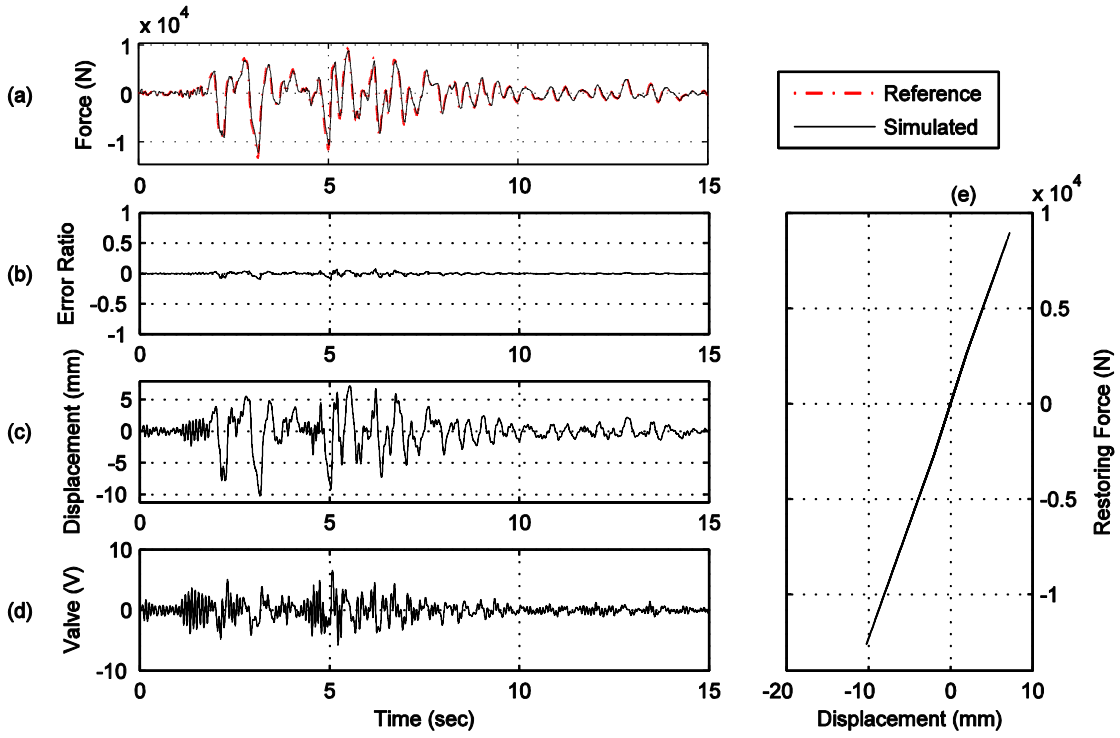

Figure A.9. Yield displacement X_y = 0.002m, post-yield stiffness $k_1 = 0.9*k_0$.

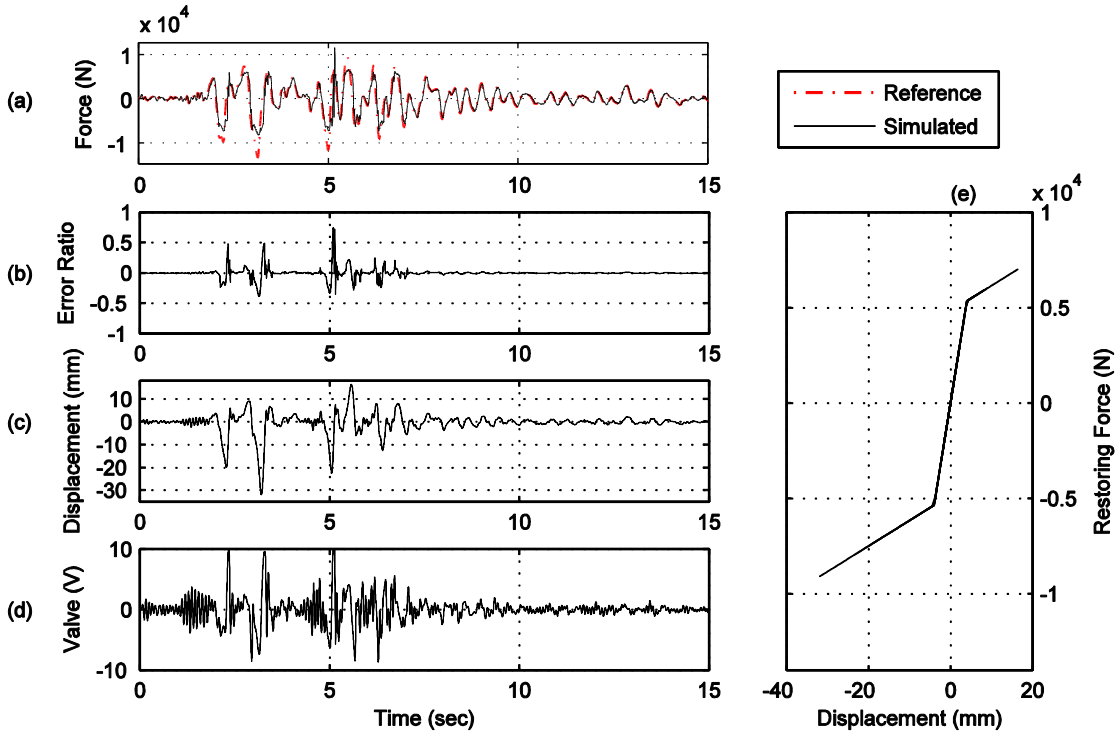

Figure A.10. Yield displacement X_y = 0.004m, post-yield stiffness $k_1 = 0.1*k_0$.

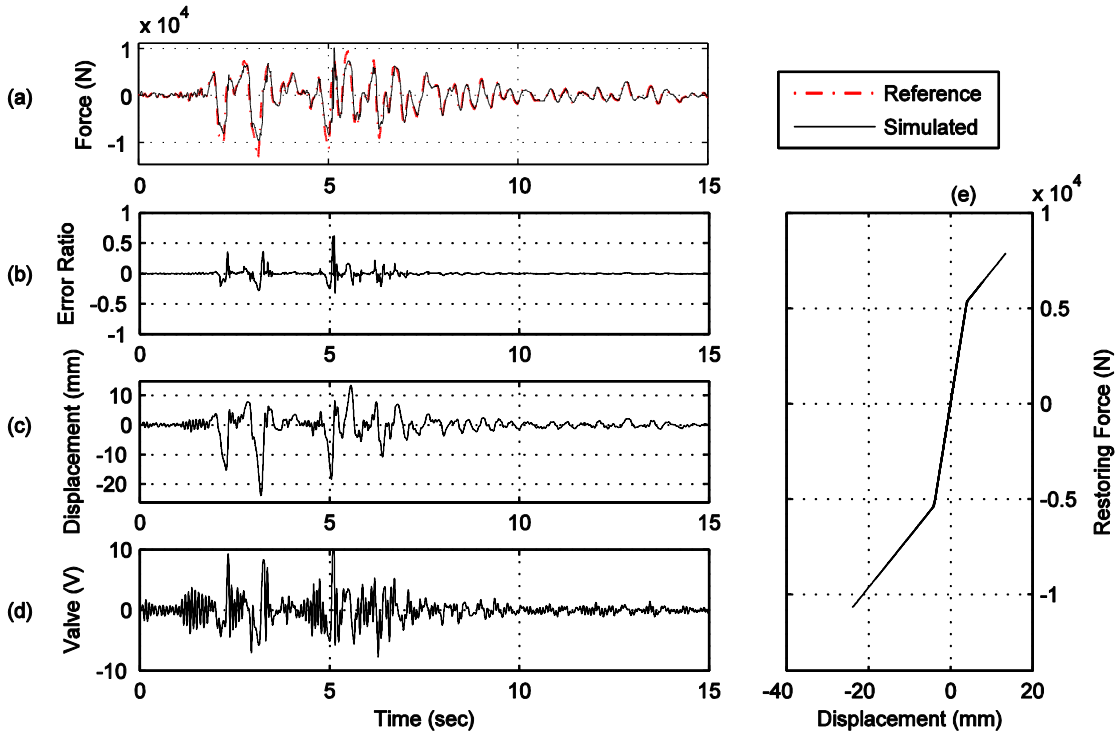

Figure A.11. Yield displacement X_y = 0.004m, post-yield stiffness $k_1 = 0.2*k_0$.

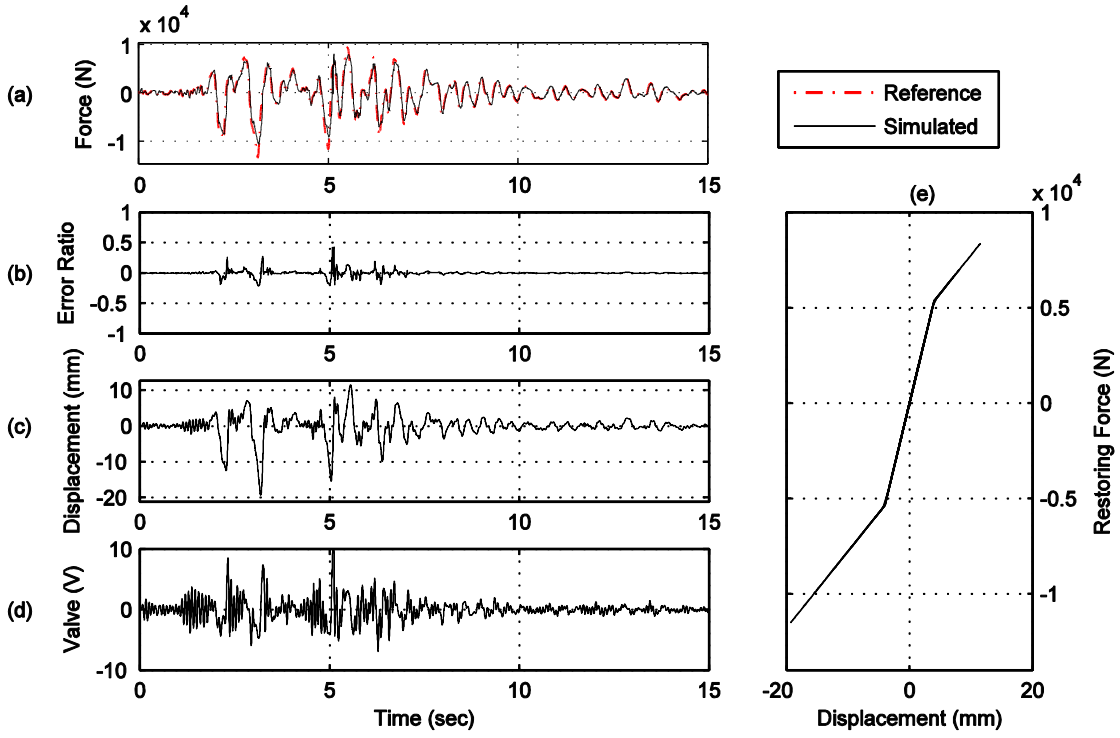

Figure A.12. Yield displacement X_y = 0.004m, post-yield stiffness $k_1 = 0.3*k_0$.

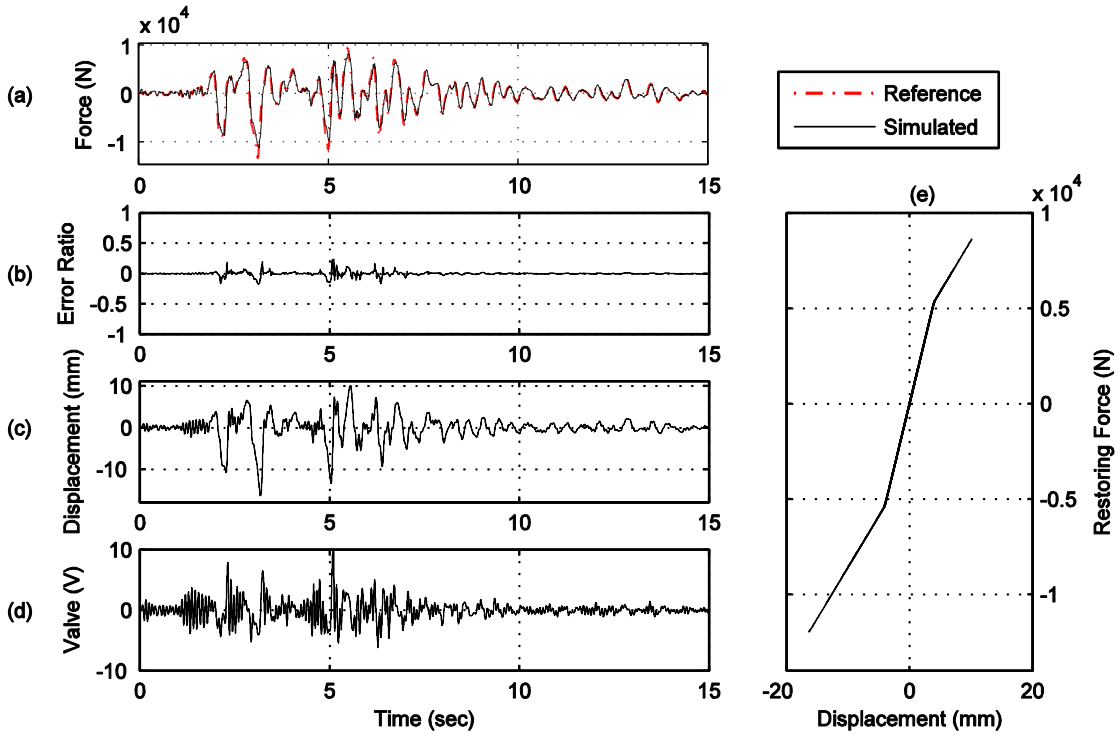

Figure A.13. Yield displacement X_y = 0.004m, post-yield stiffness $k_1 = 0.4*k_0$.

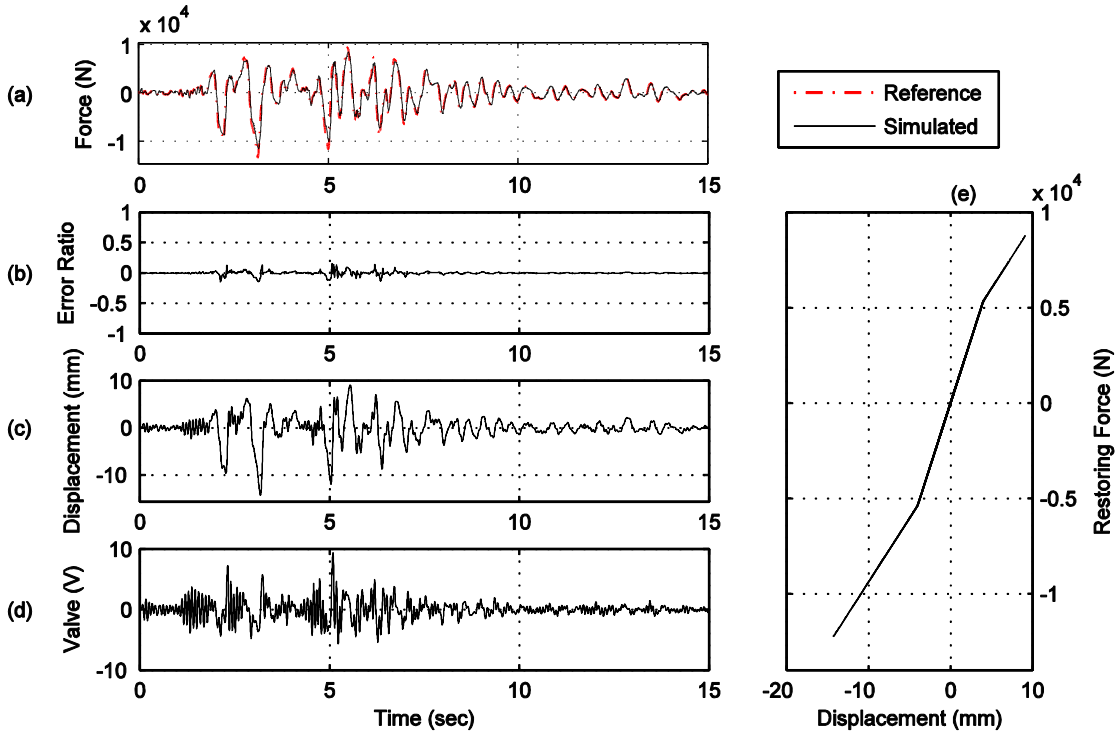

Figure A.14. Yield displacement X_y = 0.004m, post-yield stiffness $k_1 = 0.5*k_0$.

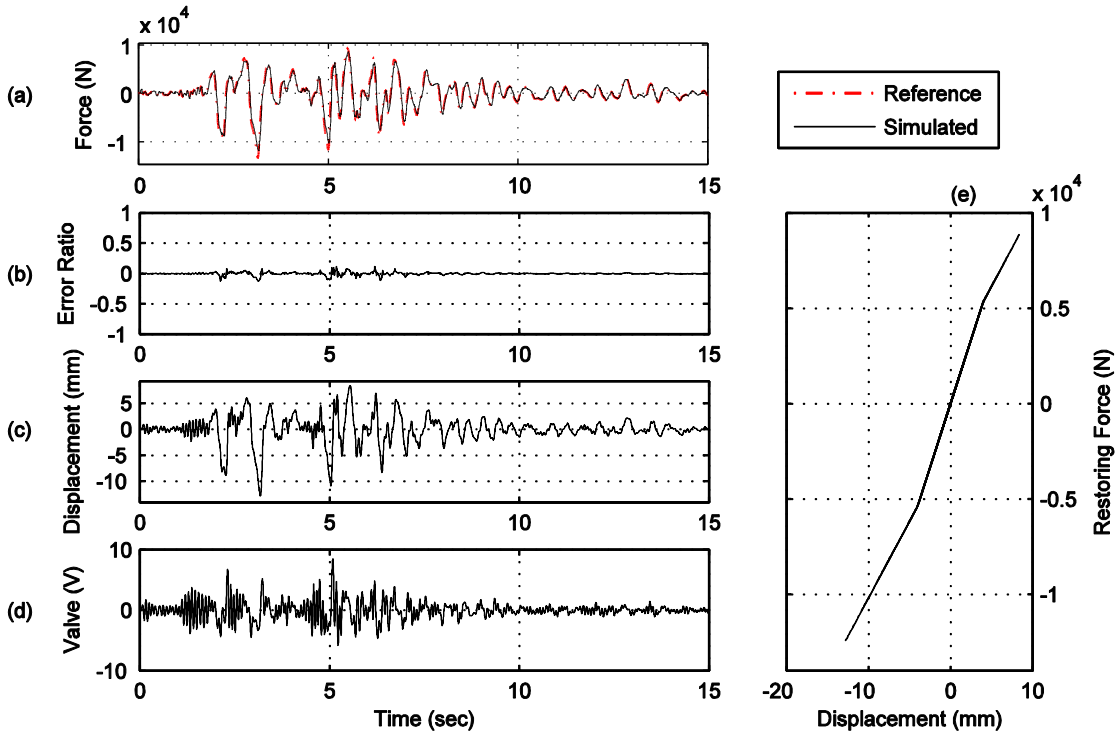

Figure A.15. Yield displacement X_y = 0.004m, post-yield stiffness $k_1 = 0.6*k_0$.

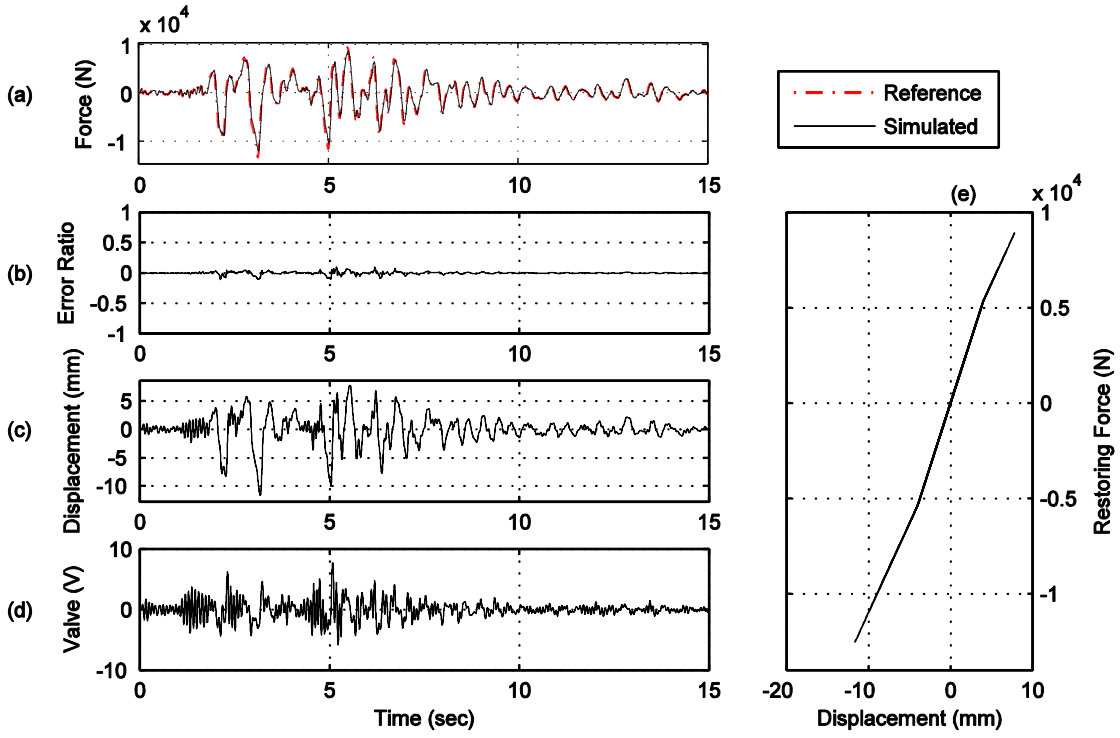

Figure A.16. Yield displacement X_y = 0.004m, post-yield stiffness $k_1 = 0.7*k_0$.

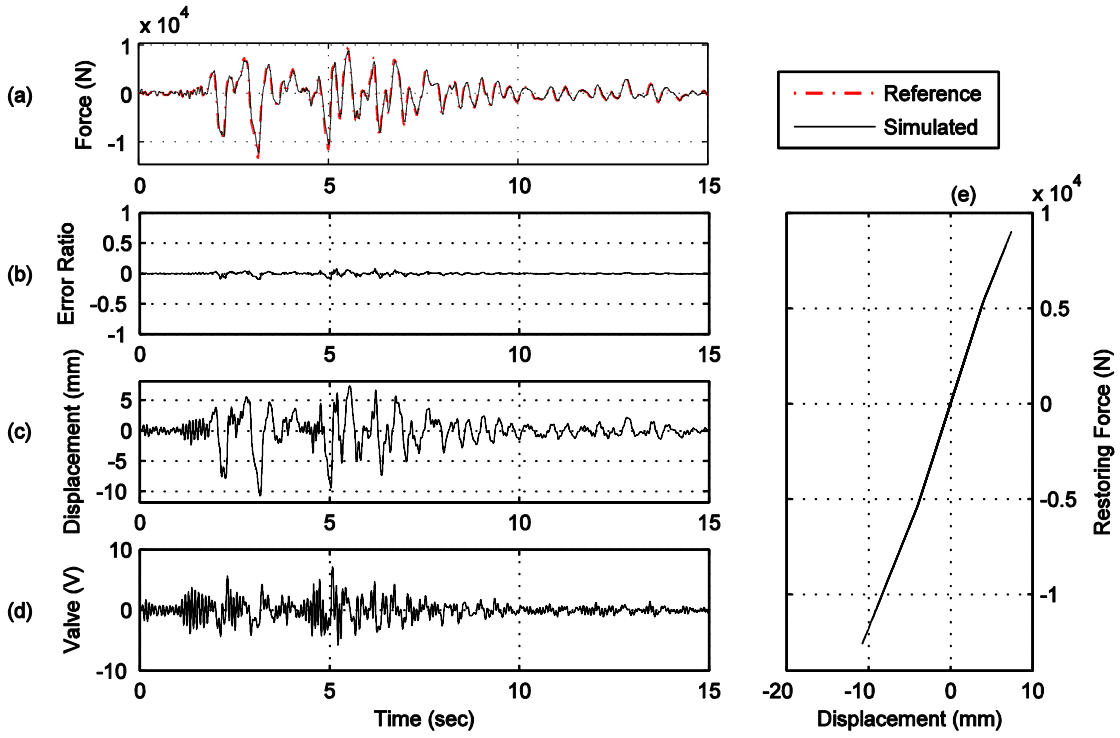

Figure A.17. Yield displacement X_y = 0.004m, post-yield stiffness $k_1 = 0.8*k_0$.

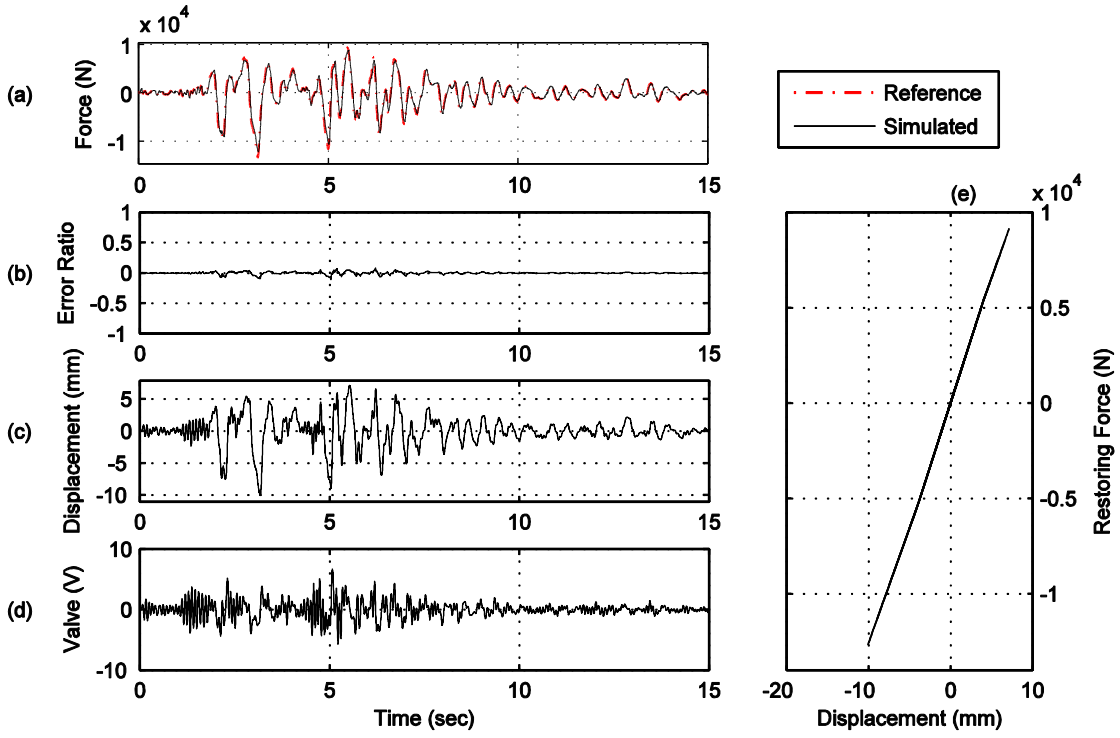

Figure A.18. Yield displacement X_y = 0.004m, post-yield stiffness $k_1 = 0.9*k_0$.

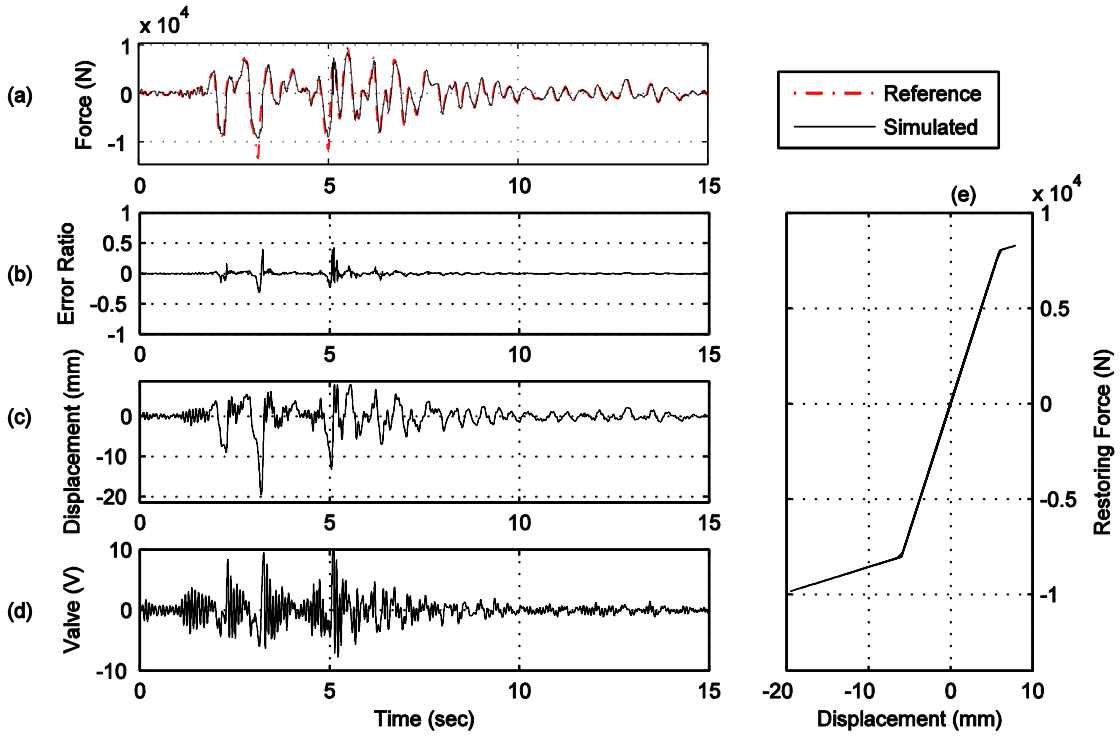

Figure A.19. Yield displacement X_y = 0.006m, post-yield stiffness $k_1 = 0.1*k_0$.

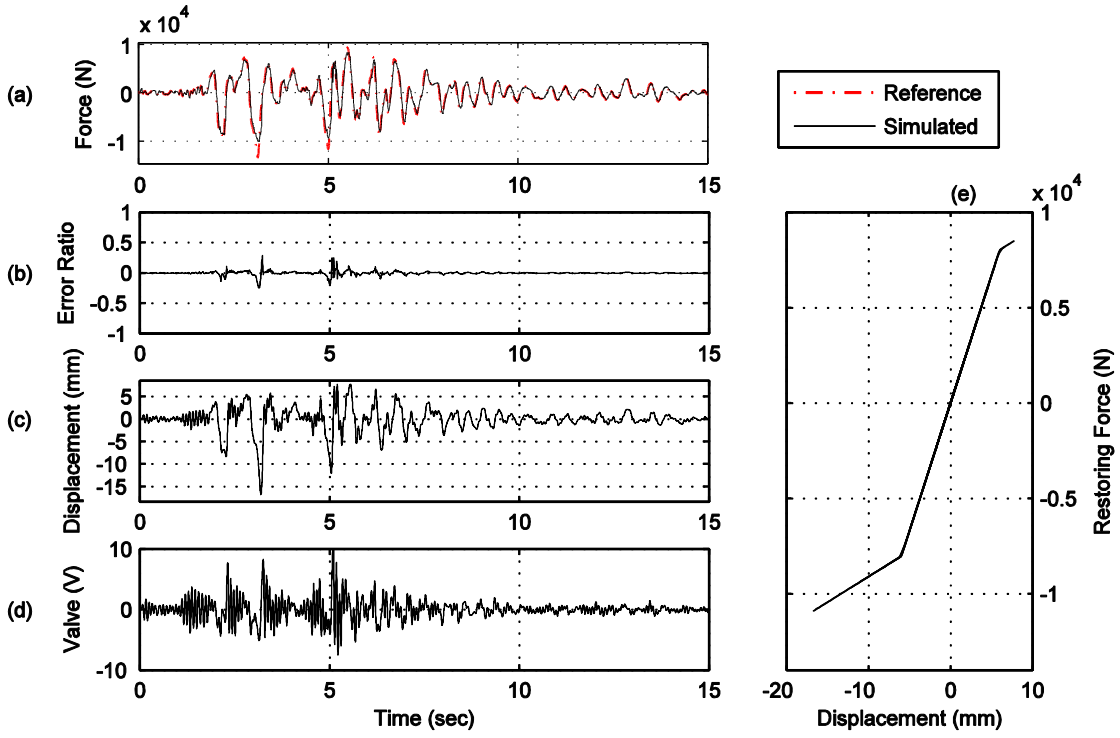

Figure A.20. Yield displacement X_y = 0.006m, post-yield stiffness $k_1 = 0.2*k_0$.

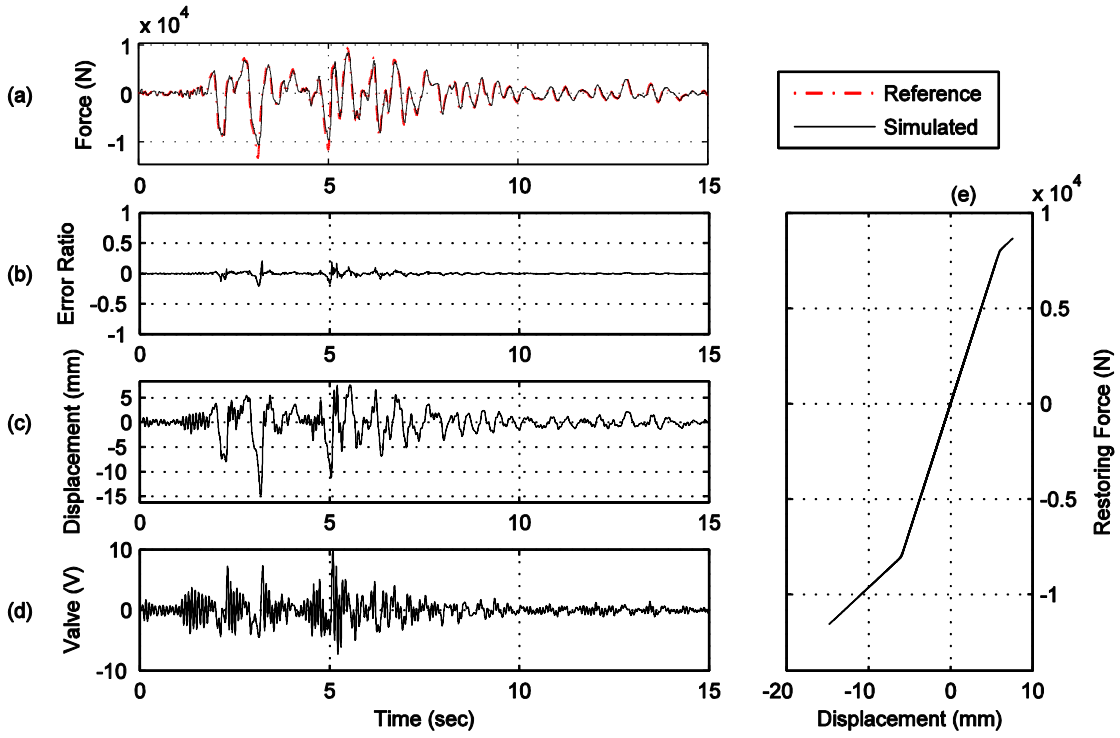

Figure A.21. Yield displacement X_y = 0.006m, post-yield stiffness $k_1 = 0.3*k_0$.

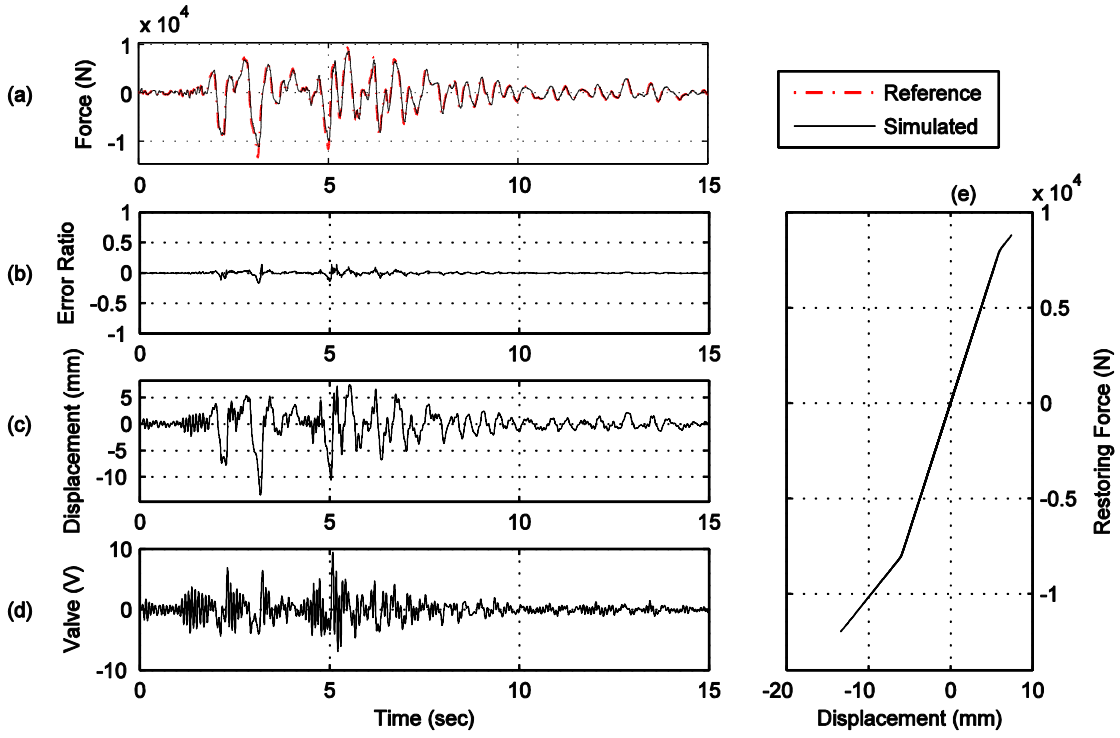

Figure A.22. Yield displacement X_y = 0.006m, post-yield stiffness $k_1 = 0.4*k_0$.

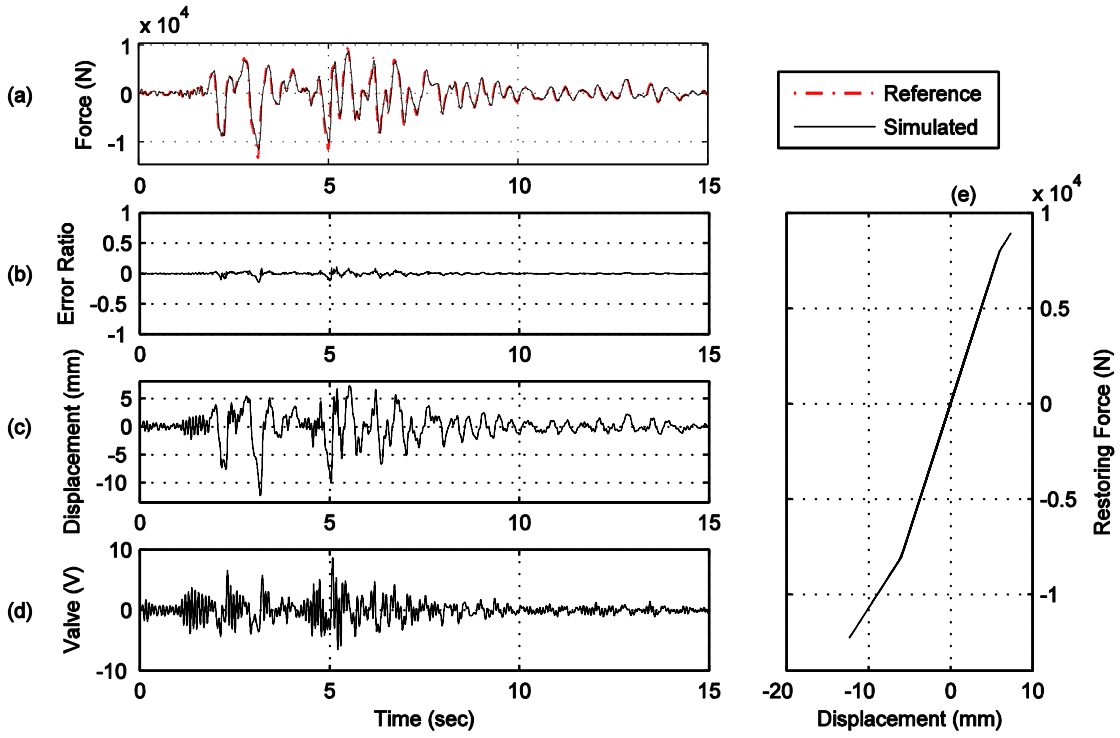

Figure A.23. Yield displacement X_y = 0.006m, post-yield stiffness $k_1 = 0.5*k_0$.

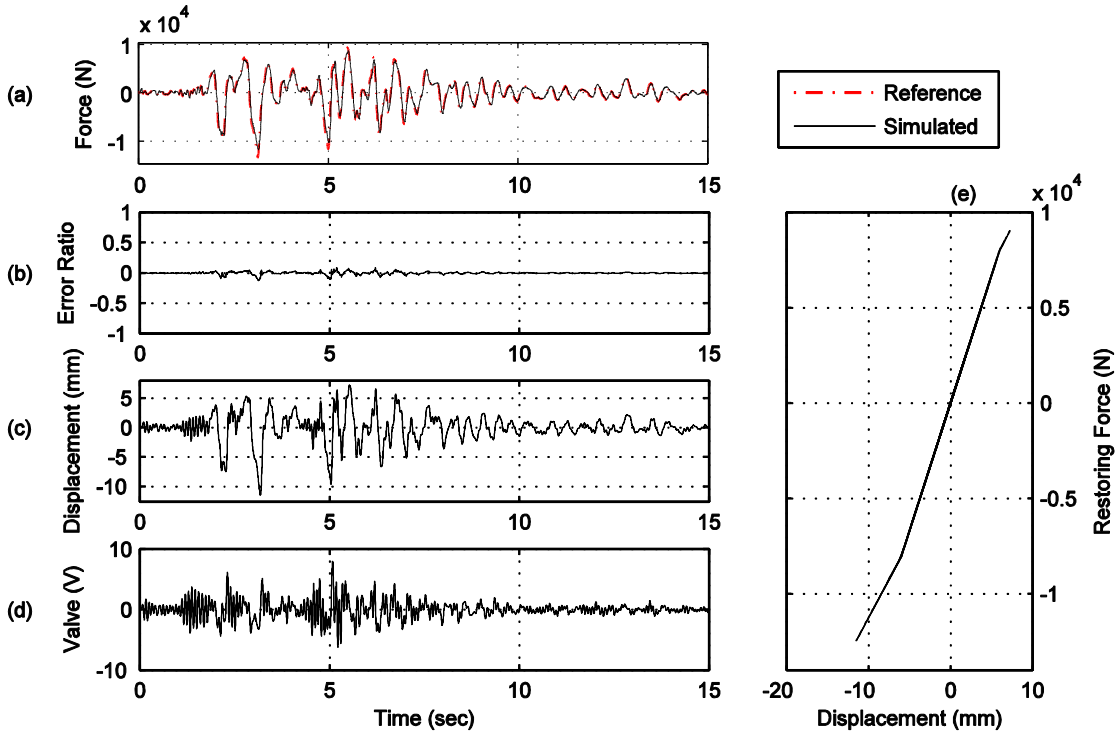

Figure A.24. Yield displacement X_y = 0.006m, post-yield stiffness $k_1 = 0.6*k_0$.

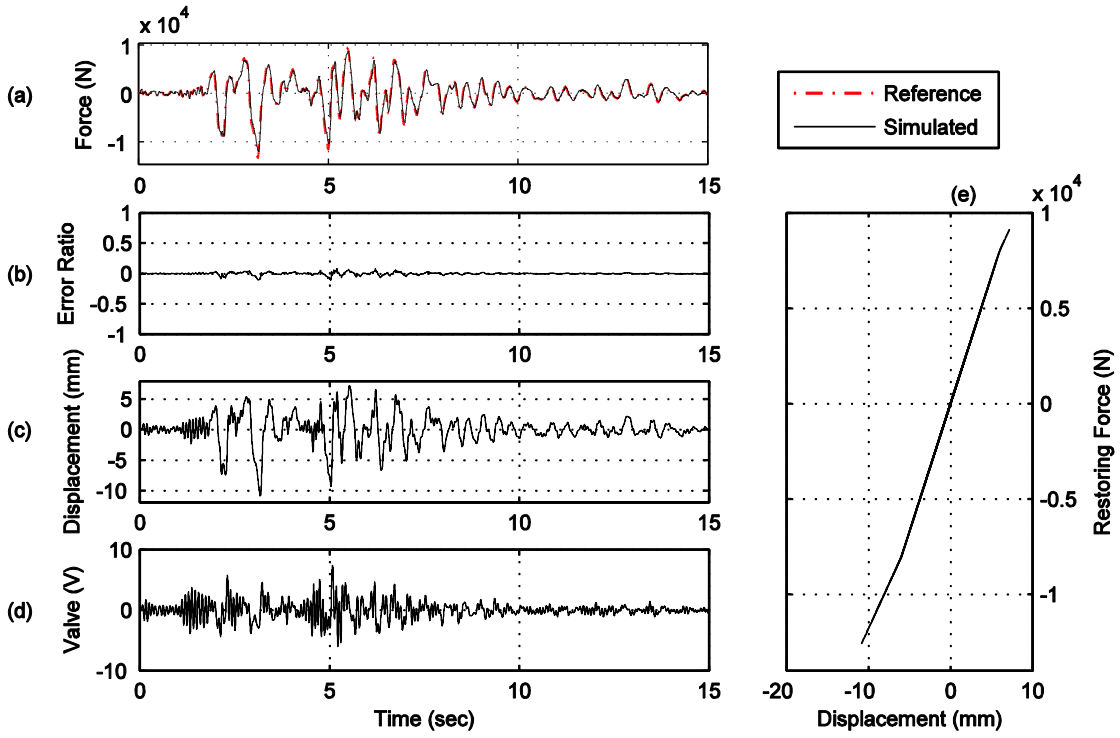

Figure A.25. Yield displacement X_y = 0.006m, post-yield stiffness $k_1 = 0.7*k_0$.

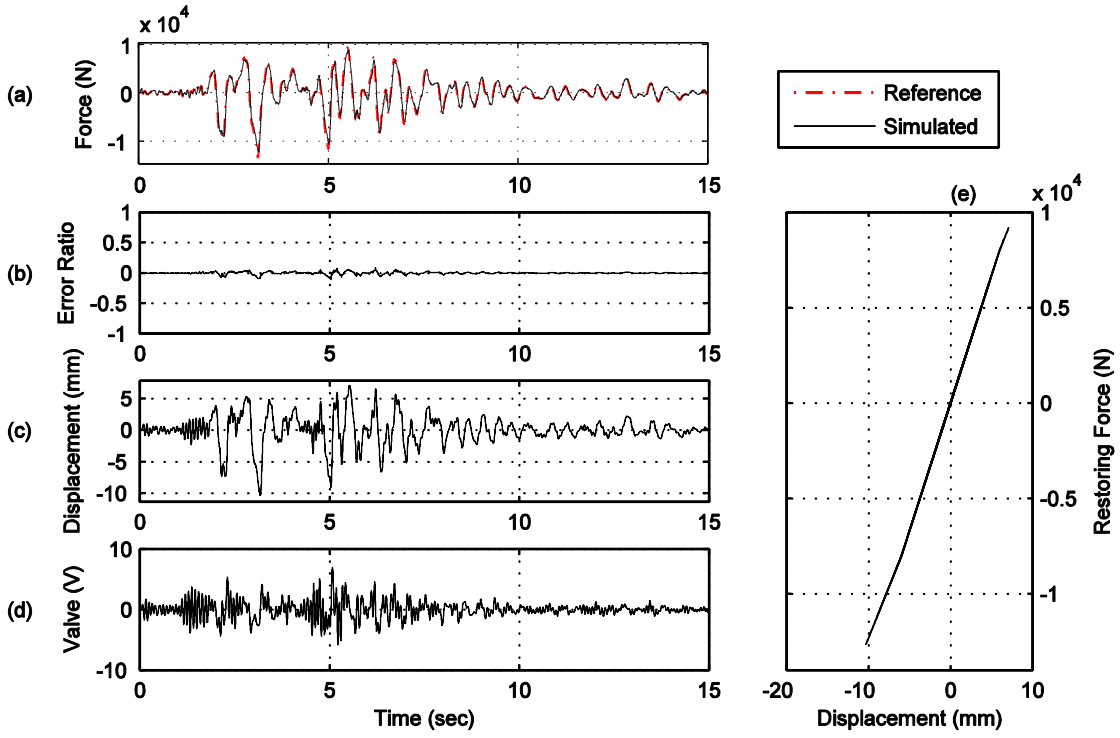

Figure A.26. Yield displacement X_y = 0.006m, post-yield stiffness $k_1 = 0.8*k_0$.

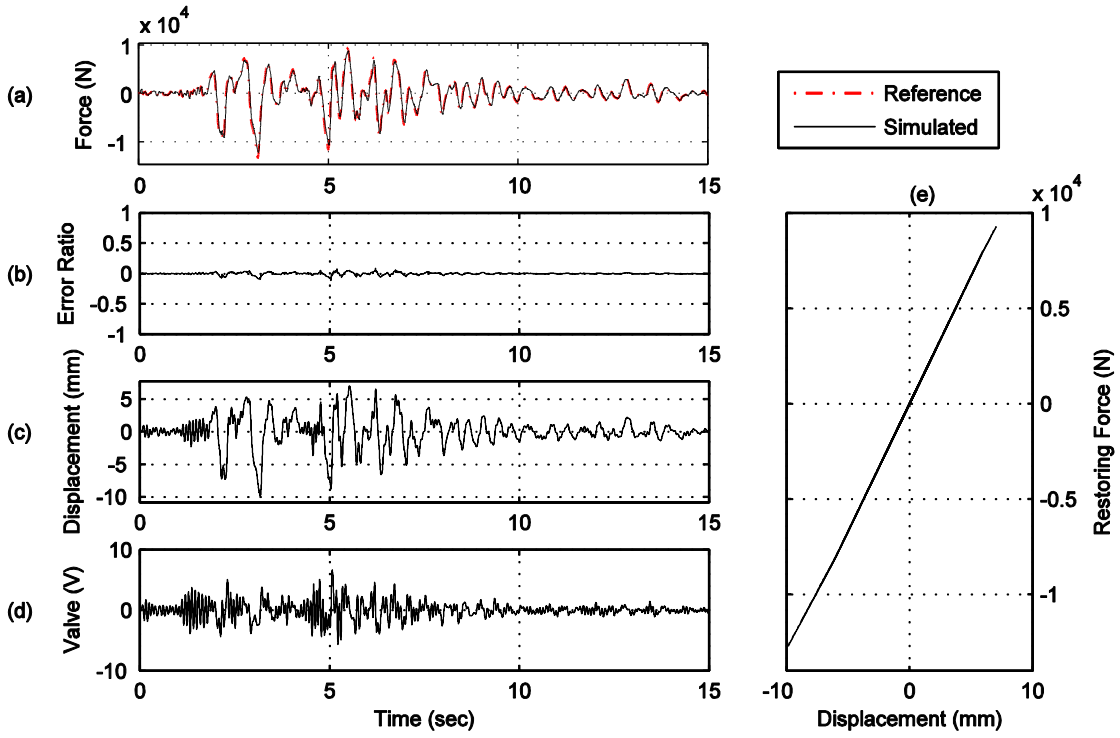

Figure A.27. Yield displacement X_y = 0.006m, post-yield stiffness $k_1 = 0.9*k_0$.

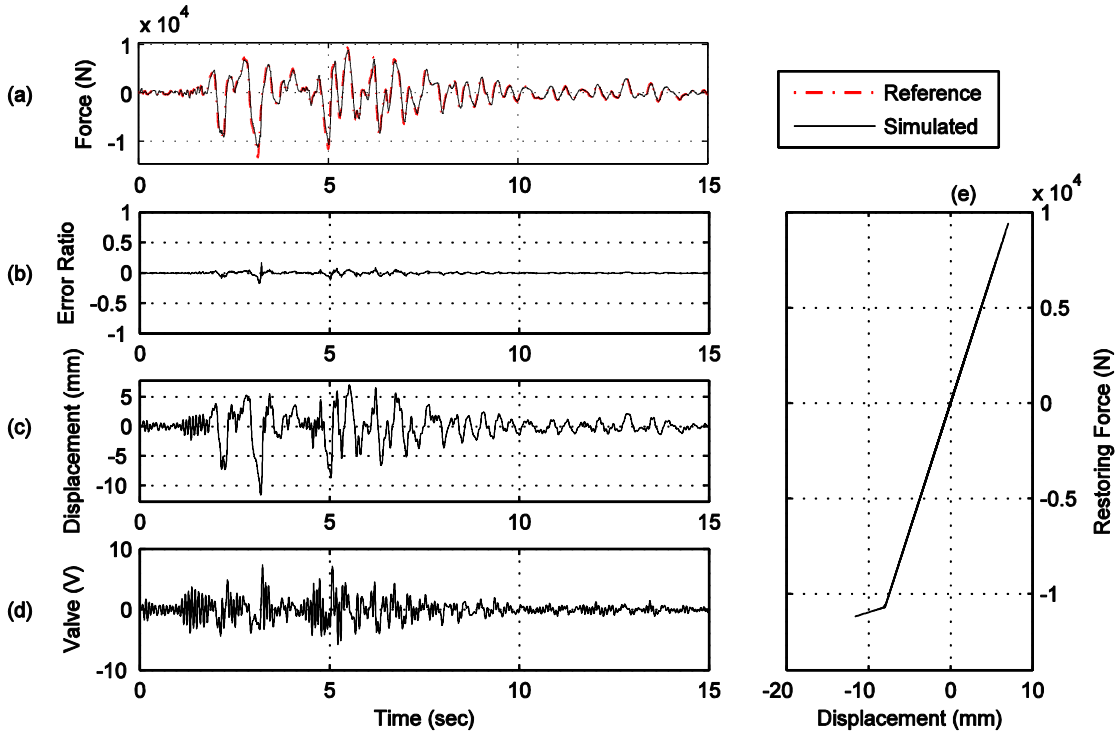

Figure A.28. Yield displacement X_y = 0.008m, post-yield stiffness $k_1 = 0.1*k_0$.

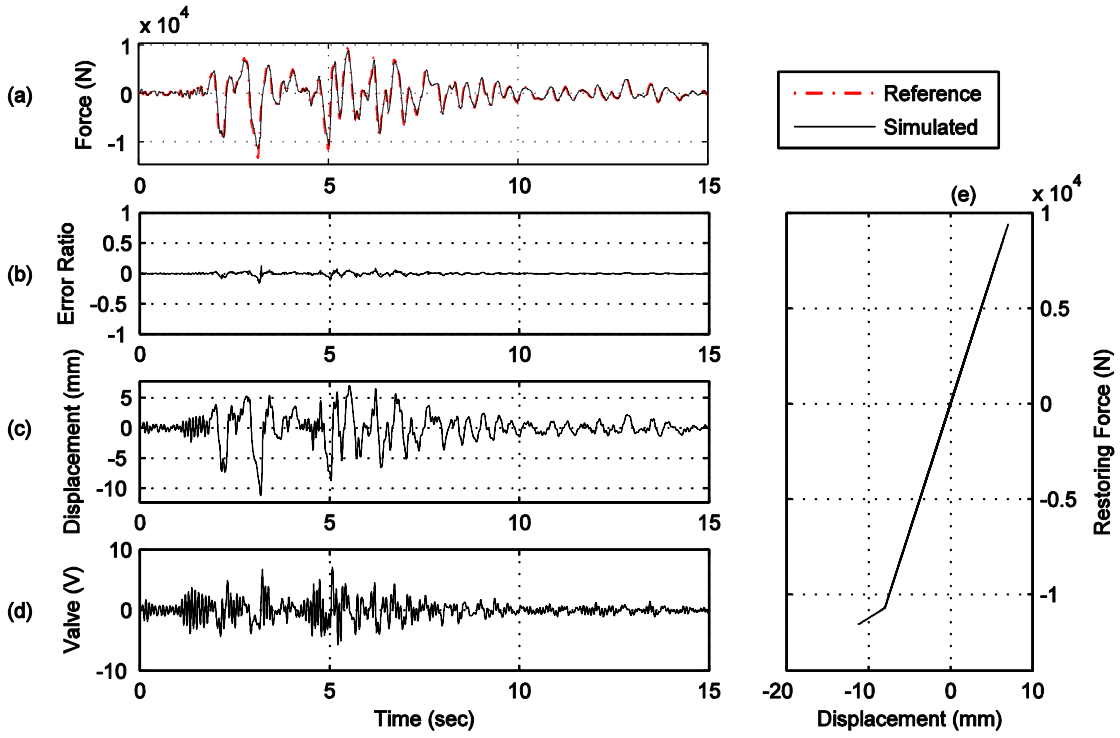

Figure A.29. Yield displacement X_y = 0.008m, post-yield stiffness $k_1 = 0.2*k_0$.

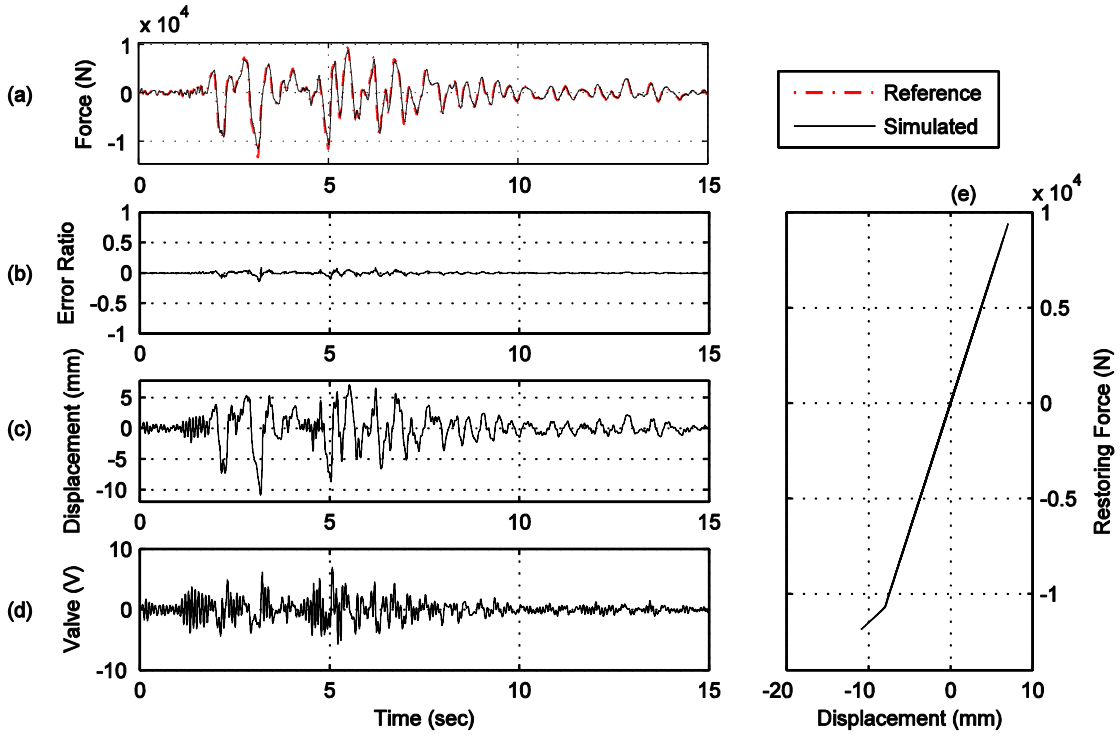

Figure A.30. Yield displacement X_y = 0.008m, post-yield stiffness $k_1 = 0.3*k_0$.

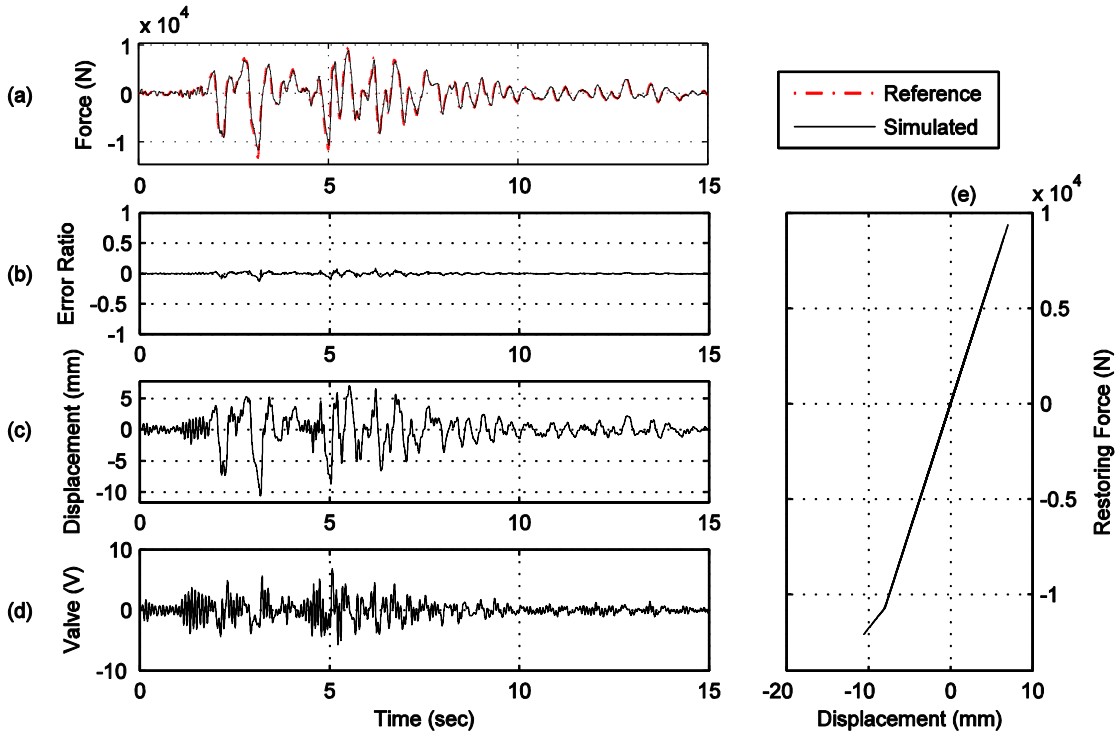

Figure A.31. Yield displacement X_y = 0.008m, post-yield stiffness $k_1 = 0.4*k_0$.

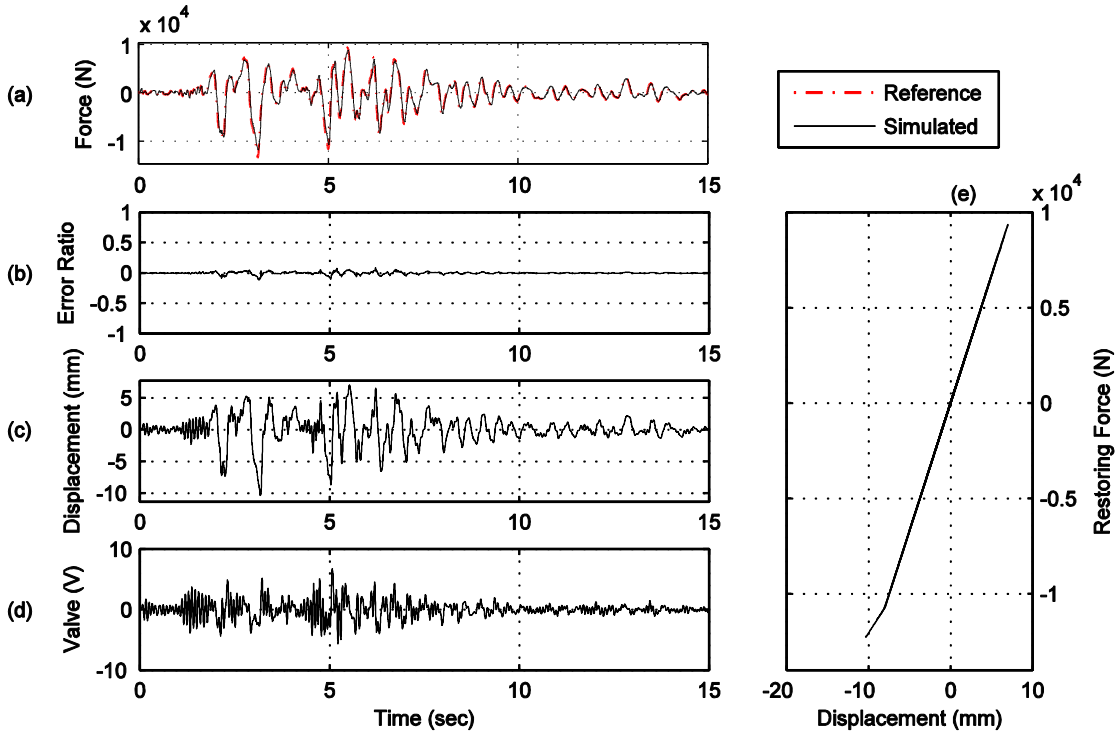

Figure A.32. Yield displacement X_y = 0.008m, post-yield stiffness $k_1 = 0.5*k_0$.

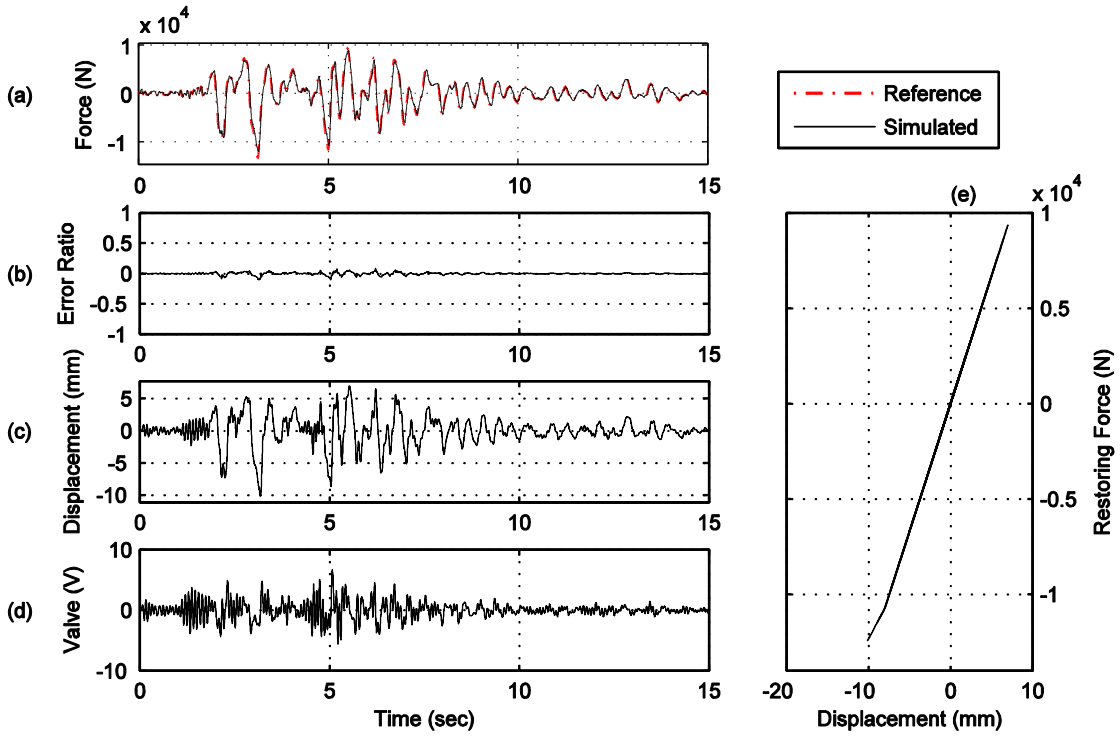

Figure A.33. Yield displacement X_y = 0.008m, post-yield stiffness $k_1 = 0.6*k_0$.

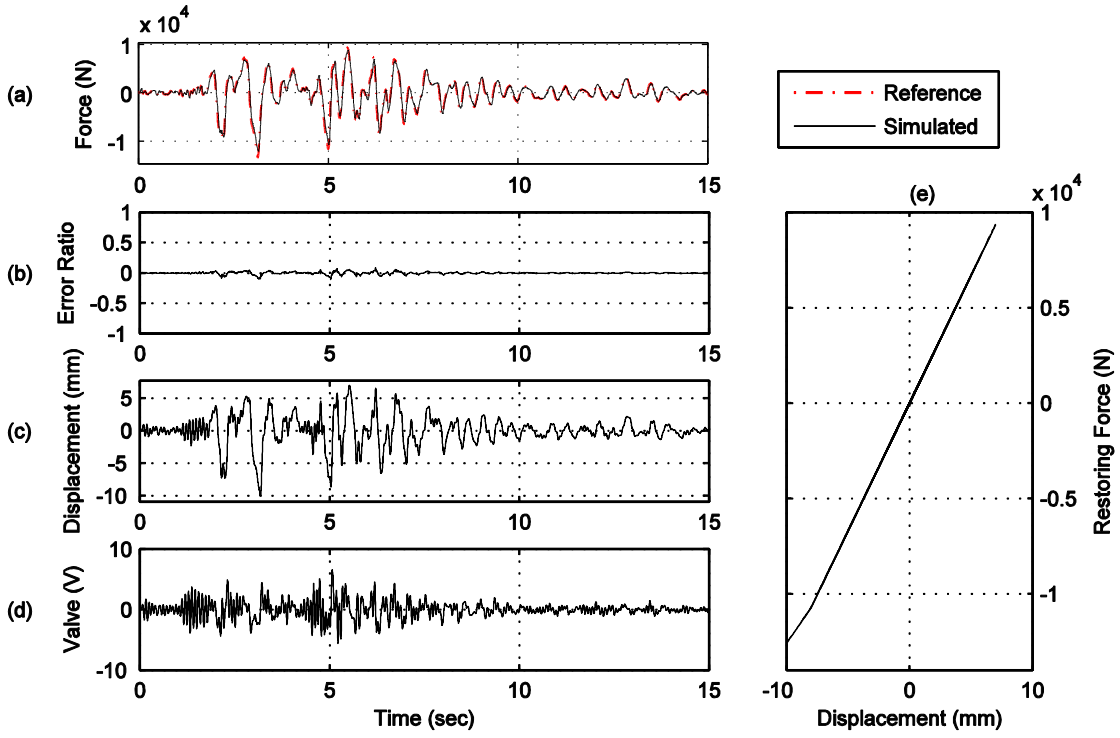

Figure A.34. Yield displacement X_y = 0.008m, post-yield stiffness $k_1 = 0.7*k_0$.

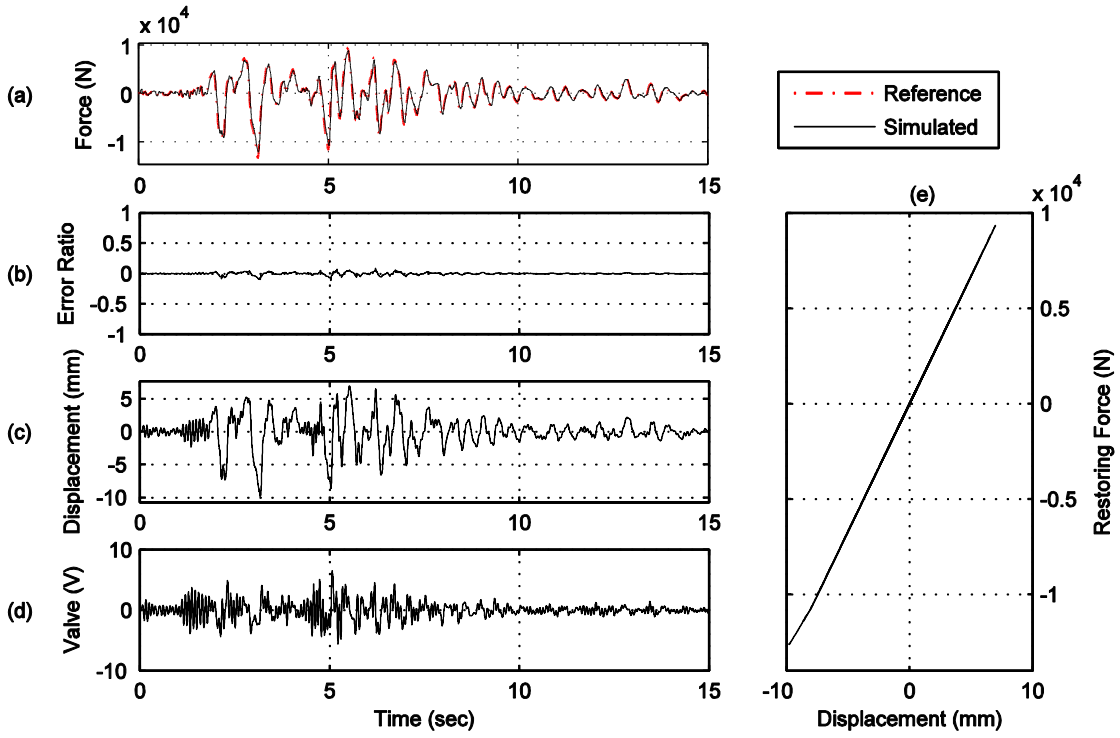

Figure A.35. Yield displacement X_y = 0.008m, post-yield stiffness $k_1 = 0.8*k_0$.

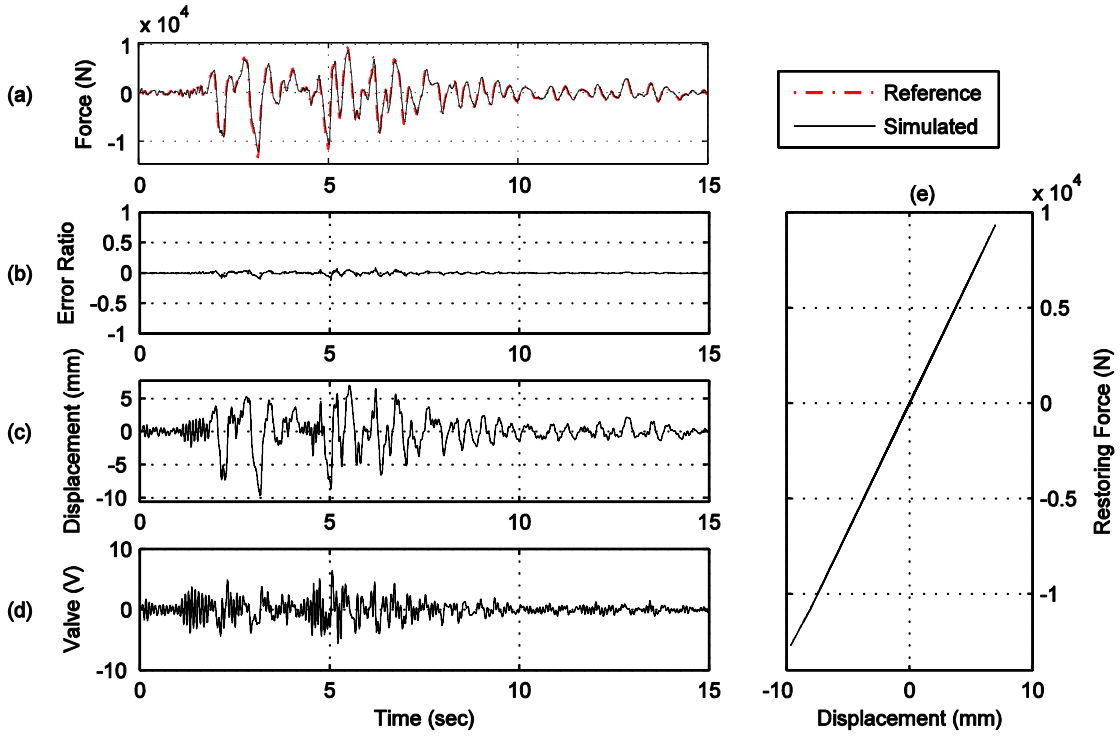

Figure A.36. Yield displacement X_y = 0.008m, post-yield stiffness $k_1 = 0.9*k_0$.

Pinned Base

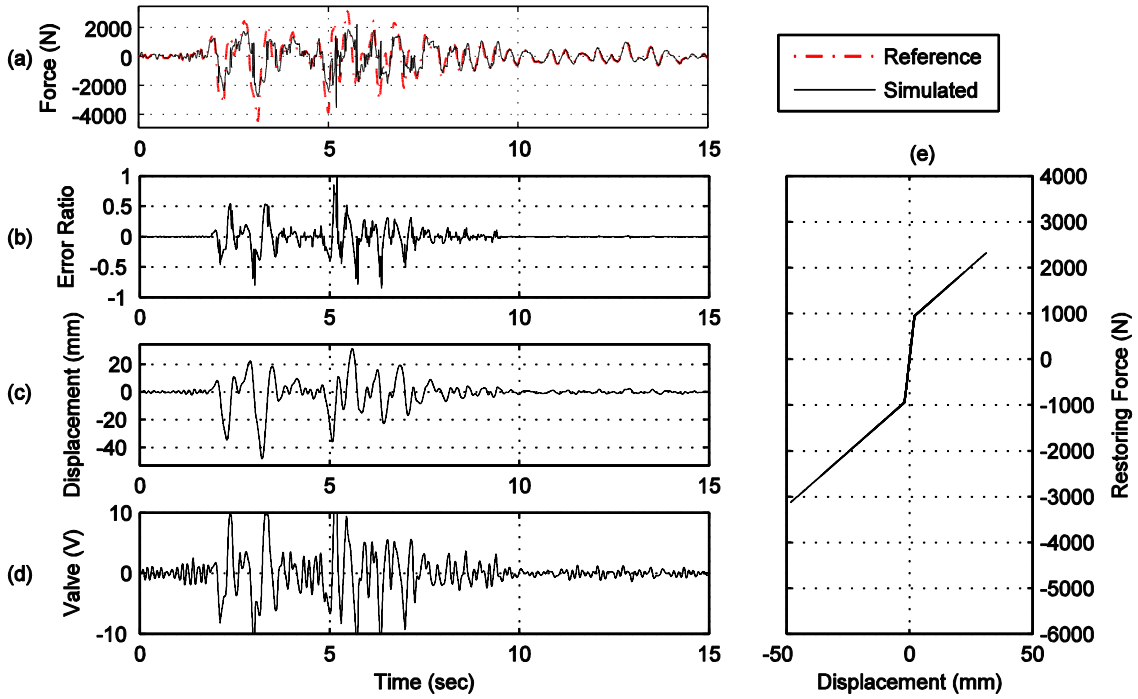

Figure A.37. Yield displacement X_y = 0.002m, post-yield stiffness $k_1 = 0.1*k_0$.

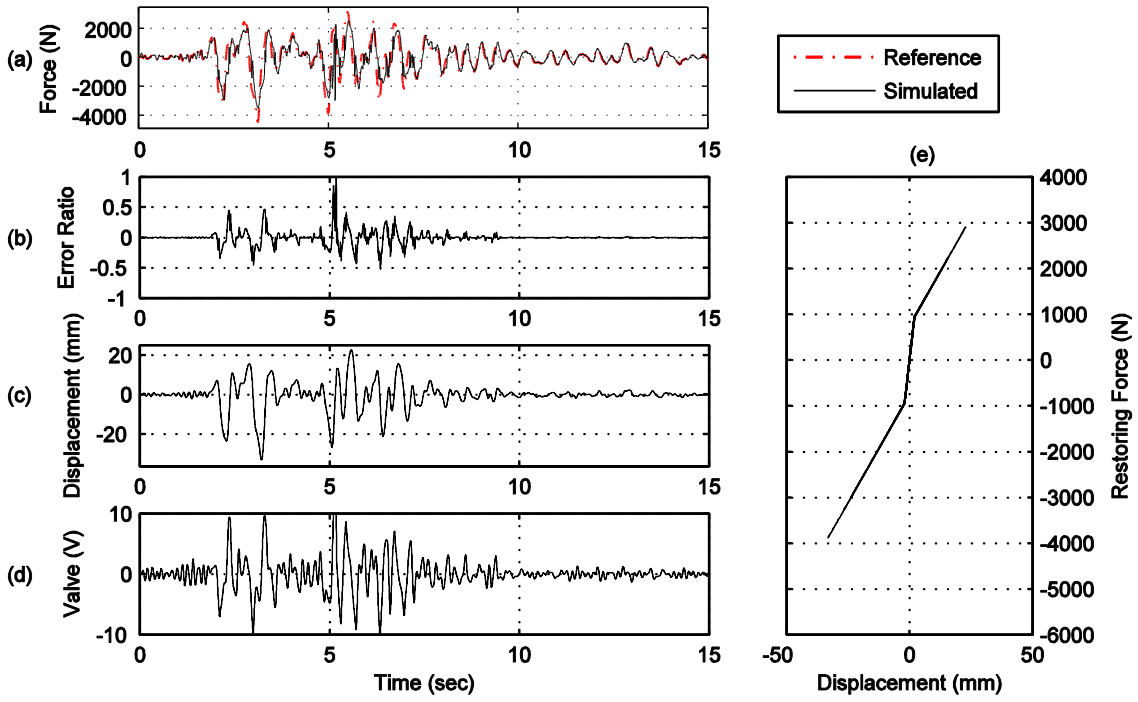

Figure A.38. Yield displacement X_y = 0.002m, post-yield stiffness $k_1 = 0.2*k_0$.

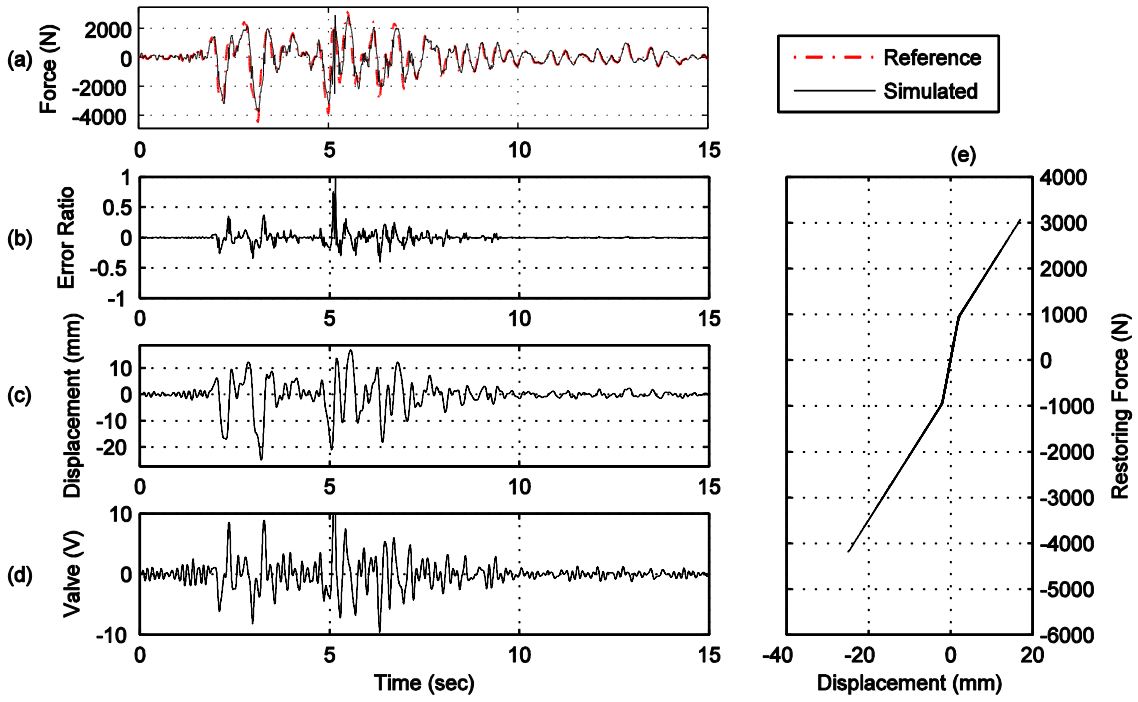

Figure A.39. Yield displacement X_y = 0.002m, post-yield stiffness $k_1 = 0.3*k_0$.

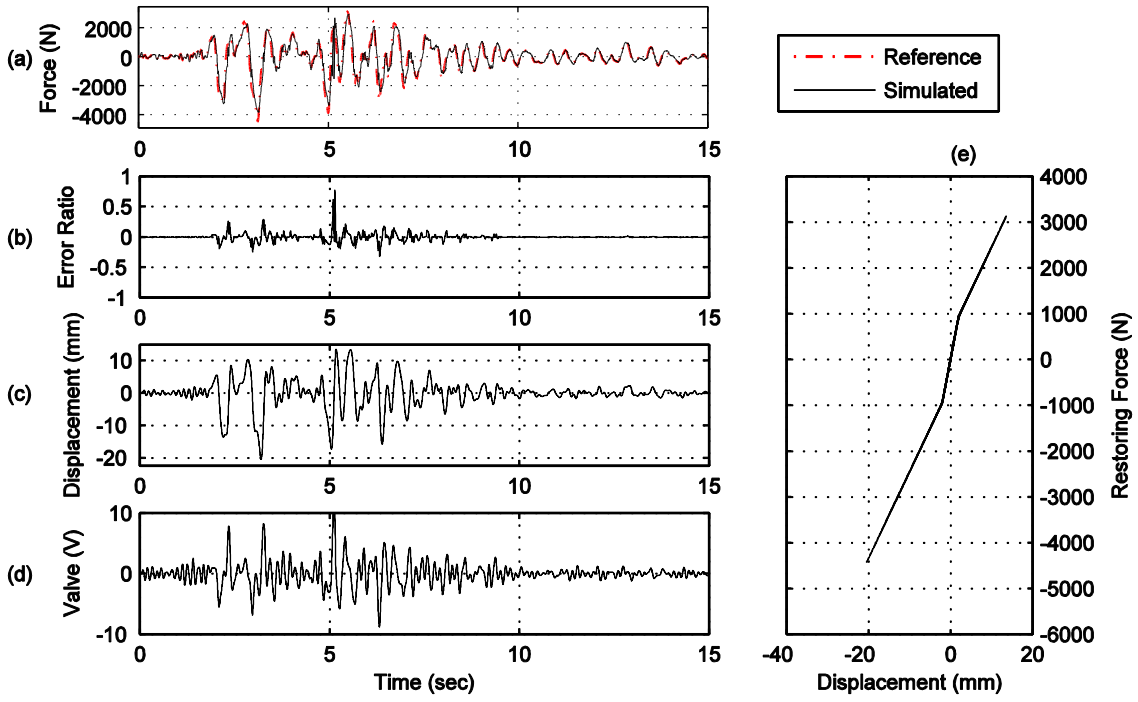

Figure A.40. Yield displacement X_y = 0.002m, post-yield stiffness $k_1 = 0.4*k_0$.

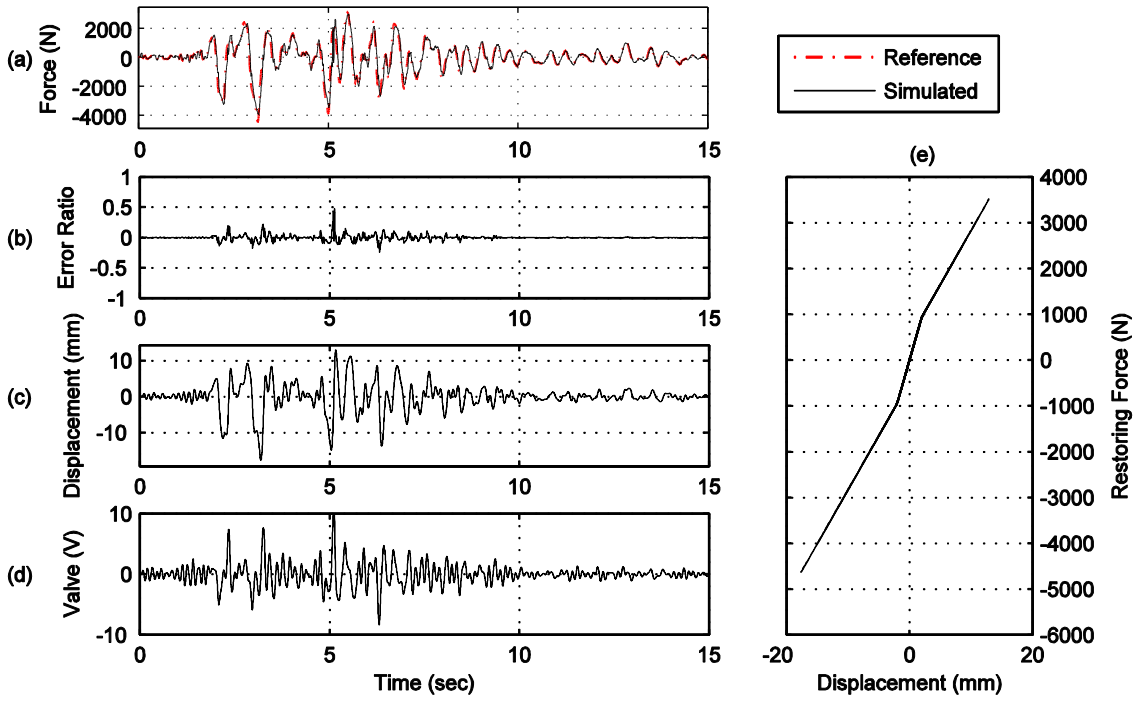

Figure A.41. Yield displacement X_y = 0.002m, post-yield stiffness $k_1 = 0.5*k_0$.

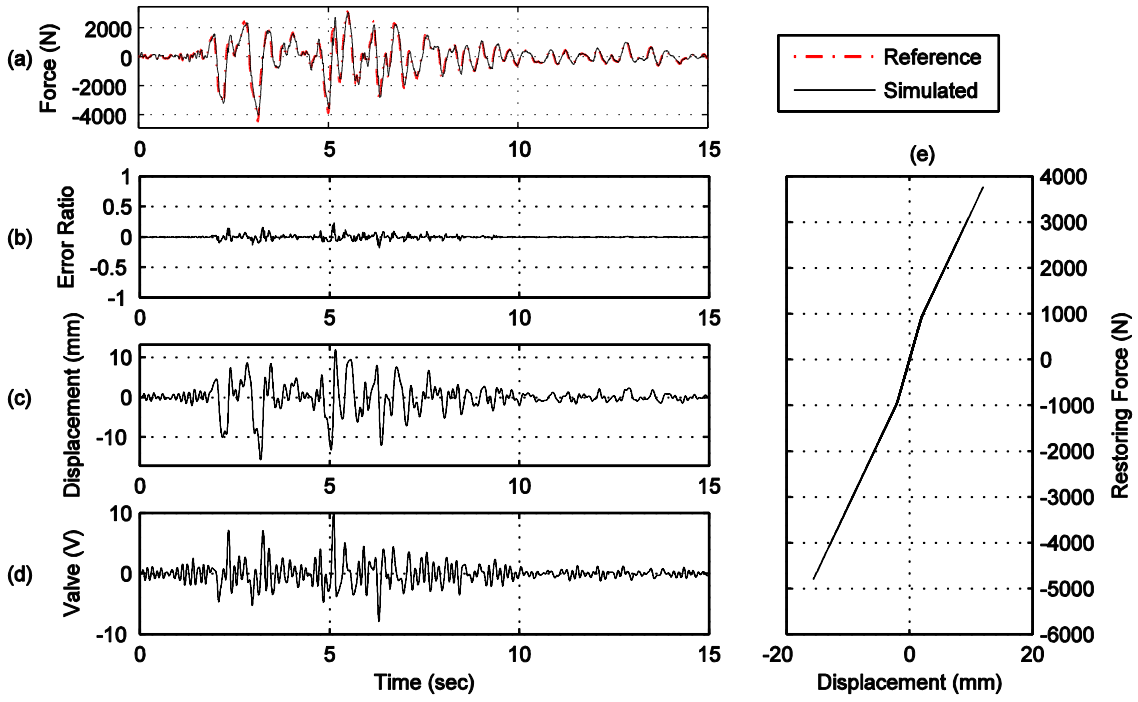

Figure A.42. Yield displacement X_y = 0.002m, post-yield stiffness $k_1 = 0.6*k_0$.

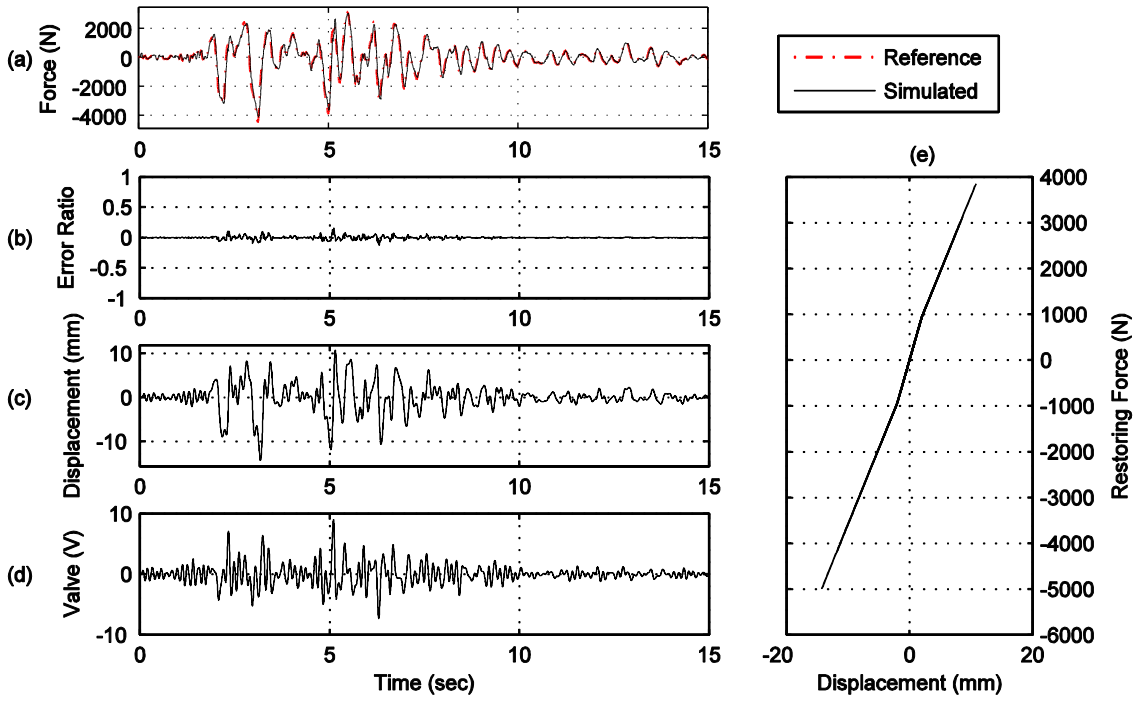

Figure A.43. Yield displacement X_y = 0.002m, post-yield stiffness $k_1 = 0.7*k_0$.

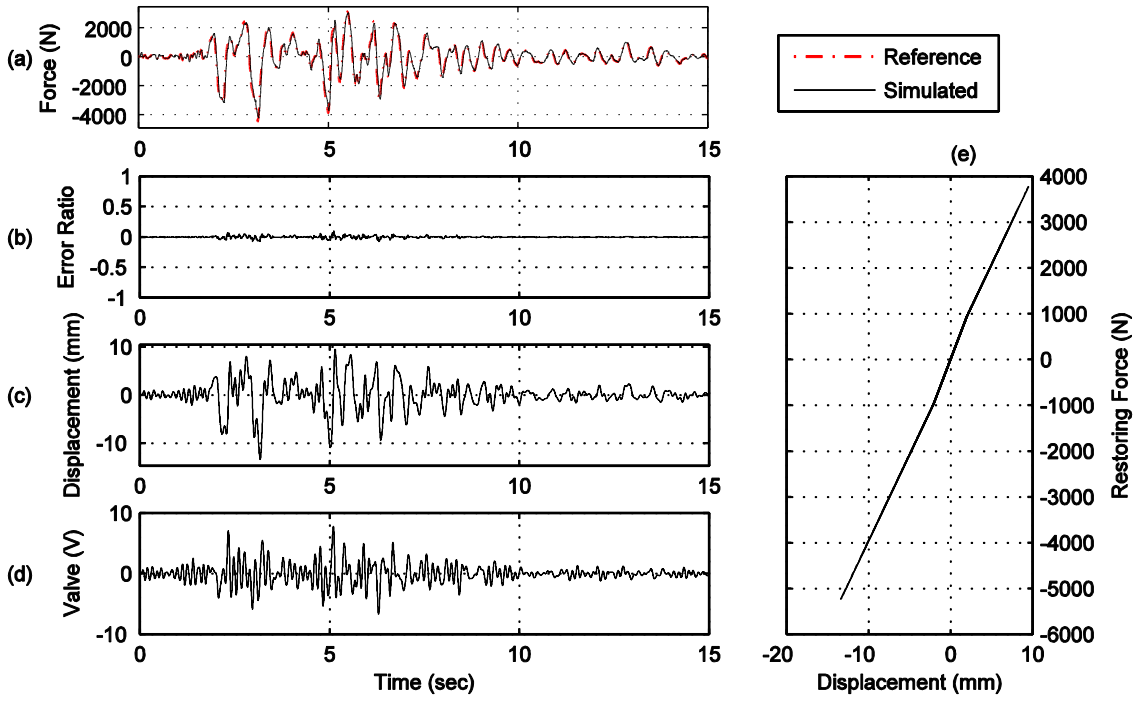

Figure A.44. Yield displacement X_y = 0.002m, post-yield stiffness $k_1 = 0.8*k_0$.

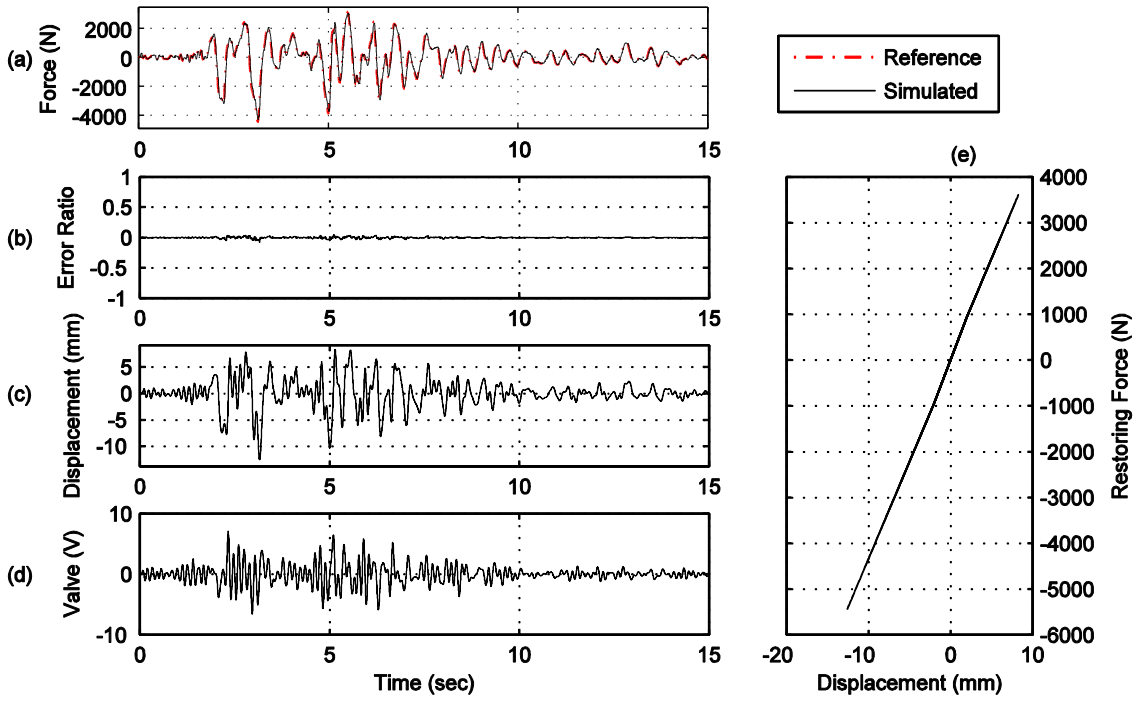

Figure A.45. Yield displacement X_y = 0.002m, post-yield stiffness $k_1 = 0.9*k_0$.

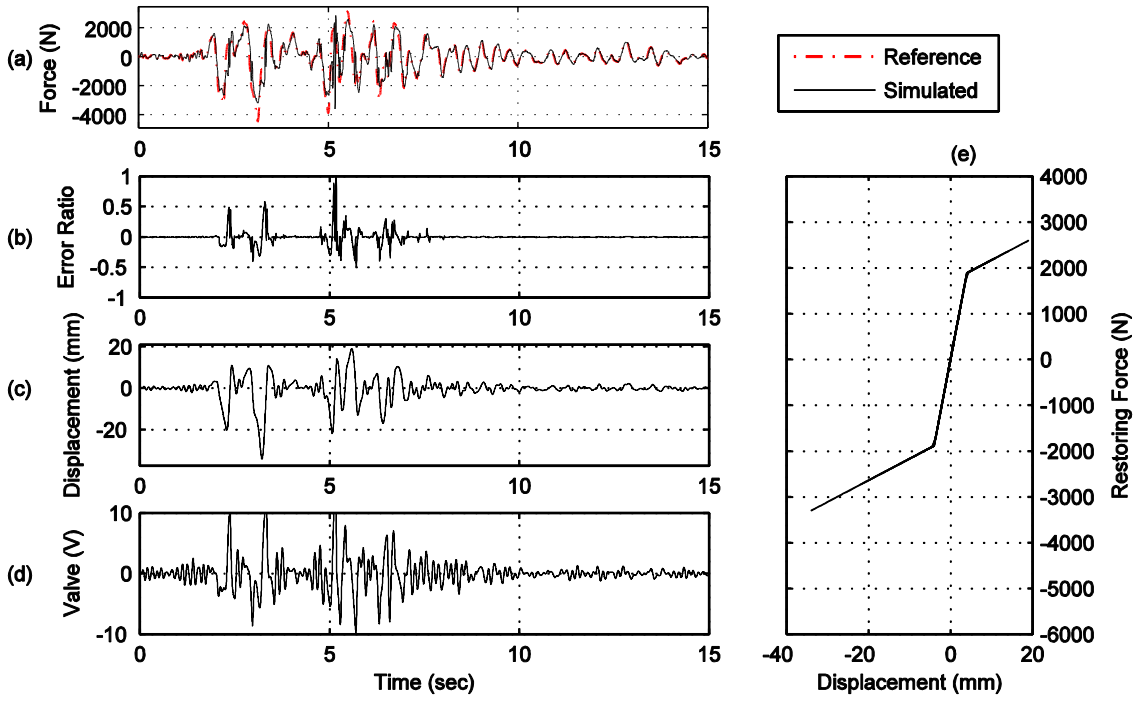

Figure A.46. Yield displacement X_y = 0.004m, post-yield stiffness $k_1 = 0.1*k_0$.

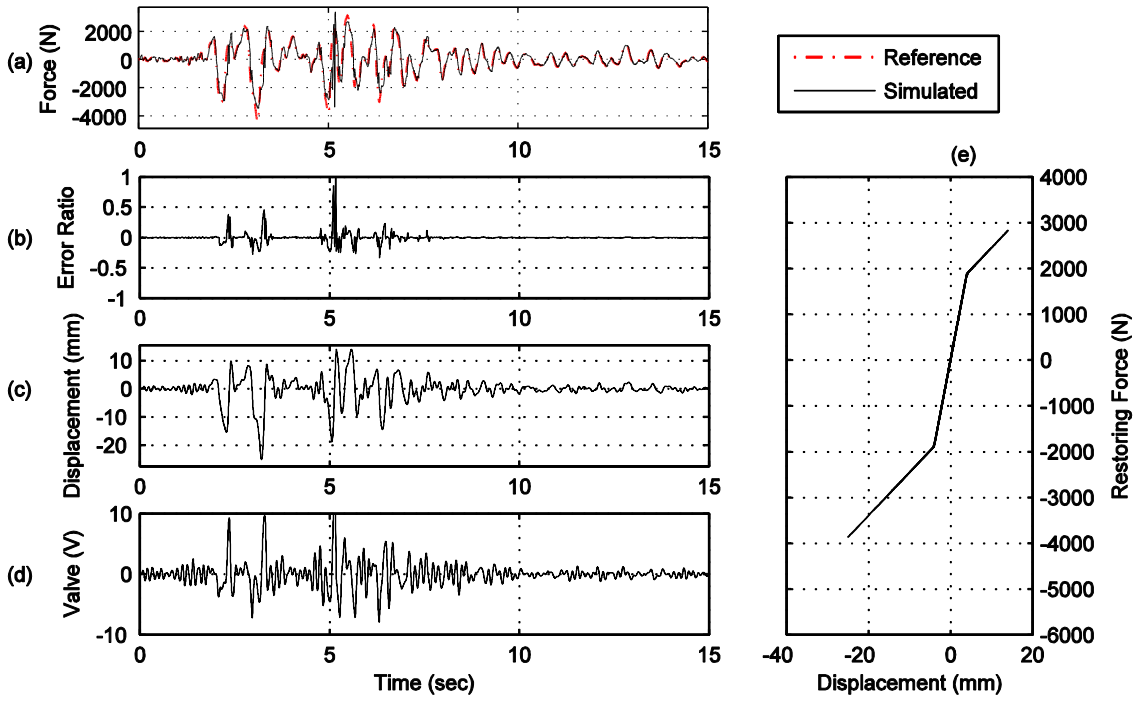

Figure A.47. Yield displacement X_y = 0.004m, post-yield stiffness $k_1 = 0.2*k_0$.

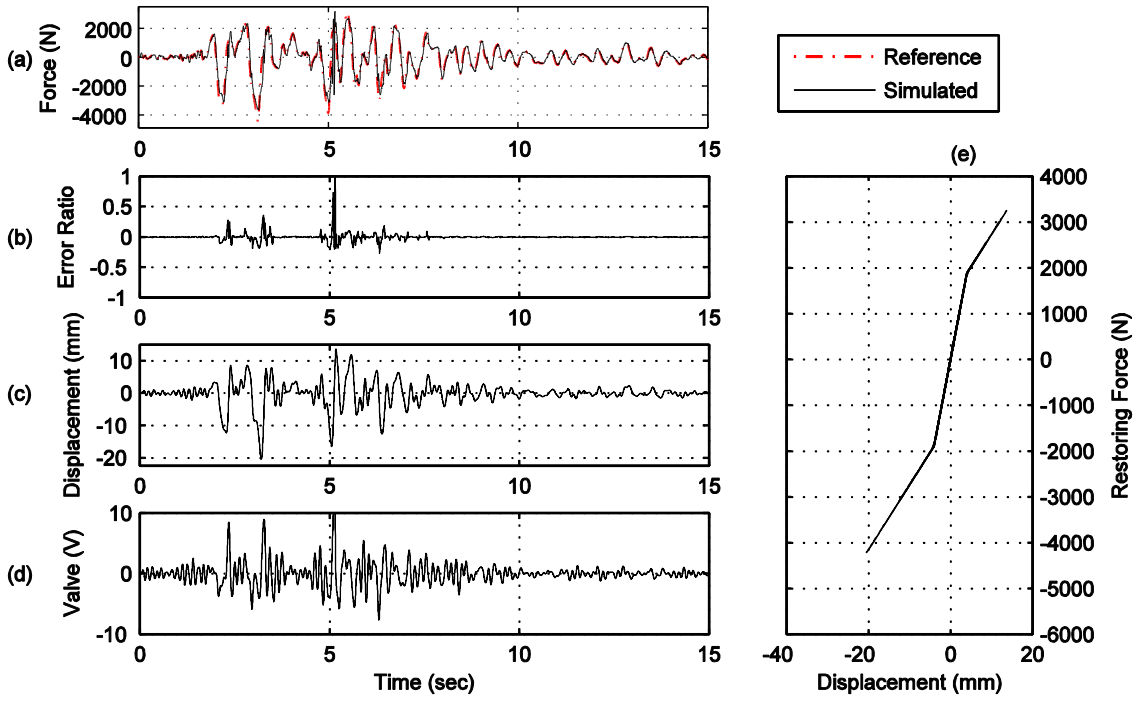

Figure A.48. Yield displacement X_y = 0.004m, post-yield stiffness $k_1 = 0.3*k_0$.

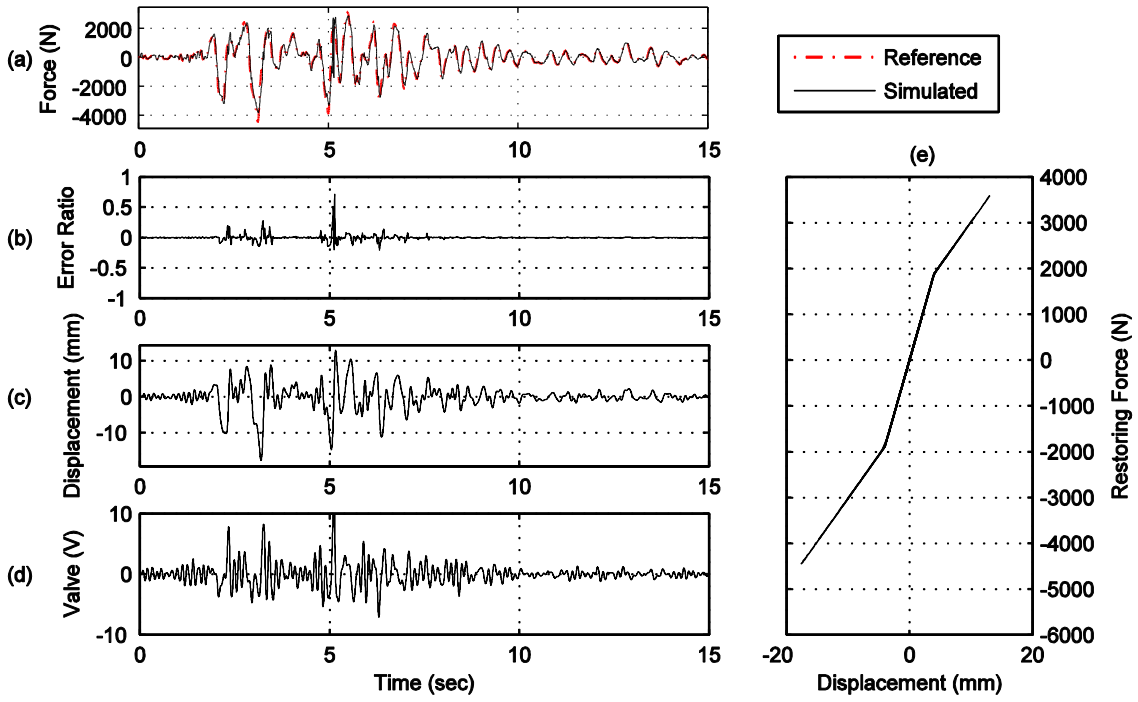

Figure A.49. Yield displacement X_y = 0.004m, post-yield stiffness $k_1 = 0.4*k_0$.

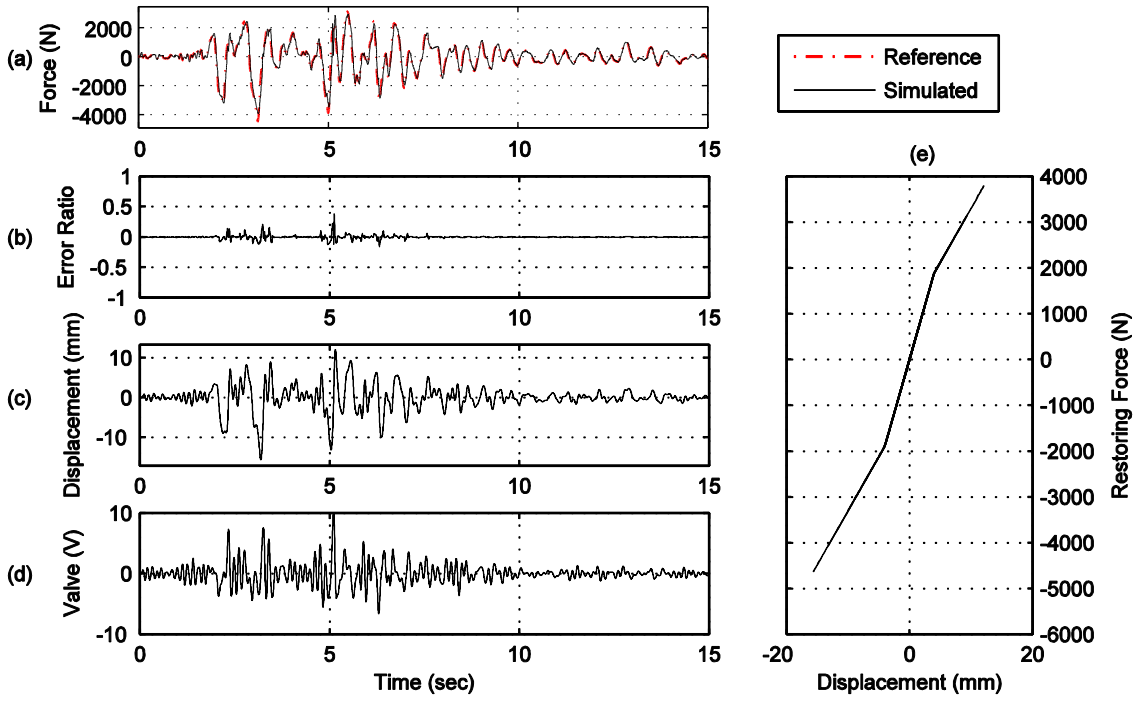

Figure A.50. Yield displacement X_y = 0.004m, post-yield stiffness $k_1 = 0.5*k_0$.

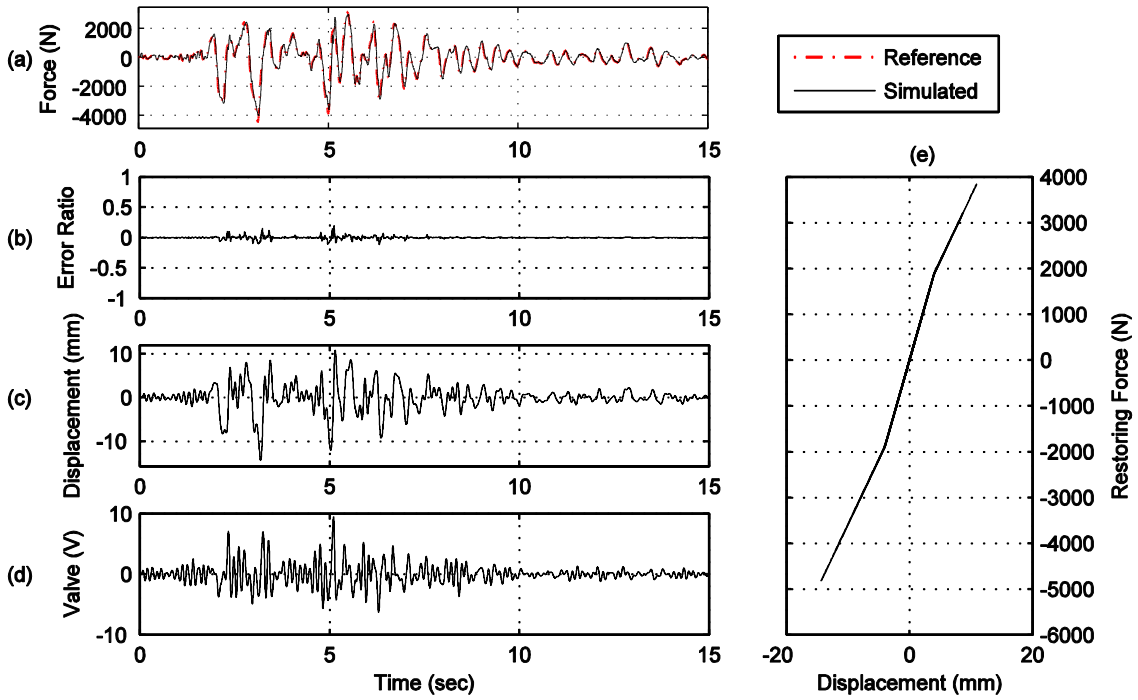

Figure A.51. Yield displacement X_y = 0.004m, post-yield stiffness $k_1 = 0.6*k_0$.

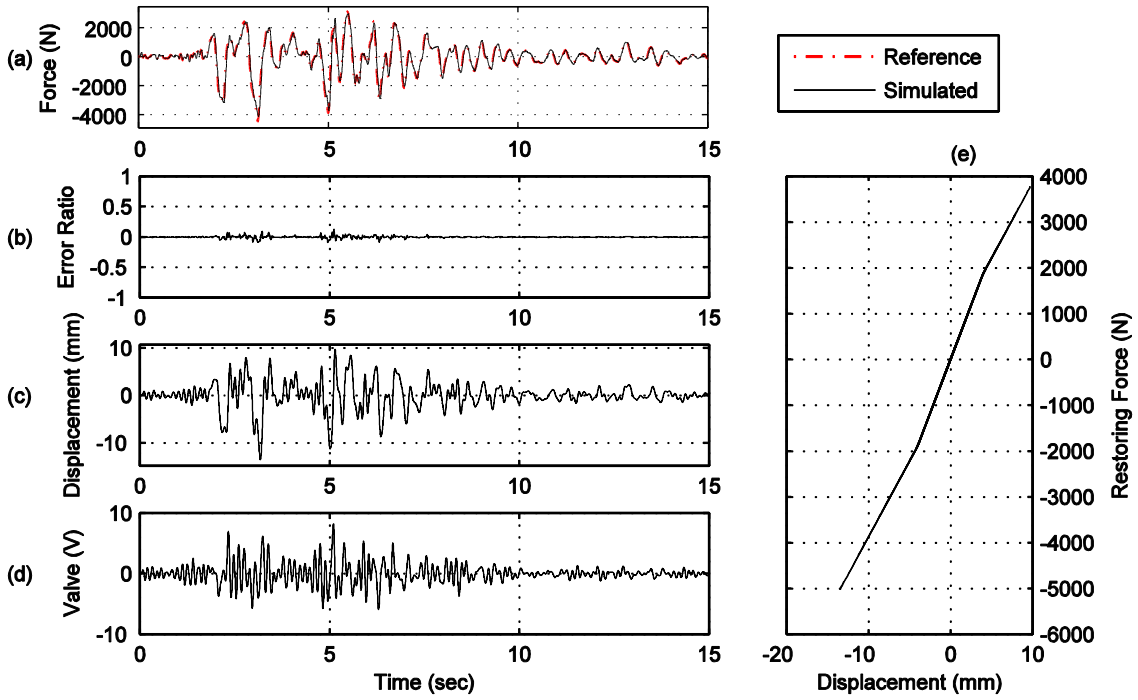

Figure A.52. Yield displacement X_y = 0.004m, post-yield stiffness $k_1 = 0.7*k_0$.

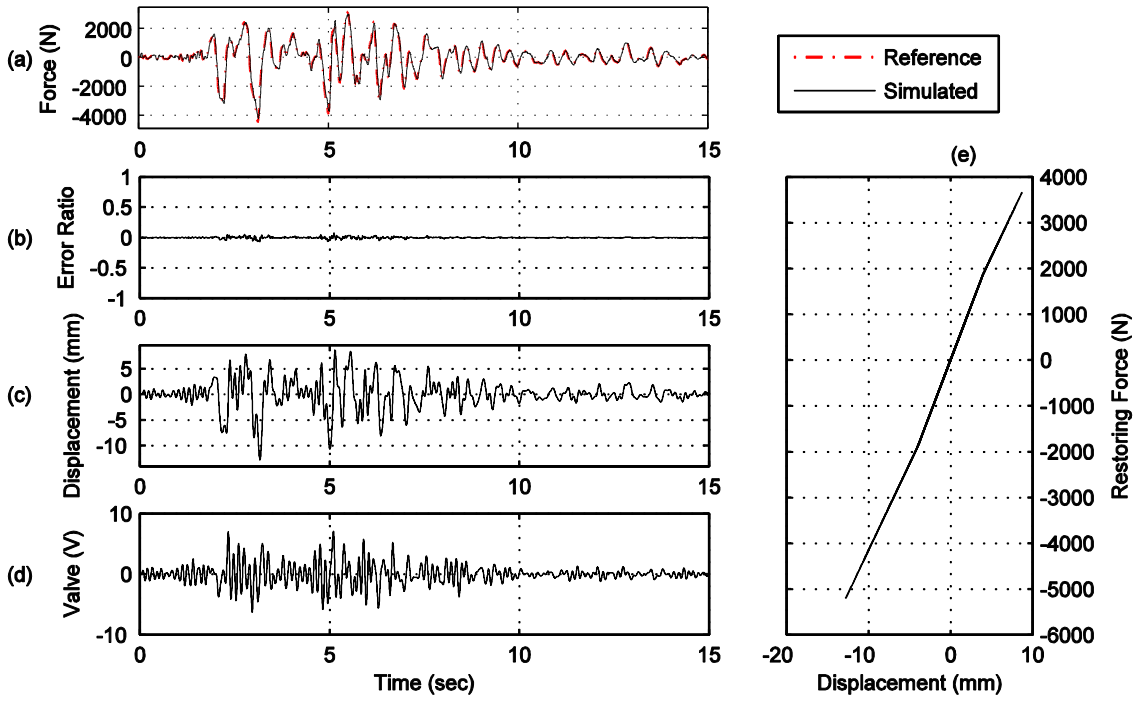

Figure A.53. Yield displacement X_y = 0.004m, post-yield stiffness $k_1 = 0.8*k_0$.

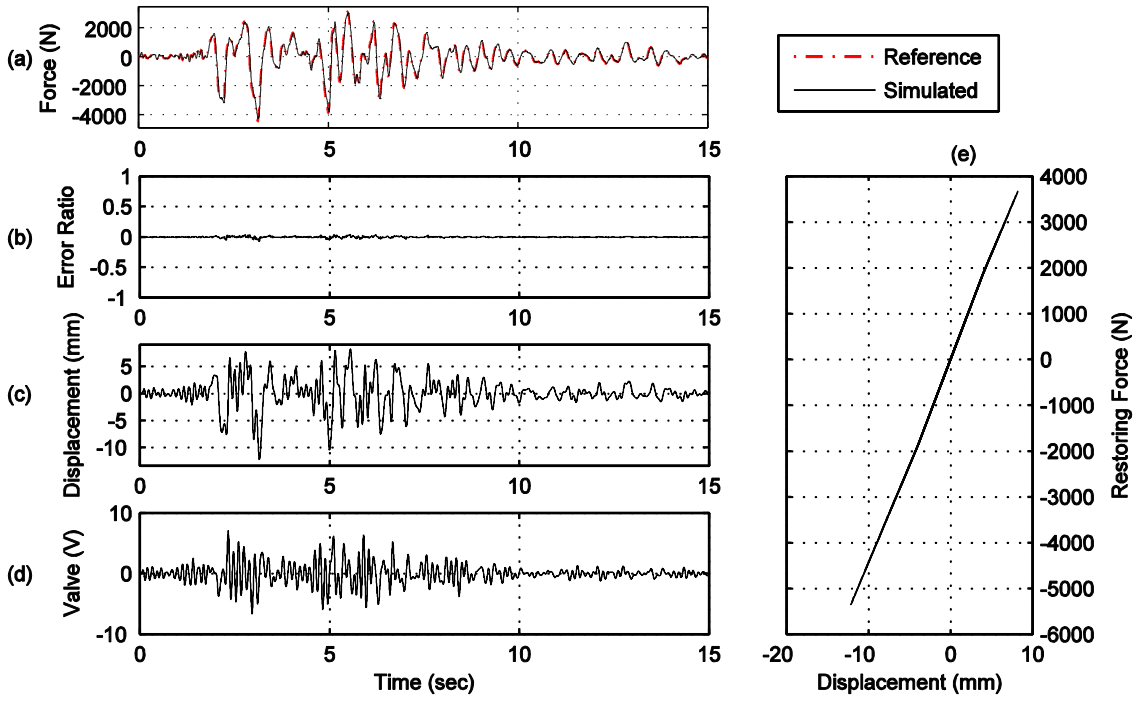

Figure A.54. Yield displacement X_y = 0.004m, post-yield stiffness $k_1 = 0.9*k_0$.

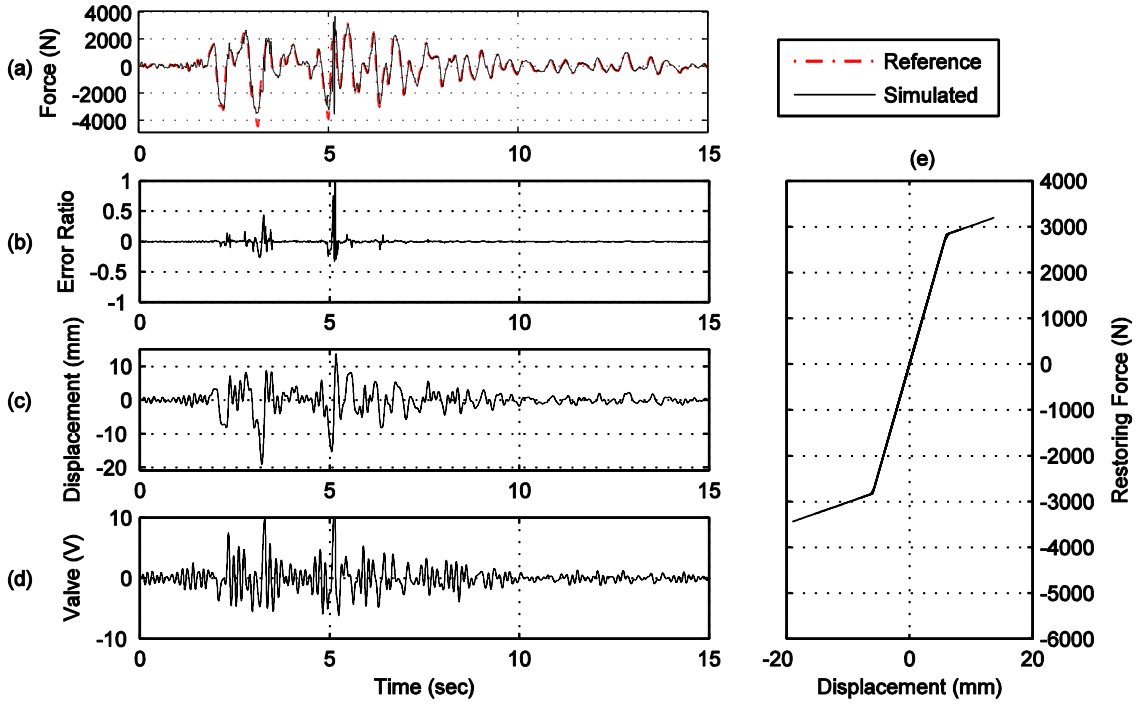

Figure A.55. Yield displacement X_y = 0.006m, post-yield stiffness $k_1 = 0.1*k_0$.

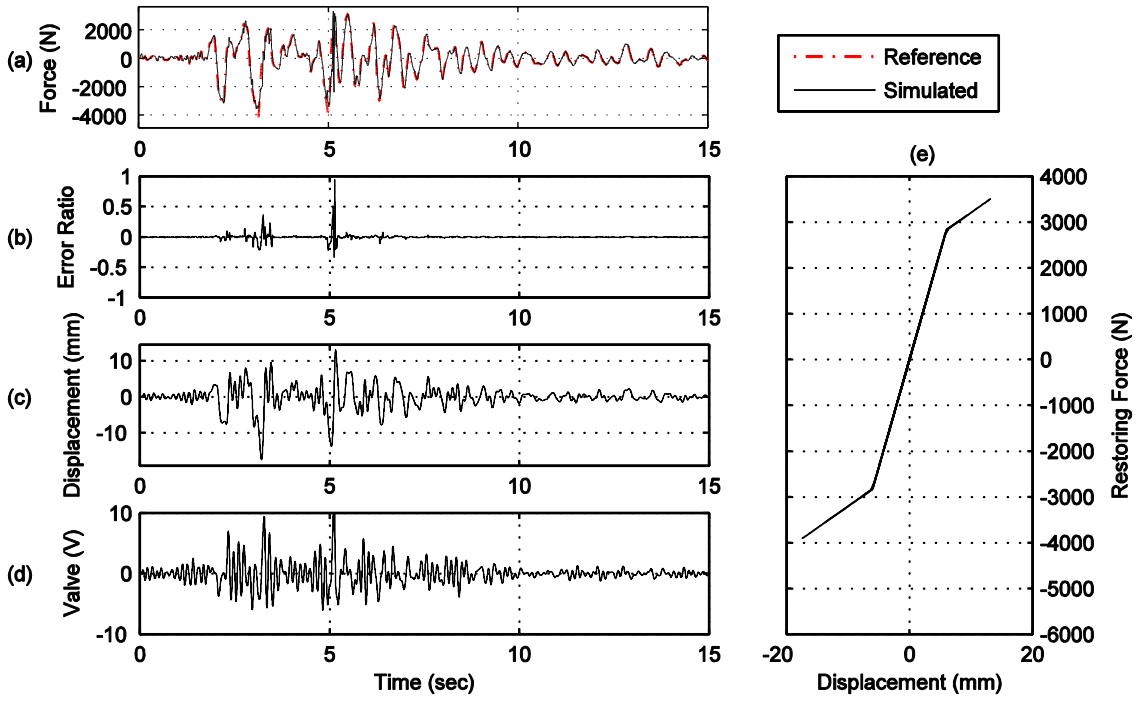

Figure A.56. Yield displacement X_y = 0.006m, post-yield stiffness $k_1 = 0.2*k_0$.

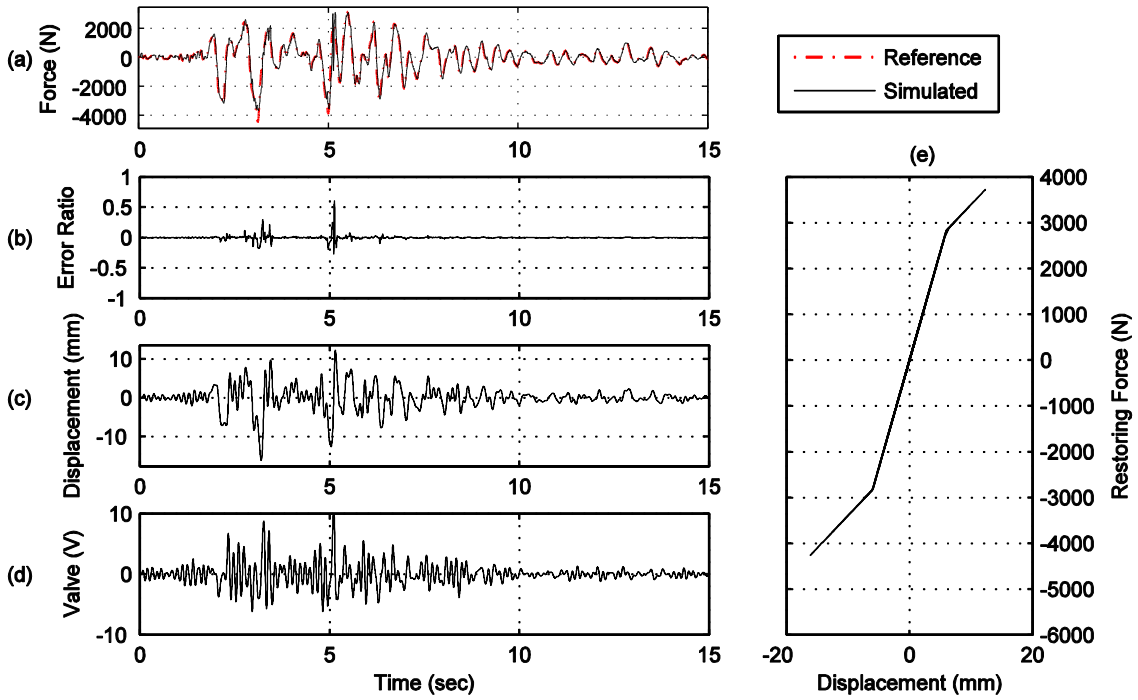

Figure A.57. Yield displacement X_y = 0.006m, post-yield stiffness $k_1 = 0.3*k_0$.

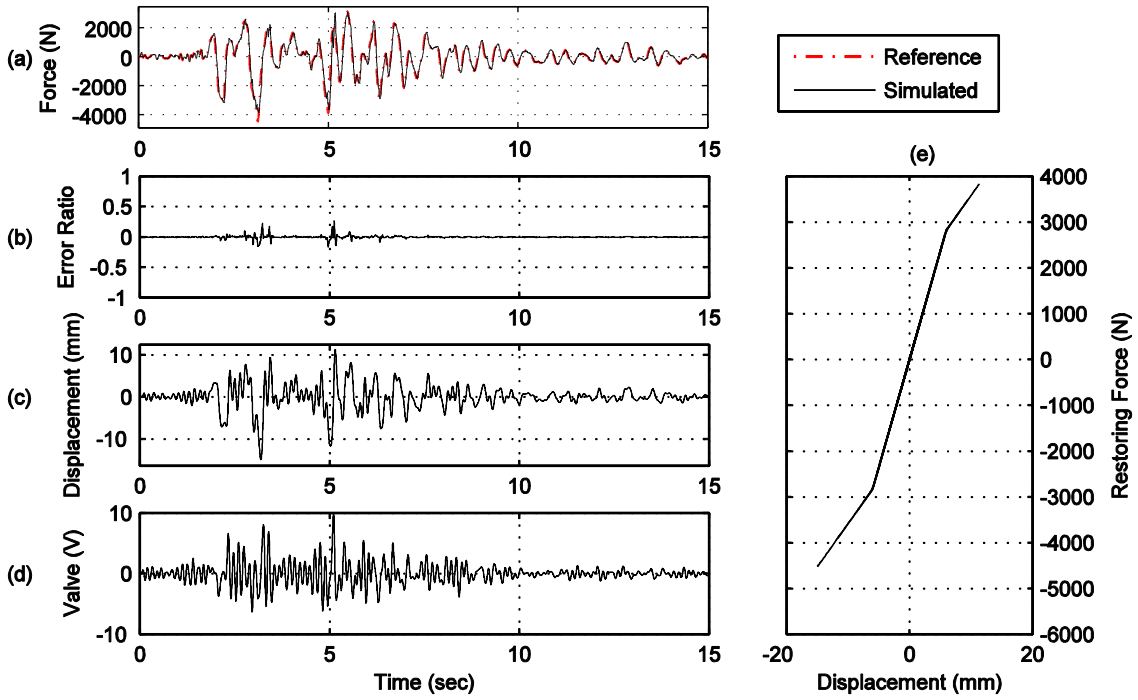

Figure A.58. Yield displacement X_y = 0.006m, post-yield stiffness $k_1 = 0.4*k_0$.

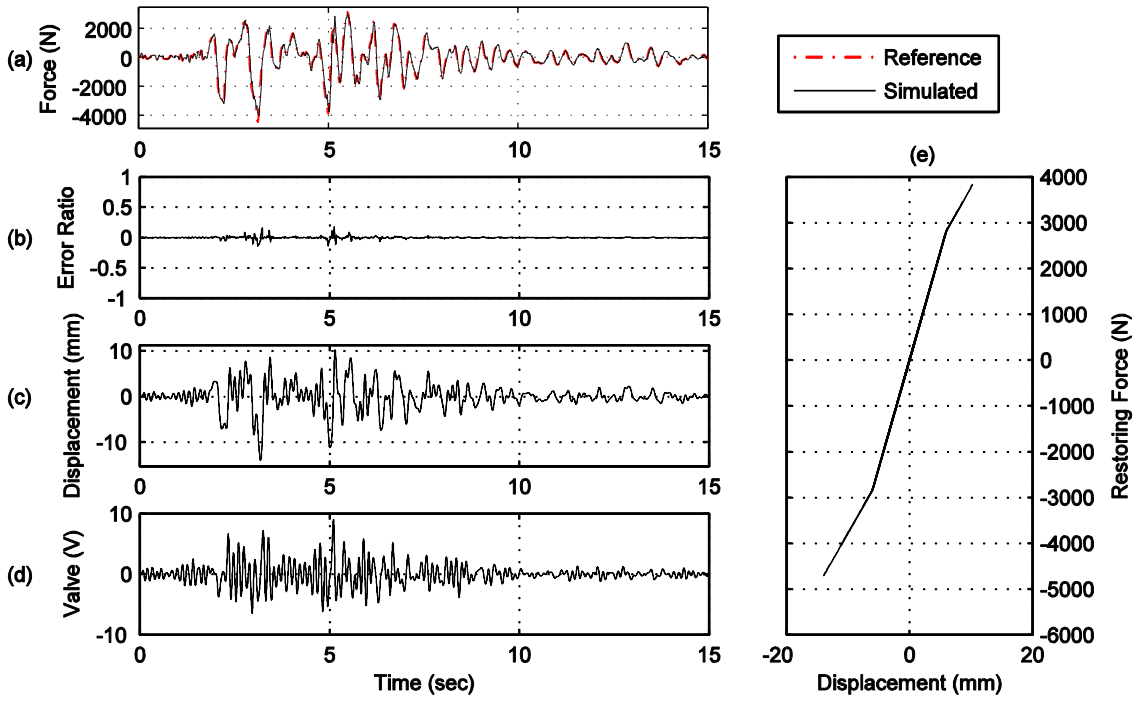

Figure A.59. Yield displacement X_y = 0.006m, post-yield stiffness $k_1 = 0.5*k_0$.

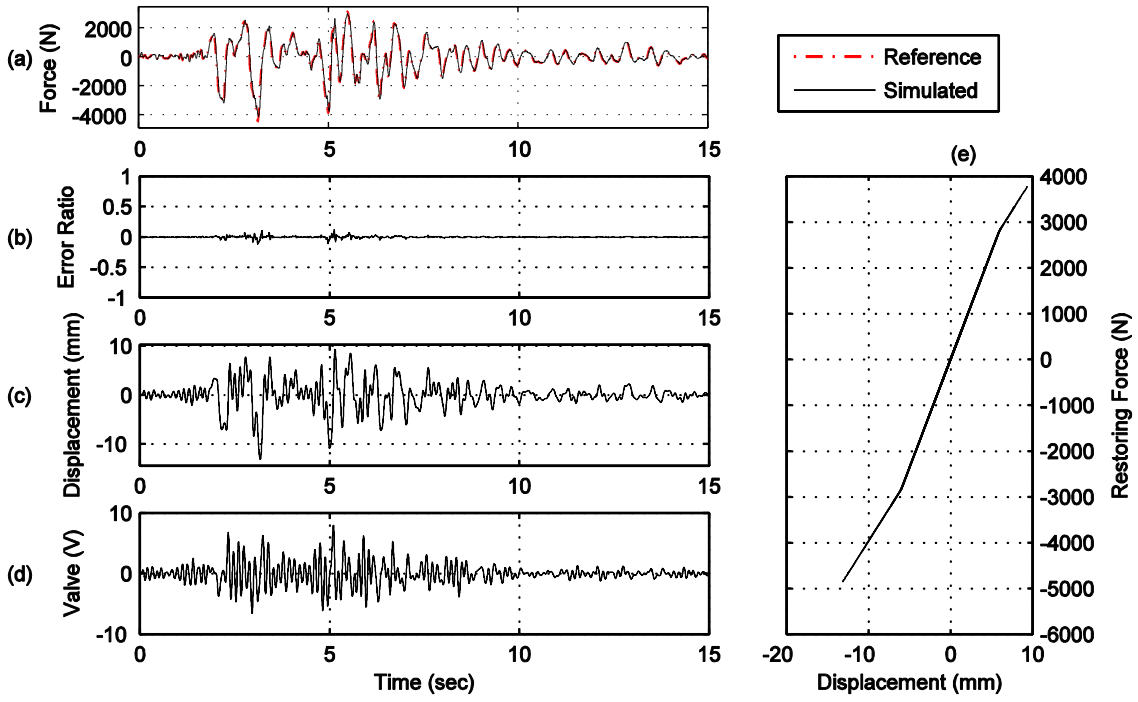

Figure A.60. Yield displacement X_y = 0.006m, post-yield stiffness $k_1 = 0.6*k_0$.

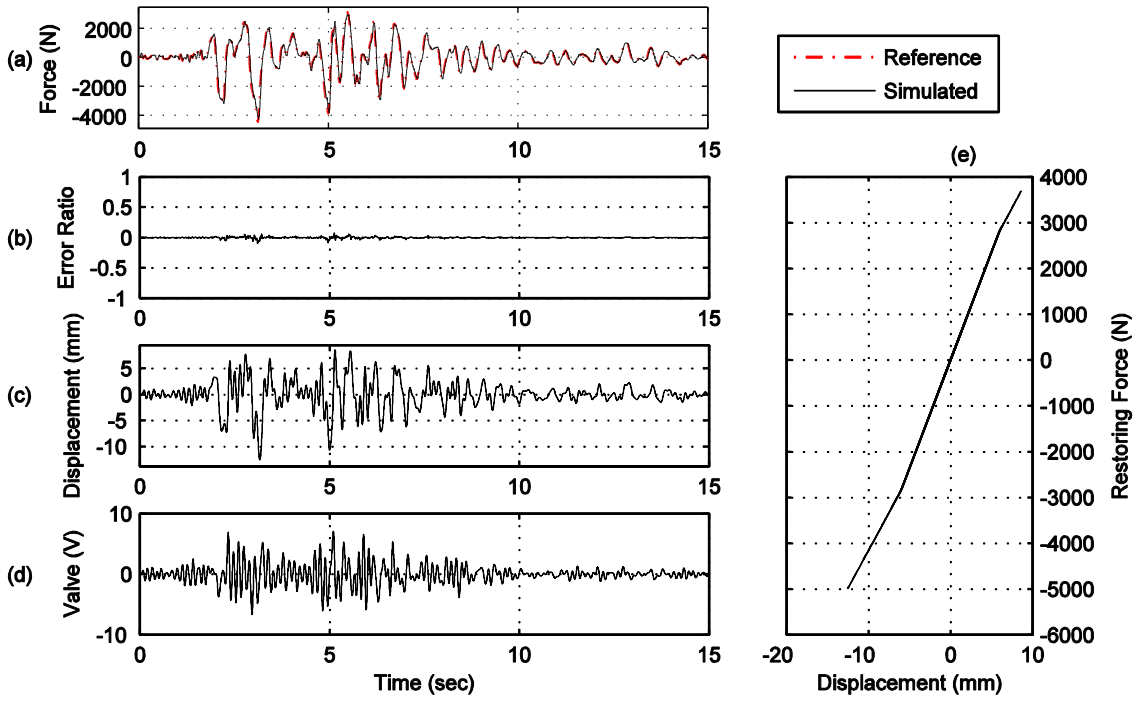

Figure A.61. Yield displacement X_y = 0.006m, post-yield stiffness $k_1 = 0.7*k_0$.

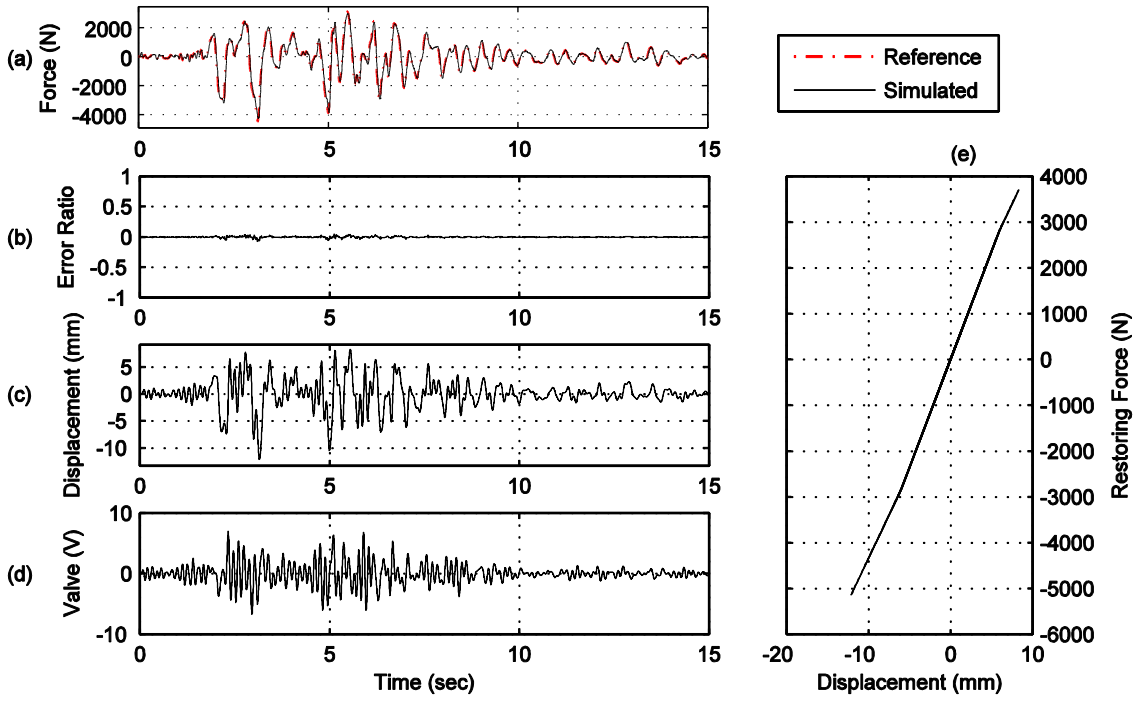

Figure A.62. Yield displacement X_y = 0.006m, post-yield stiffness $k_1 = 0.8*k_0$.

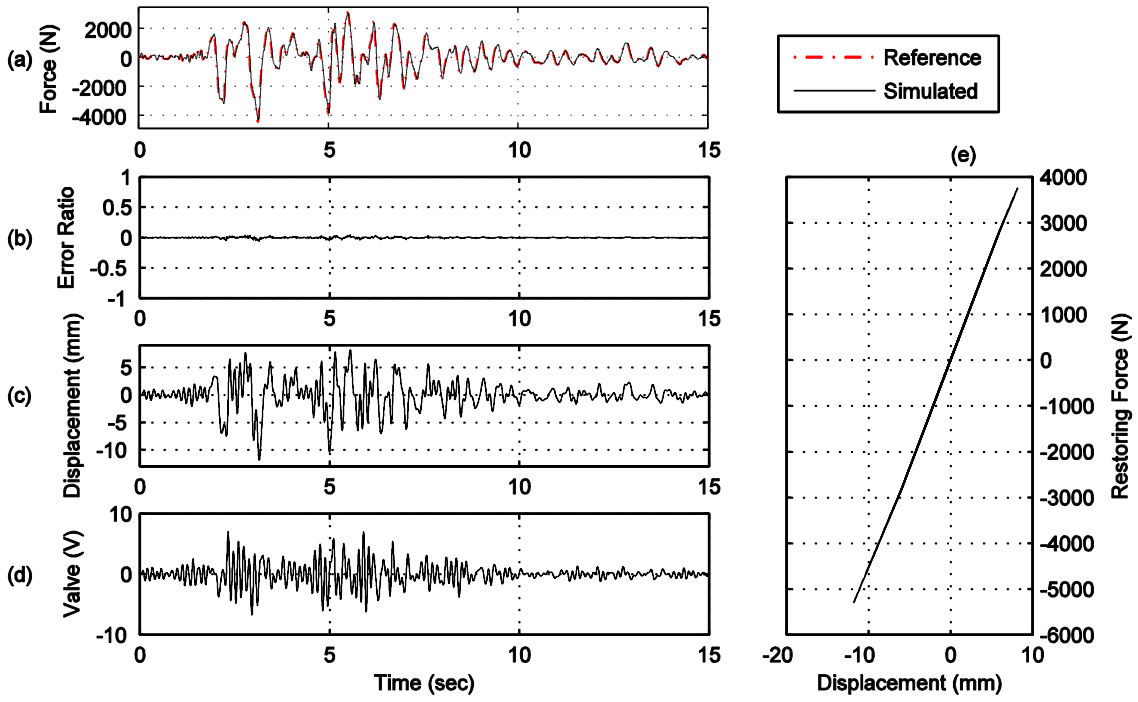

Figure A.63. Yield displacement X_y = 0.006m, post-yield stiffness $k_1 = 0.9*k_0$.

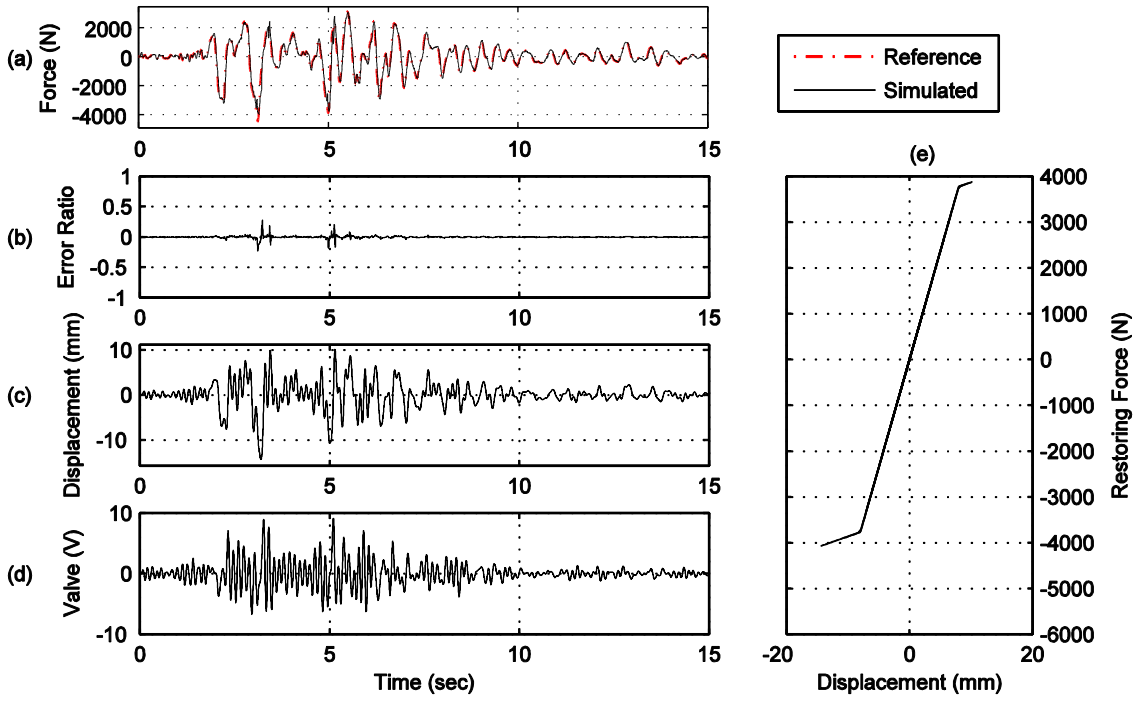

Figure A.64. Yield displacement X_y = 0.008m, post-yield stiffness $k_1 = 0.1*k_0$.

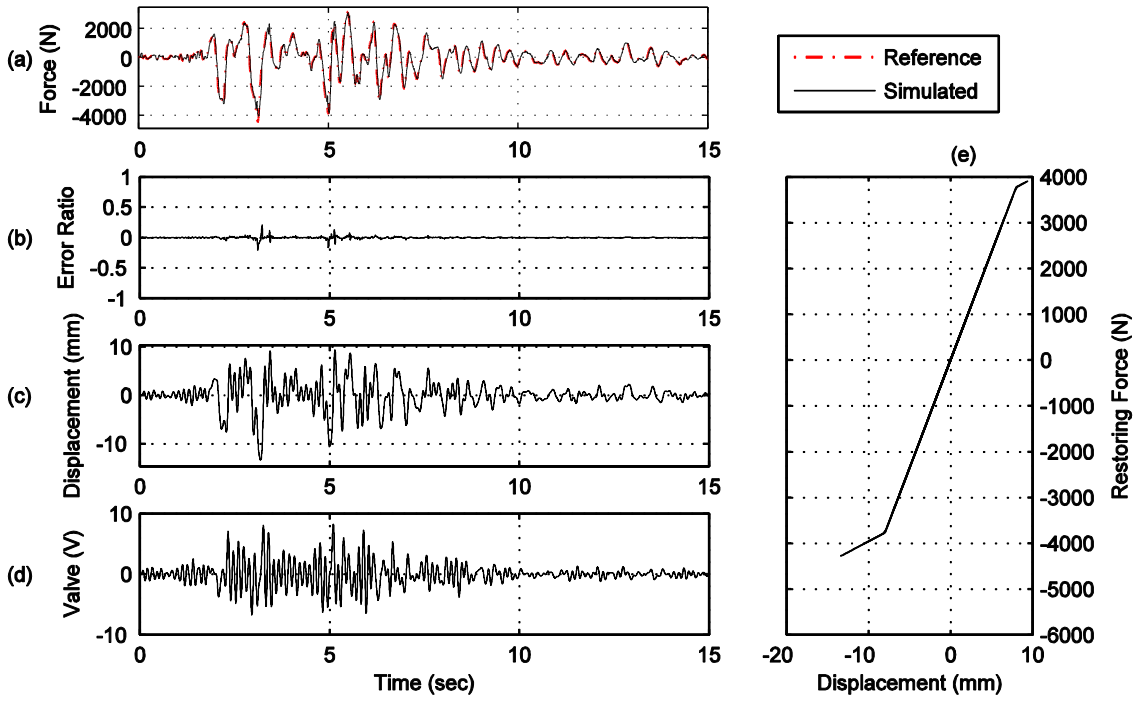

Figure A.65. Yield displacement X_y = 0.008m, post-yield stiffness $k_1 = 0.2*k_0$.

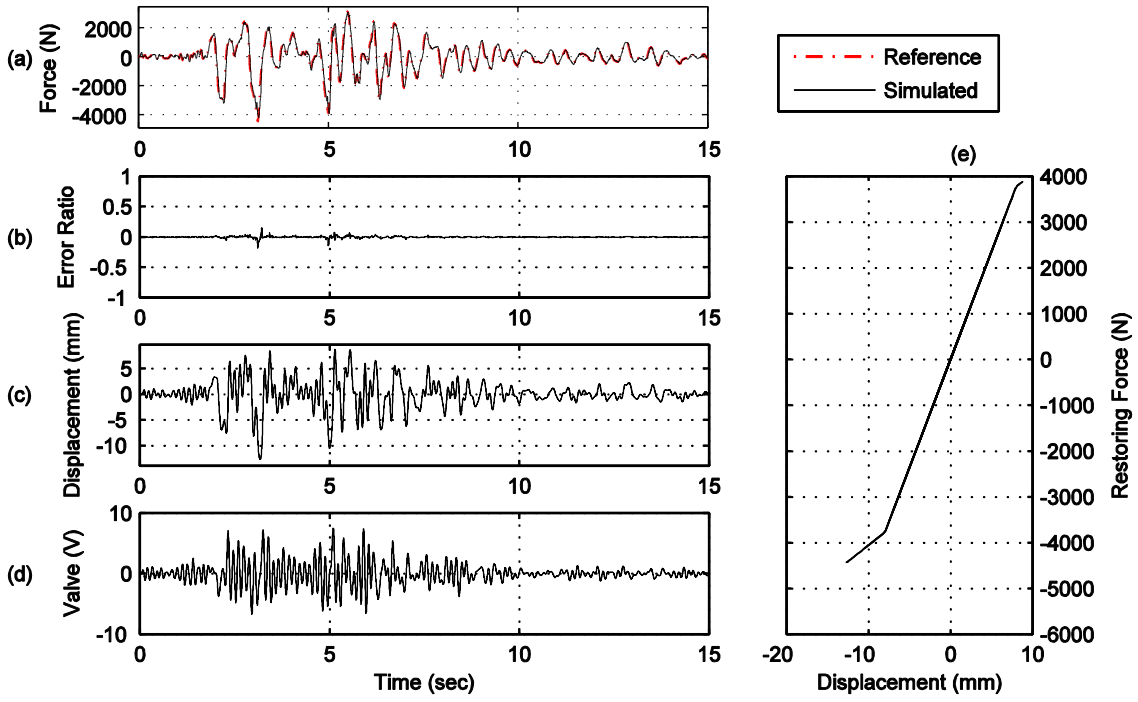

Figure A.66. Yield displacement X_y = 0.008m, post-yield stiffness $k_1 = 0.3*k_0$.

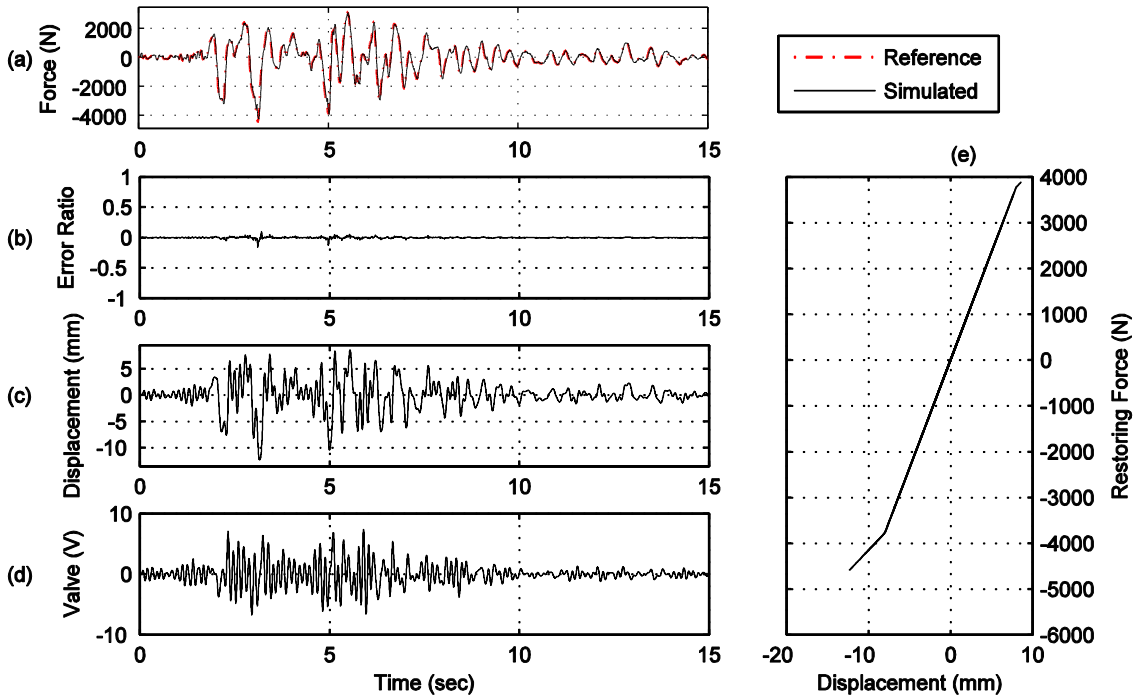

Figure A.67. Yield displacement X_y = 0.008m, post-yield stiffness $k_1 = 0.4*k_0$.

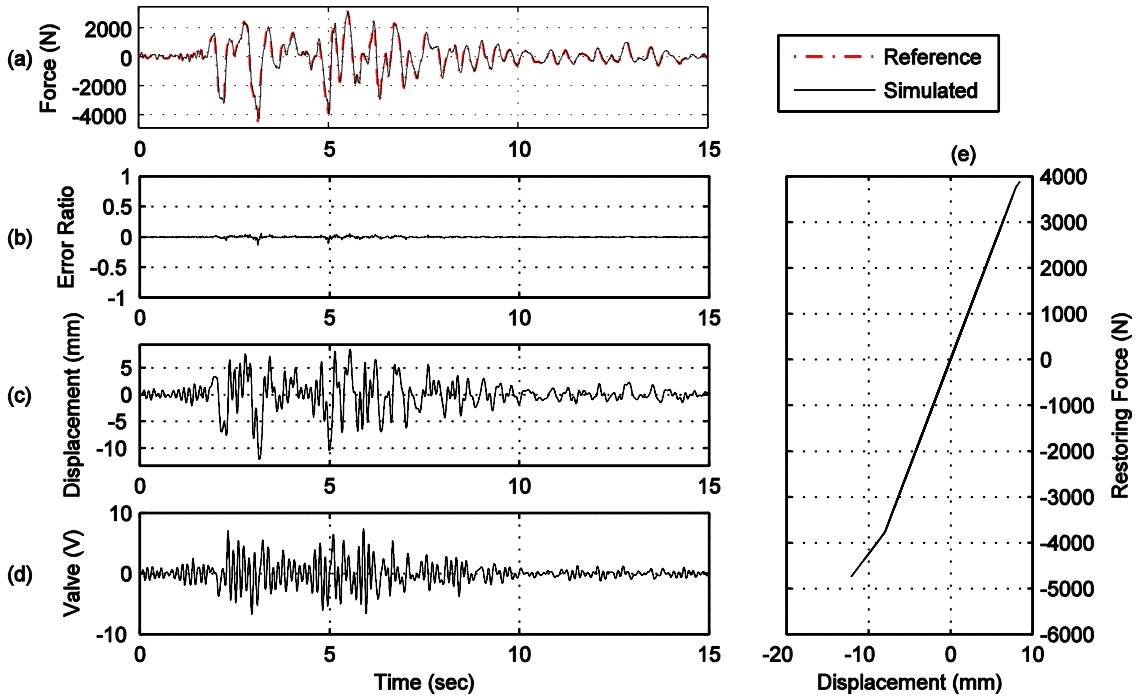

Figure A.68. Yield displacement X_y = 0.008m, post-yield stiffness $k_1 = 0.5*k_0$.

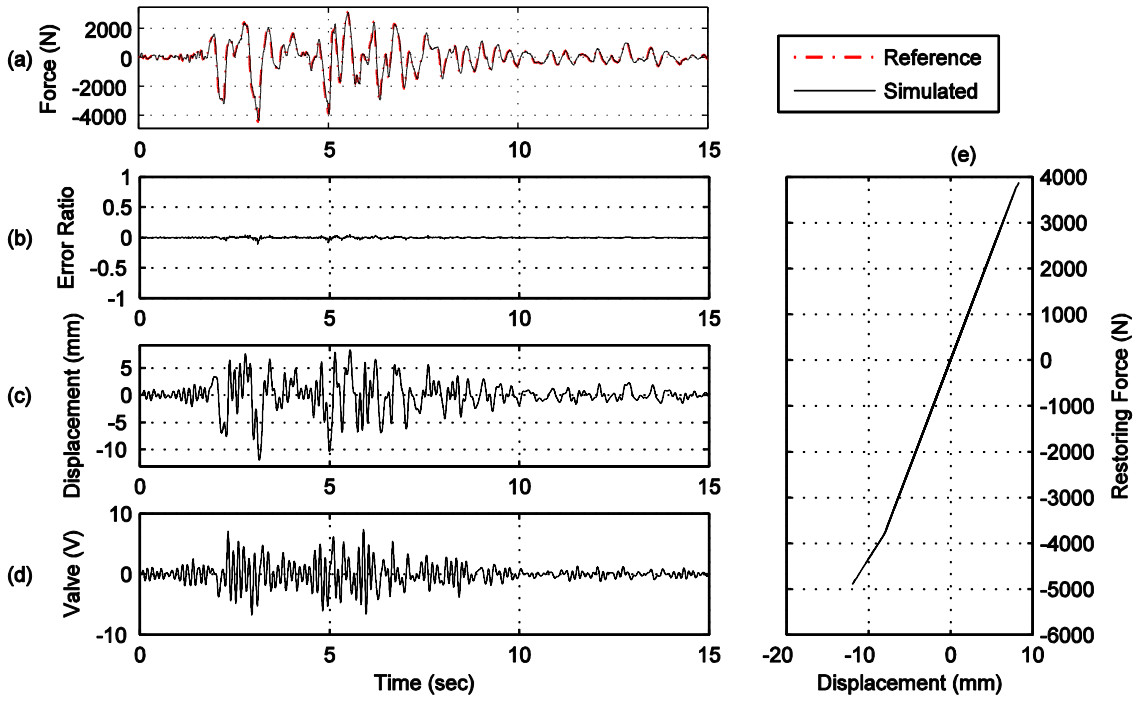

Figure A.69. Yield displacement X_y = 0.008m, post-yield stiffness $k_1 = 0.6*k_0$.

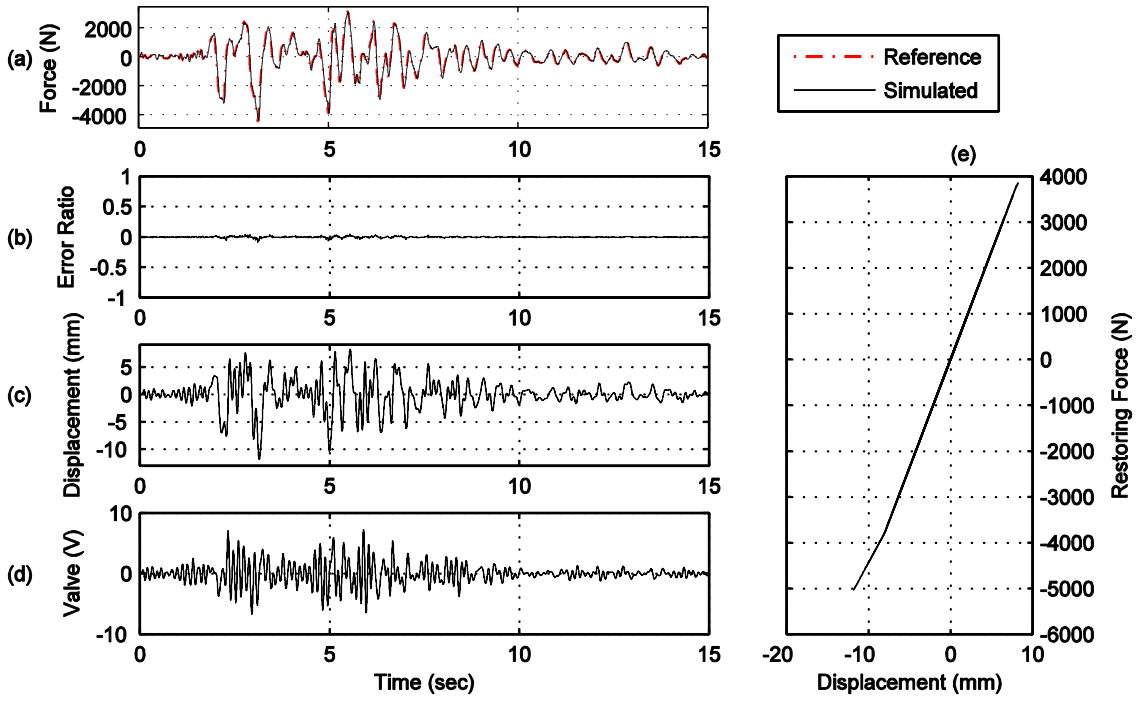

Figure A.70. Yield displacement X_y = 0.008m, post-yield stiffness $k_1 = 0.7*k_0$.

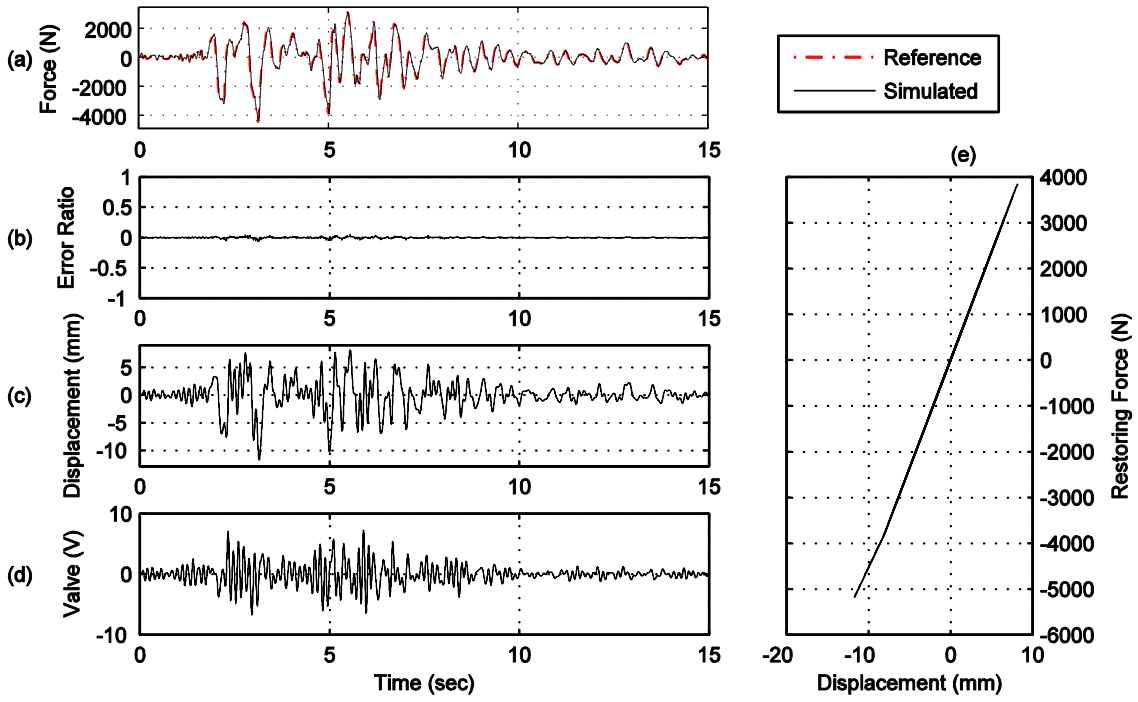

Figure A.71. Yield displacement X_y = 0.008m, post-yield stiffness $k_1 = 0.8*k_0$.

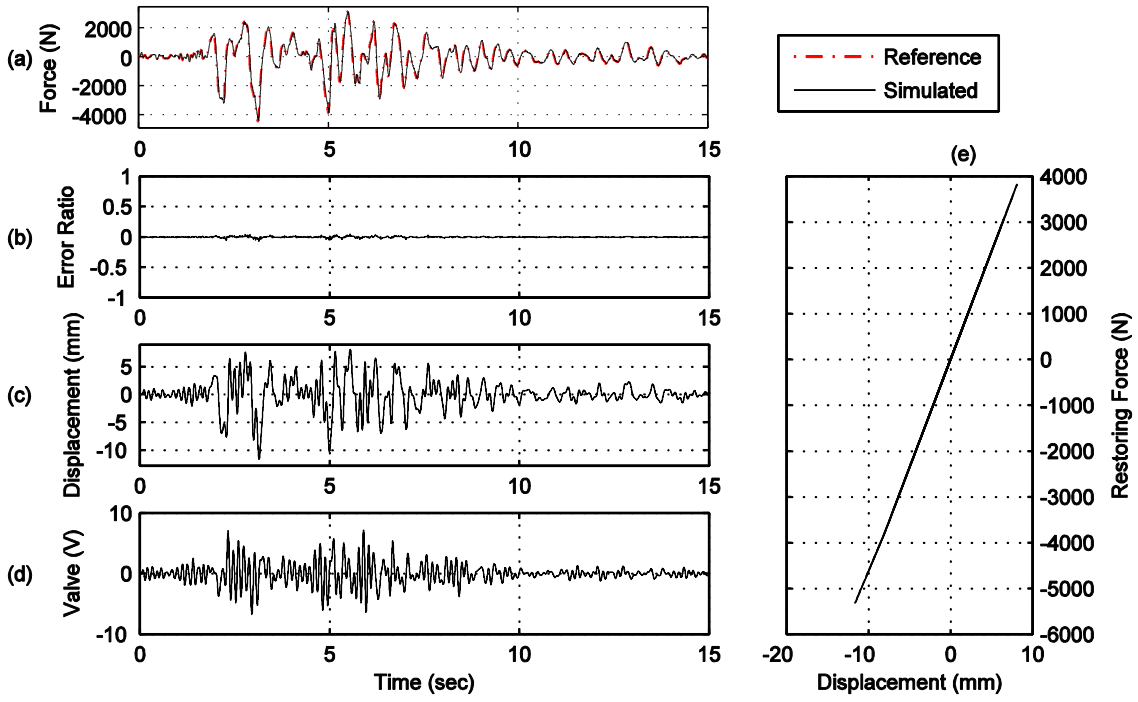

Figure A.72. Yield displacement X_y = 0.008m, post-yield stiffness $k_1 = 0.9*k_0$.

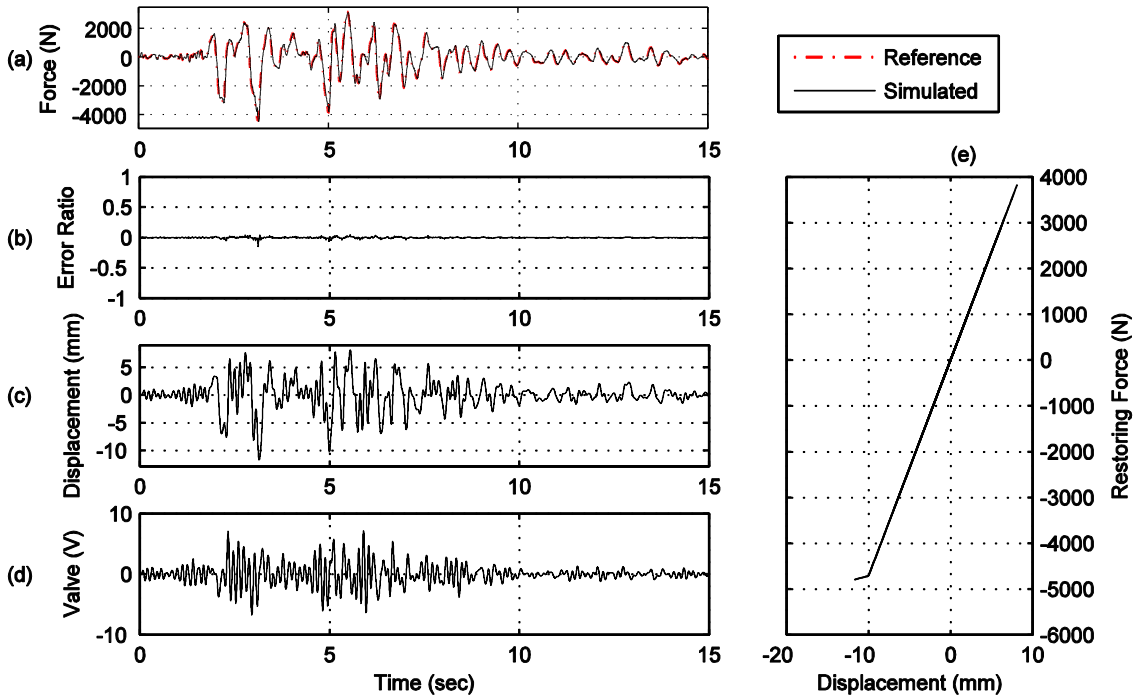

Figure A.73. Yield displacement X_y = 0.010m, post-yield stiffness $k_1 = 0.1*k_0$.

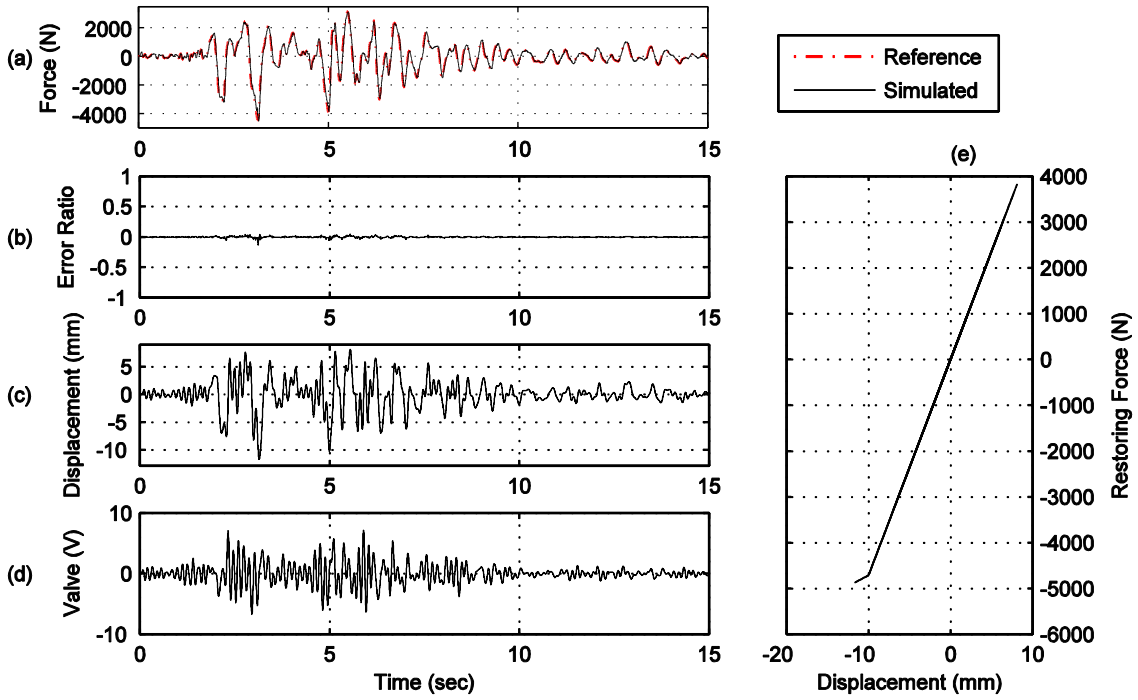

Figure A.74. Yield displacement X_y = 0.010m, post-yield stiffness $k_1 = 0.2*k_0$.

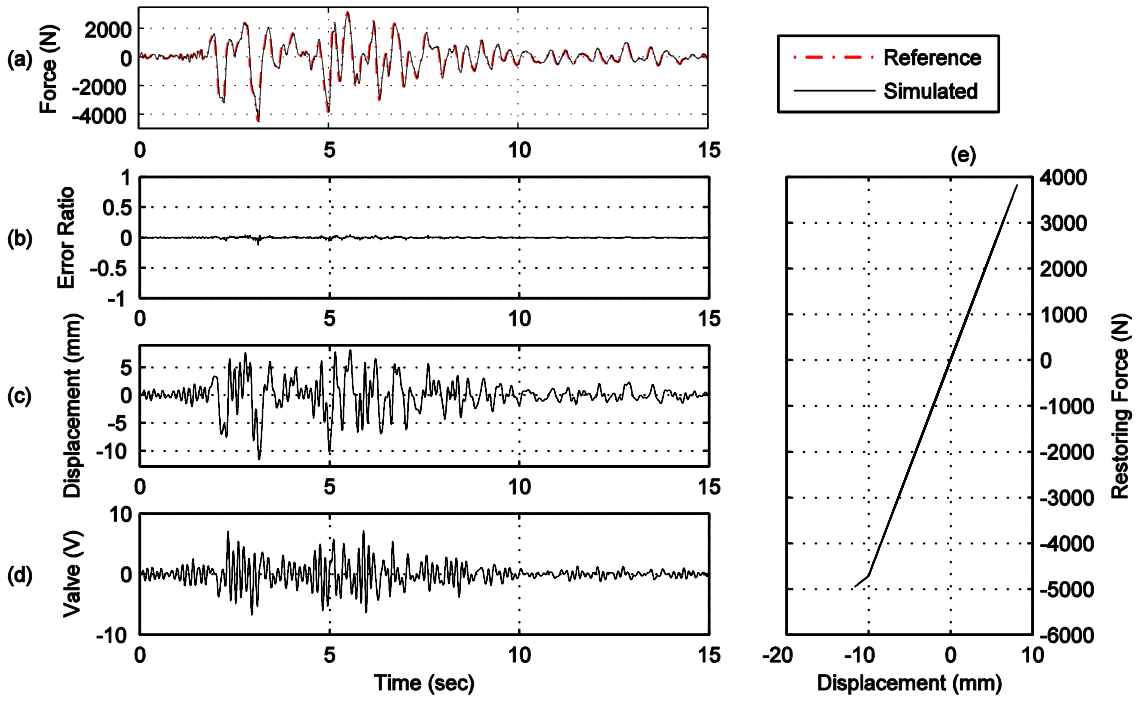

Figure A.75. Yield displacement X_y = 0.010m, post-yield stiffness $k_1 = 0.3*k_0$.

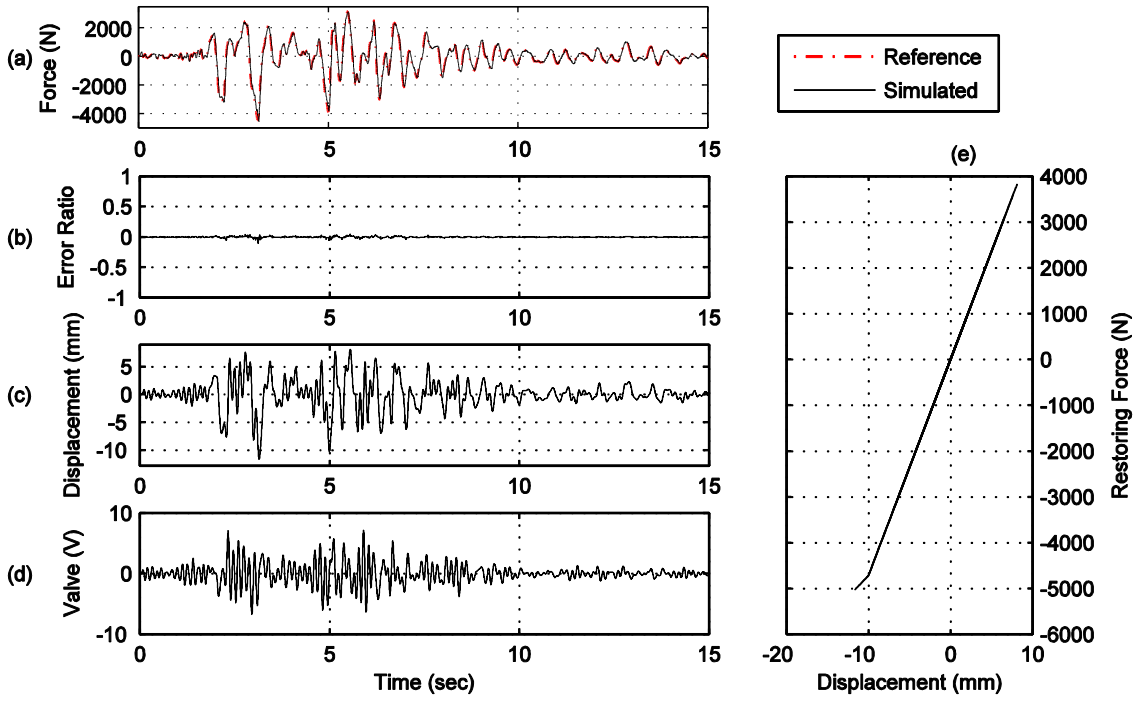

Figure A.76. Yield displacement X_y = 0.010m, post-yield stiffness $k_1 = 0.4*k_0$.

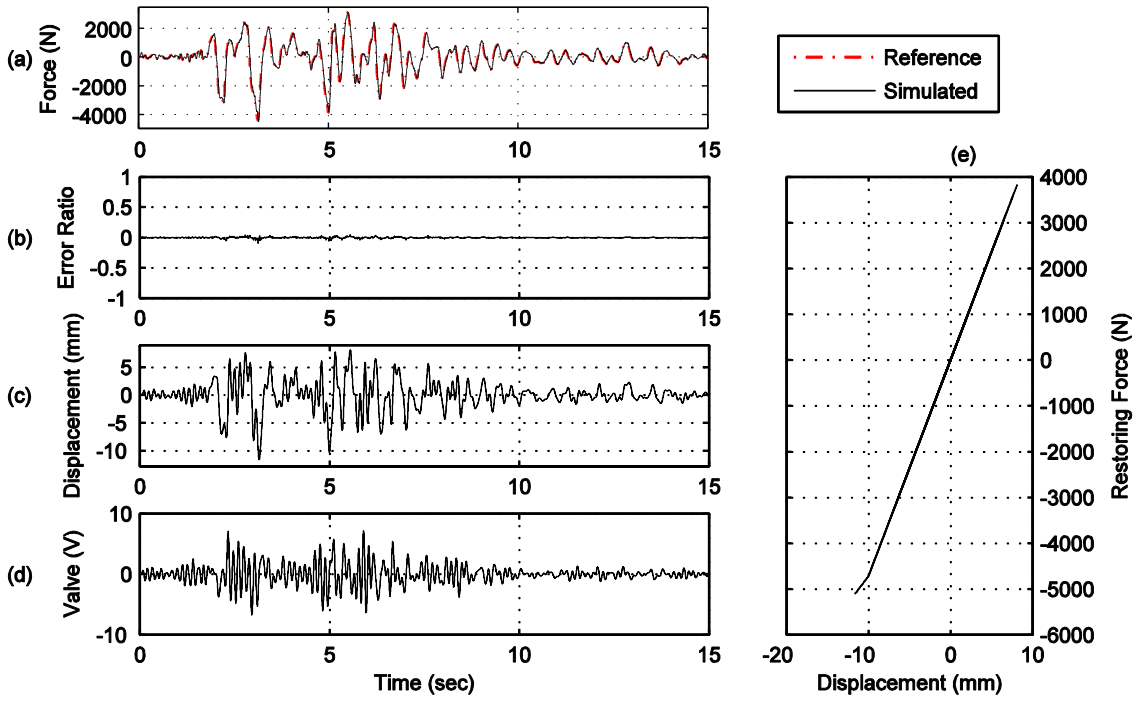

Figure A.77. Yield displacement X_y = 0.010m, post-yield stiffness $k_1 = 0.5*k_0$.

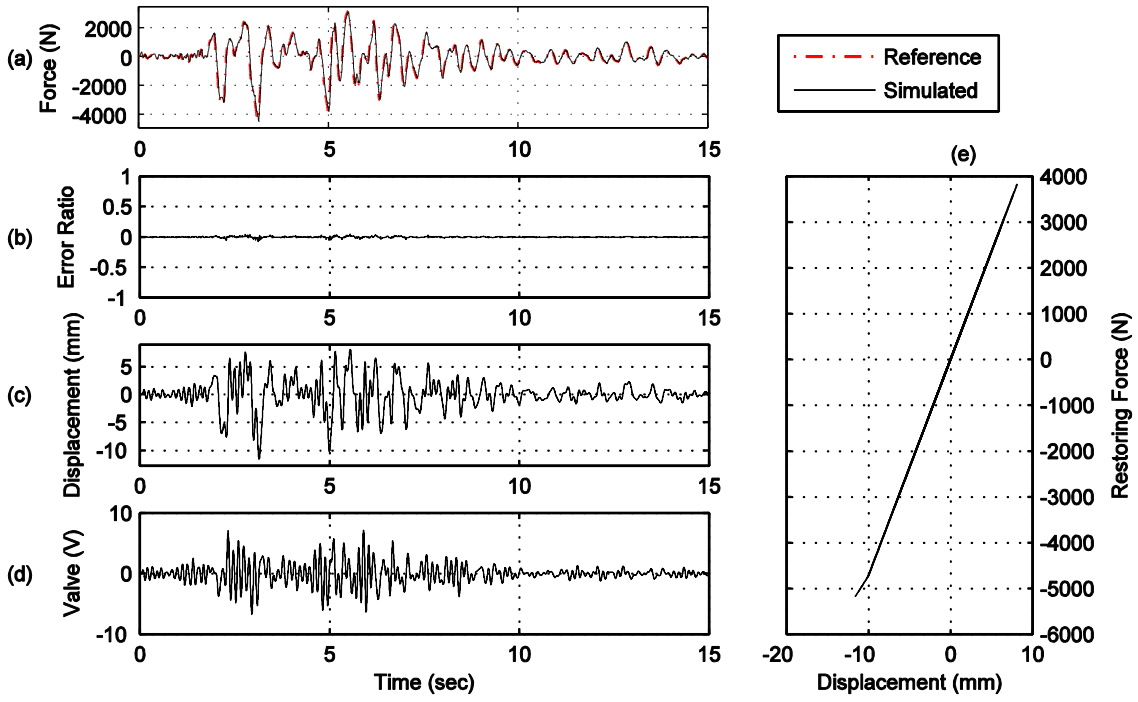

Figure A.78. Yield displacement X_y = 0.010m, post-yield stiffness $k_1 = 0.6*k_0$.

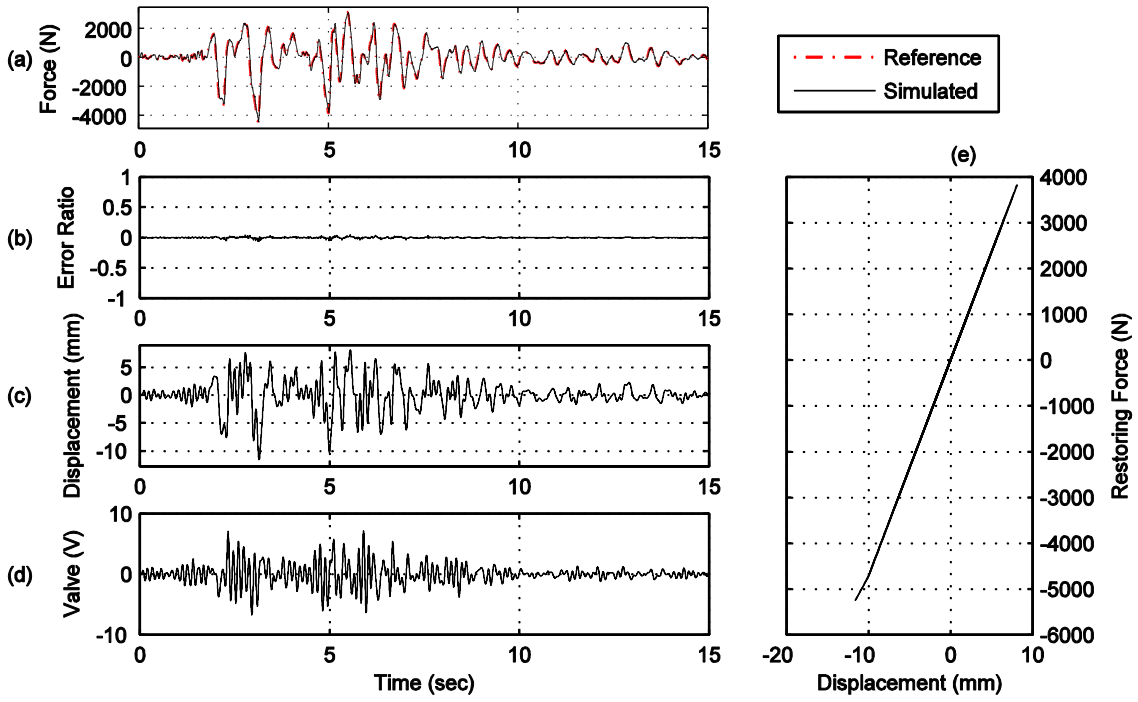

Figure A.79. Yield displacement X_y = 0.010m, post-yield stiffness $k_1 = 0.7*k_0$.

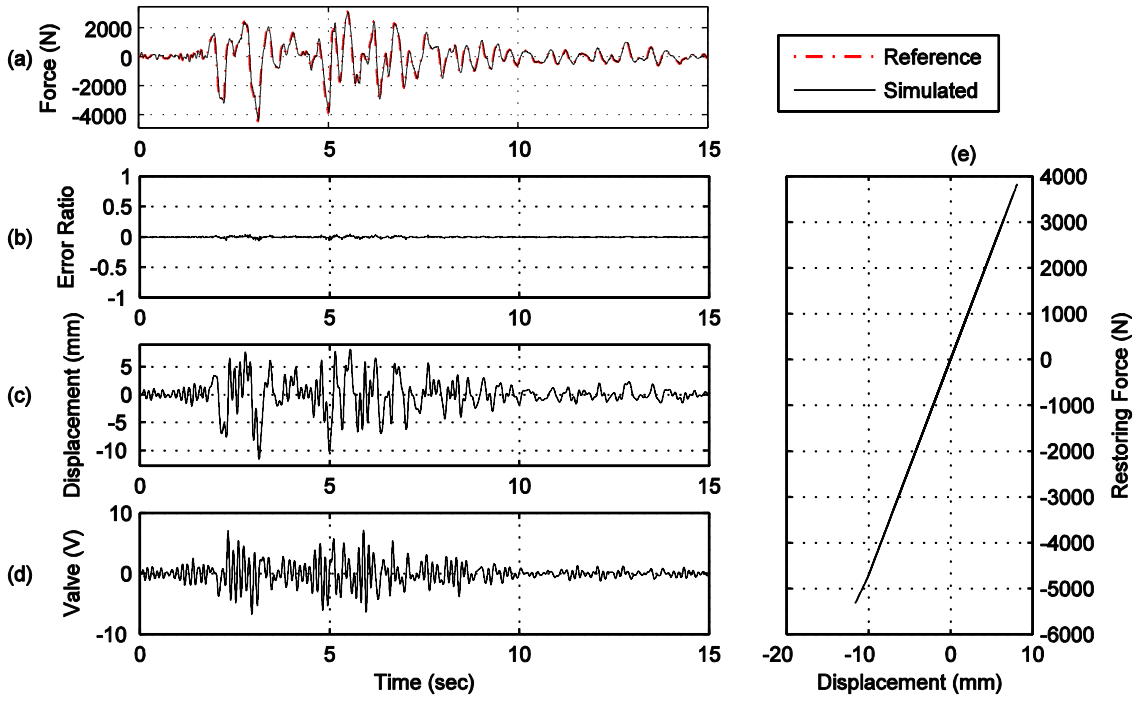

Figure A.80. Yield displacement X_y = 0.010m, post-yield stiffness $k_1 = 0.8*k_0$.

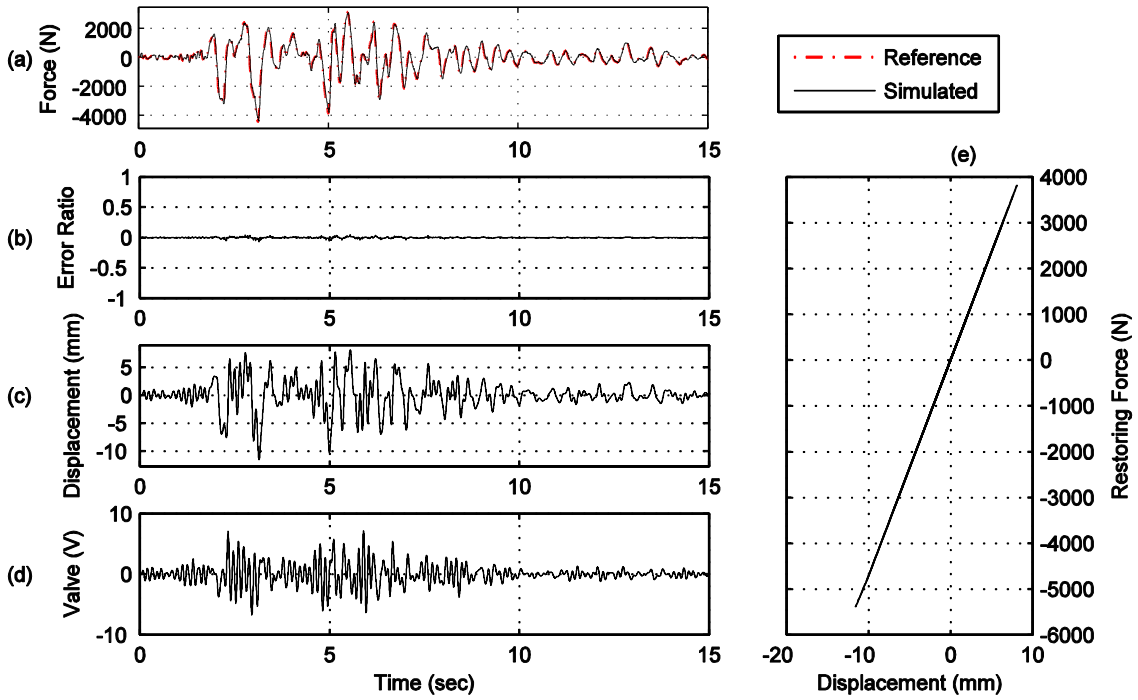

Figure A.81. Yield displacement X_y = 0.010m, post-yield stiffness $k_1 = 0.9*k_0$.

Appendix B

Computational EFT Results for Bilinear Hysteretic Model

Rigid Base

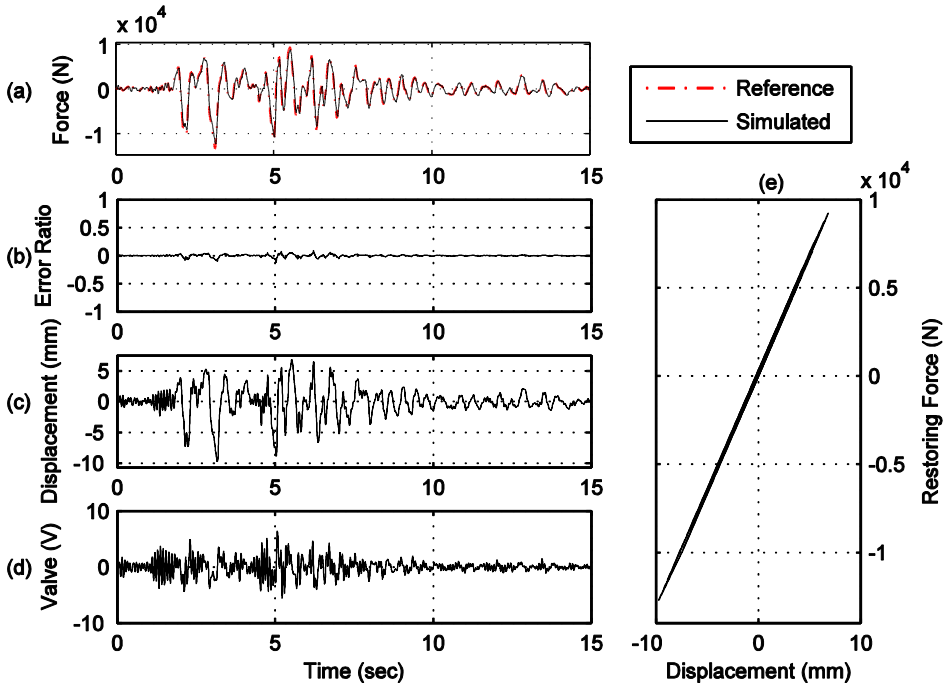

Figure B.1. Yield strength Y_y = 1,000 N, post-yield stiffness $k_1 = 0.9*k_0$.

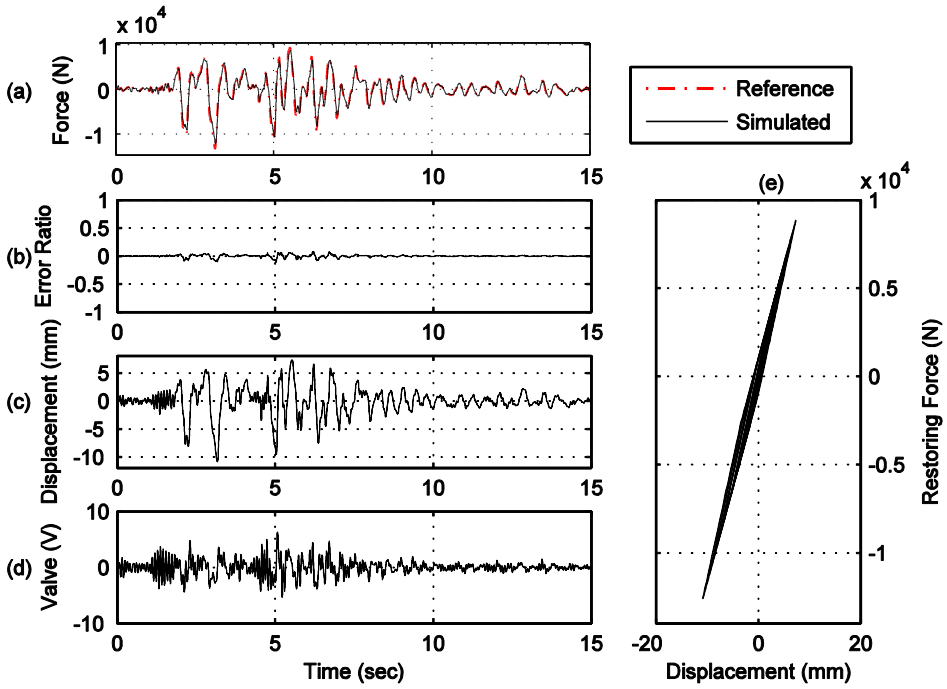

Figure B.2. Yield strength Y_y = 1,000 N, post-yield stiffness $k_1 = 0.8*k_0$.

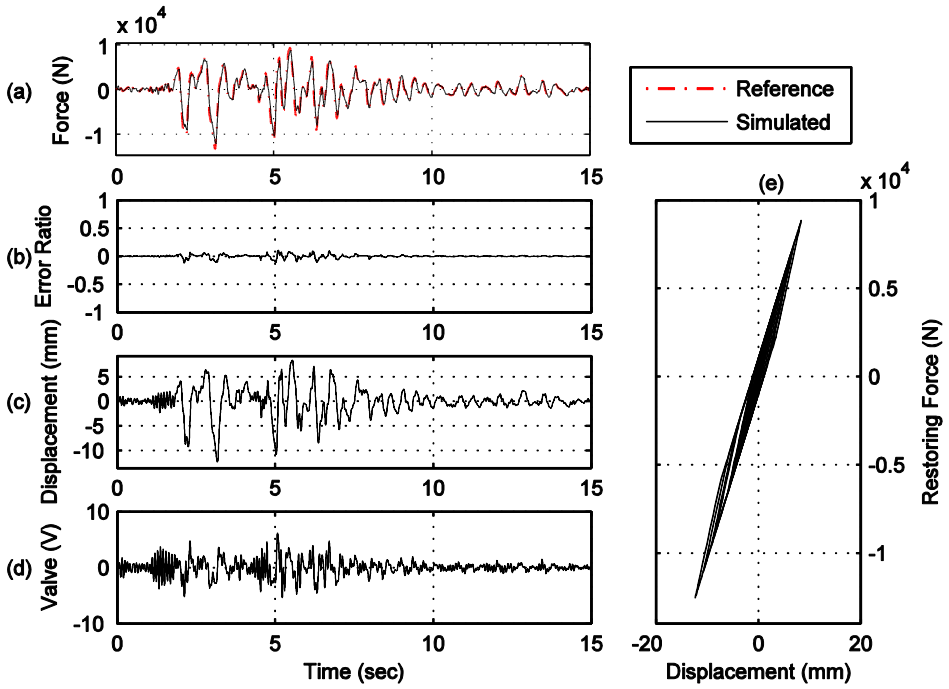

Figure B.3. Yield strength Y_y = 1,000 N, post-yield stiffness $k_1 = 0.7*k_0$.

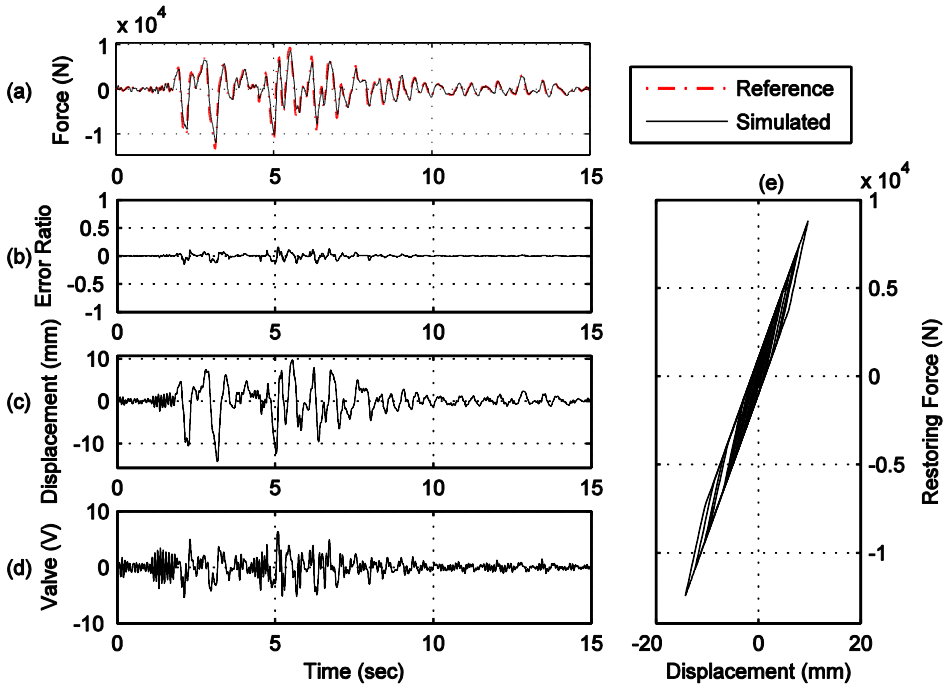

Figure B.4. Yield strength Y_y = 1,000 N, post-yield stiffness $k_1 = 0.6*k_0$.

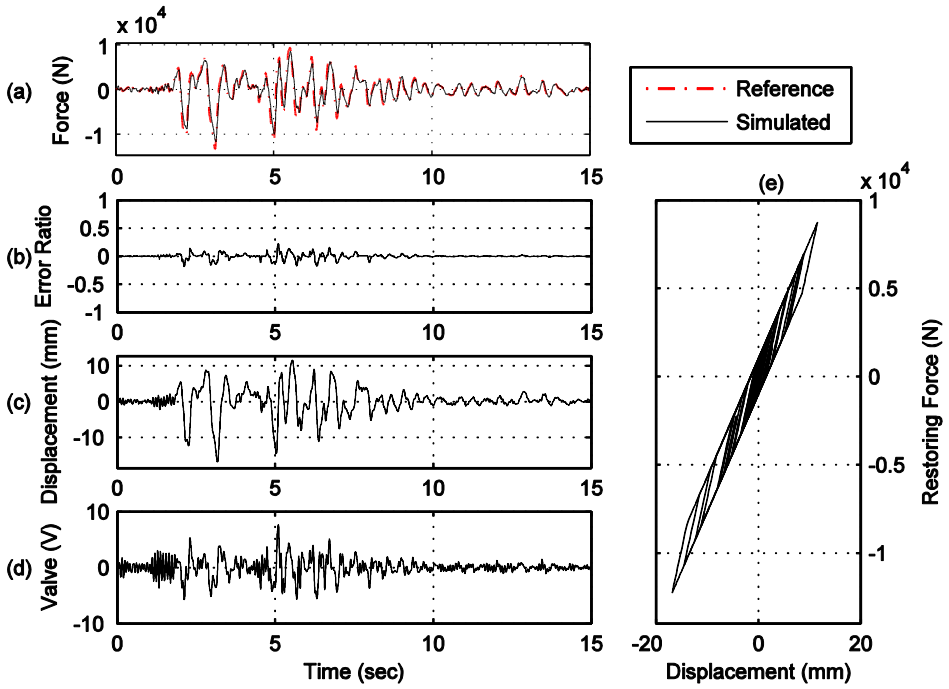

Figure B.5. Yield strength Y_y = 1,000 N, post-yield stiffness $k_1 = 0.5*k_0$.

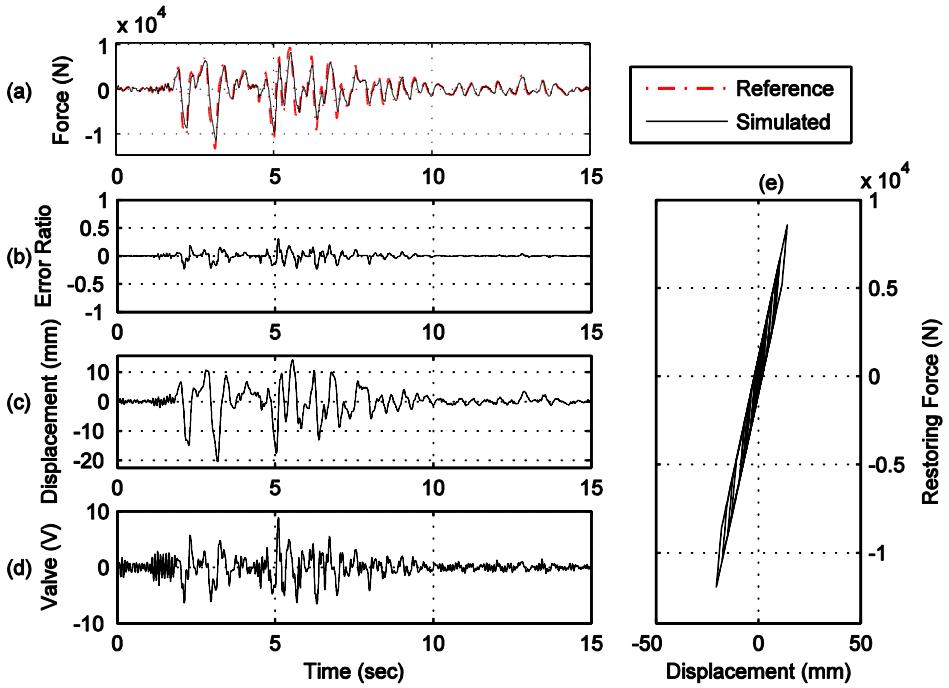

Figure B.6. Yield strength Y_y = 1,000 N, post-yield stiffness $k_1 = 0.4*k_0$.

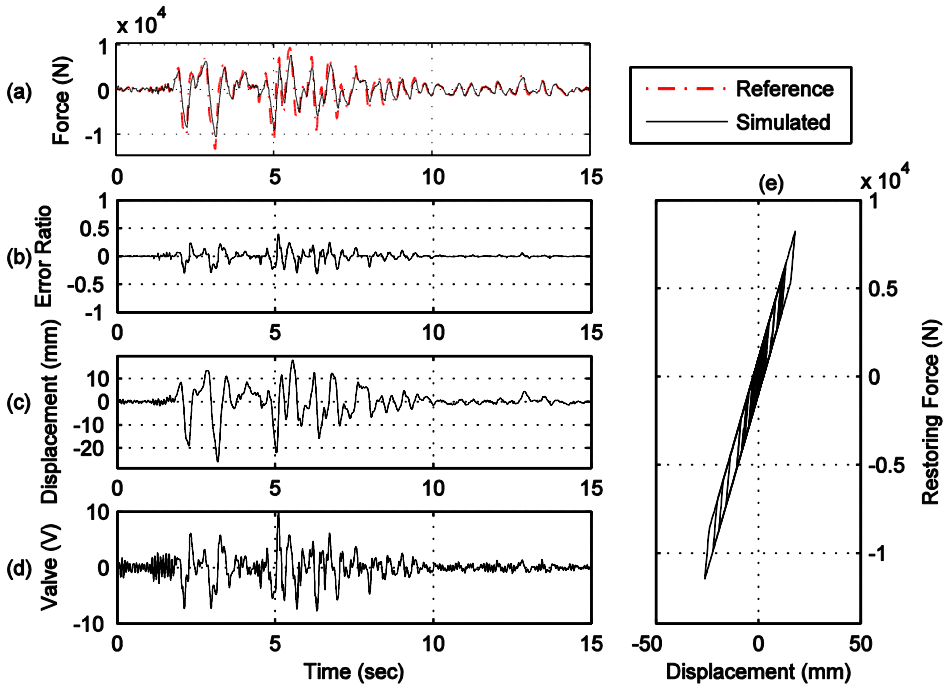

Figure B.7. Yield strength Y_y = 1,000 N, post-yield stiffness $k_1 = 0.3*k_0$.

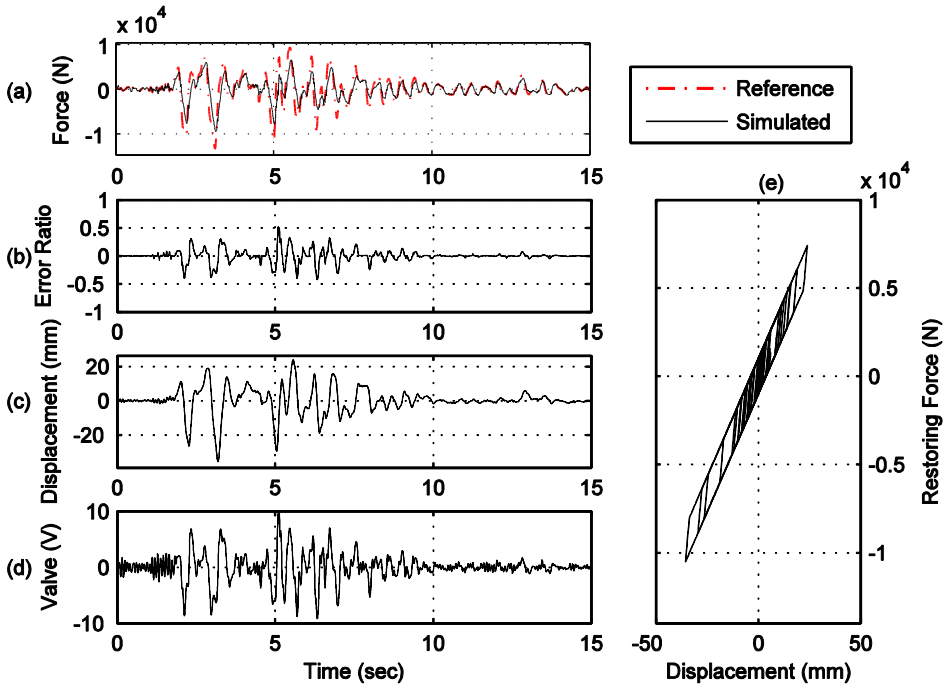

Figure B.8. Yield strength Y_y = 1,000 N, post-yield stiffness $k_1 = 0.2*k_0$.

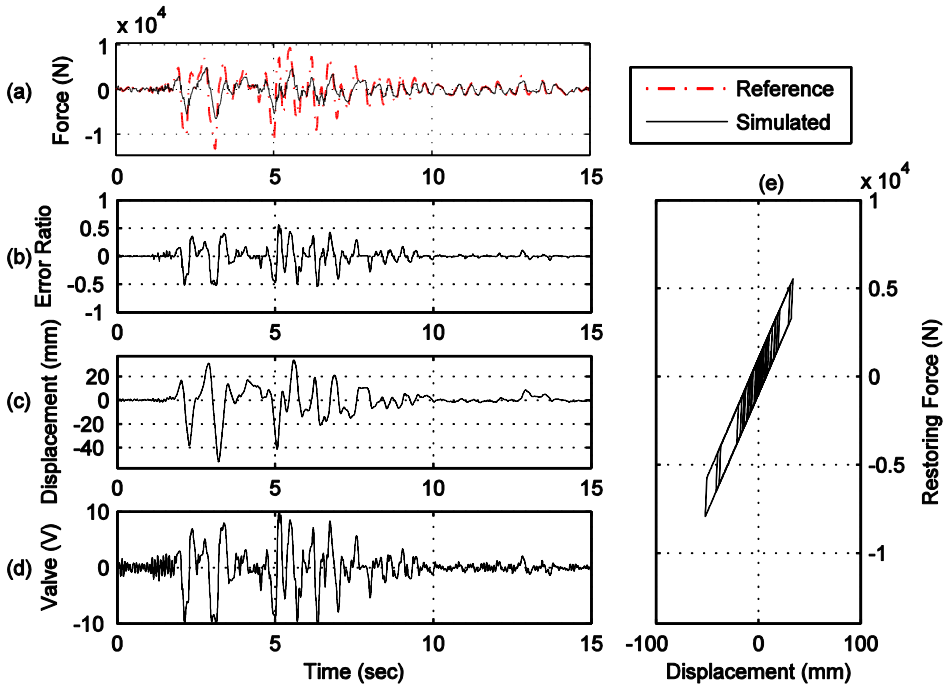

Figure B.9. Yield strength Y_y = 1,000 N, post-yield stiffness $k_1 = 0.1*k_0$.

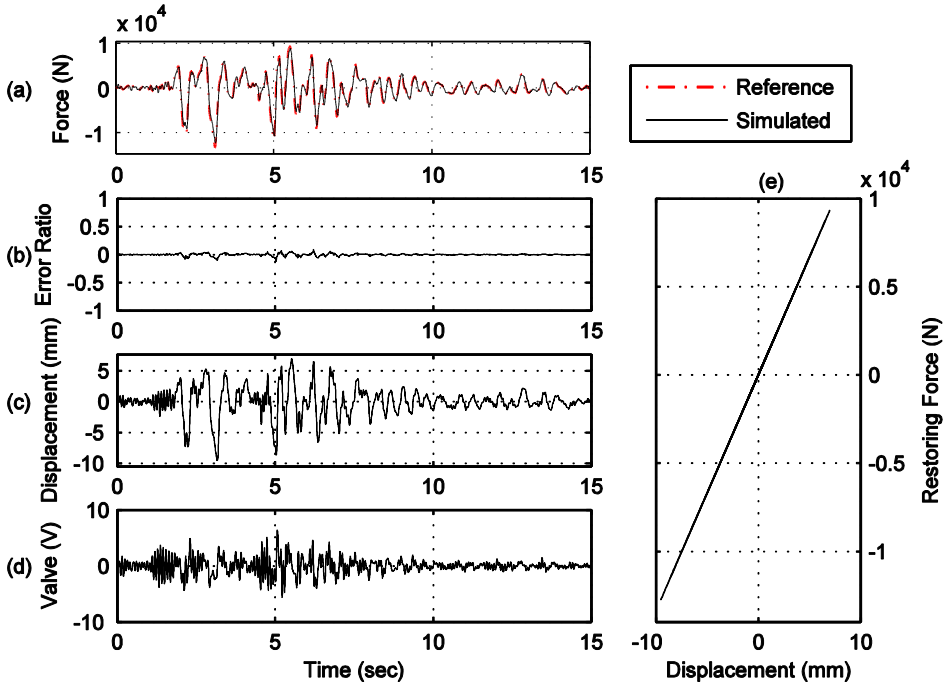

Figure B.10. Yield strength Y_y = 3,000 N, post-yield stiffness $k_1 = 0.9*k_0$.

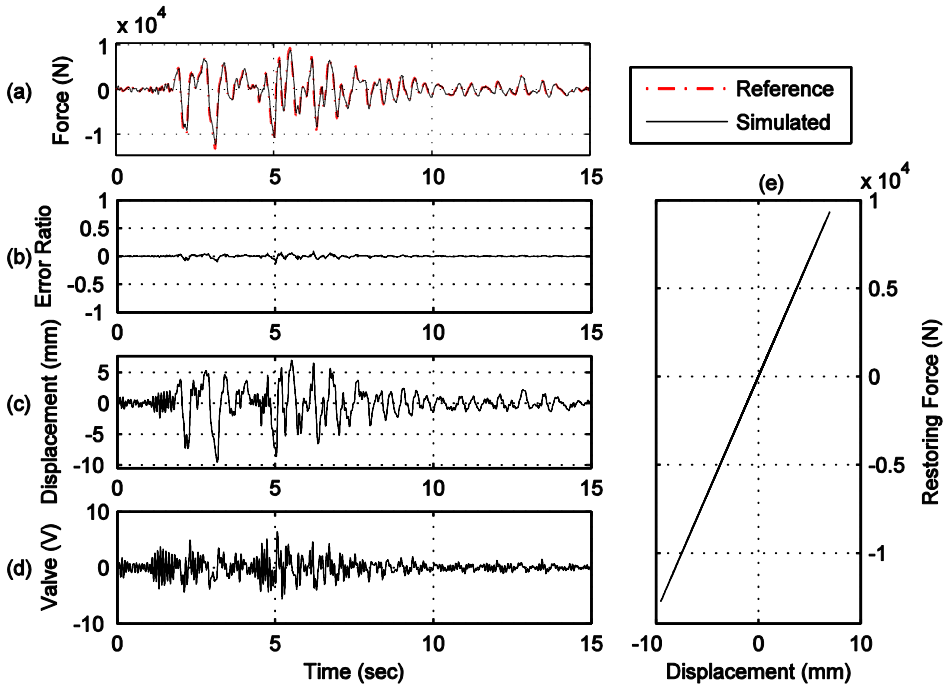

Figure B.11. Yield strength Y_y = 3,000 N, post-yield stiffness $k_1 = 0.8*k_0$.

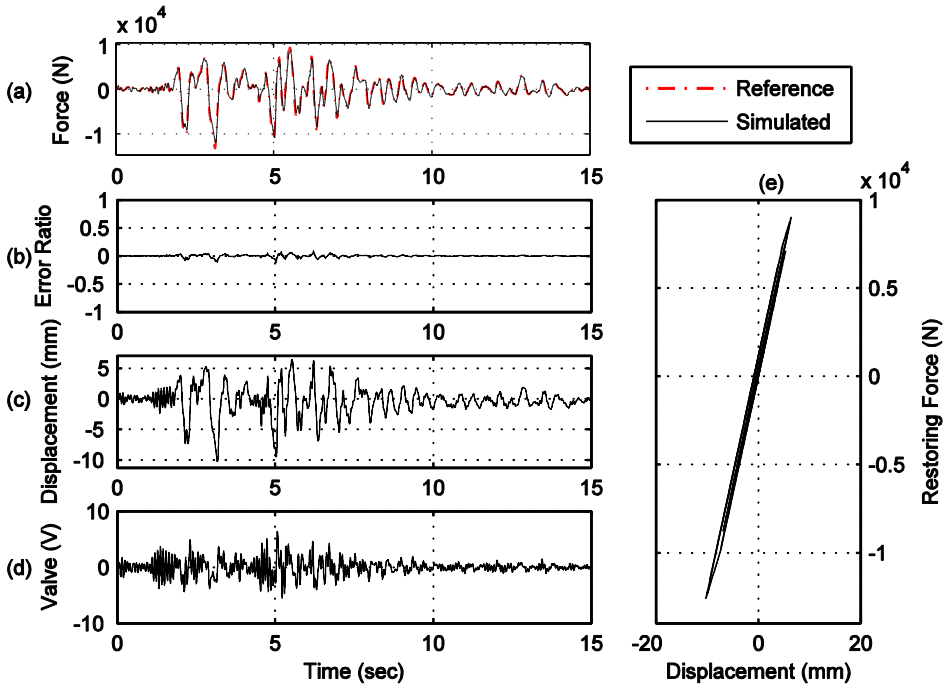

Figure B.12. Yield strength Y_y = 3,000 N, post-yield stiffness $k_1 = 0.7*k_0$.

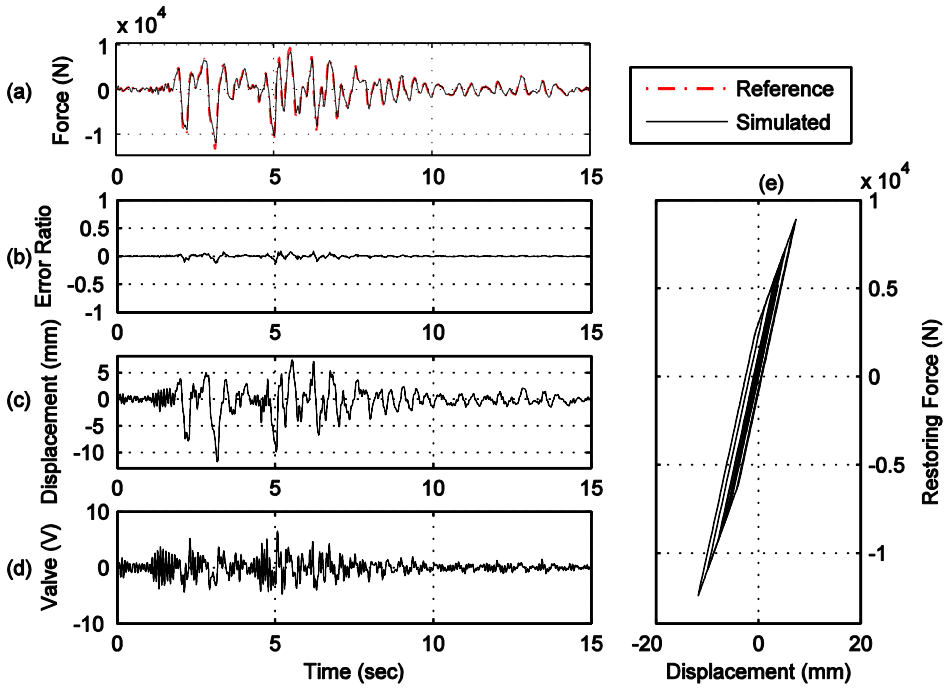

Figure B.13. Yield strength Y_y = 3,000 N, post-yield stiffness $k_1 = 0.6*k_0$.

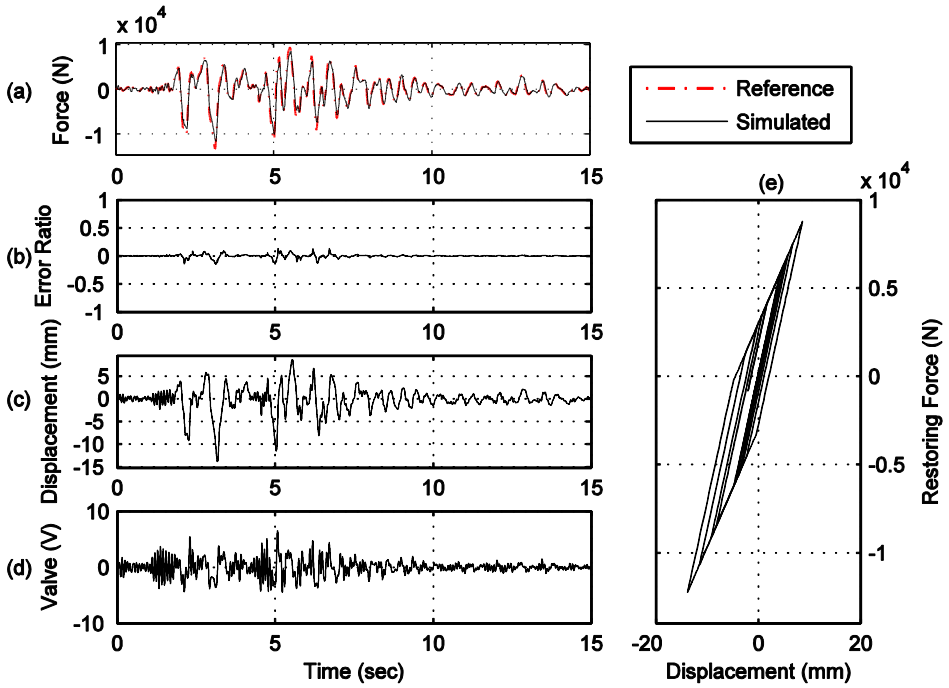

Figure B.14. Yield strength Y_y = 3,000 N, post-yield stiffness $k_1 = 0.5*k_0$.

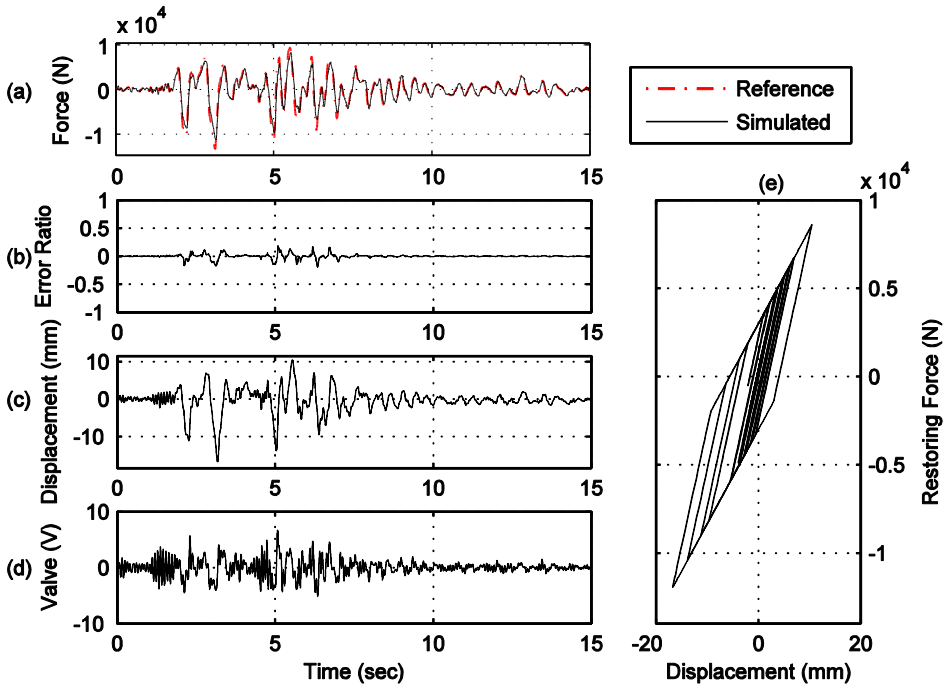

Figure B.15. Yield strength Y_y = 3,000 N, post-yield stiffness $k_1 = 0.4*k_0$.

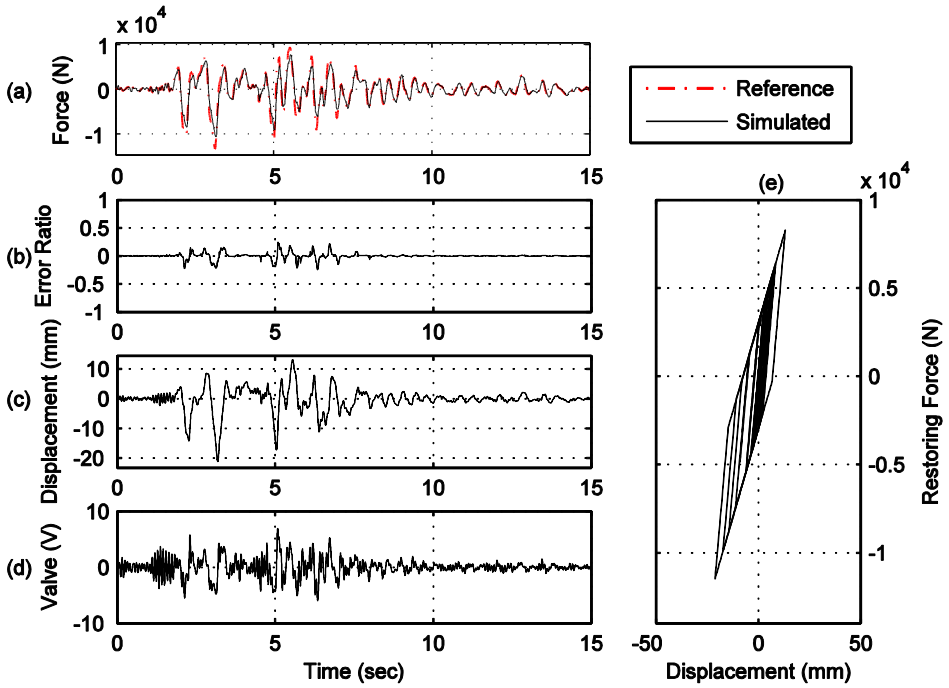

Figure B.16. Yield strength Y_y = 3,000 N, post-yield stiffness $k_1 = 0.3*k_0$.

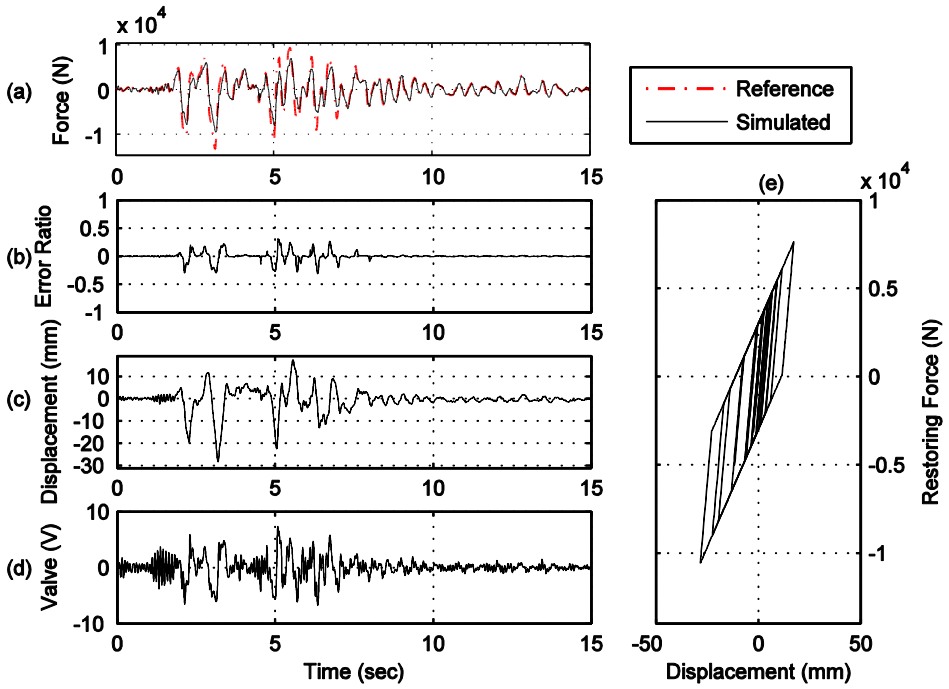

Figure B.17. Yield strength Y_y = 3,000 N, post-yield stiffness $k_1 = 0.2*k_0$.

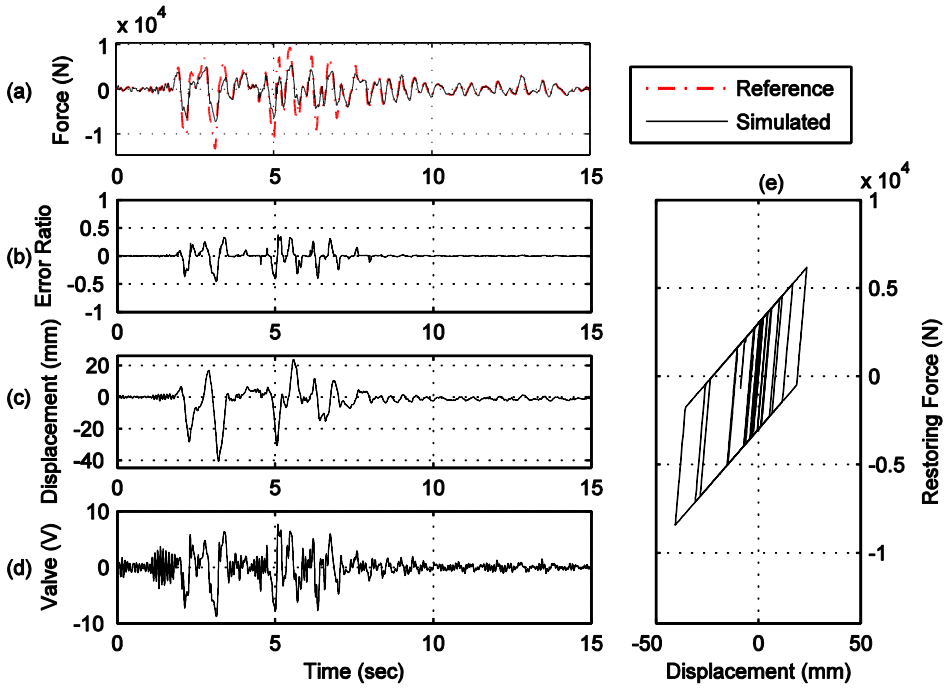

Figure B.18. Yield strength Y_y = 3,000 N, post-yield stiffness $k_1 = 0.1*k_0$.

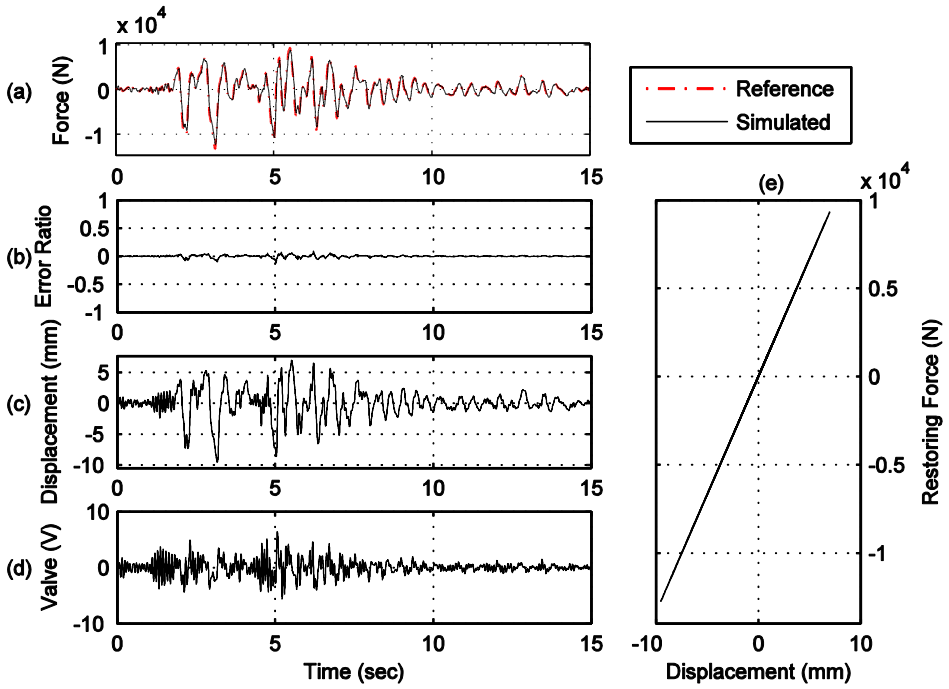

Figure B.19. Yield strength Y_y = 5,000 N, post-yield stiffness $k_1 = 0.9*k_0$.

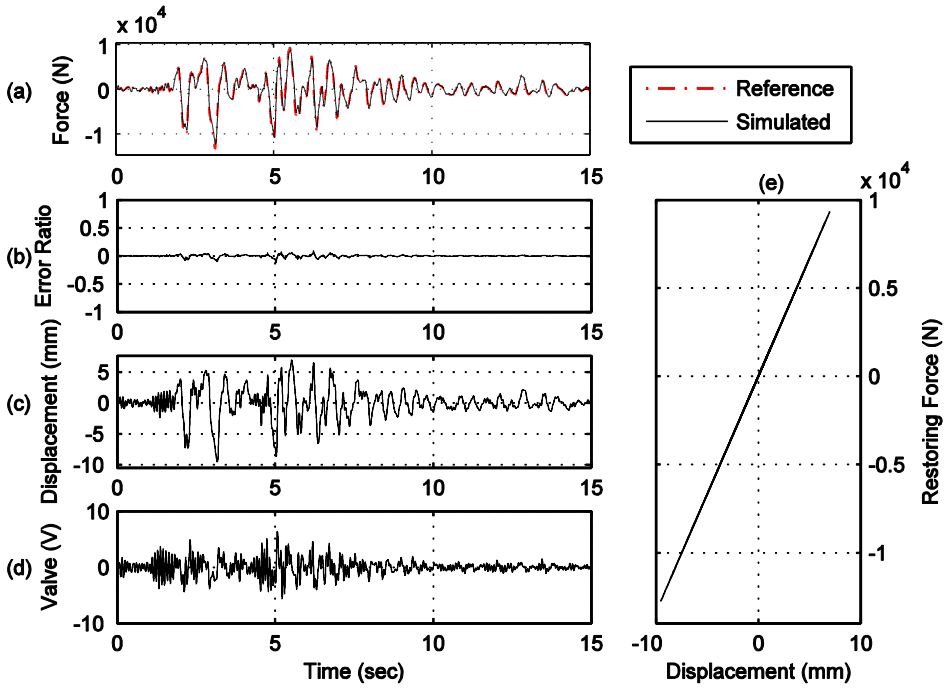

Figure B.20. Yield strength Y_y = 5,000 N, post-yield stiffness $k_1 = 0.8*k_0$.

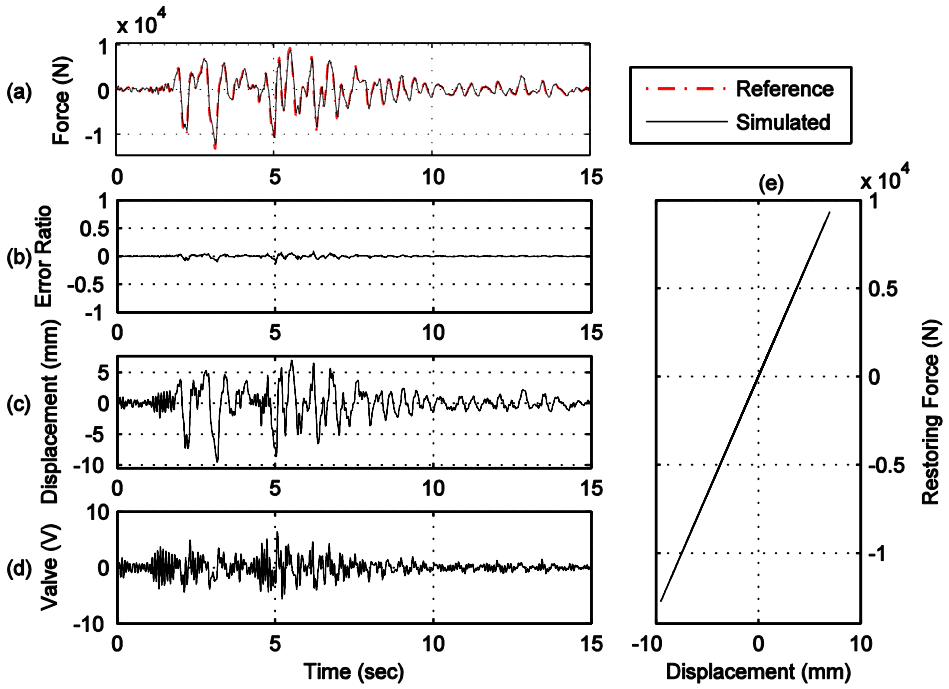

Figure B.21. Yield strength Y_y = 5,000 N, post-yield stiffness $k_1 = 0.7*k_0$.

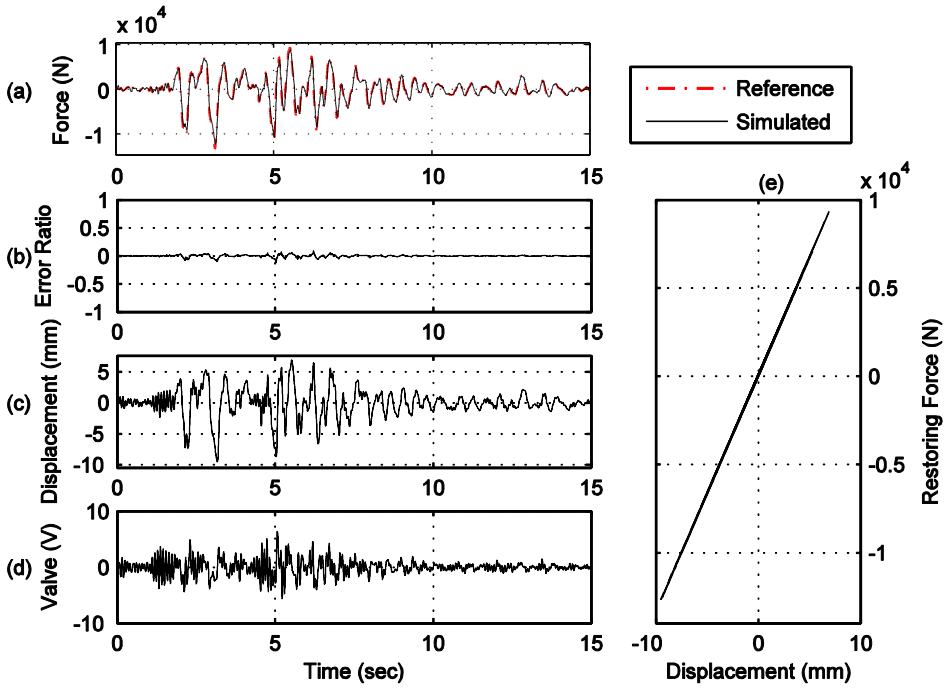

Figure B.22. Yield strength Y_y = 5,000 N, post-yield stiffness $k_1 = 0.6*k_0$.

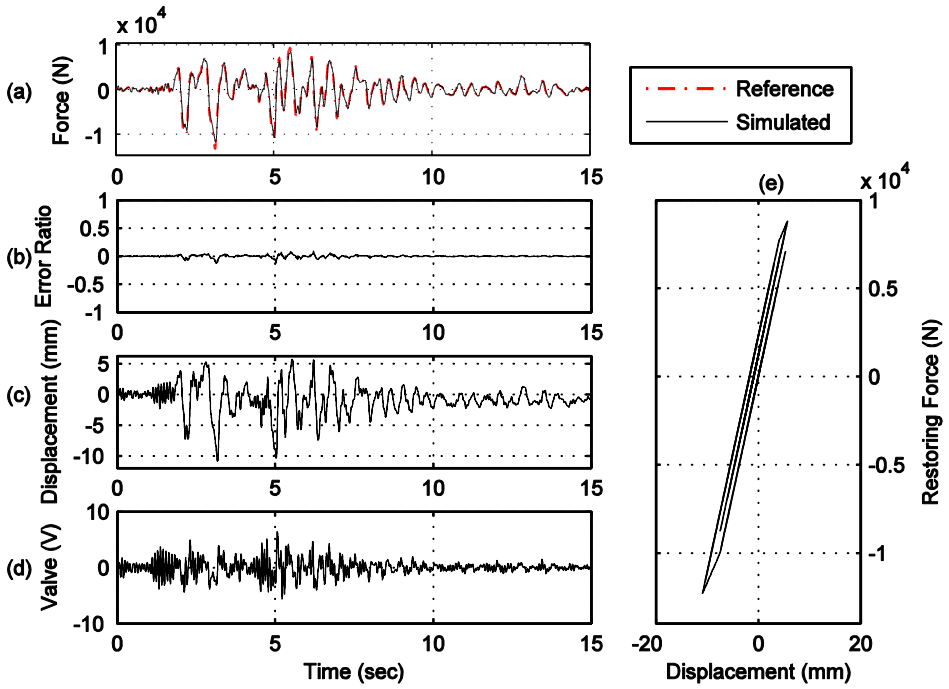

Figure B.23. Yield strength Y_y = 5,000 N, post-yield stiffness $k_1 = 0.5*k_0$.

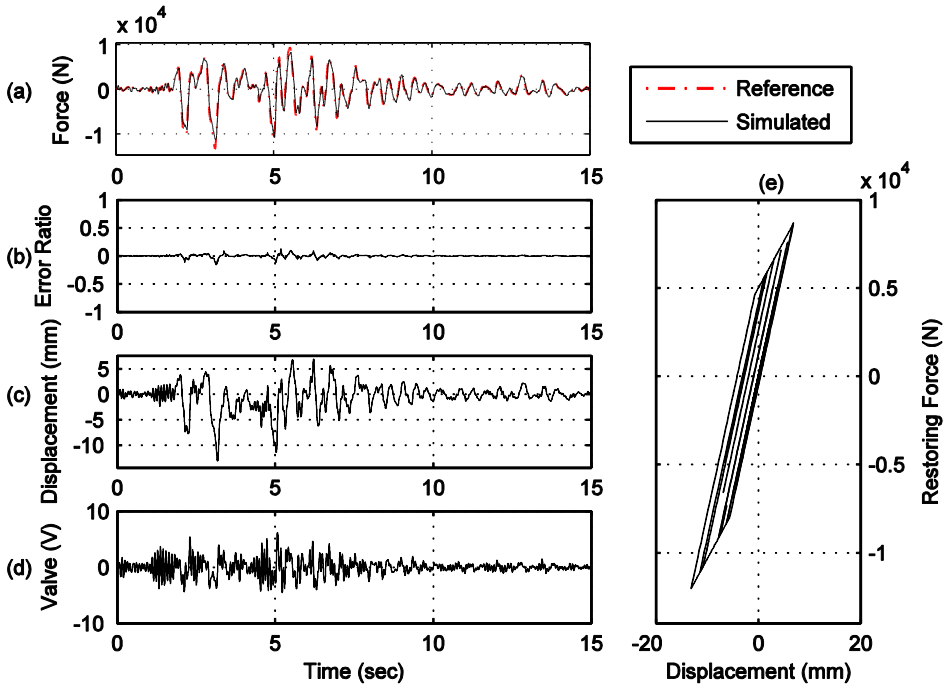

Figure B.24. Yield strength Y_y = 5,000 N, post-yield stiffness $k_1 = 0.4*k_0$.

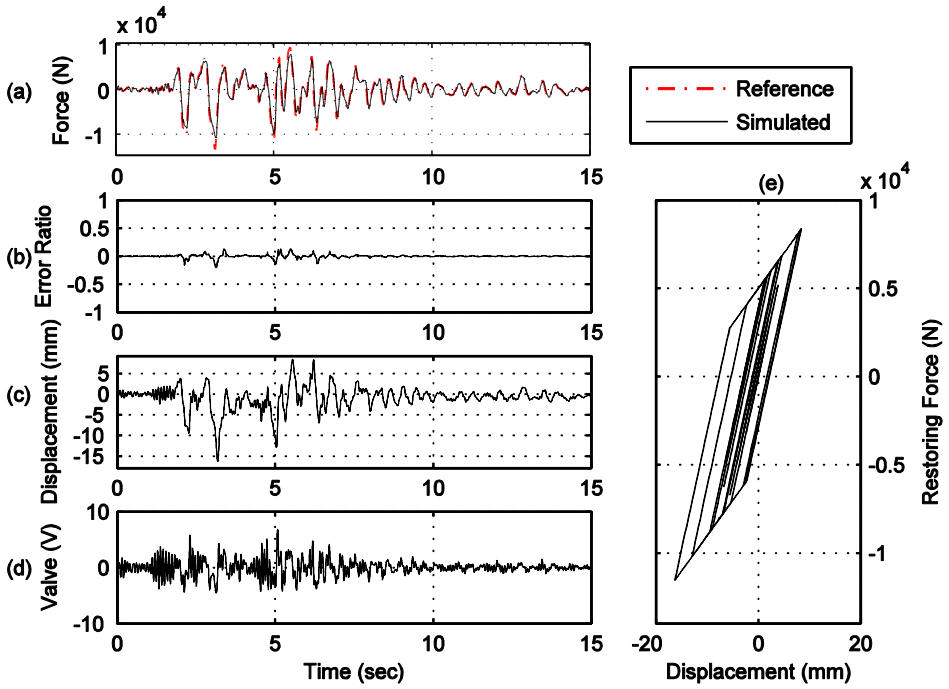

Figure B.25. Yield strength Y_y = 5,000 N, post-yield stiffness $k_1 = 0.3*k_0$.

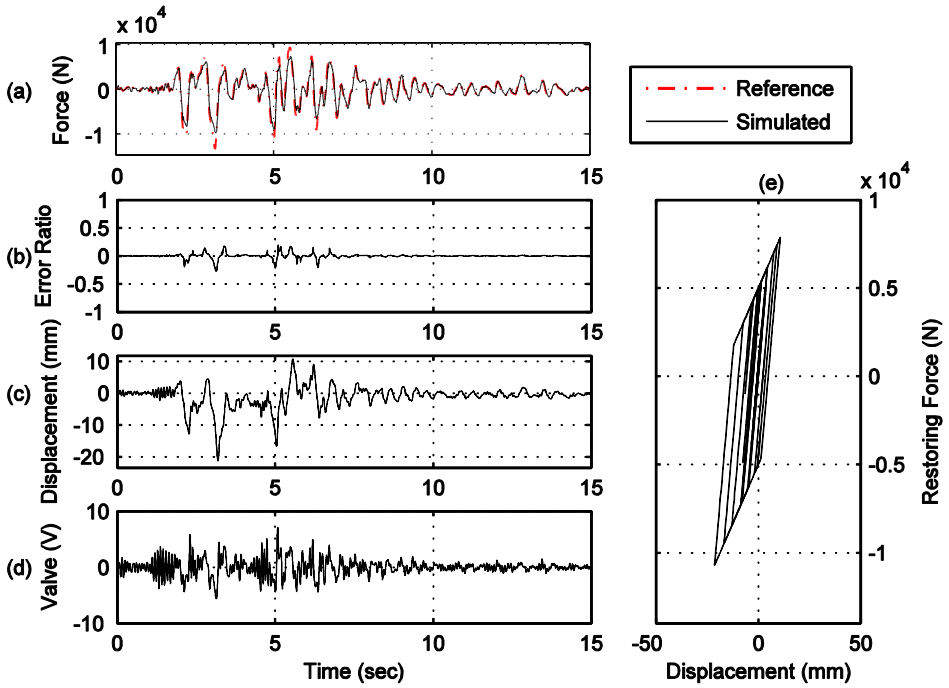

Figure B.26. Yield strength Y_y = 5,000 N, post-yield stiffness $k_1 = 0.2*k_0$.

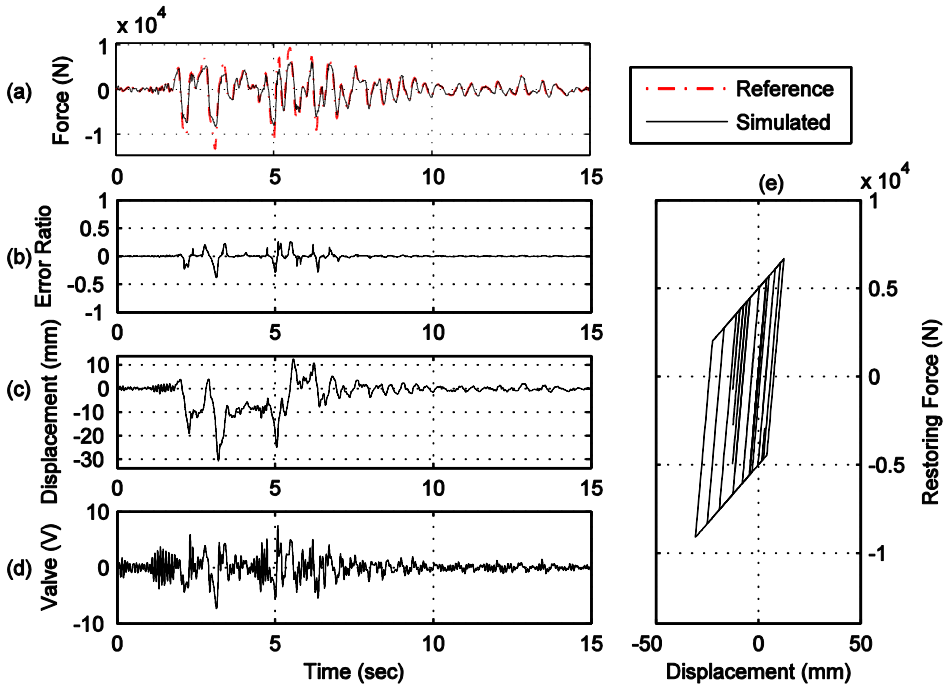

Figure B.27. Yield strength Y_y = 5,000 N, post-yield stiffness $k_1 = 0.1*k_0$.

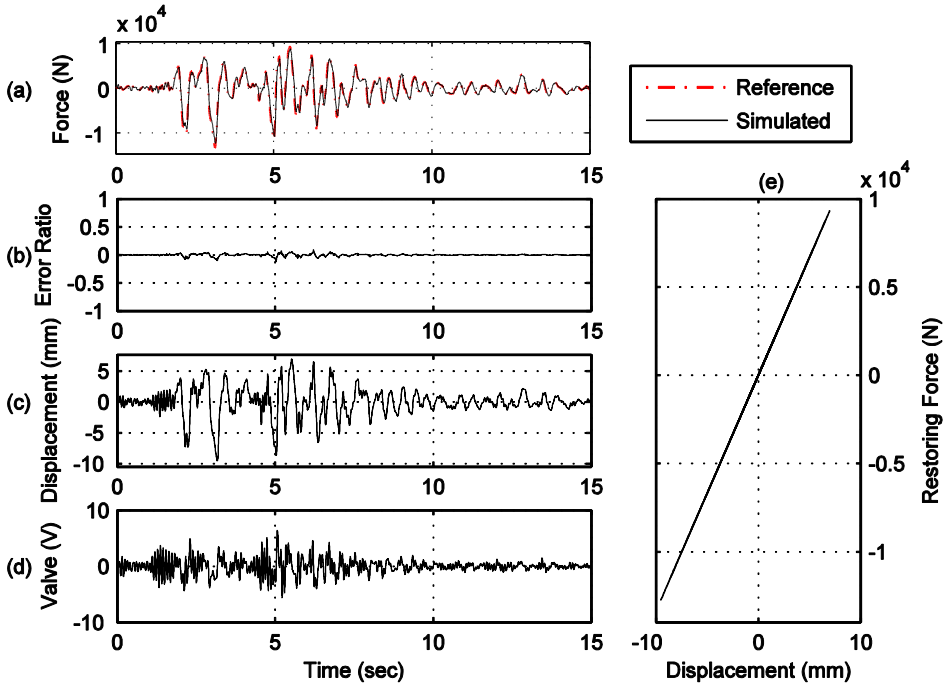

Figure B.28. Yield strength Y_y = 7,000 N, post-yield stiffness $k_1 = 0.9*k_0$.

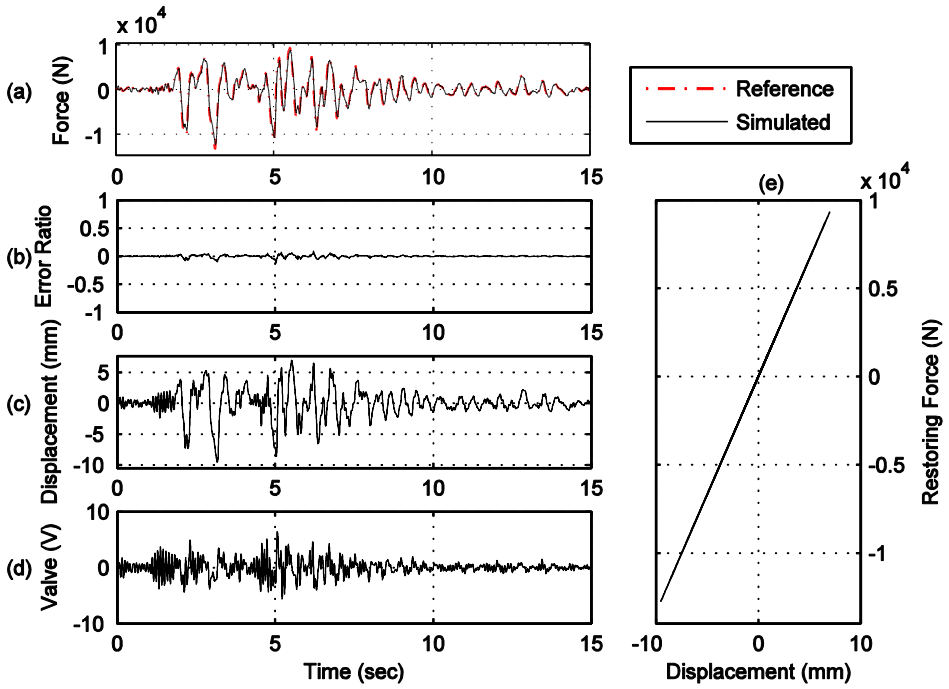

Figure B.29. Yield strength Y_y = 7,000 N, post-yield stiffness $k_1 = 0.8*k_0$.

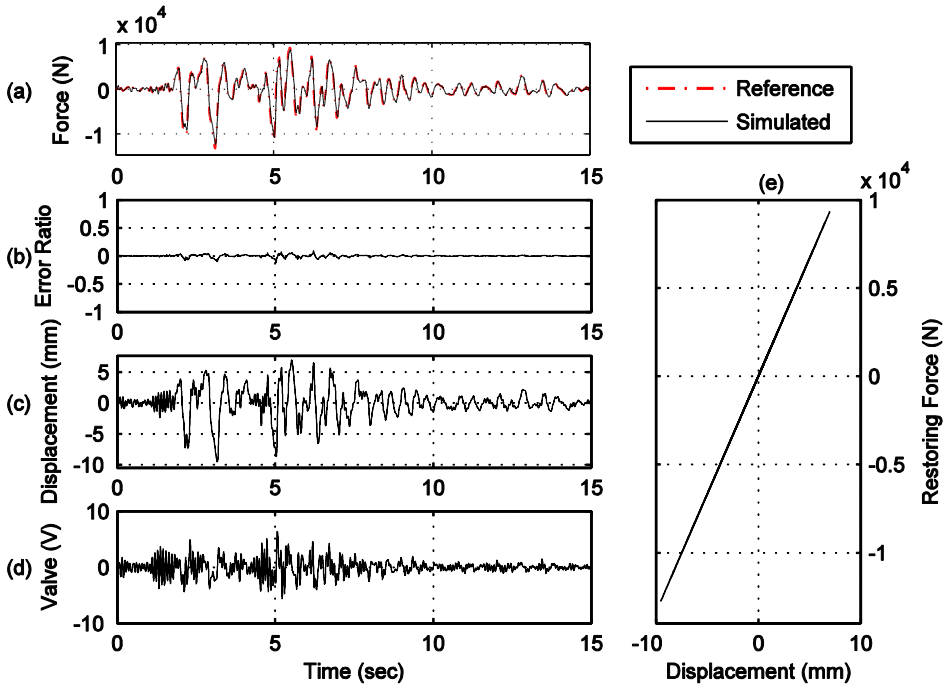

Figure B.30. Yield strength Y_y = 7,000 N, post-yield stiffness $k_1 = 0.7*k_0$.

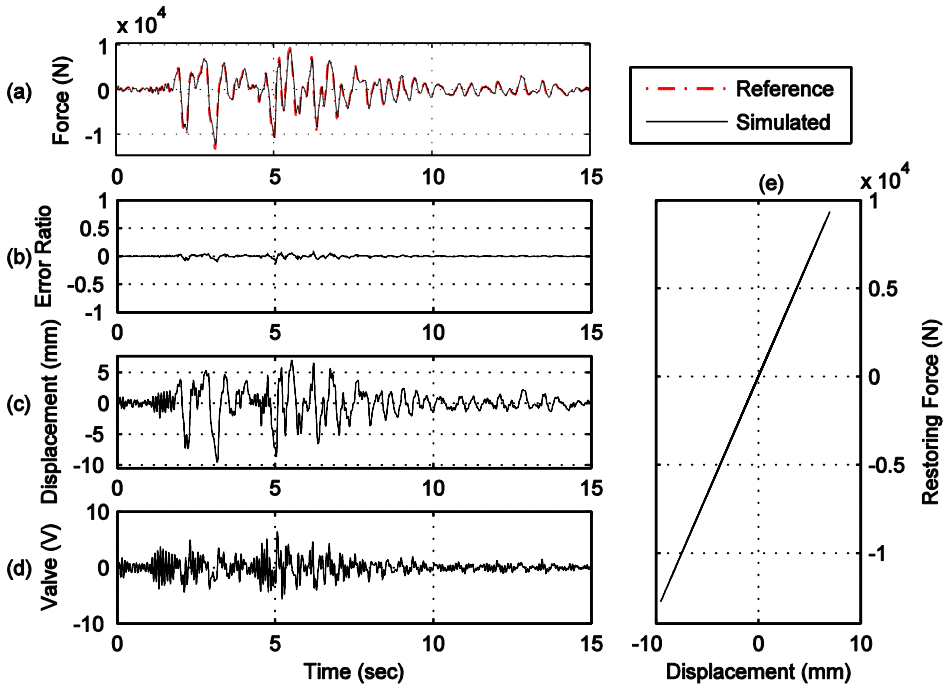

Figure B.31. Yield strength Y_y = 7,000 N, post-yield stiffness $k_1 = 0.6*k_0$.

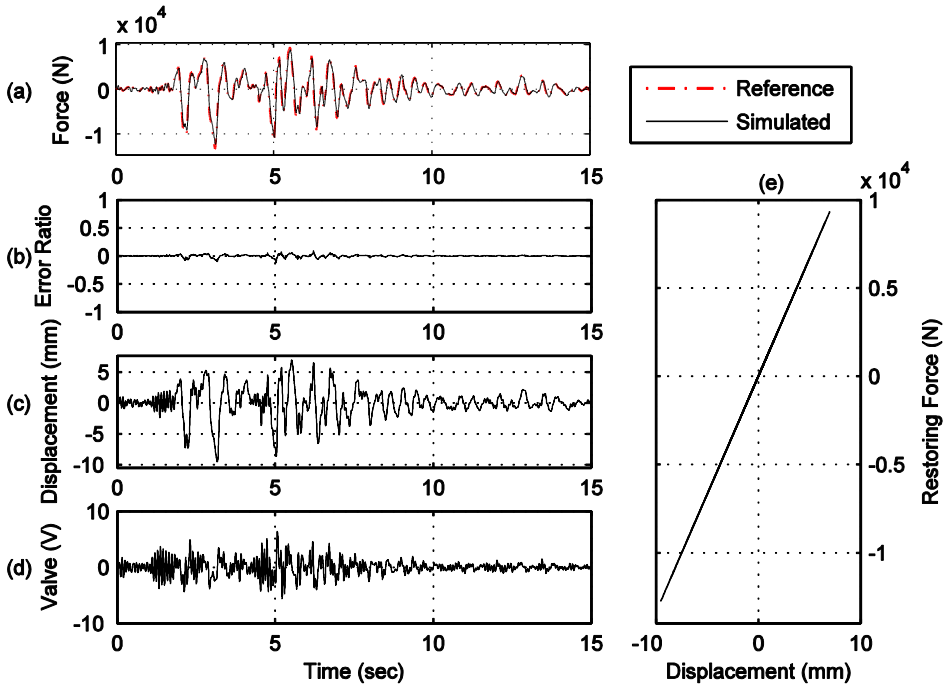

Figure B.32. Yield strength Y_y = 7,000 N, post-yield stiffness $k_1 = 0.5*k_0$.

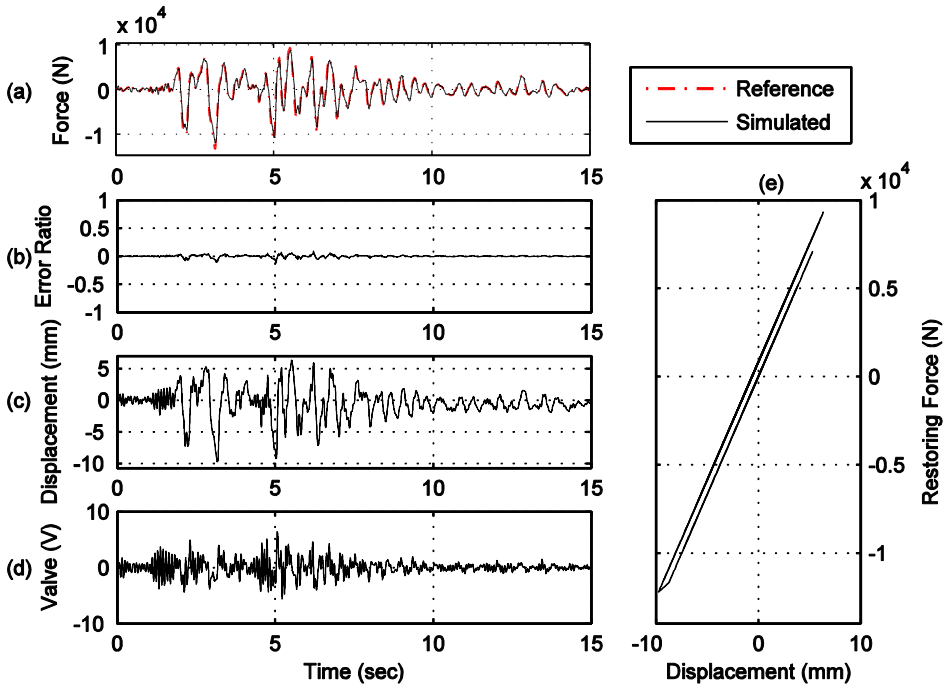

Figure B.33. Yield strength Y_y = 7,000 N, post-yield stiffness $k_1 = 0.4*k_0$.

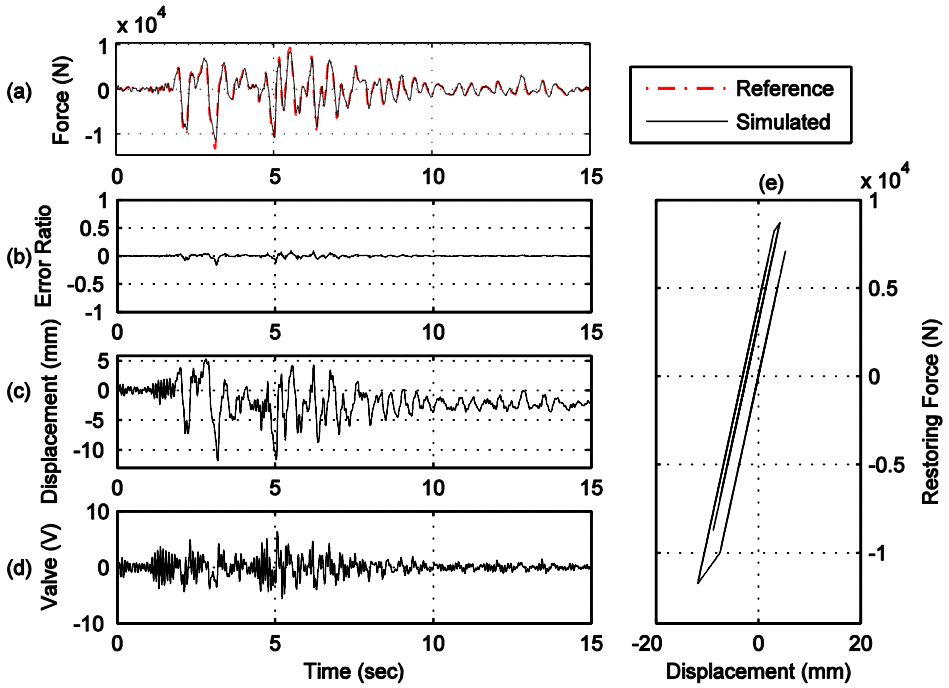

Figure B.34. Yield strength Y_y = 7,000 N, post-yield stiffness $k_1 = 0.3*k_0$.

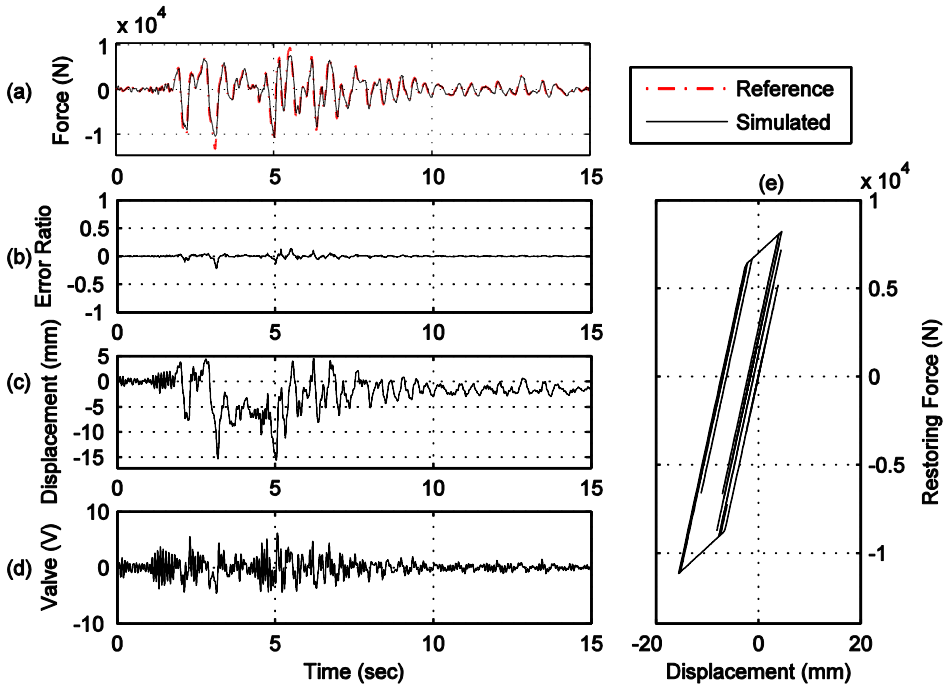

Figure B.35. Yield strength Y_y = 7,000 N, post-yield stiffness $k_1 = 0.2*k_0$.

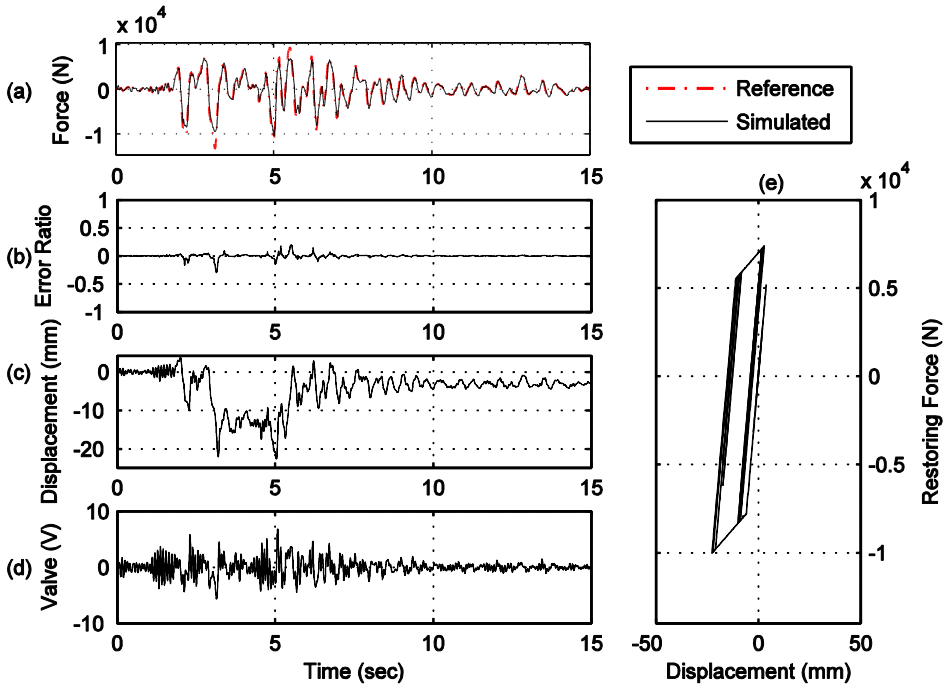

Figure B.36. Yield strength Y_y = 7,000 N, post-yield stiffness $k_1 = 0.1*k_0$.

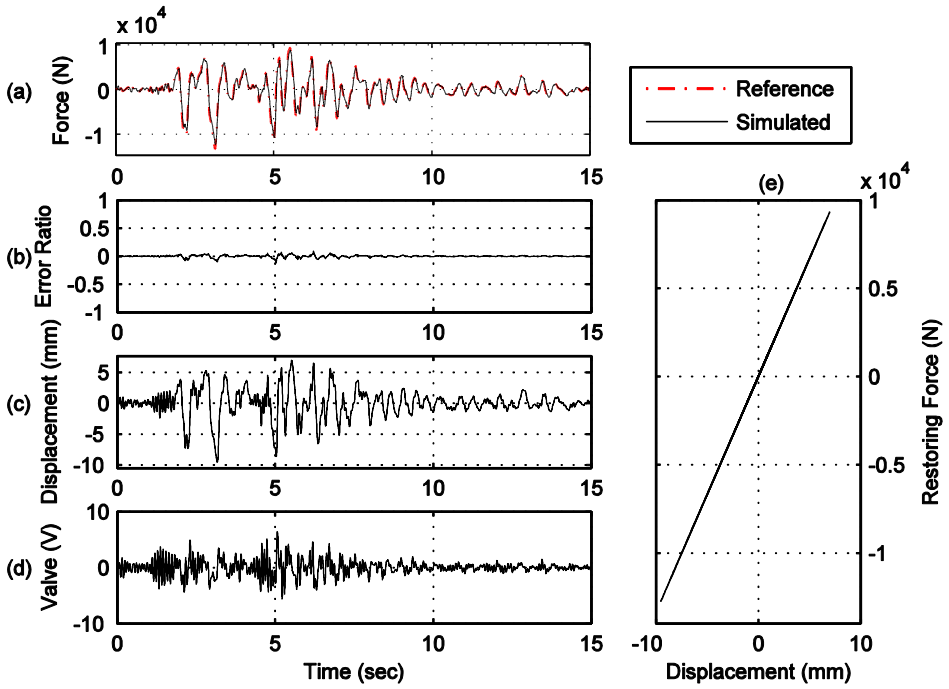

Figure B.37. Yield strength Y_y = 9,000 N, post-yield stiffness $k_1 = 0.9*k_0$.

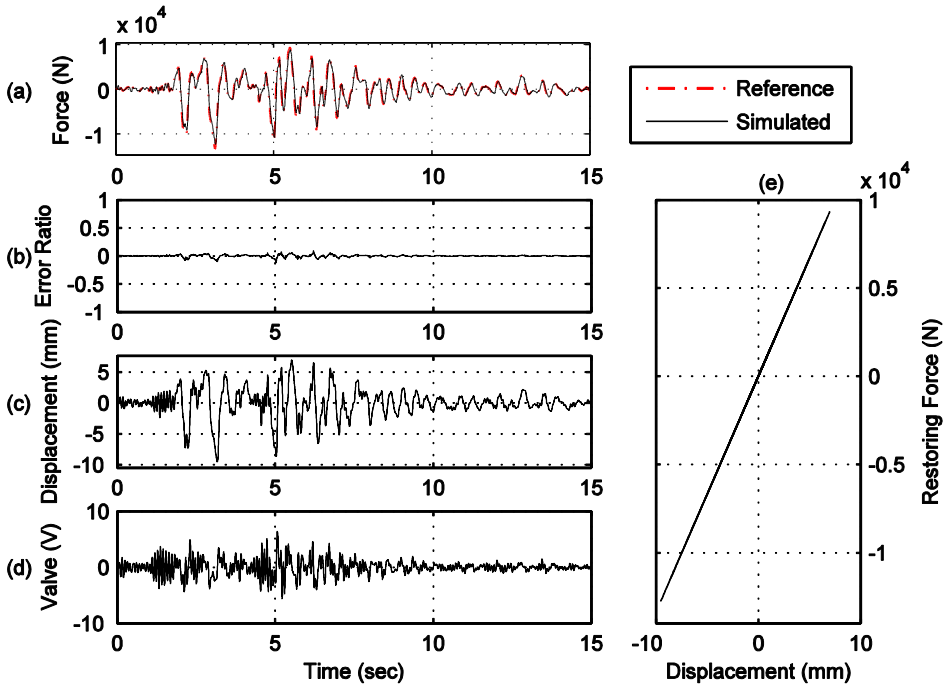

Figure B.38. Yield strength Y_y = 9,000 N, post-yield stiffness $k_1 = 0.8*k_0$.

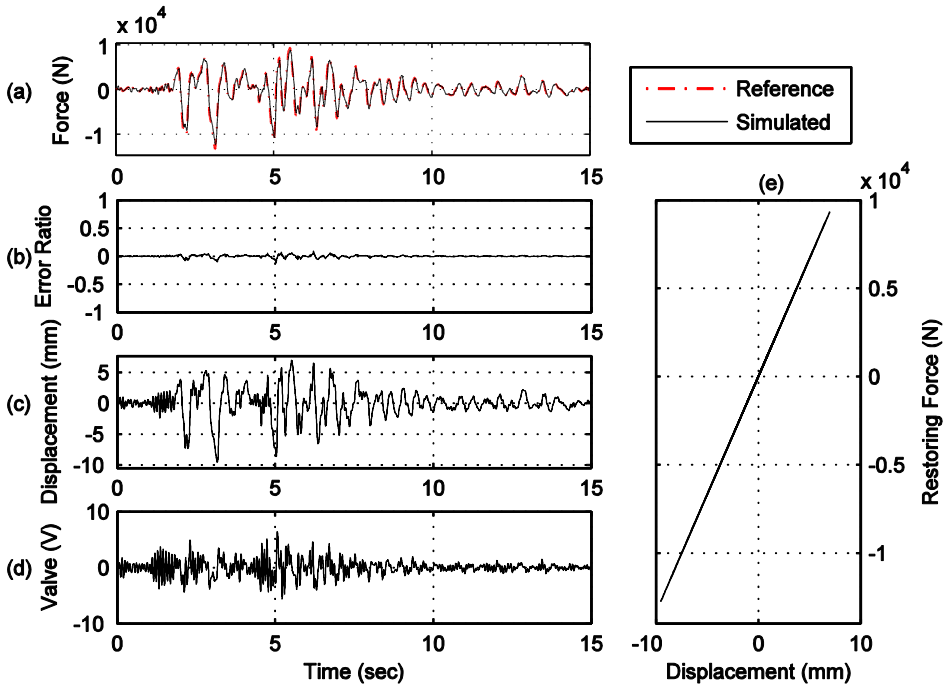

Figure B.39. Yield strength Y_y = 9,000 N, post-yield stiffness $k_1 = 0.7*k_0$.

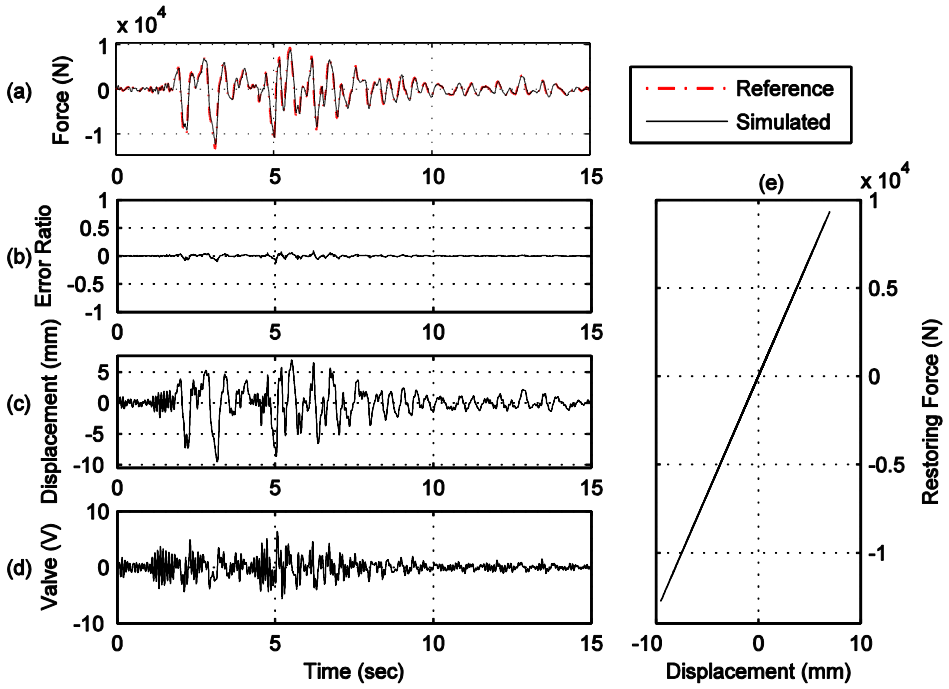

Figure B.40. Yield strength Y_y = 9,000 N, post-yield stiffness $k_1 = 0.6*k_0$.

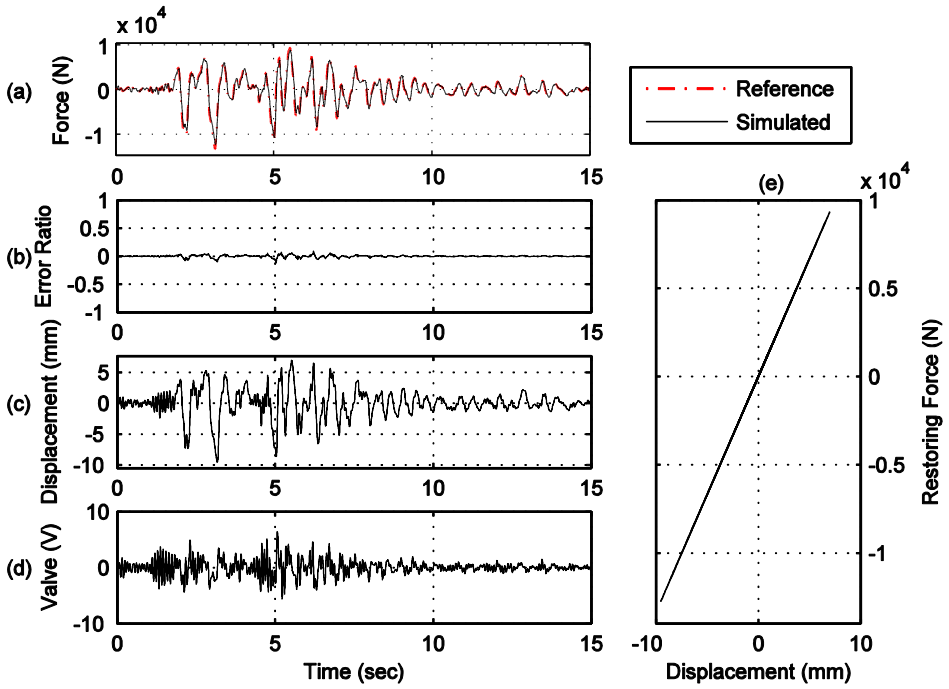

Figure B.41. Yield strength Y_y = 9,000 N, post-yield stiffness $k_1 = 0.5*k_0$.

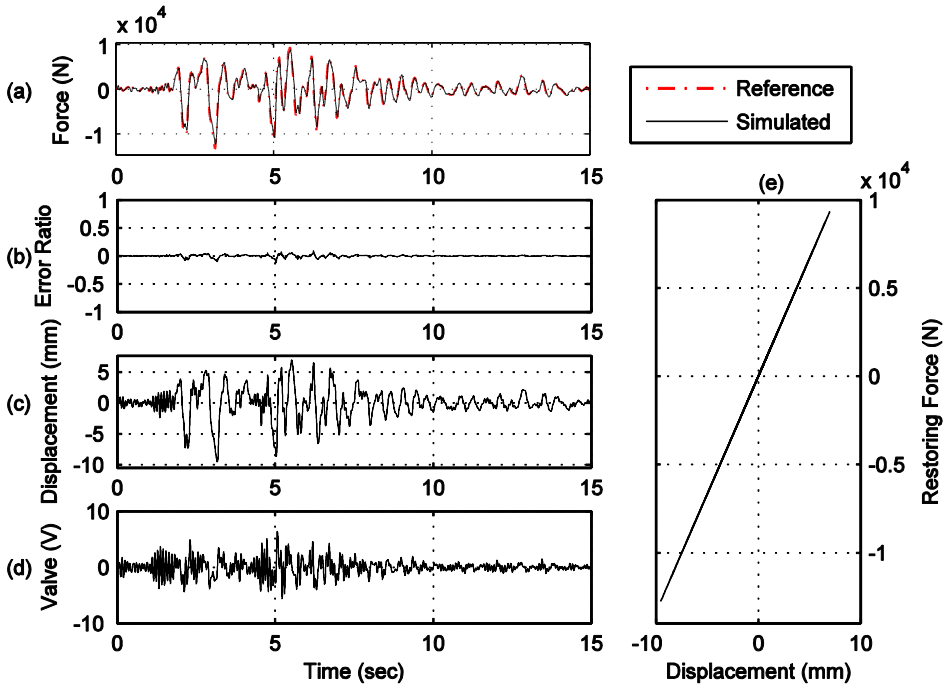

Figure B.42. Yield strength Y_y = 9,000 N, post-yield stiffness $k_1 = 0.4*k_0$.

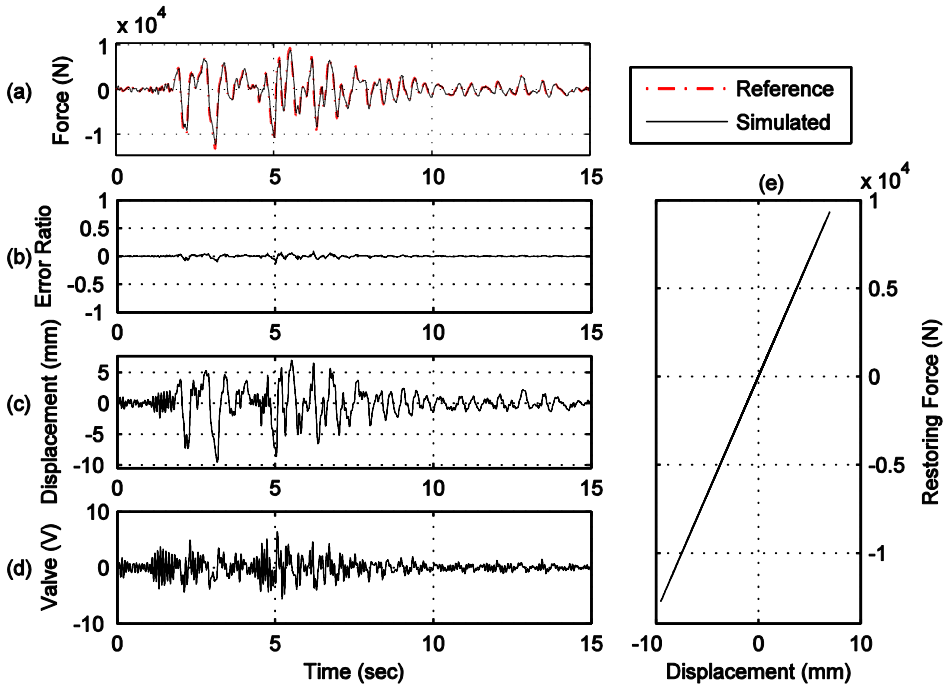

Figure B.43. Yield strength Y_y = 9,000 N, post-yield stiffness $k_1 = 0.3*k_0$.

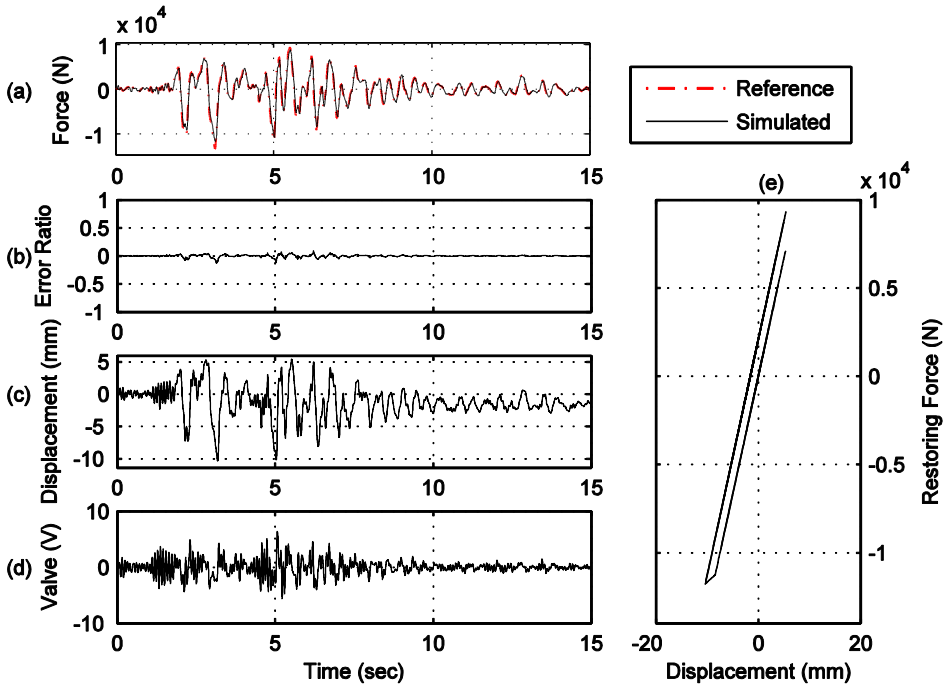

Figure B.44. Yield strength Y_y = 9,000 N, post-yield stiffness $k_1 = 0.2*k_0$.

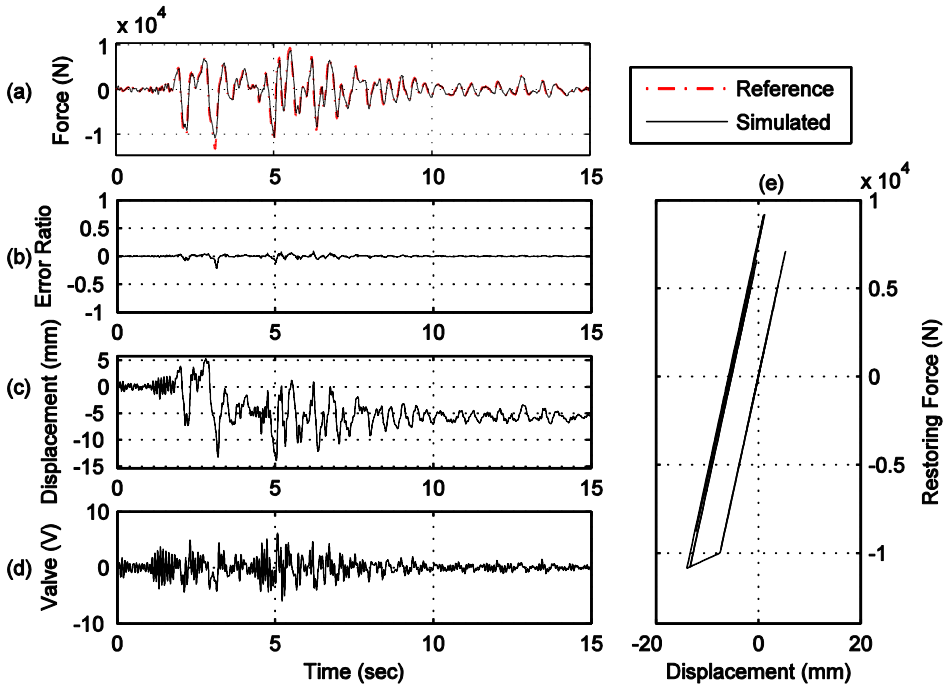

Figure B.45. Yield strength Y_y = 9,000 N, post-yield stiffness $k_1 = 0.1*k_0$.

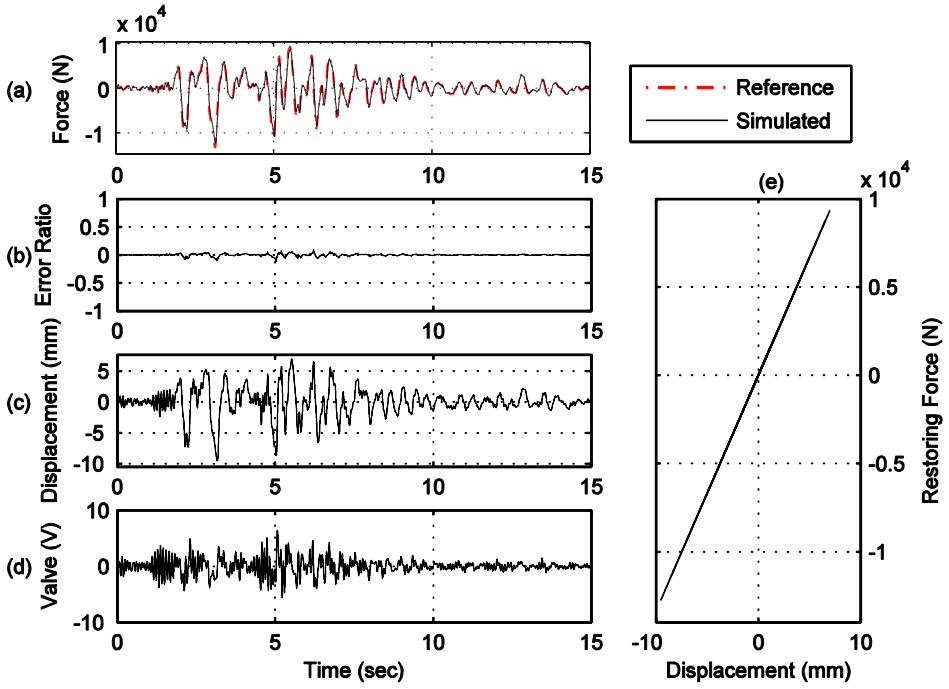

Figure B.46. Yield strength Y_y = 11,000 N, post-yield stiffness $k_1 = 0.9*k_0$.

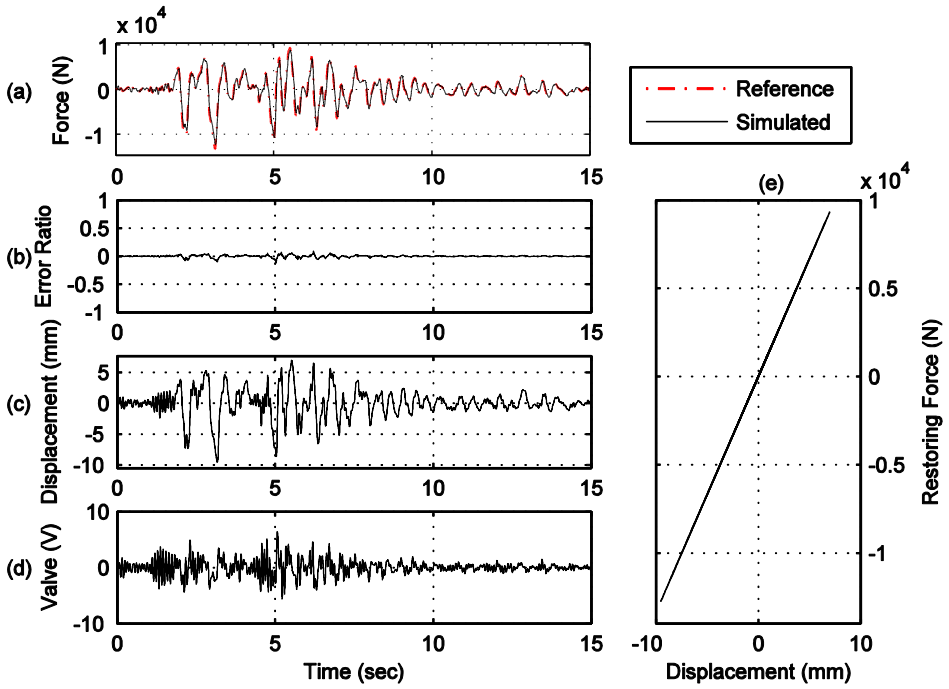

Figure B.47. Yield strength Y_y = 11,000 N, post-yield stiffness $k_1 = 0.8*k_0$.

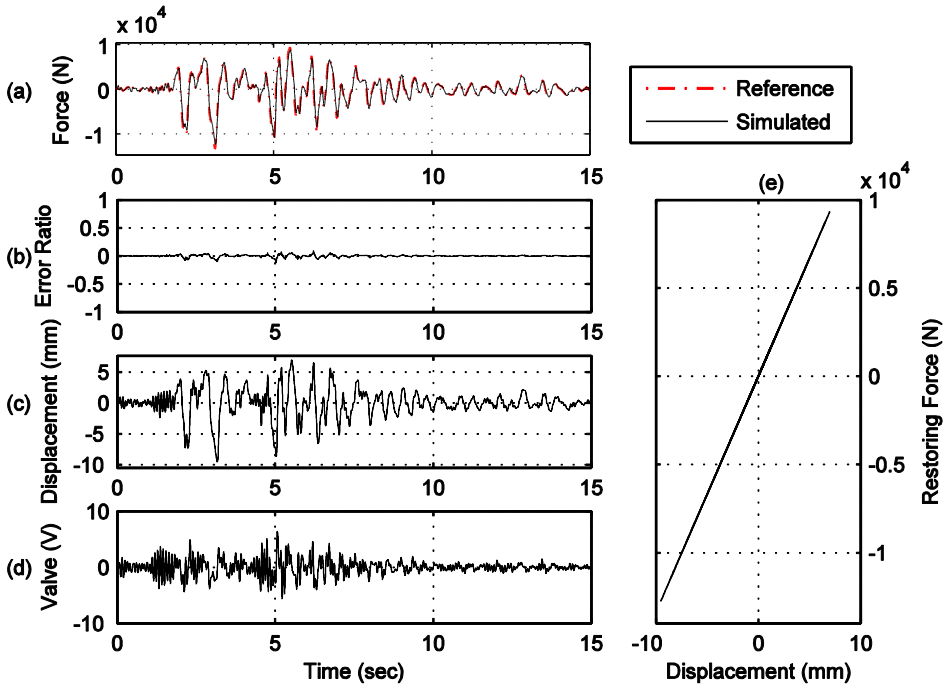

Figure B.48. Yield strength Y_y = 11,000 N, post-yield stiffness $k_1 = 0.7*k_0$.

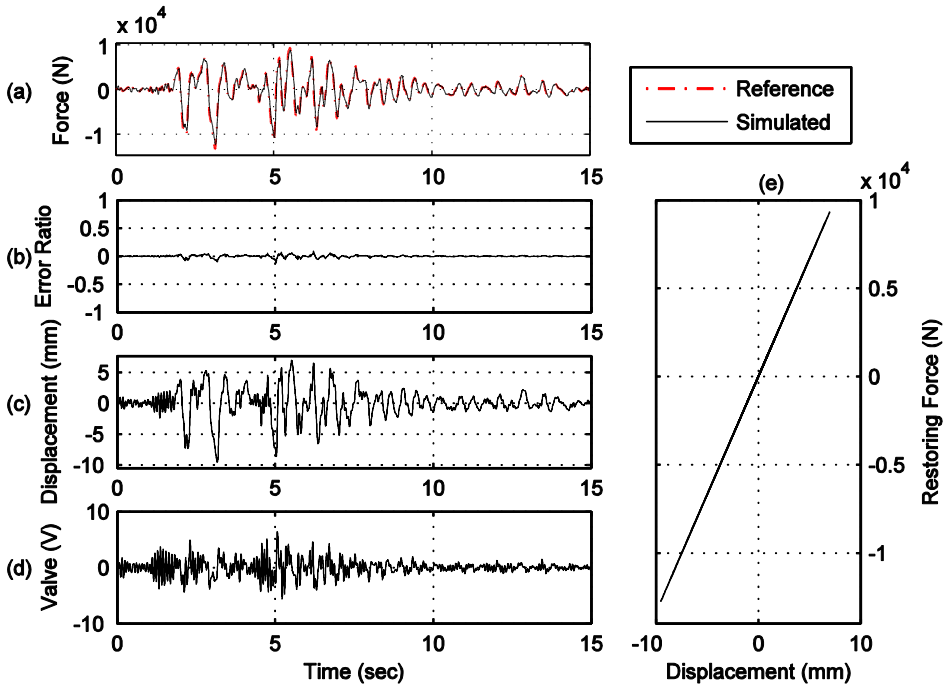

Figure B.49. Yield strength Y_y = 11,000 N, post-yield stiffness $k_1 = 0.6*k_0$.

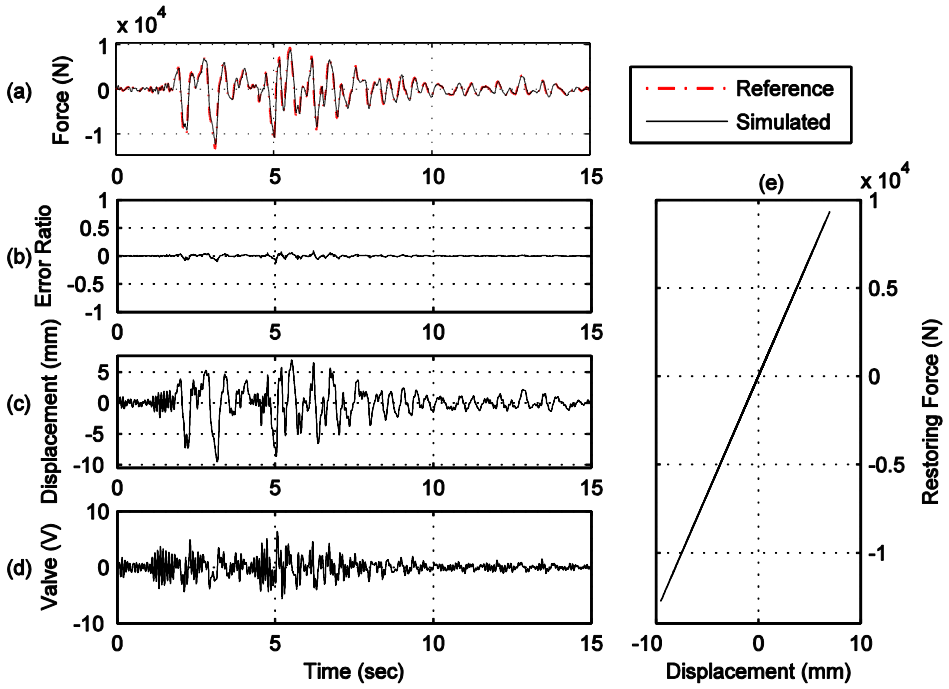

Figure B.50. Yield strength Y_y = 11,000 N, post-yield stiffness $k_1 = 0.5*k_0$.

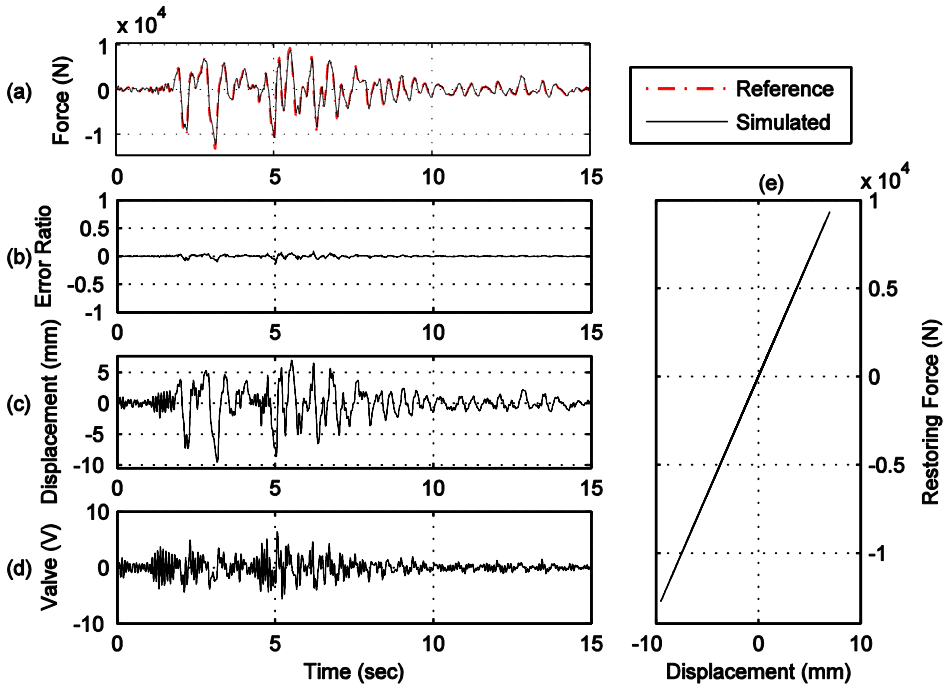

Figure B.51. Yield strength Y_y = 11,000 N, post-yield stiffness $k_1 = 0.4*k_0$.

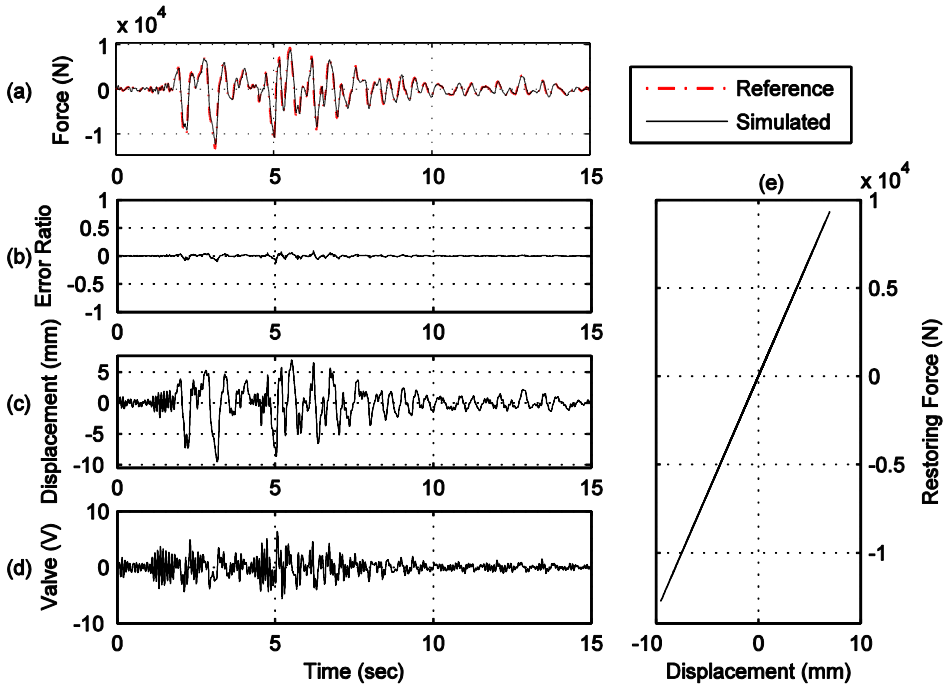

Figure B.52. Yield strength Y_y = 11,000 N, post-yield stiffness $k_1 = 0.3*k_0$.

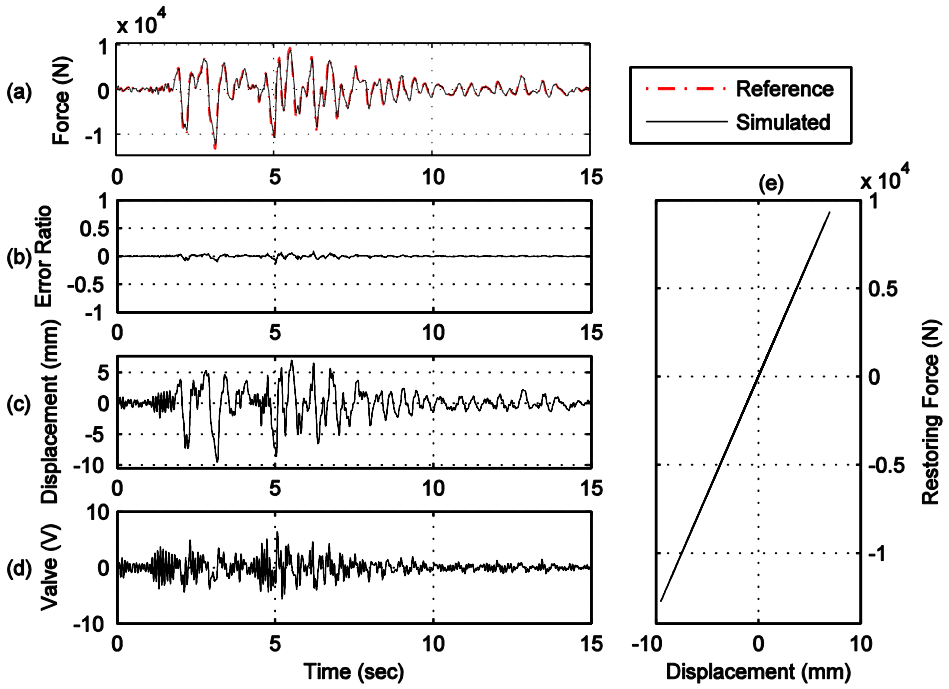

Figure B.53. Yield strength Y_y = 11,000 N, post-yield stiffness $k_1 = 0.2*k_0$.

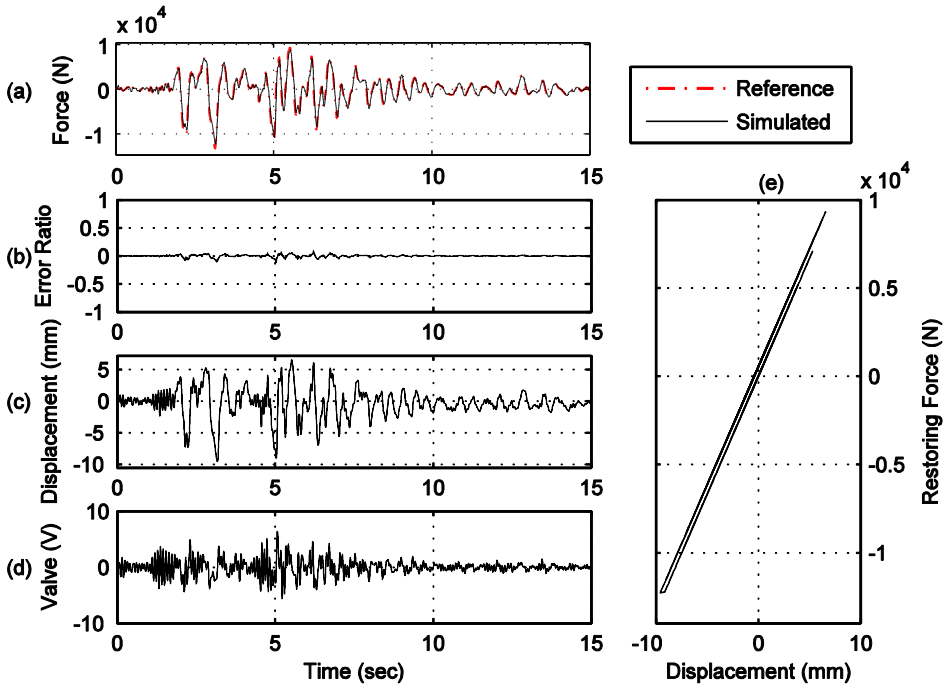

Figure B.54. Yield strength Y_y = 11,000 N, post-yield stiffness $k_1 = 0.1*k_0$.

Pinned Base

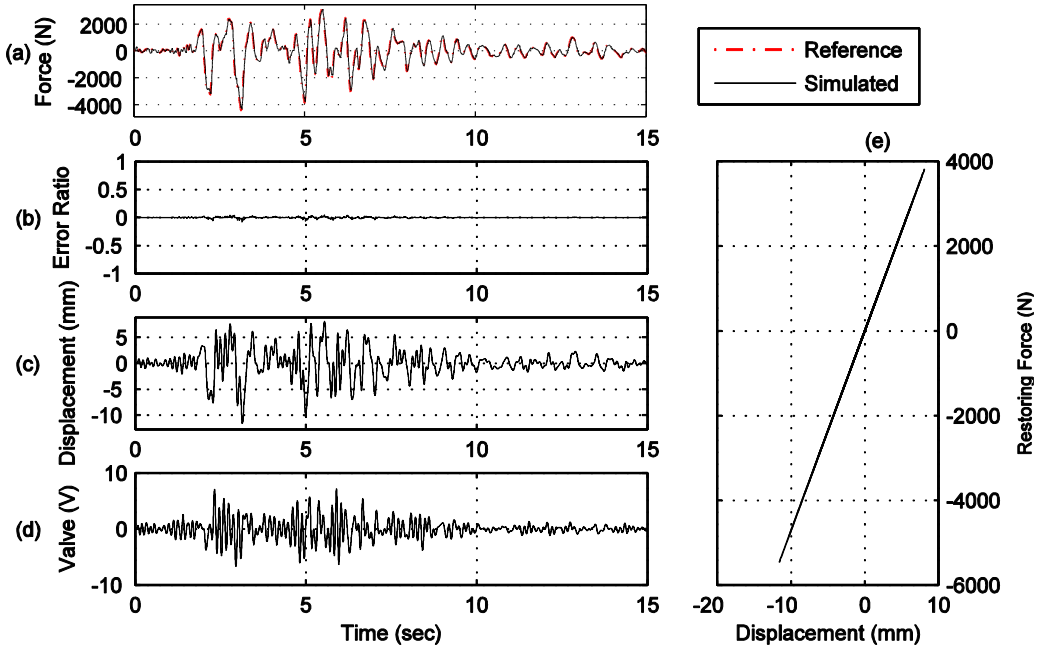

Figure B.55. Yield strength Y_y = 1,000 N, post-yield stiffness $k_1 = 0.9*k_0$.

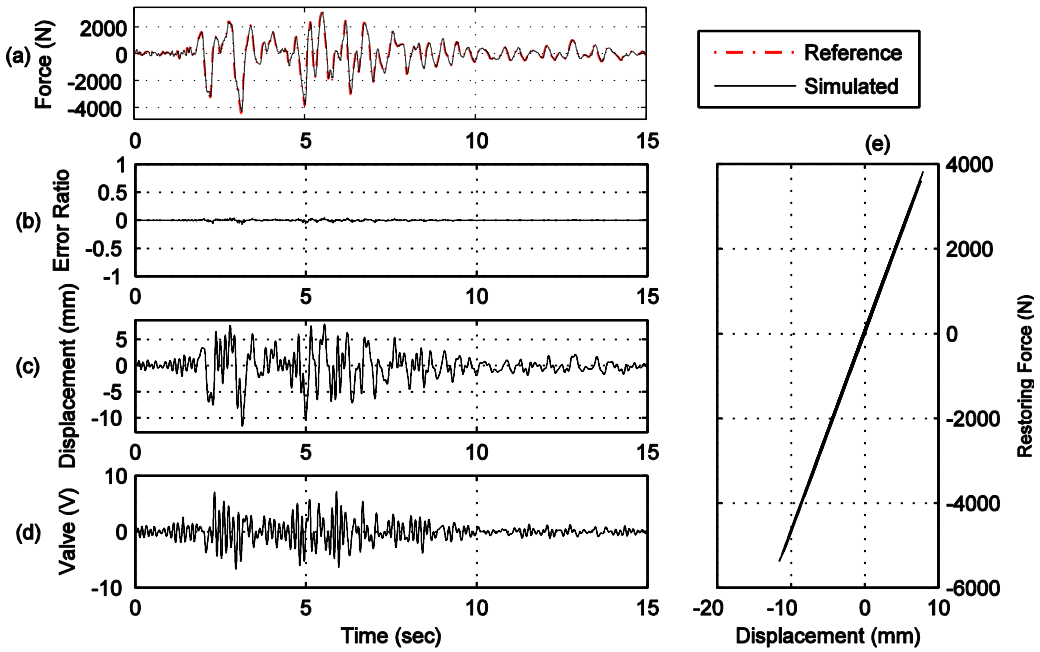

Figure B.56. Yield strength Y_y = 1,000 N, post-yield stiffness $k_1 = 0.8*k_0$.

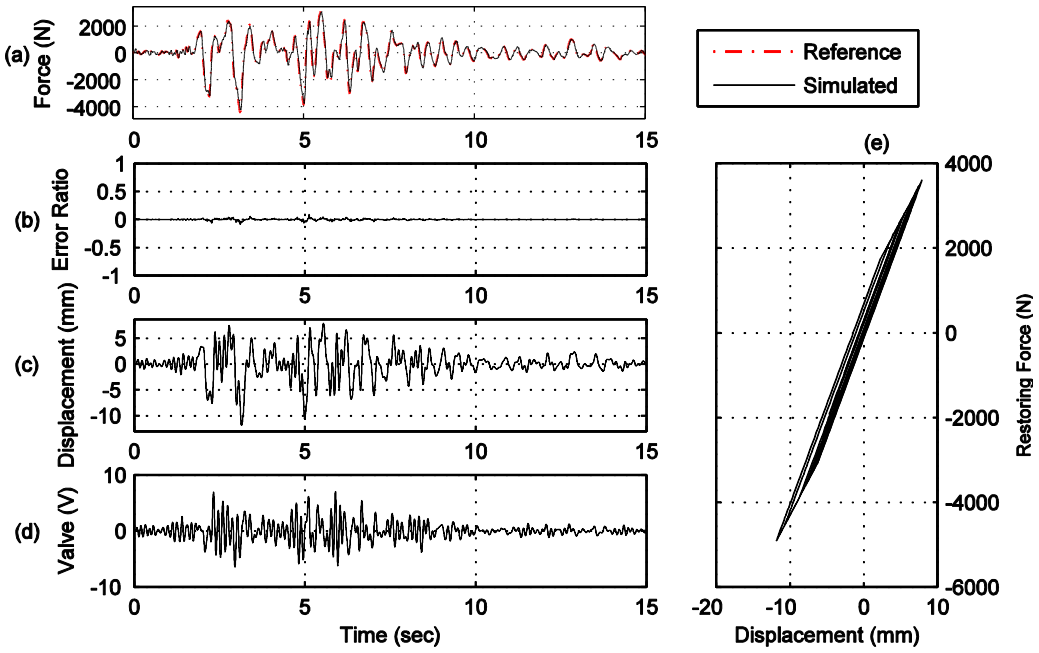

Figure B.57. Yield strength Y_y = 1,000 N, post-yield stiffness $k_1 = 0.7*k_0$.

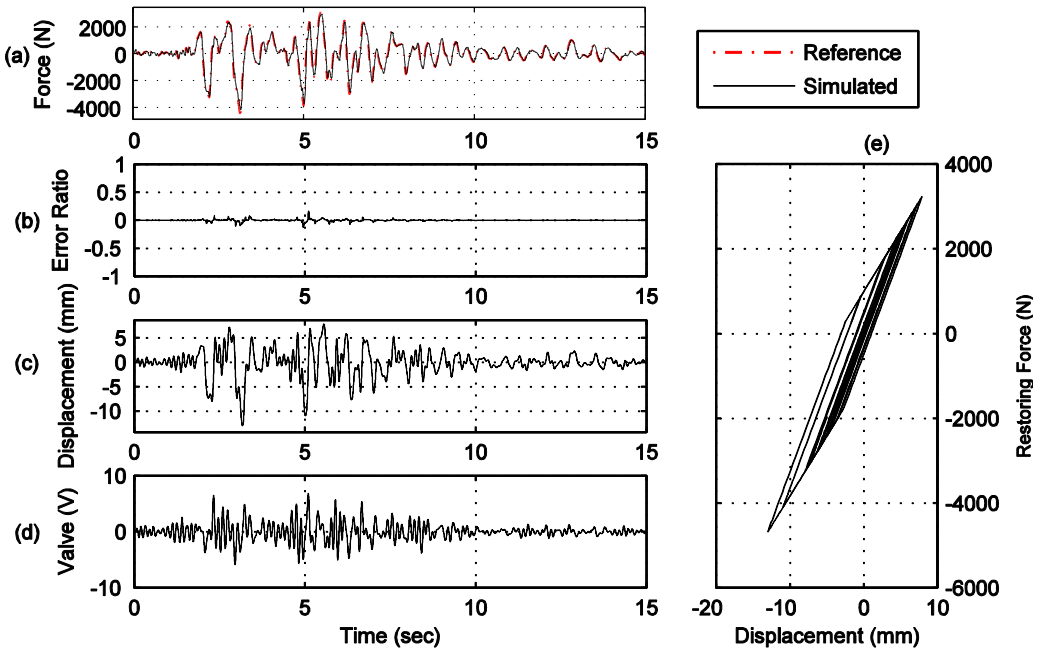

Figure B.58. Yield strength Y_y = 1,000 N, post-yield stiffness $k_1 = 0.6*k_0$.

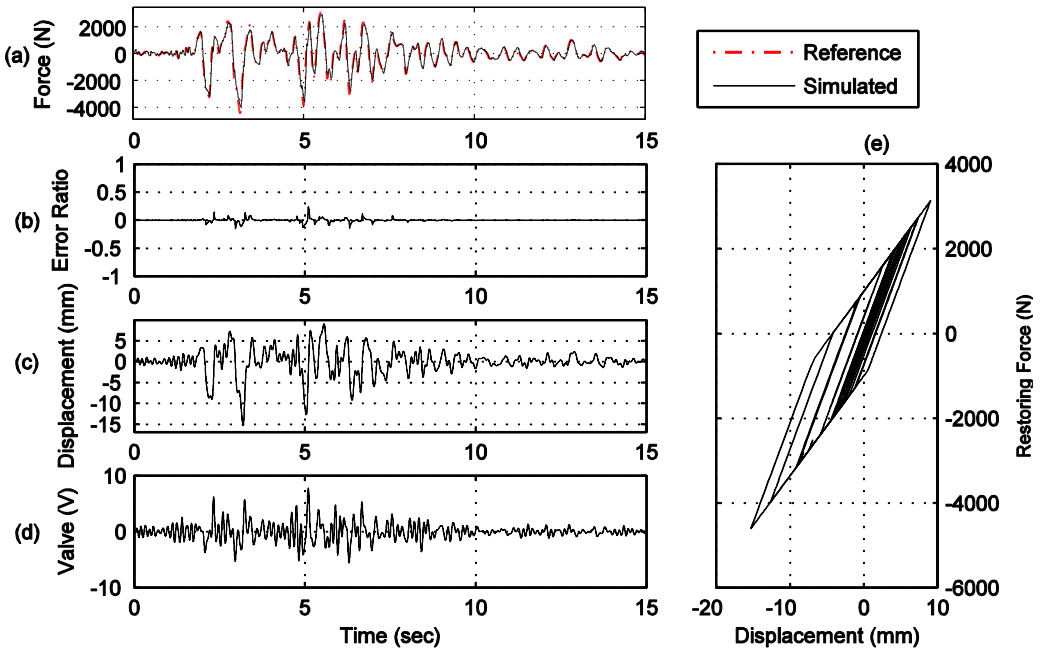

Figure B.59. Yield strength Y_y = 1,000 N, post-yield stiffness $k_1 = 0.5*k_0$.

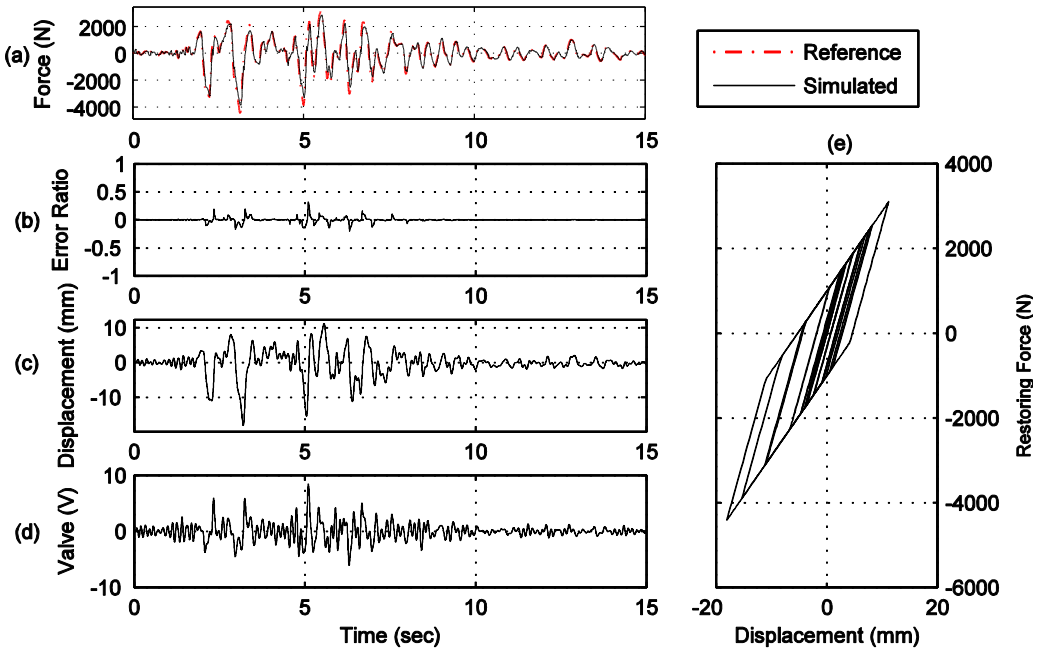

Figure B.60. Yield strength Y_y = 1,000 N, post-yield stiffness $k_1 = 0.4*k_0$.

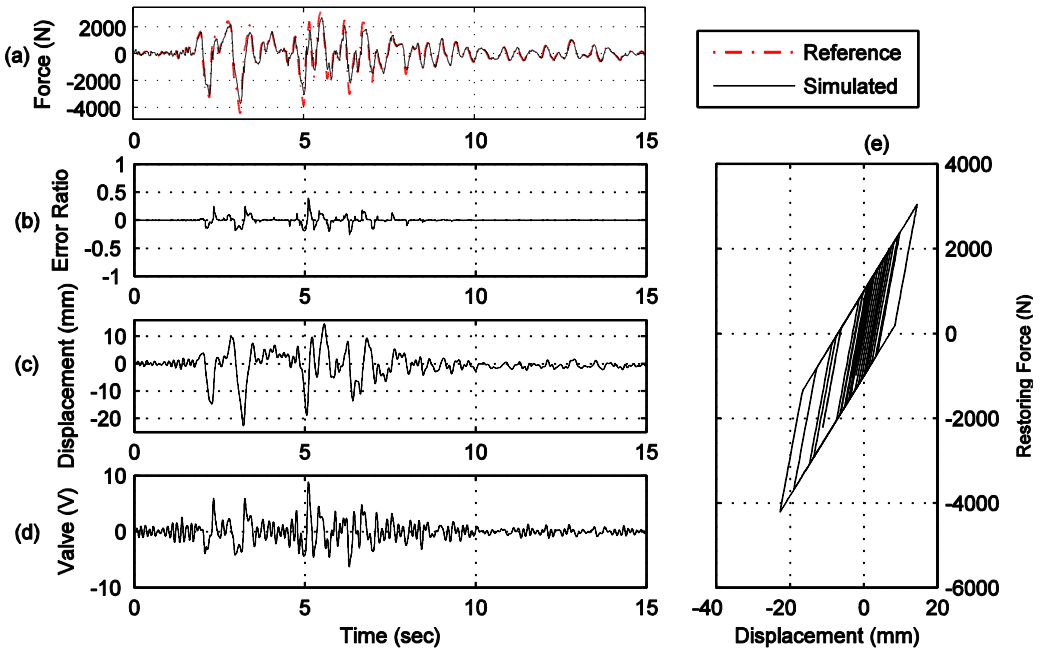

Figure B.61. Yield strength Y_y = 1,000 N, post-yield stiffness $k_1 = 0.3*k_0$.

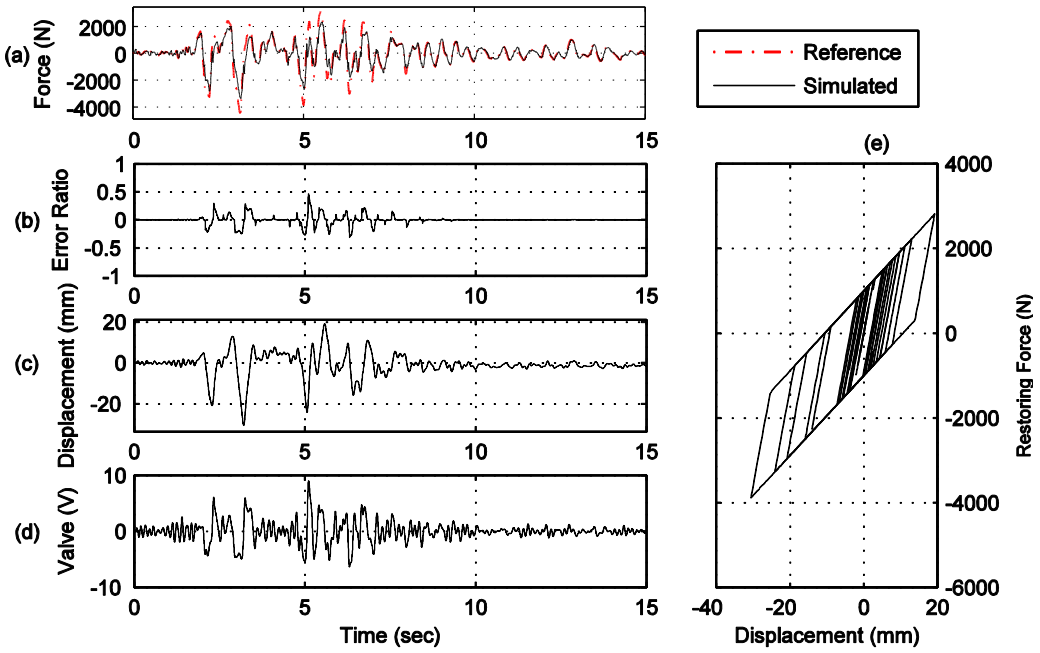

Figure B.62. Yield strength Y_y = 1,000 N, post-yield stiffness $k_1 = 0.2*k_0$.

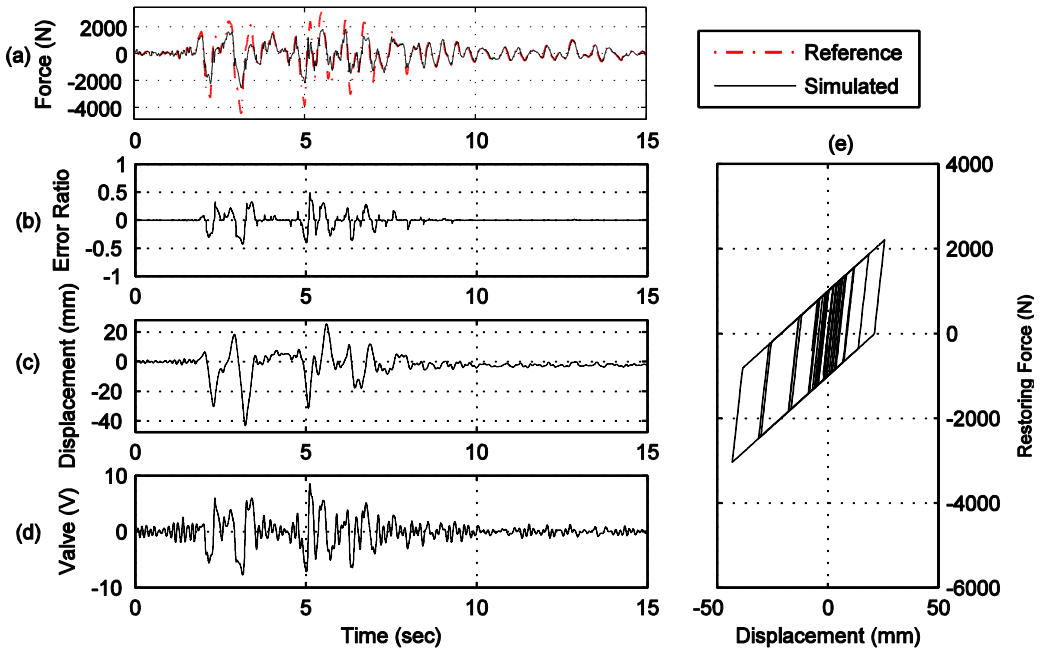

Figure B.63. Yield strength Y_y = 1,000 N, post-yield stiffness $k_1 = 0.1*k_0$.

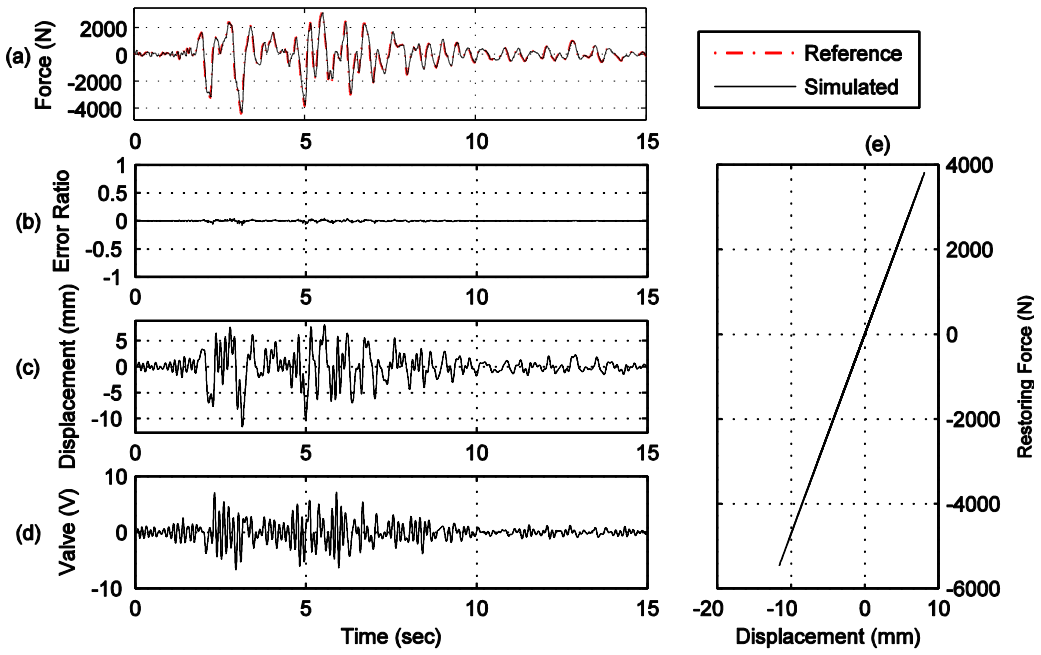

Figure B.64. Yield strength Y_y = 1,500 N, post-yield stiffness $k_1 = 0.9*k_0$.

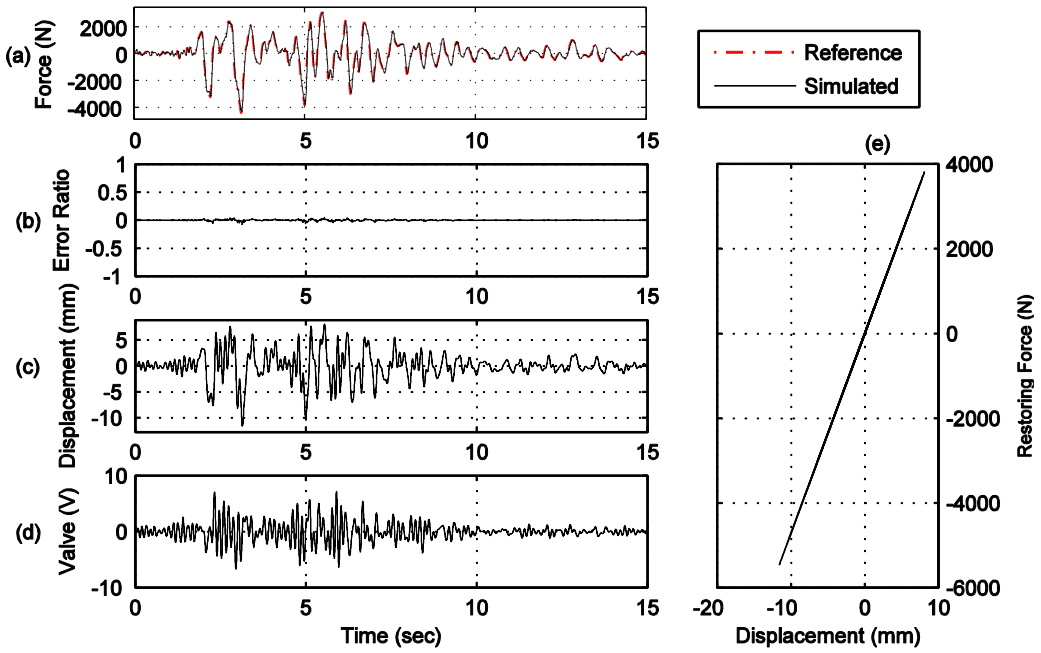

Figure B.65. Yield strength Y_y = 1,500 N, post-yield stiffness $k_1 = 0.8*k_0$.

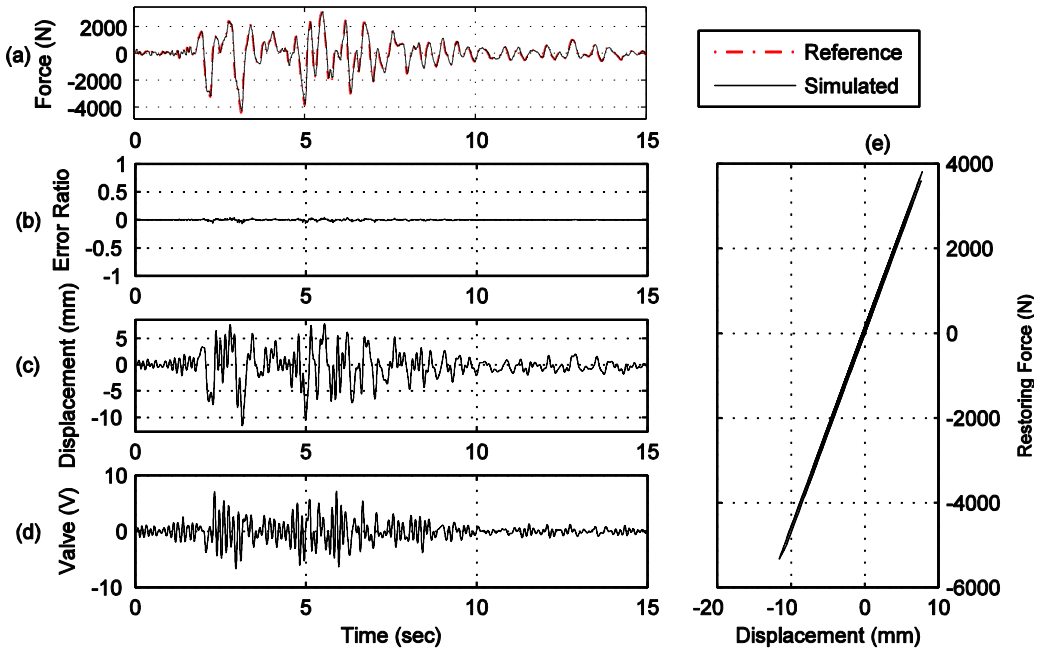

Figure B.66. Yield strength Y_y = 1,500 N, post-yield stiffness $k_1 = 0.7*k_0$.

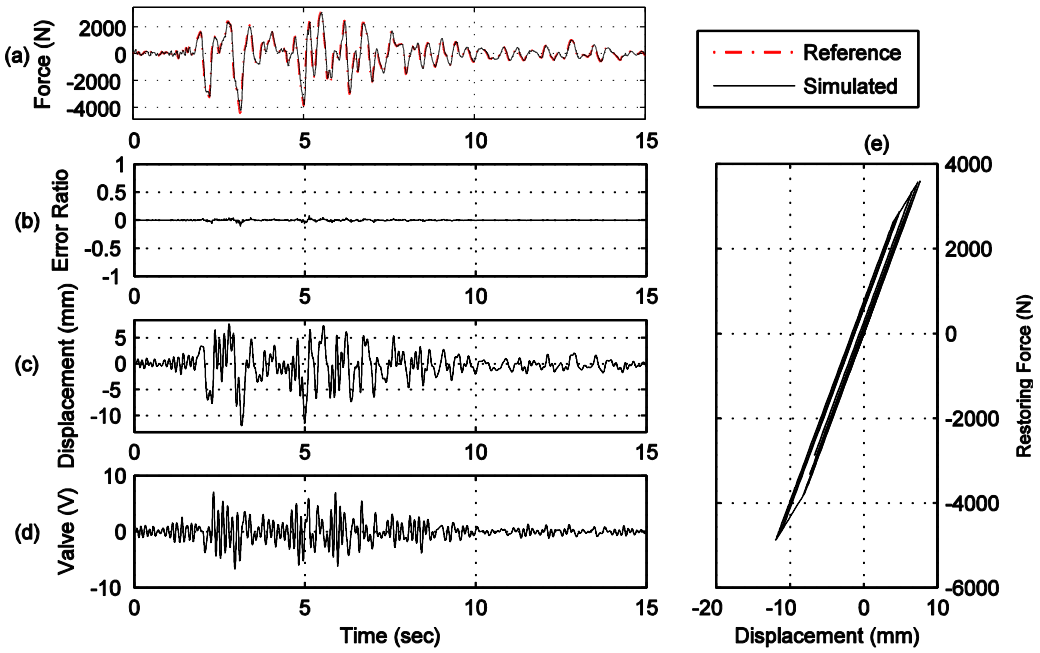

Figure B.67. Yield strength Y_y = 1,500 N, post-yield stiffness $k_1 = 0.6*k_0$.

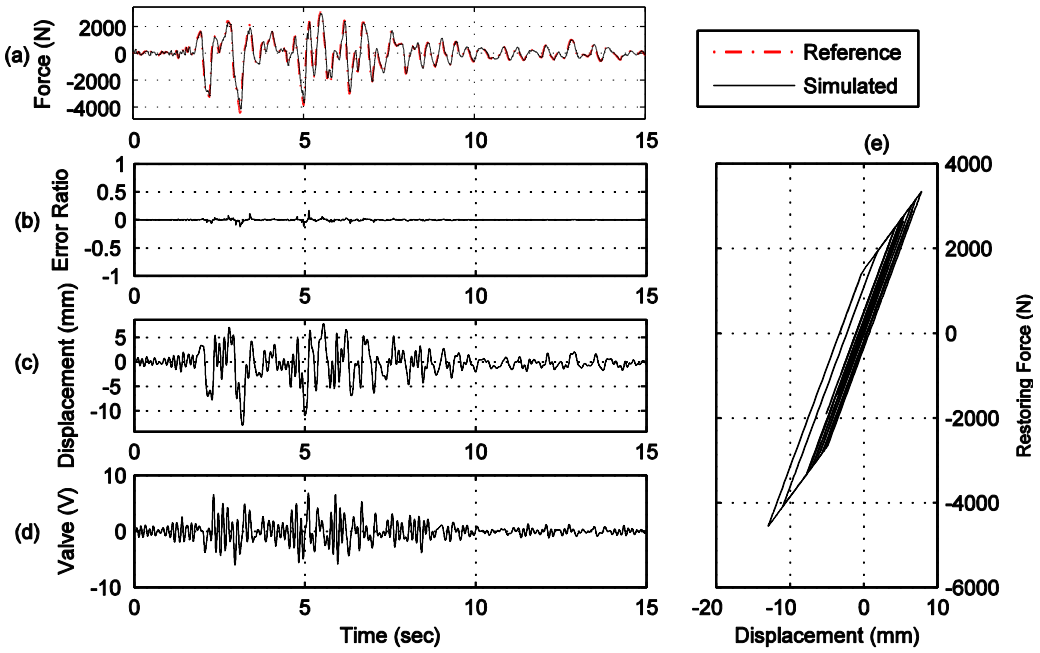

Figure B.68. Yield strength Y_y = 1,500 N, post-yield stiffness $k_1 = 0.5*k_0$.

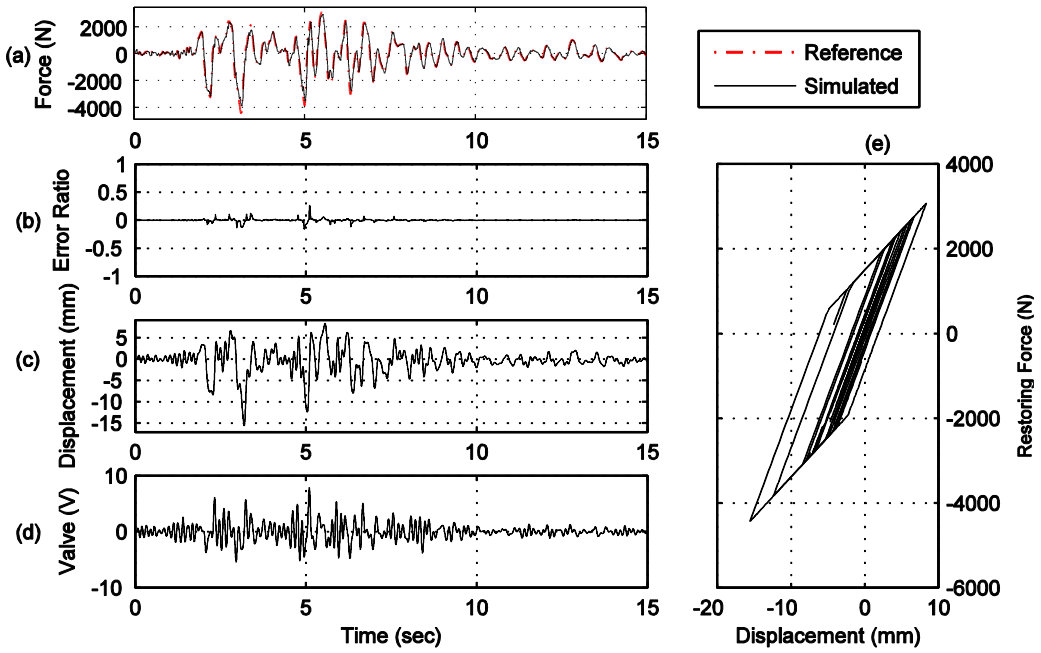

Figure B.69. Yield strength Y_y = 1,500 N, post-yield stiffness $k_1 = 0.4*k_0$.

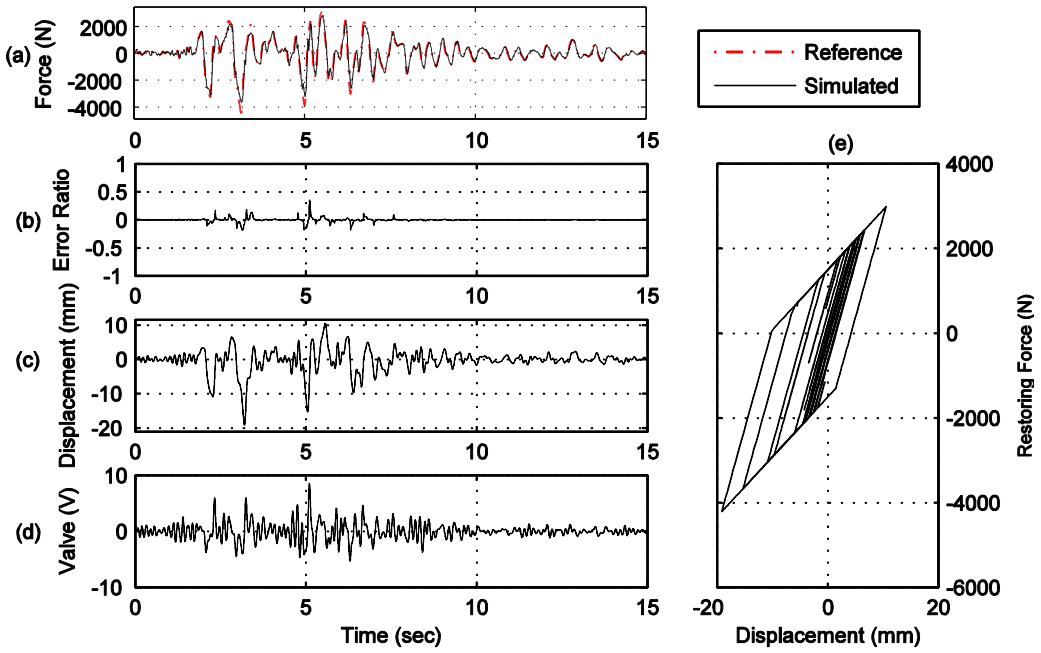

Figure B.70. Yield strength Y_y = 1,500 N, post-yield stiffness $k_1 = 0.3*k_0$.

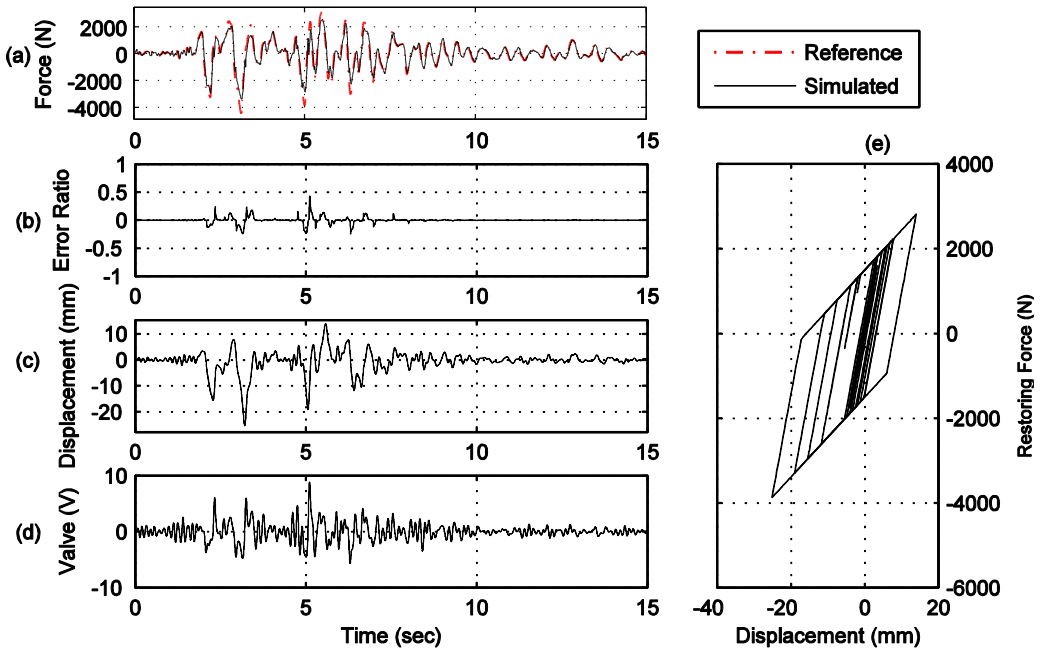

Figure B.71. Yield strength Y_y = 1,500 N, post-yield stiffness $k_1 = 0.2*k_0$.

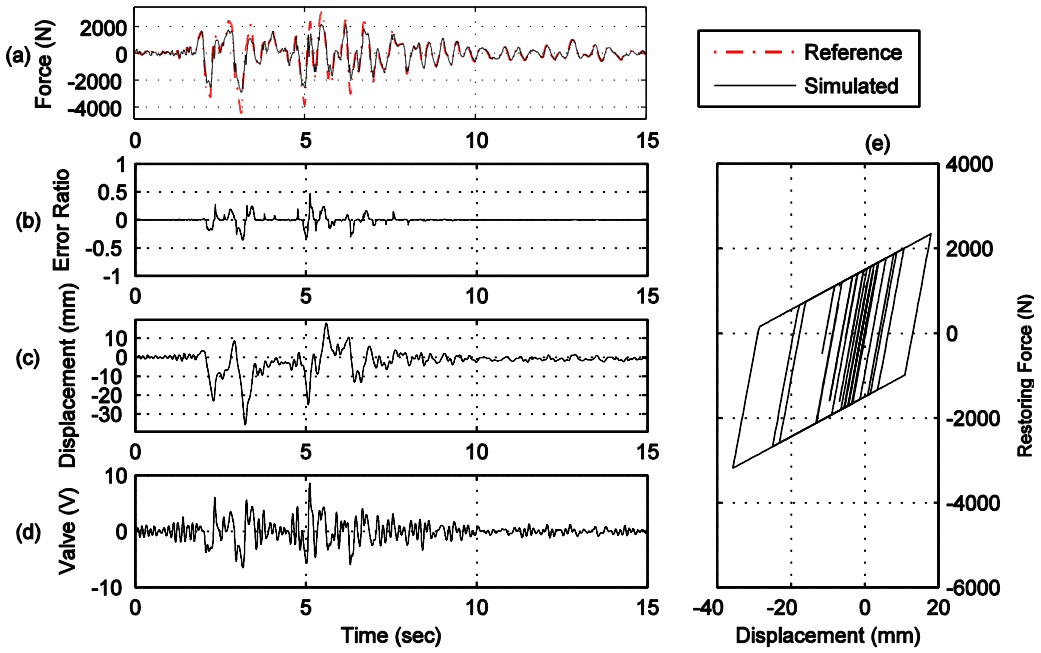

Figure B.72. Yield strength Y_y = 1,500 N, post-yield stiffness $k_1 = 0.1*k_0$.

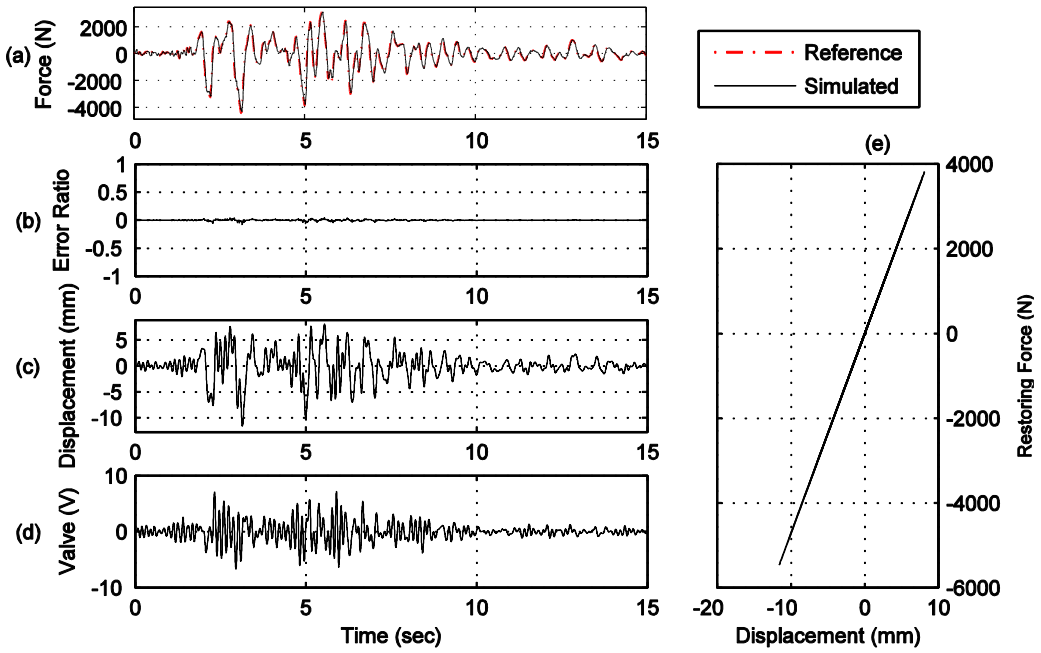

Figure B.73. Yield strength Y_y = 2,000 N, post-yield stiffness $k_1 = 0.9*k_0$.

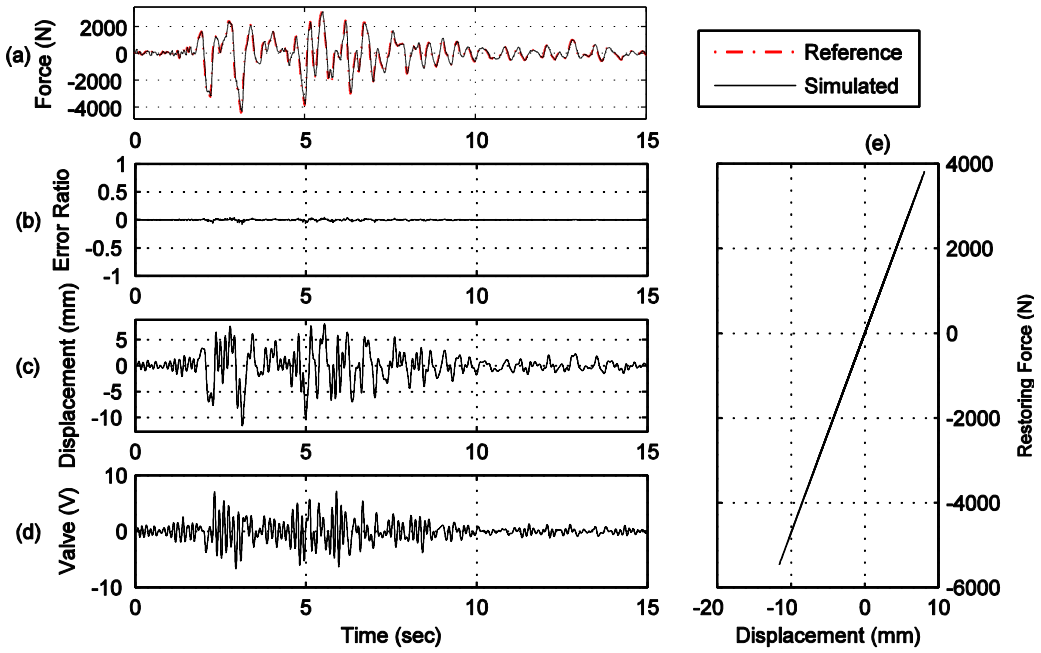

Figure B.74. Yield strength Y_y = 2,000 N, post-yield stiffness $k_1 = 0.8*k_0$.

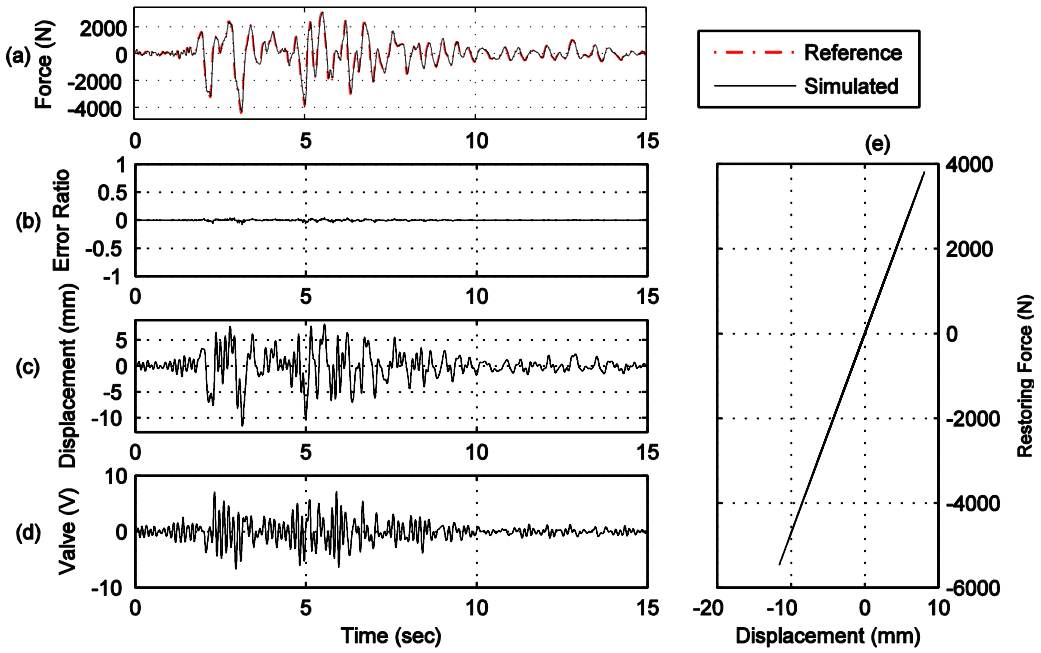

Figure B.75. Yield strength Y_y = 2,000 N, post-yield stiffness $k_1 = 0.7*k_0$.

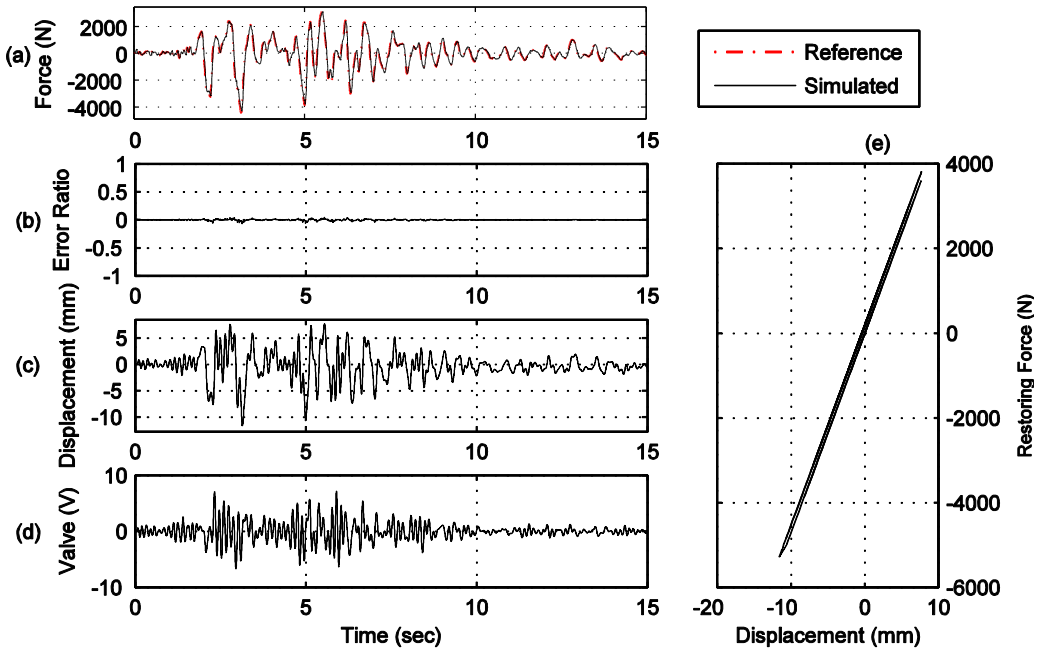

Figure B.76. Yield strength Y_y = 2,000 N, post-yield stiffness $k_1 = 0.6*k_0$.

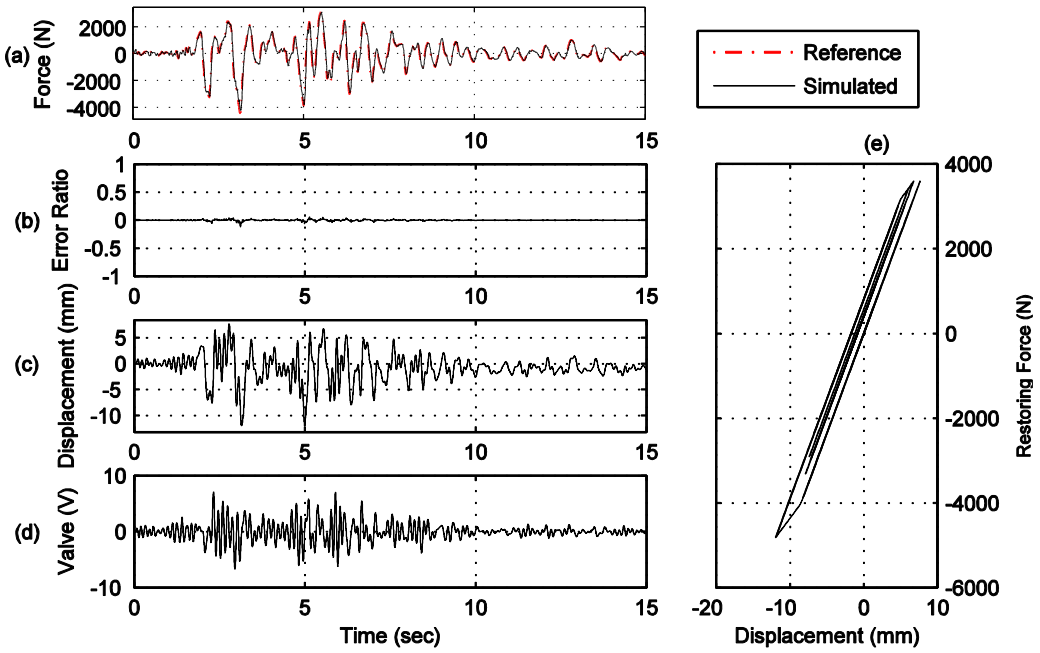

Figure B.77. Yield strength Y_y = 2,000 N, post-yield stiffness $k_1 = 0.5*k_0$.

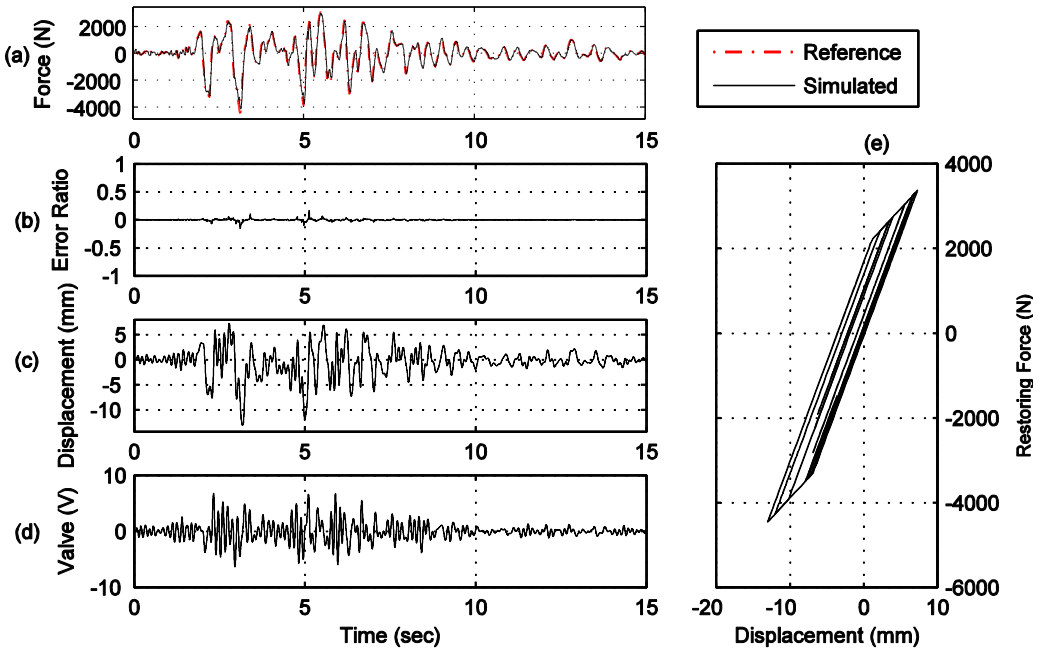

Figure B.78. Yield strength Y_y = 2,000 N, post-yield stiffness $k_1 = 0.4*k_0$.

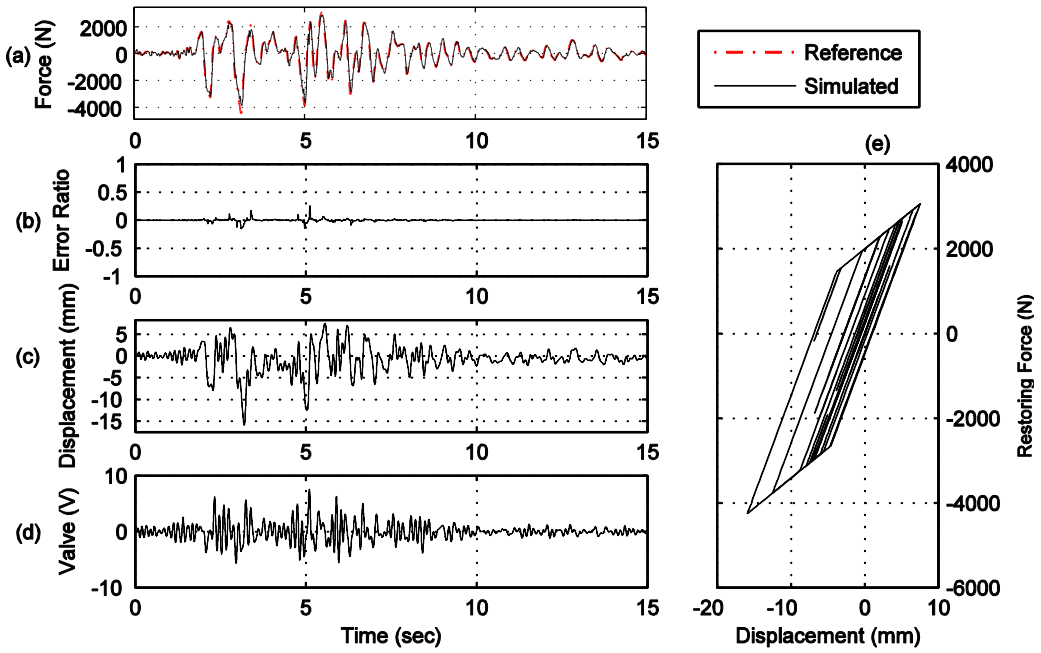

Figure B.79. Yield strength Y_y = 2,000 N, post-yield stiffness $k_1 = 0.3*k_0$.

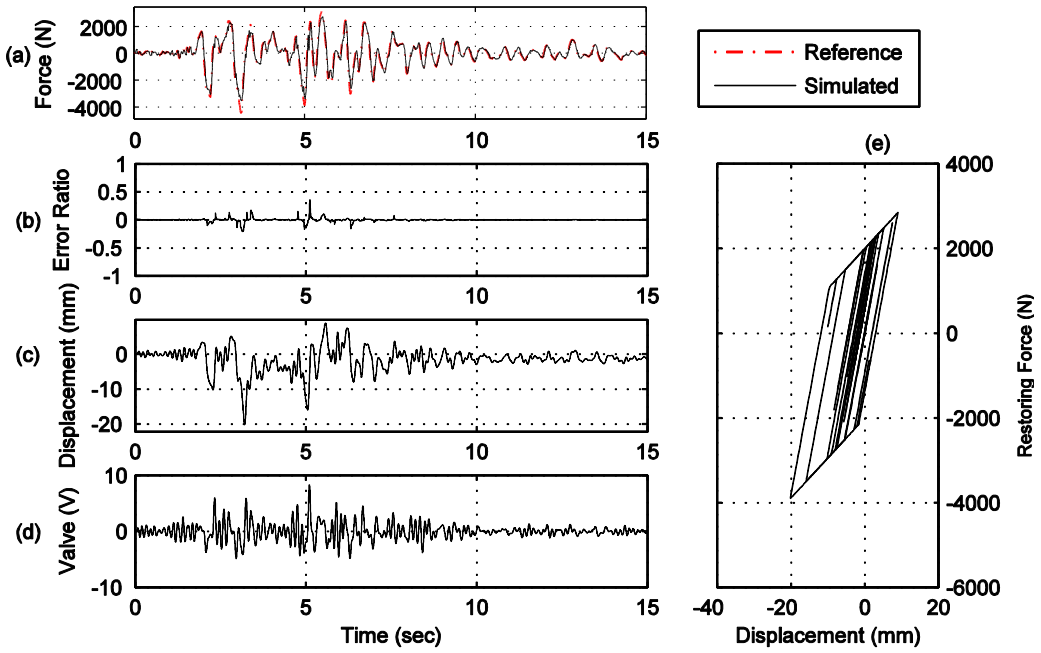

Figure B.80. Yield strength Y_y = 2,000 N, post-yield stiffness $k_1 = 0.2*k_0$.

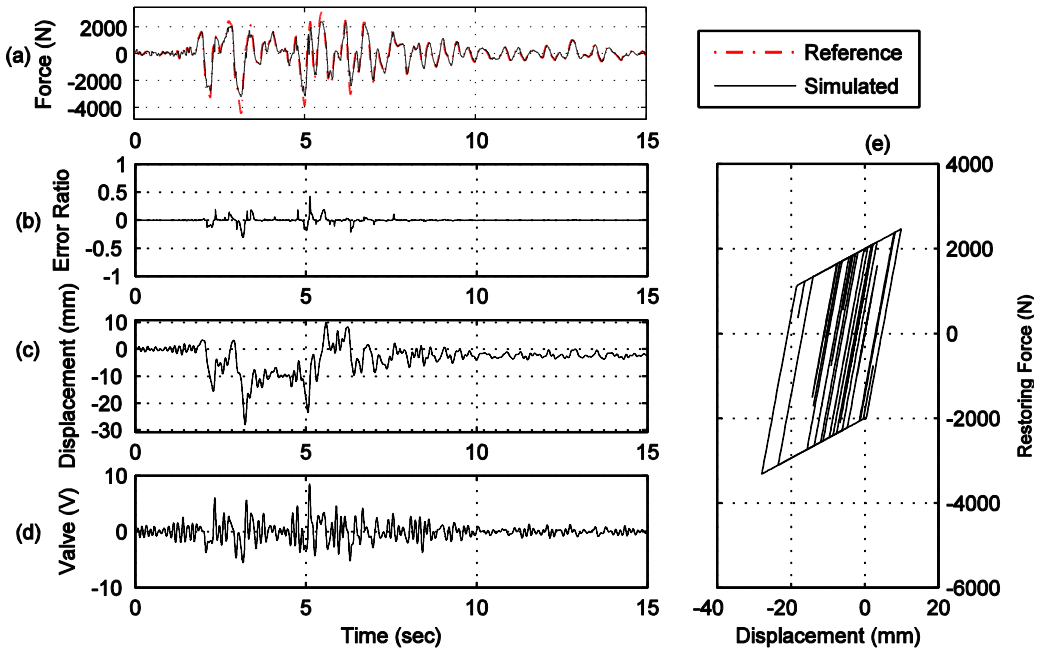

Figure B.81. Yield strength Y_y = 2,000 N, post-yield stiffness $k_1 = 0.1*k_0$.

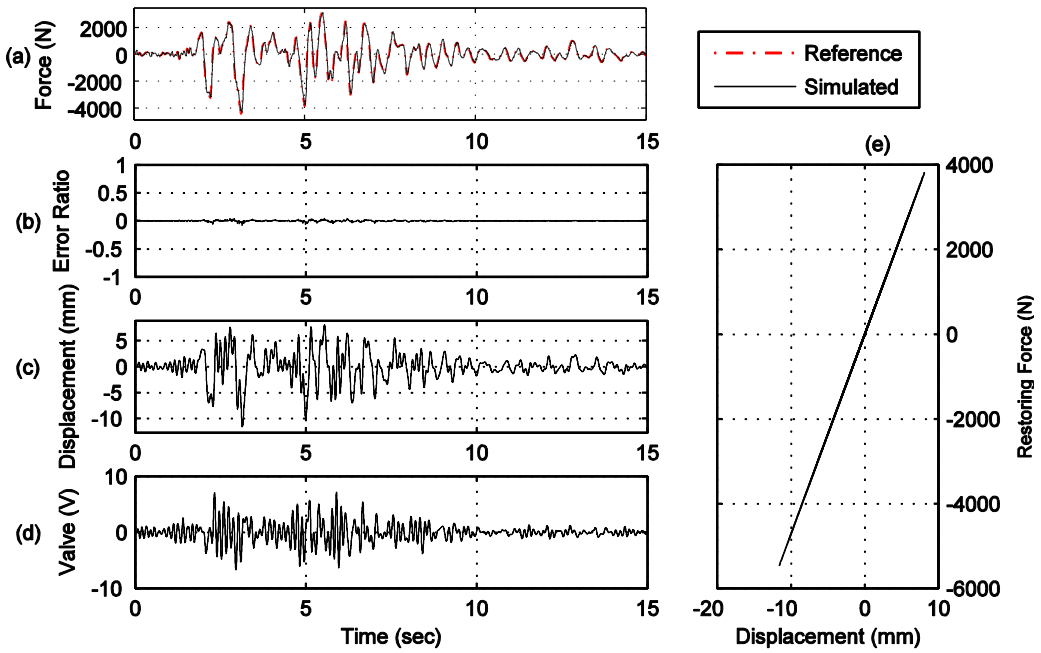

Figure B.82. Yield strength Y_y = 2,500 N, post-yield stiffness $k_1 = 0.9*k_0$.

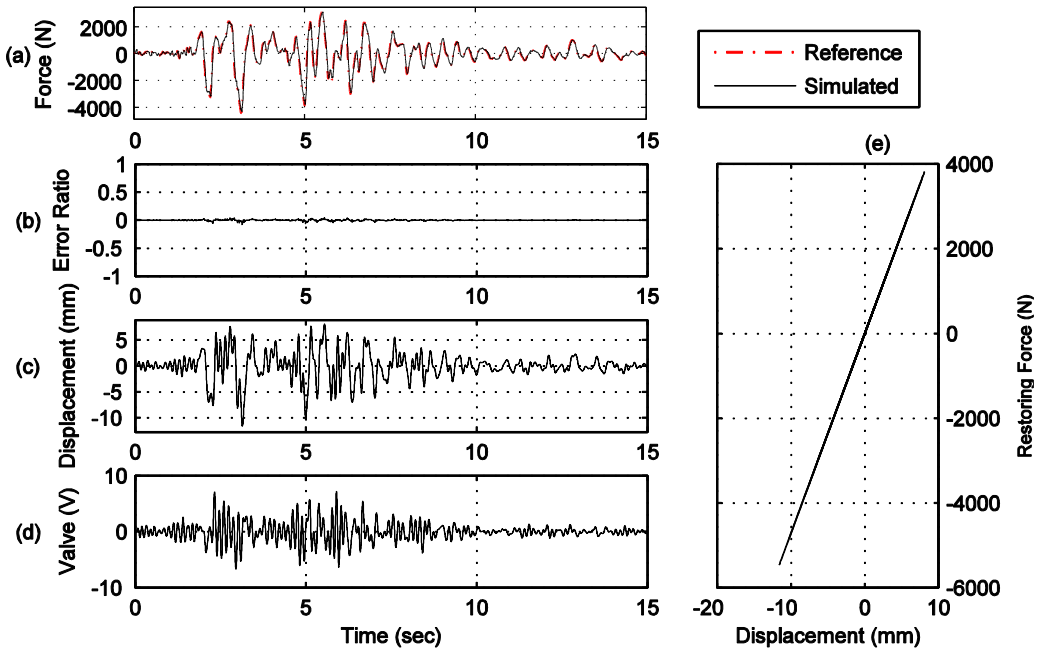

Figure B.83. Yield strength Y_y = 2,500 N, post-yield stiffness $k_1 = 0.8*k_0$.

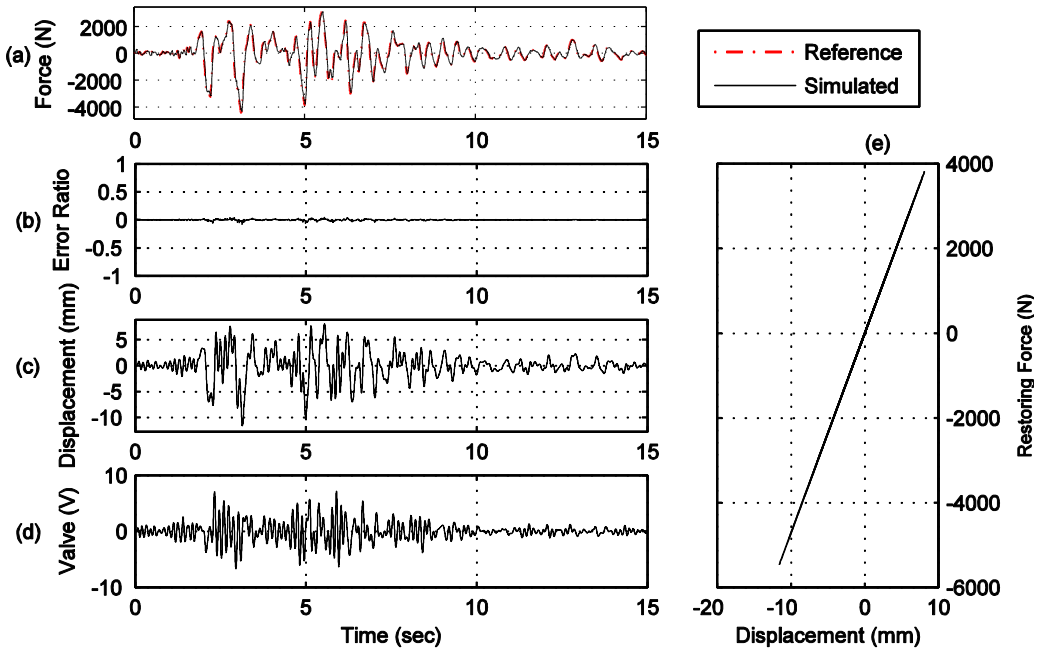

Figure B.84. Yield strength Y_y = 2,500 N, post-yield stiffness $k_1 = 0.7*k_0$.

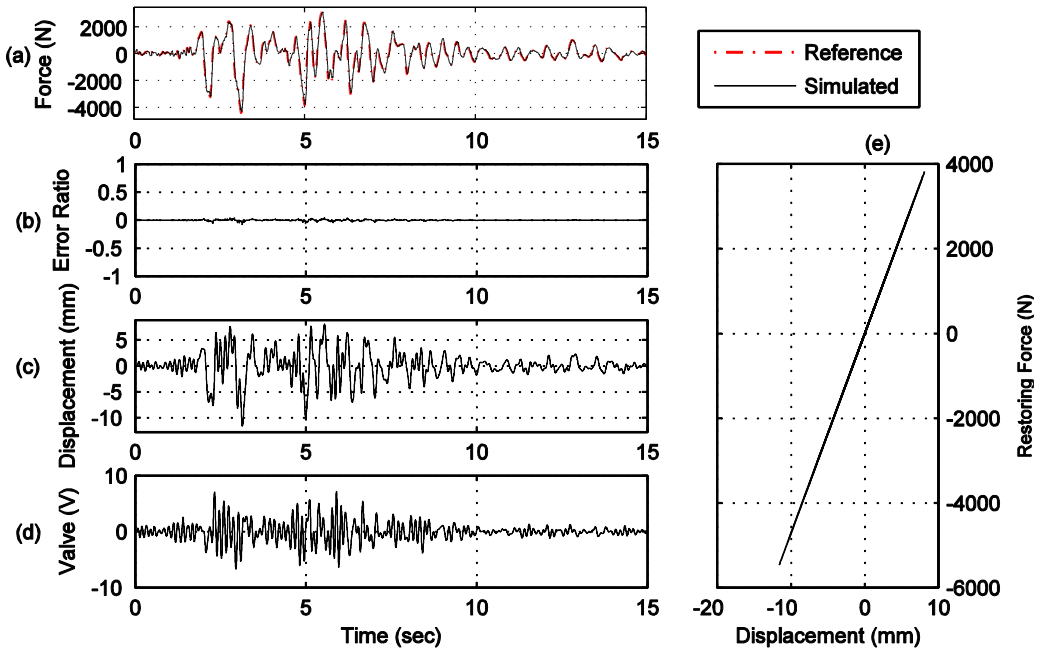

Figure B.85. Yield strength Y_y = 2,500 N, post-yield stiffness $k_1 = 0.6*k_0$.

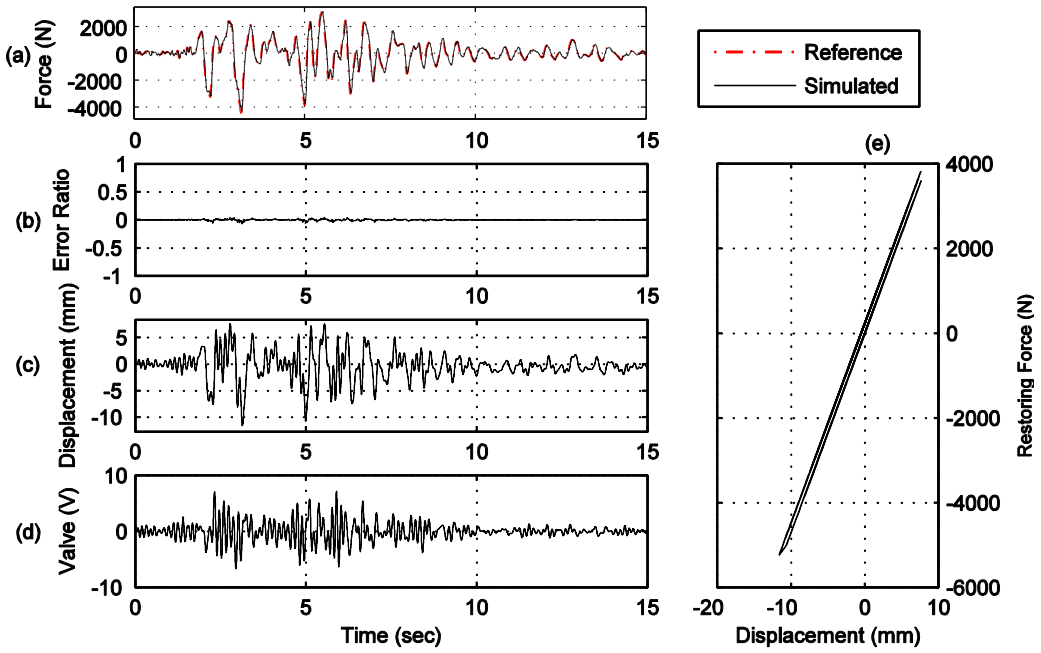

Figure B.86. Yield strength Y_y = 2,500 N, post-yield stiffness $k_1 = 0.5*k_0$.

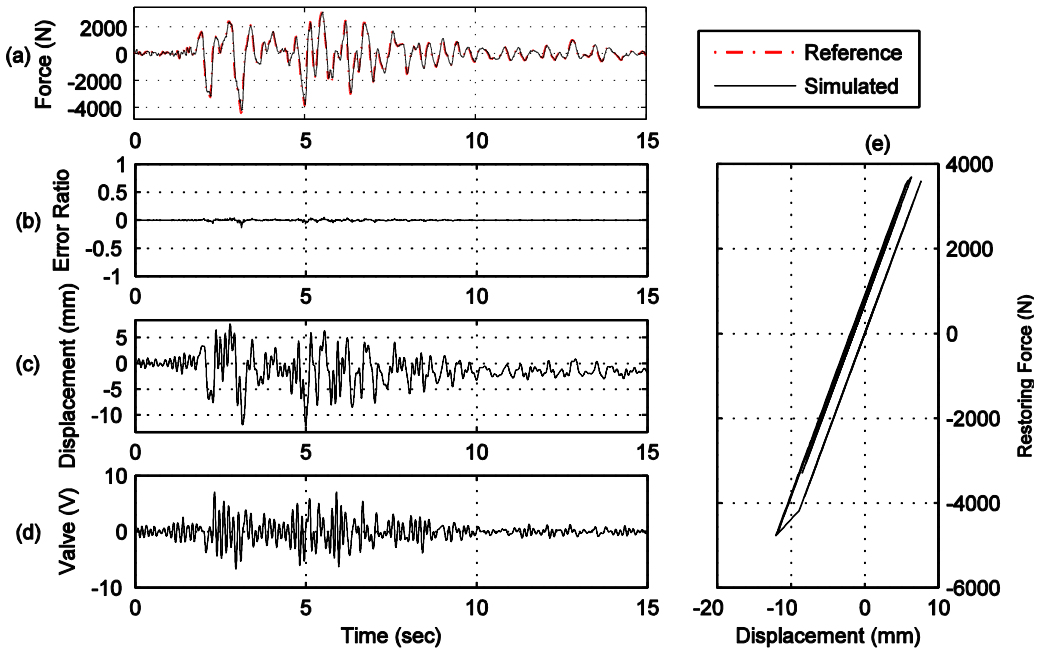

Figure B.87. Yield strength Y_y = 2,500 N, post-yield stiffness $k_1 = 0.4*k_0$.

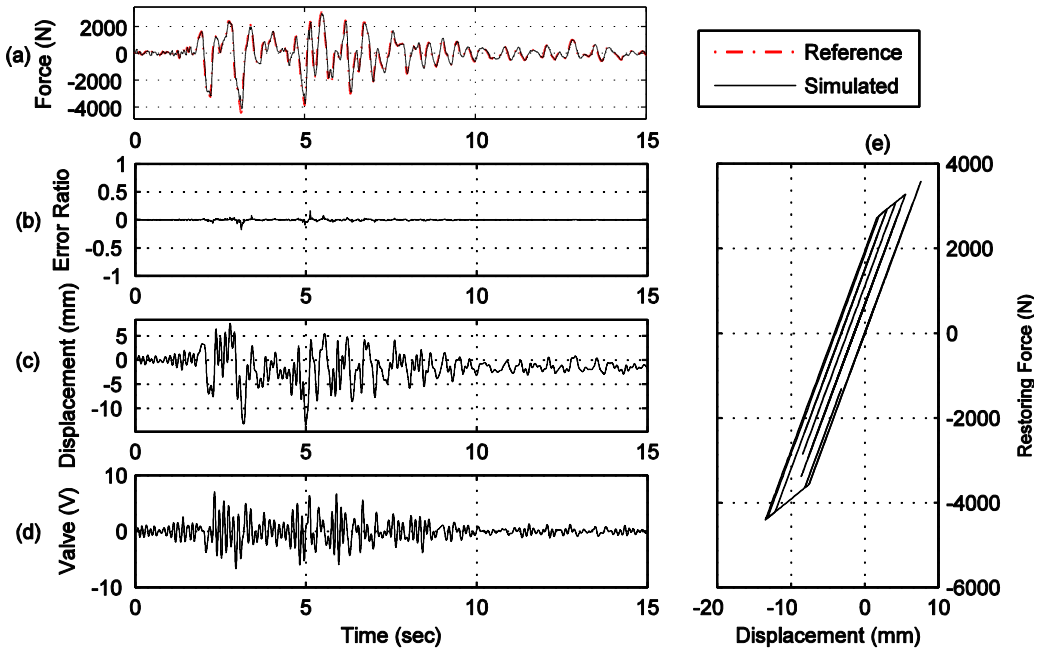

Figure B.88. Yield strength Y_y = 2,500 N, post-yield stiffness $k_1 = 0.3*k_0$.

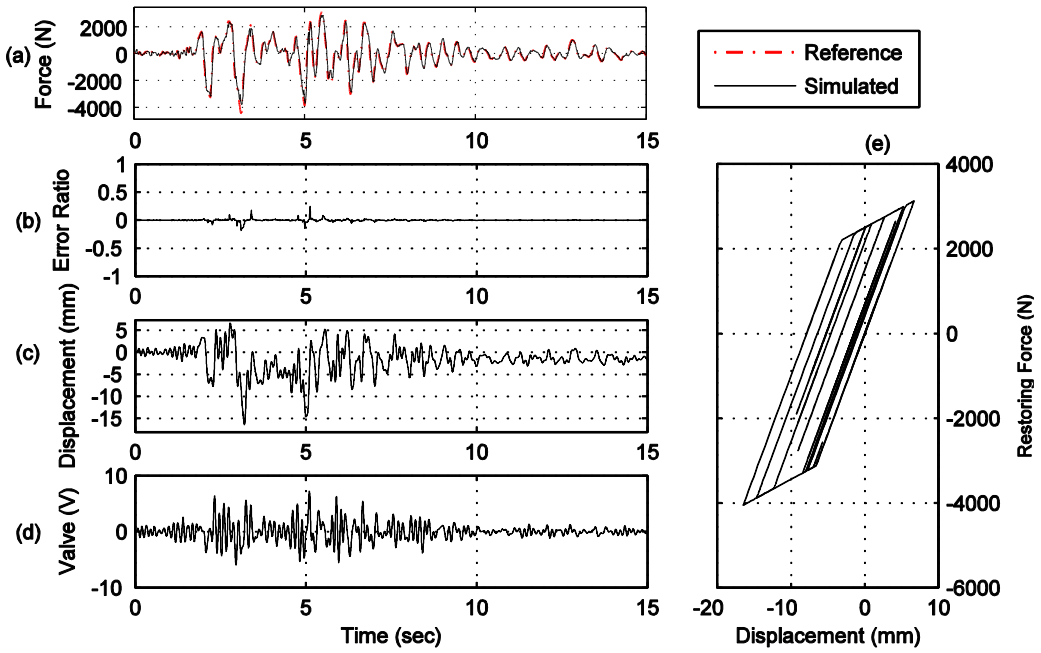

Figure B.89. Yield strength Y_y = 2,500 N, post-yield stiffness $k_1 = 0.2*k_0$.

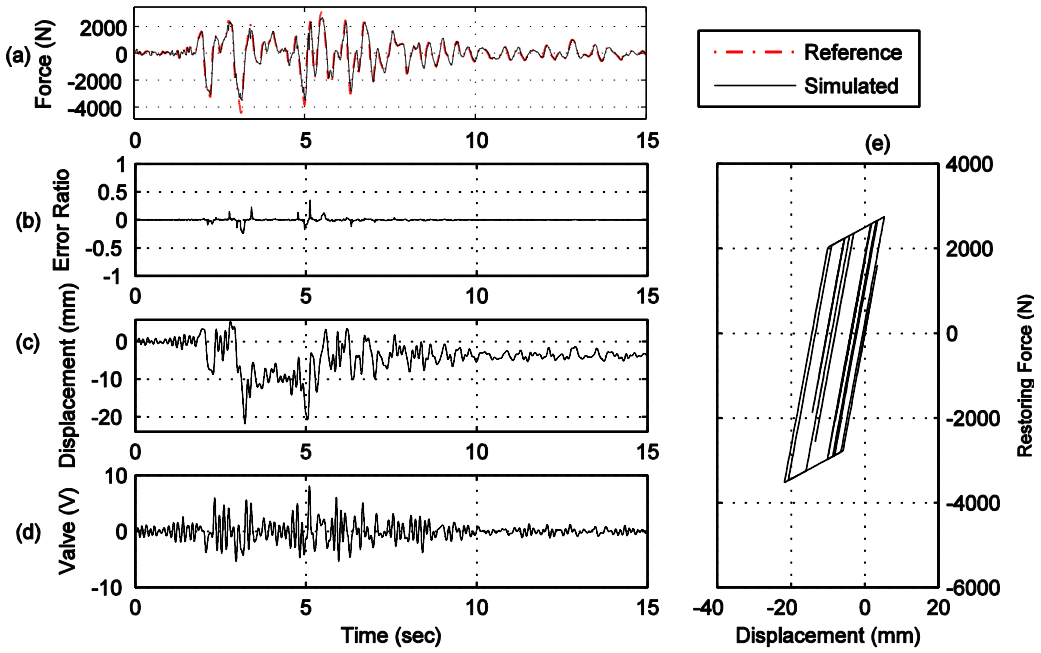

Figure B.90. Yield strength Y_y = 2,500 N, post-yield stiffness $k_1 = 0.1*k_0$.

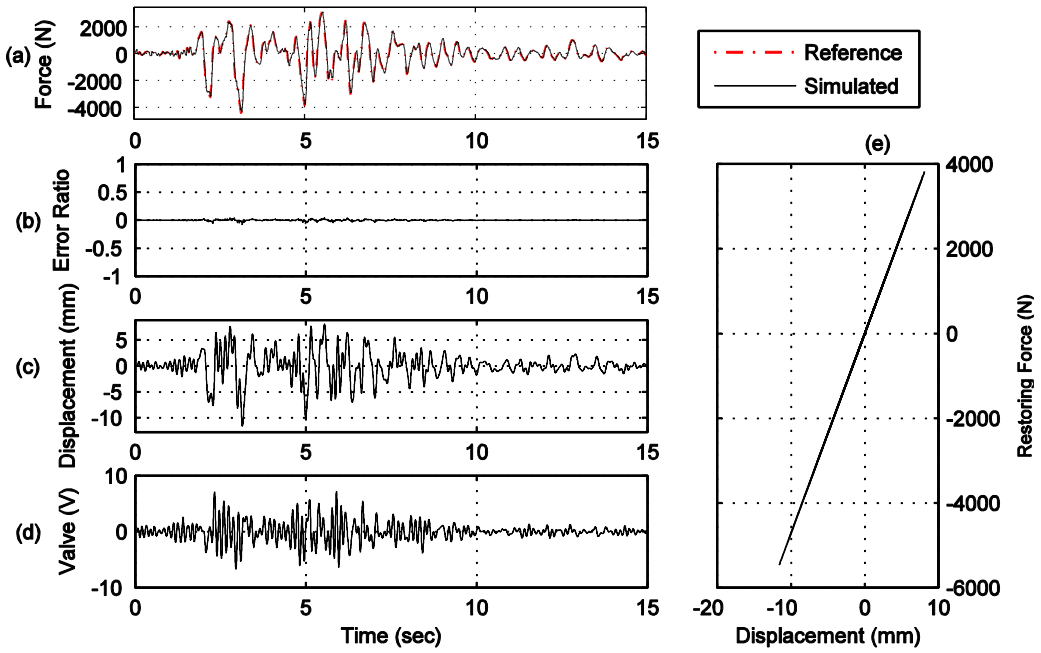

Figure B.91. Yield strength Y_y = 3,000 N, post-yield stiffness $k_1 = 0.9*k_0$.

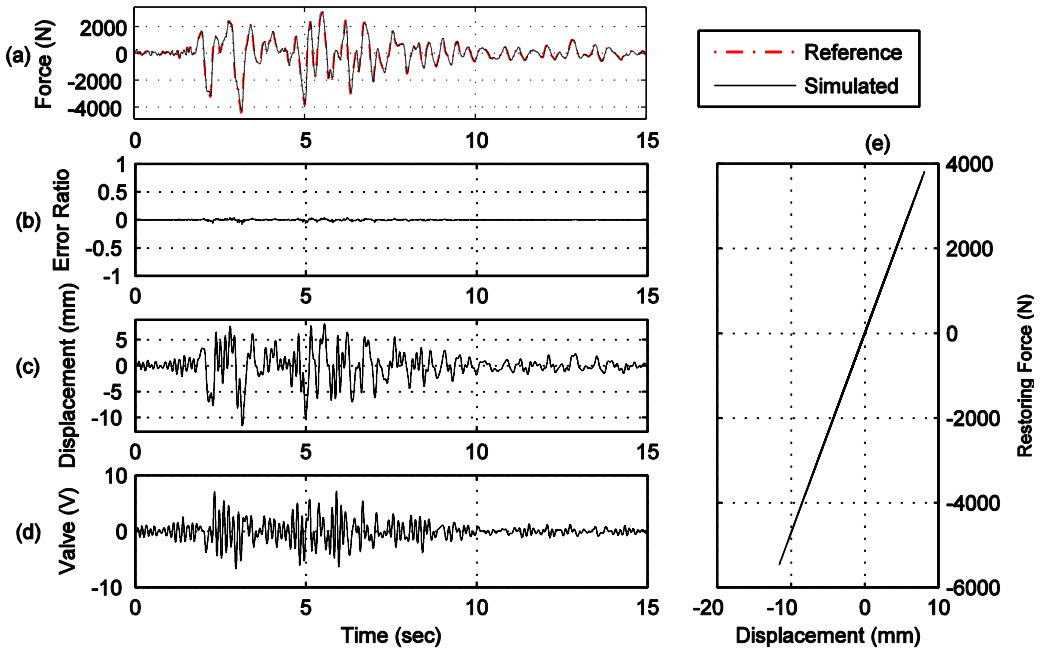

Figure B.92. Yield strength Y_y = 3,000 N, post-yield stiffness $k_1 = 0.8*k_0$.

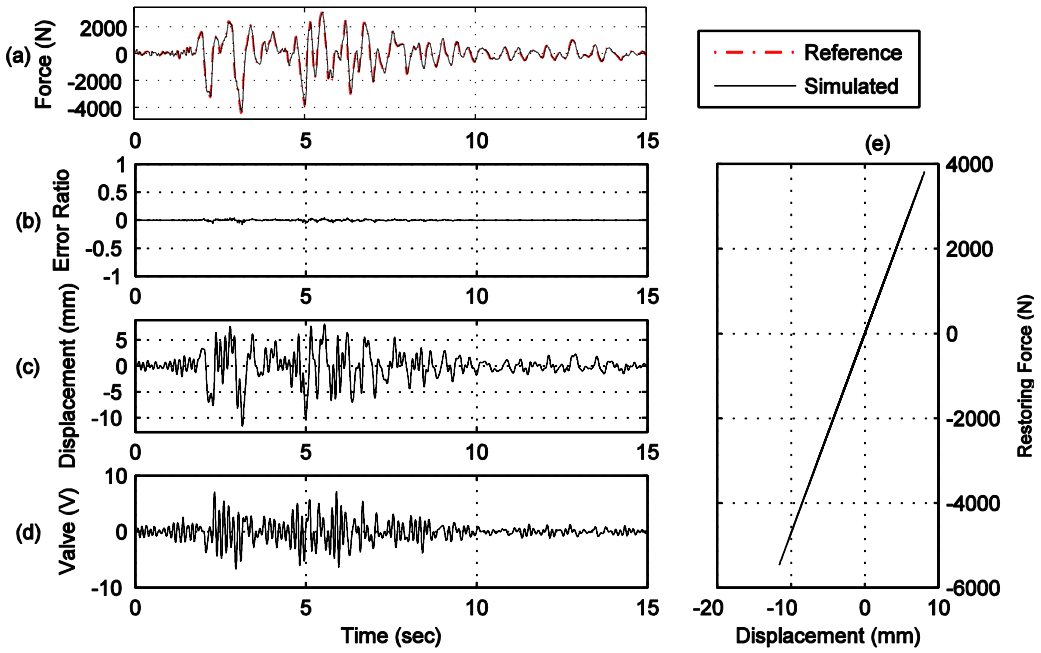

Figure B.93. Yield strength Y_y = 3,000 N, post-yield stiffness $k_1 = 0.7*k_0$.

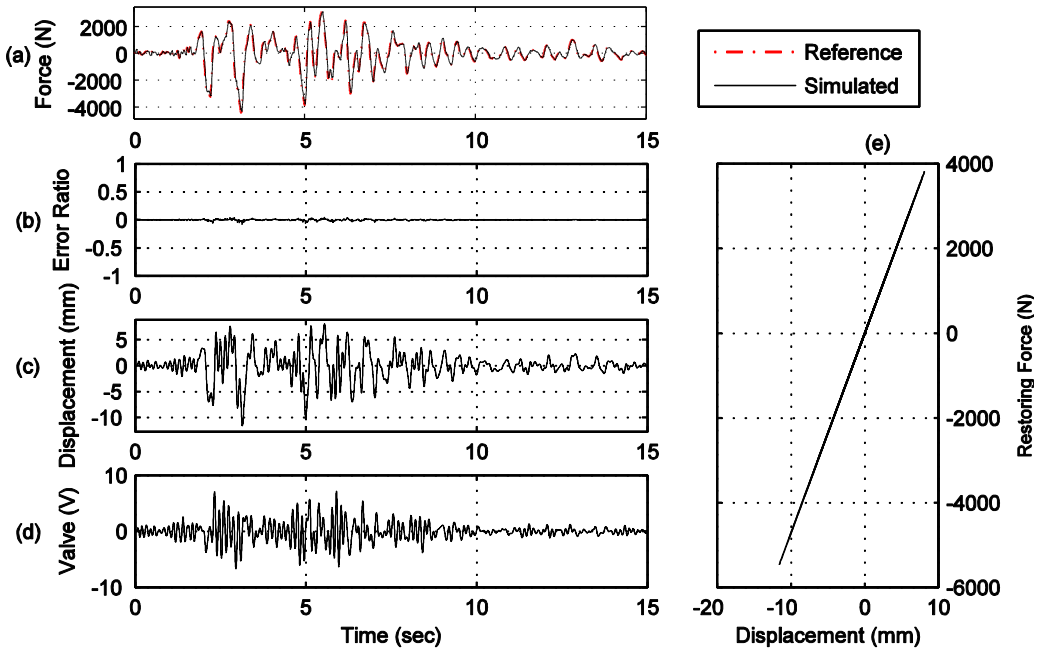

Figure B.94. Yield strength Y_y = 3,000 N, post-yield stiffness $k_1 = 0.6*k_0$.

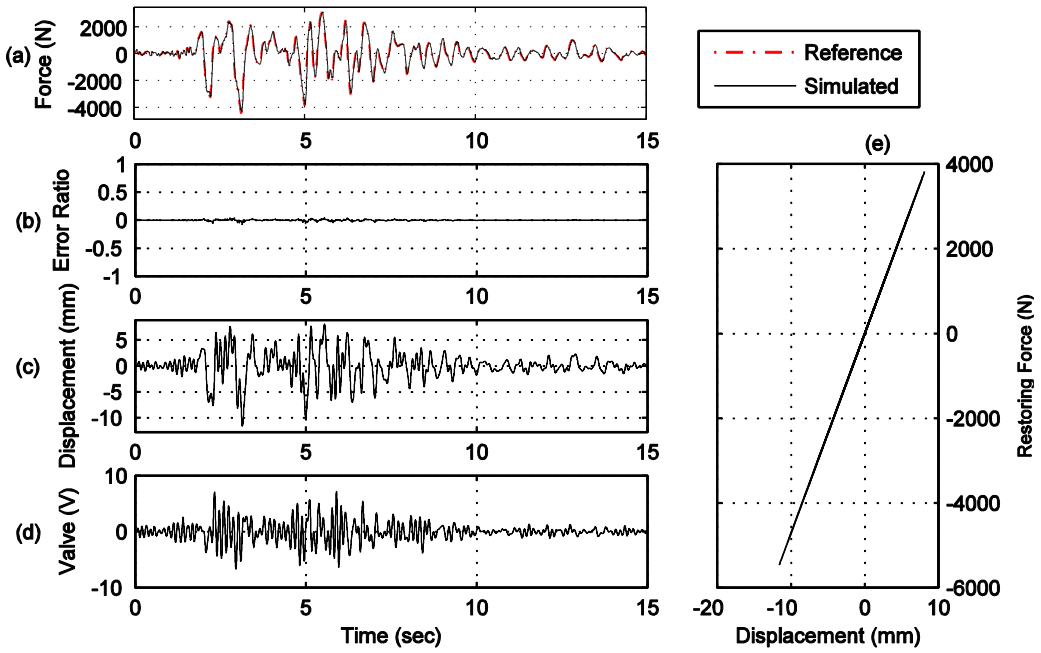

Figure B.95. Yield strength Y_y = 3,000 N, post-yield stiffness $k_1 = 0.5*k_0$.

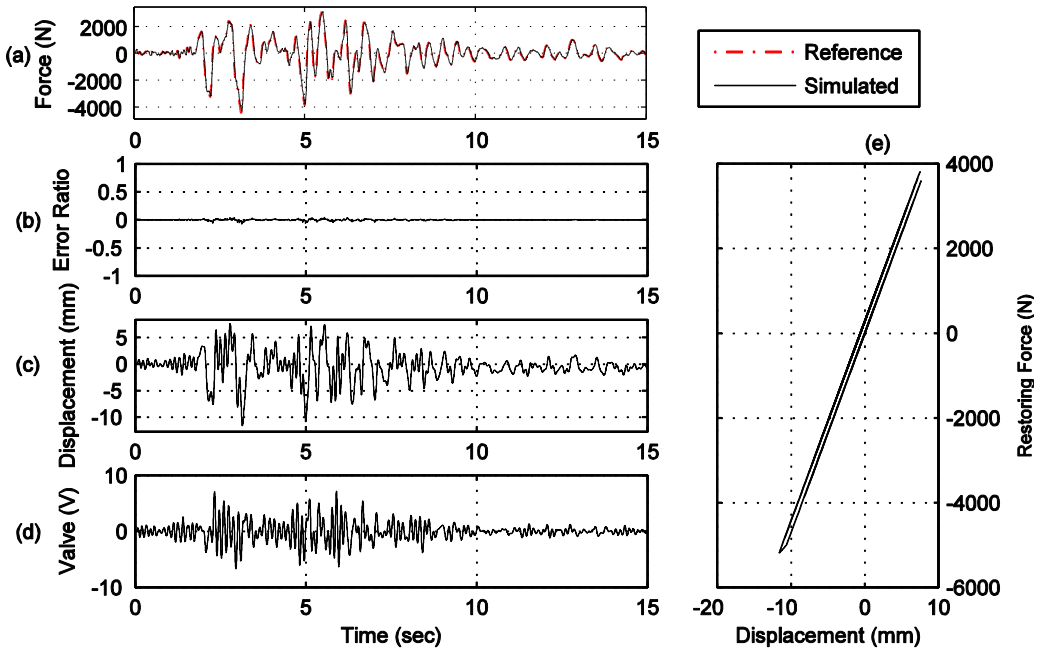

Figure B.96. Yield strength Y_y = 3,000 N, post-yield stiffness $k_1 = 0.4*k_0$.

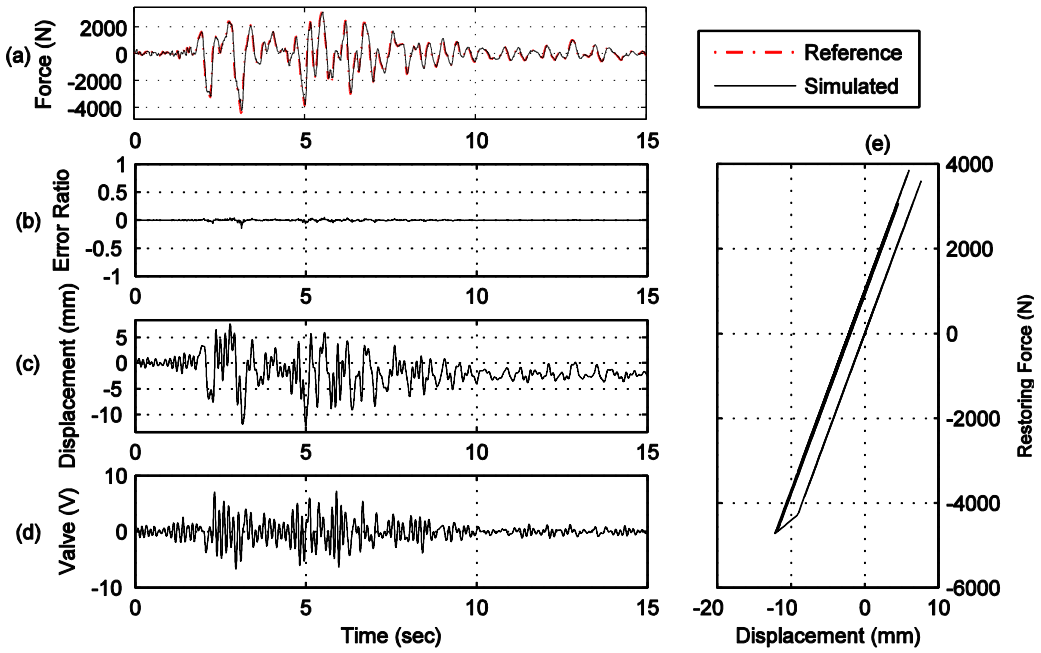

Figure B.97. Yield strength Y_y = 3,000 N, post-yield stiffness $k_1 = 0.3*k_0$.

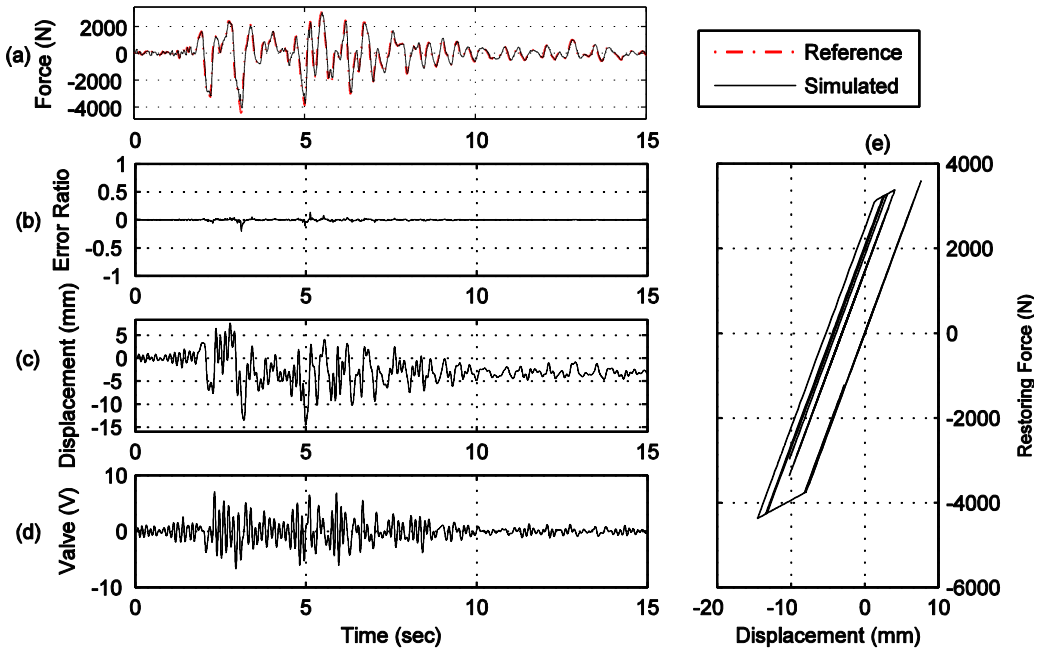

Figure B.98. Yield strength Y_y = 3,000 N, post-yield stiffness $k_1 = 0.2*k_0$.

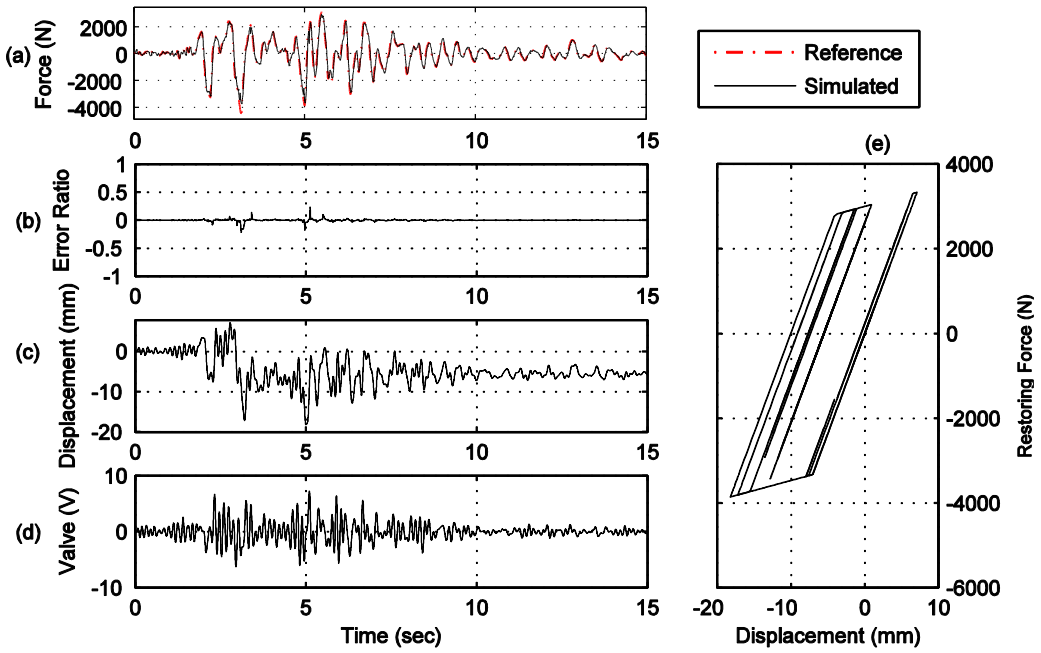

Figure B.99. Yield strength Y_y = 3,000 N, post-yield stiffness $k_1 = 0.1*k_0$.

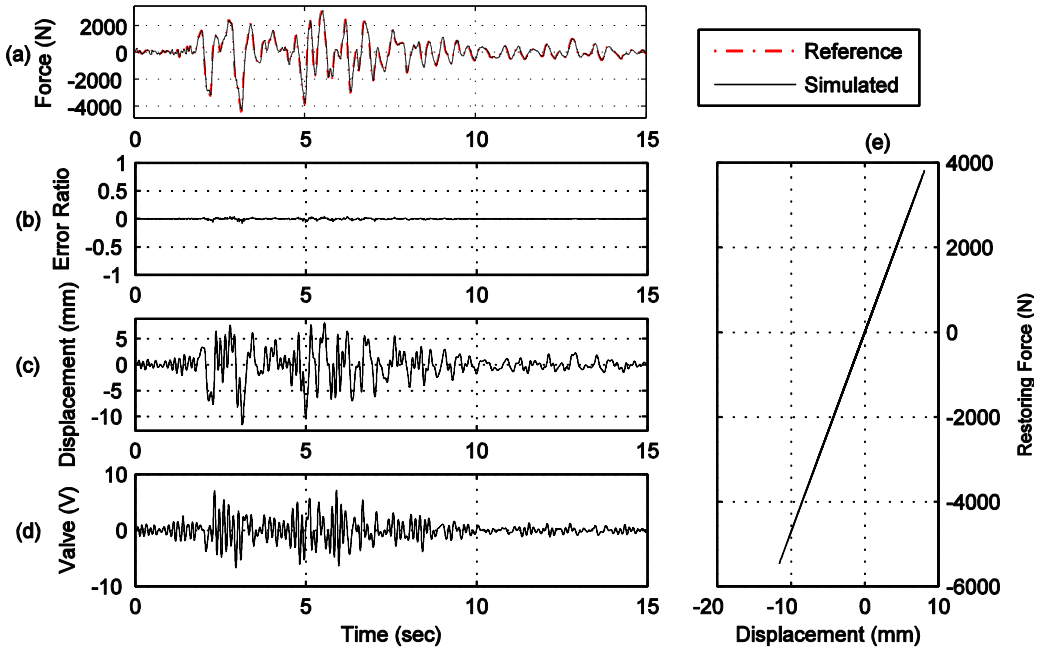

Figure B.100. Yield strength Y_y = 3,500 N, post-yield stiffness $k_1 = 0.9*k_0$.

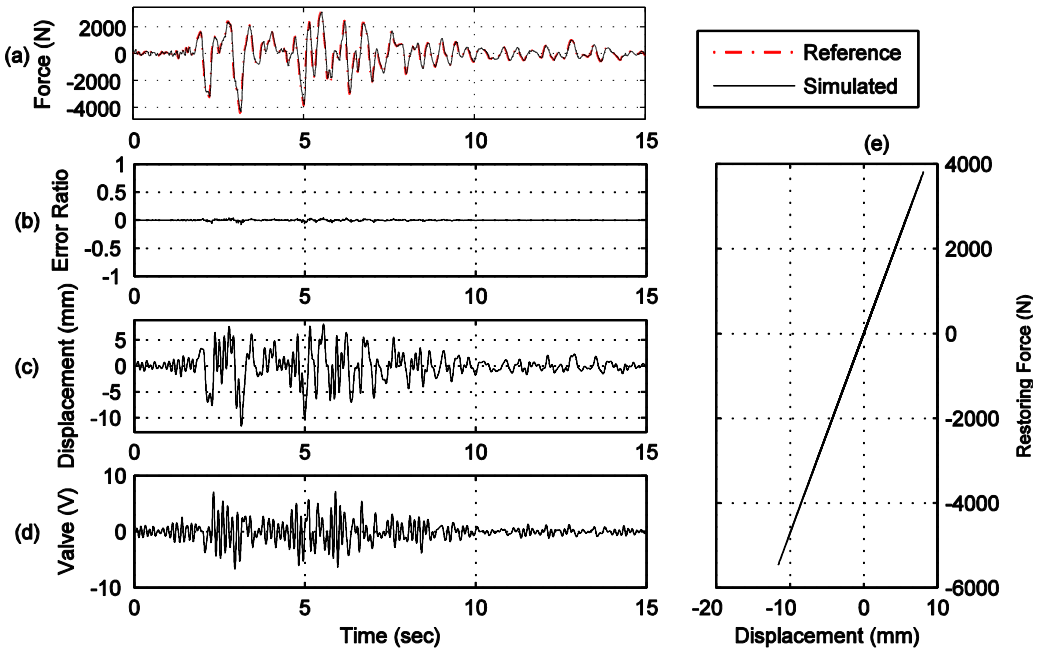

Figure B.101. Yield strength Y_y = 3,500 N, post-yield stiffness $k_1 = 0.8*k_0$.

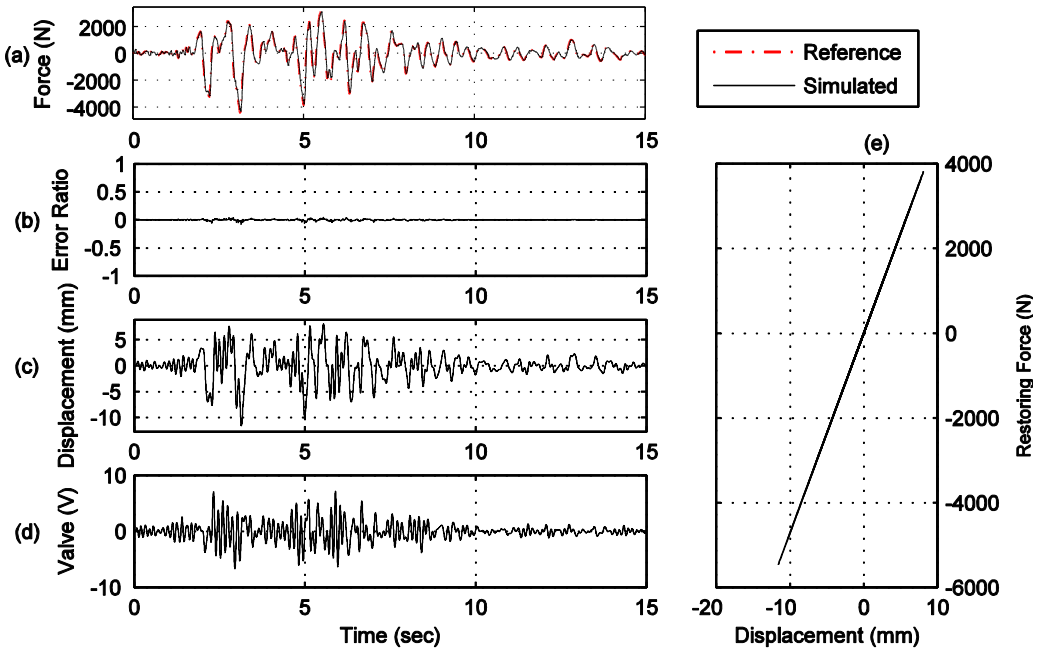

Figure B.102. Yield strength Y_y = 3,500 N, post-yield stiffness $k_1 = 0.7*k_0$.

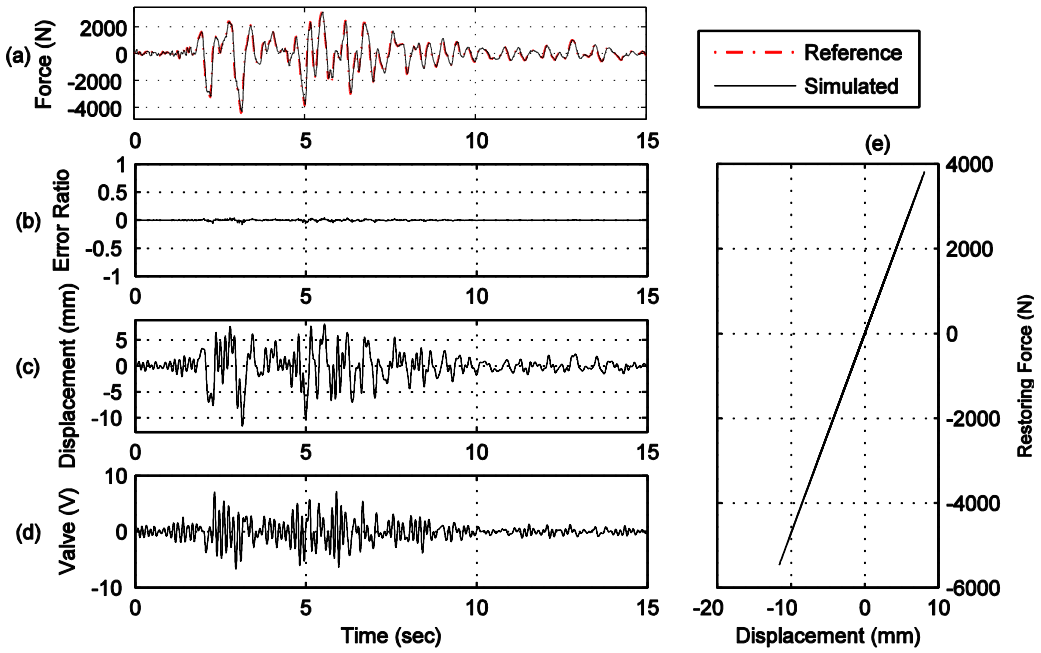

Figure B.103. Yield strength Y_y = 3,500 N, post-yield stiffness $k_1 = 0.6*k_0$.

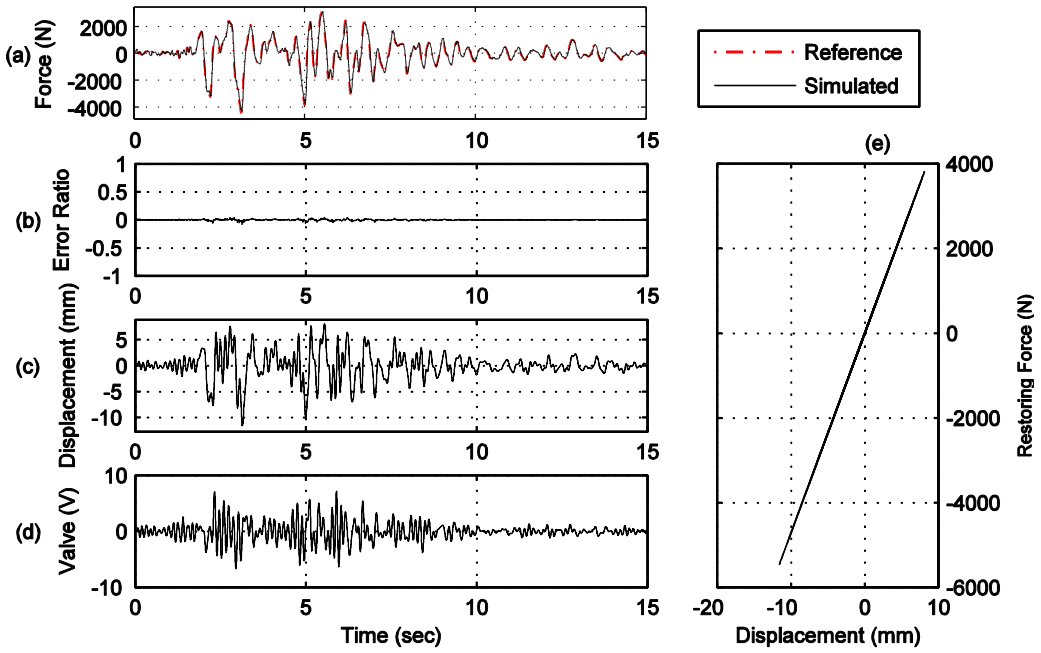

Figure B.104. Yield strength Y_y = 3,500 N, post-yield stiffness $k_1 = 0.5*k_0$.

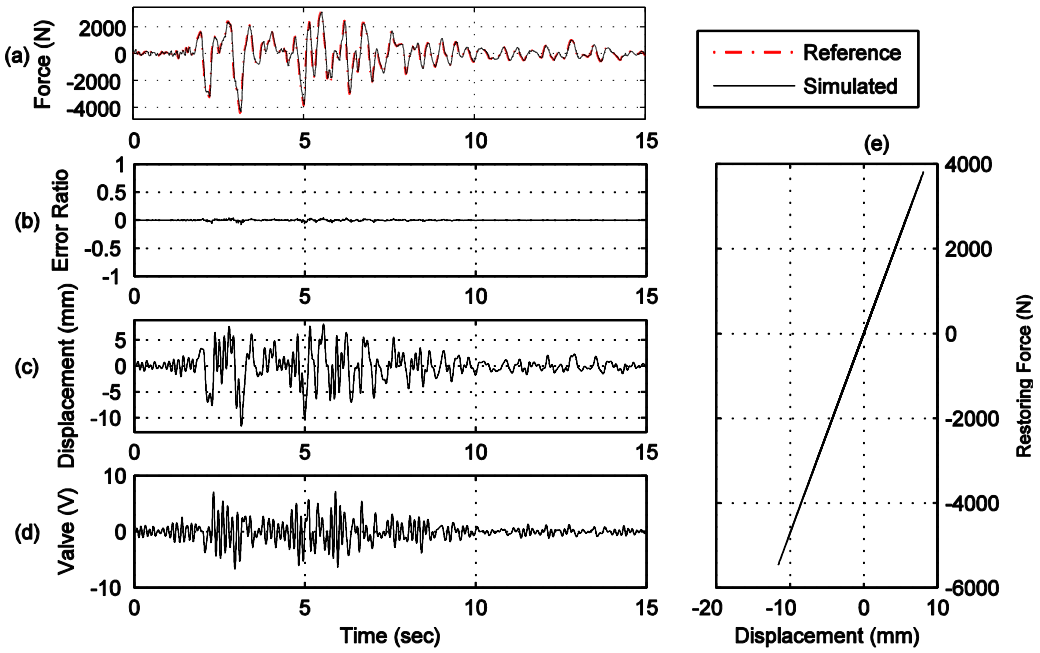

Figure B.105. Yield strength Y_y = 3,500 N, post-yield stiffness $k_1 = 0.4*k_0$.

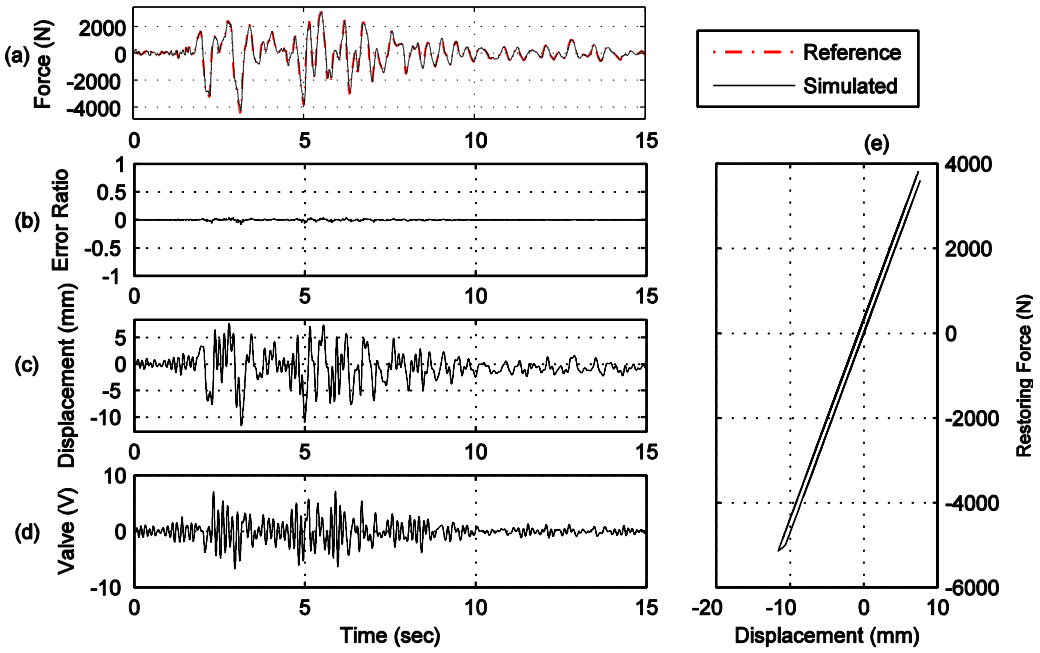

Figure B.106. Yield strength Y_y = 3,500 N, post-yield stiffness $k_1 = 0.3*k_0$.

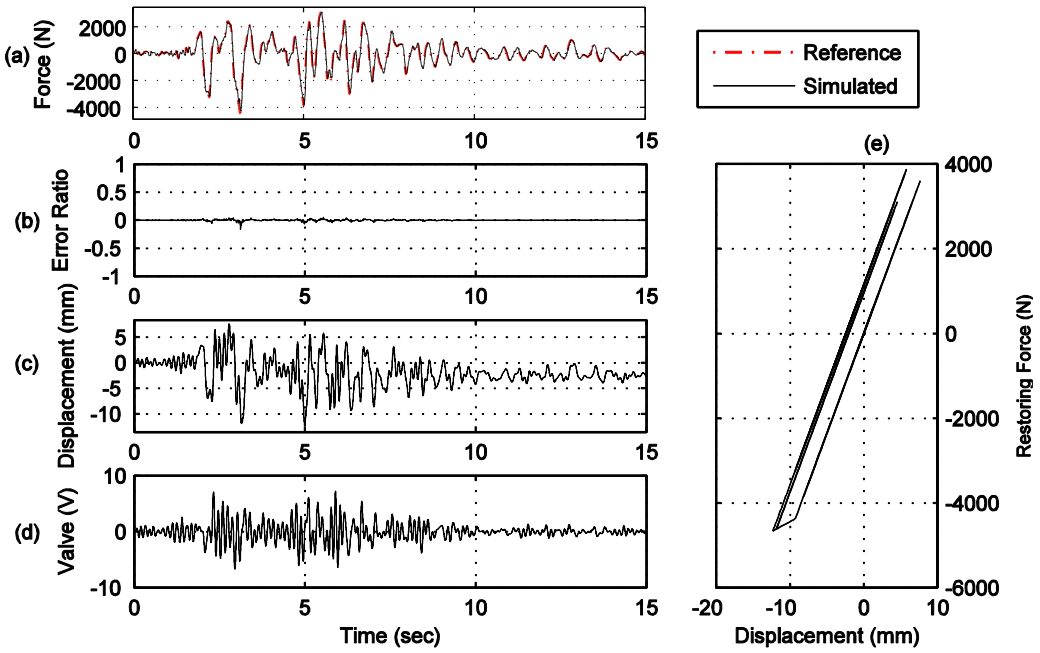

Figure B.107. Yield strength Y_y = 3,500 N, post-yield stiffness $k_1 = 0.2*k_0$.

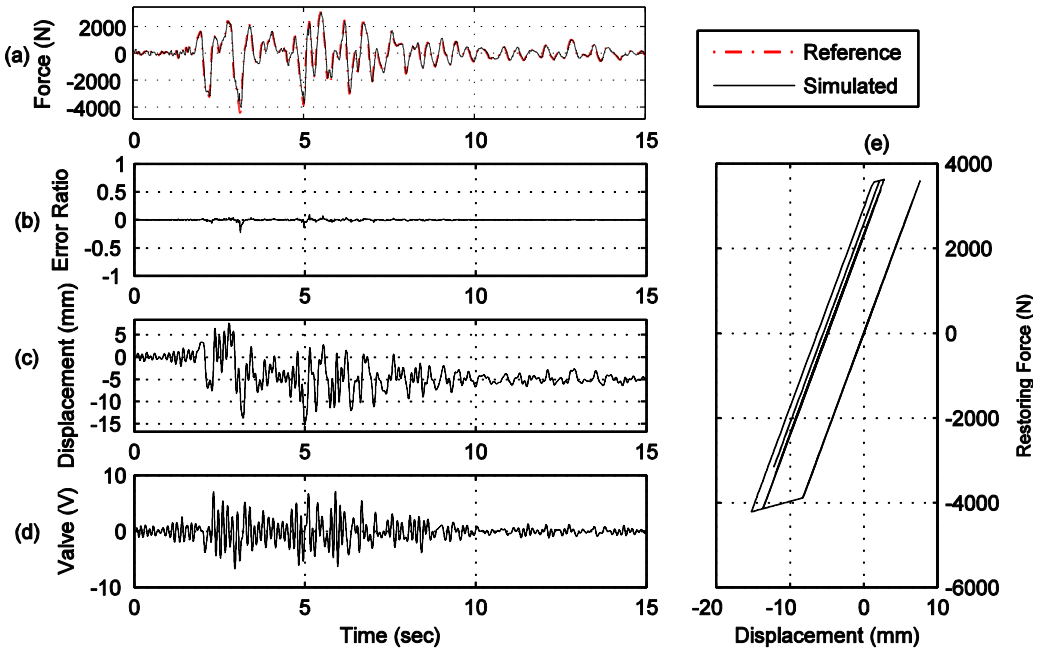

Figure B.108. Yield strength Y_y = 3,500 N, post-yield stiffness $k_1 = 0.1*k_0$.

Appendix C

Computational EFT Results for Bilinear Hysteretic Pinching Model

Rigid Base

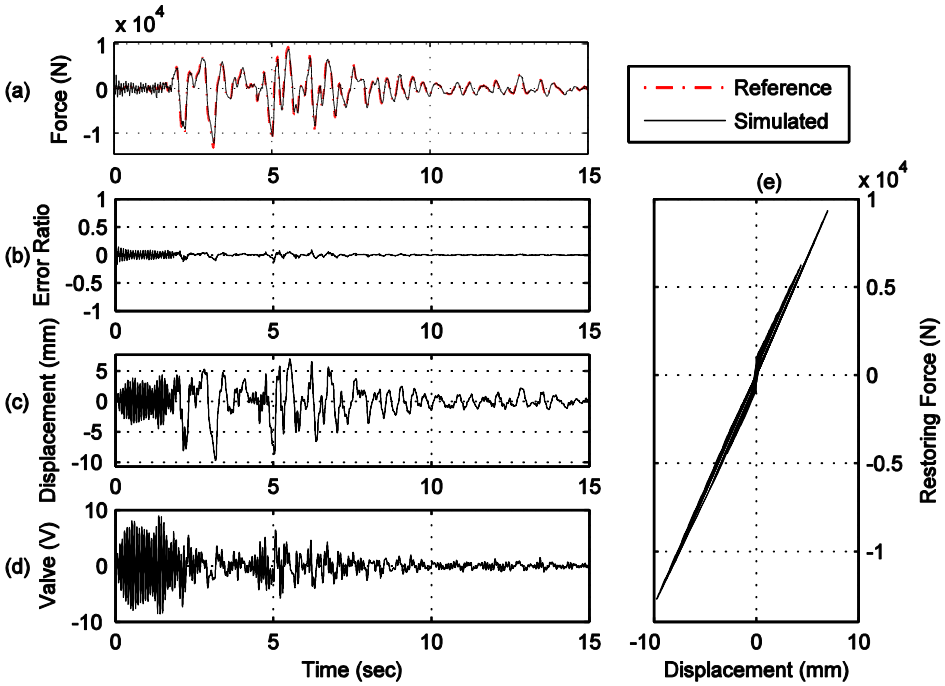

Figure C.1. Yield strength Y_y = 1,000 N, post-yield stiffness $k_1 = 0.9*k_0$.

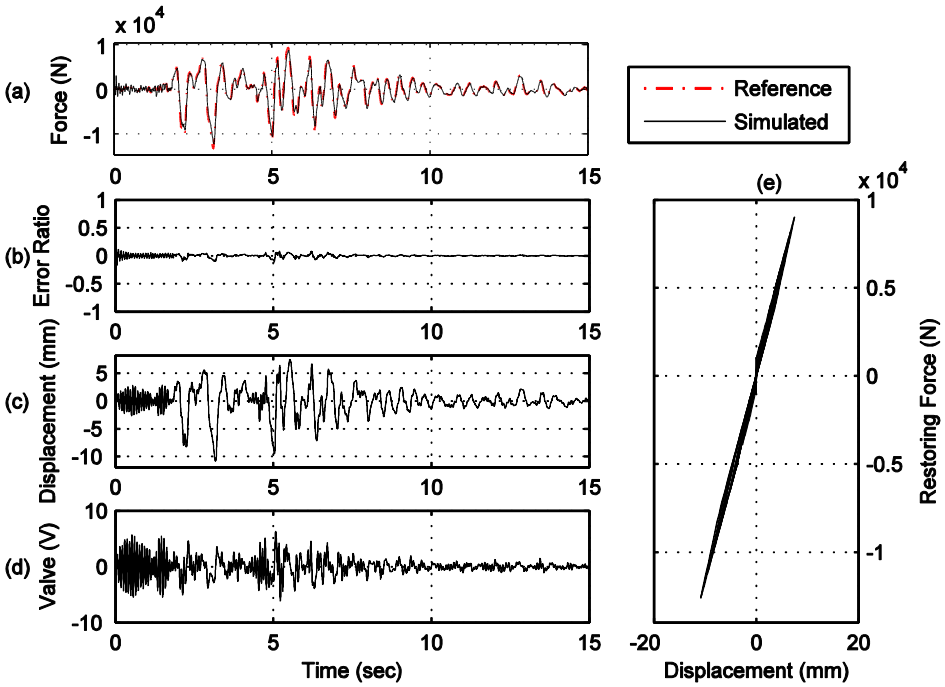

Figure C.2. Yield strength Y_y = 1,000 N, post-yield stiffness $k_1 = 0.8*k_0$.

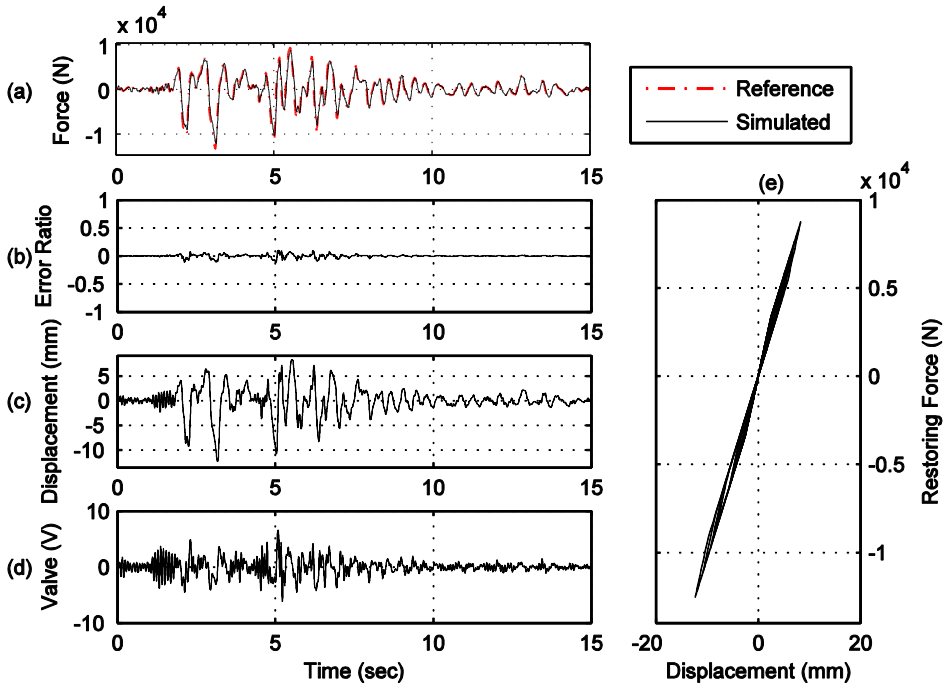

Figure C.3. Yield strength Y_y = 1,000 N, post-yield stiffness $k_1 = 0.7*k_0$.

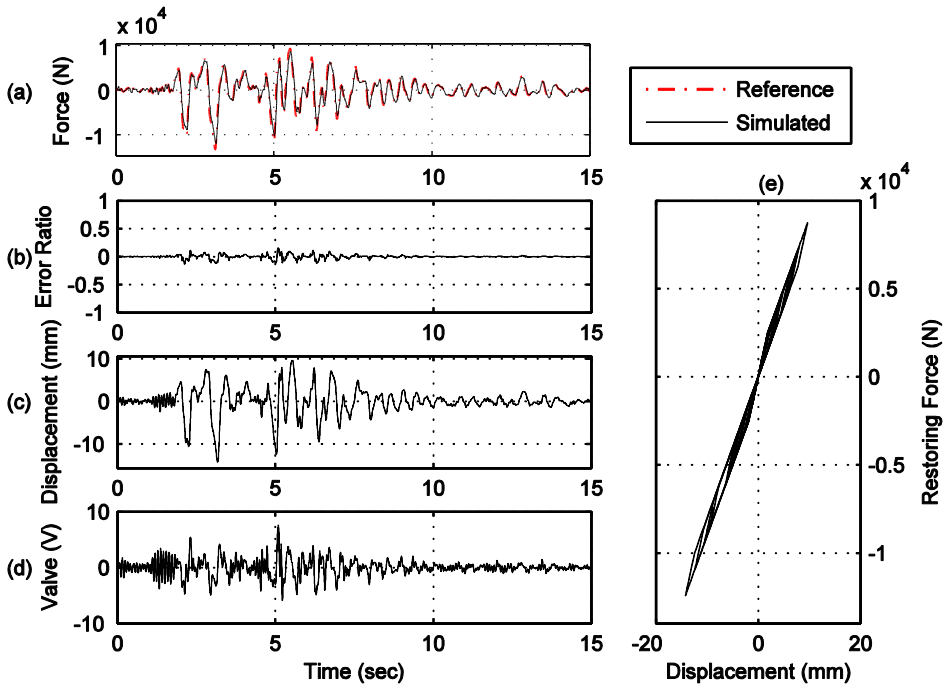

Figure C.4. Yield strength Y_y = 1,000 N, post-yield stiffness $k_1 = 0.6*k_0$.

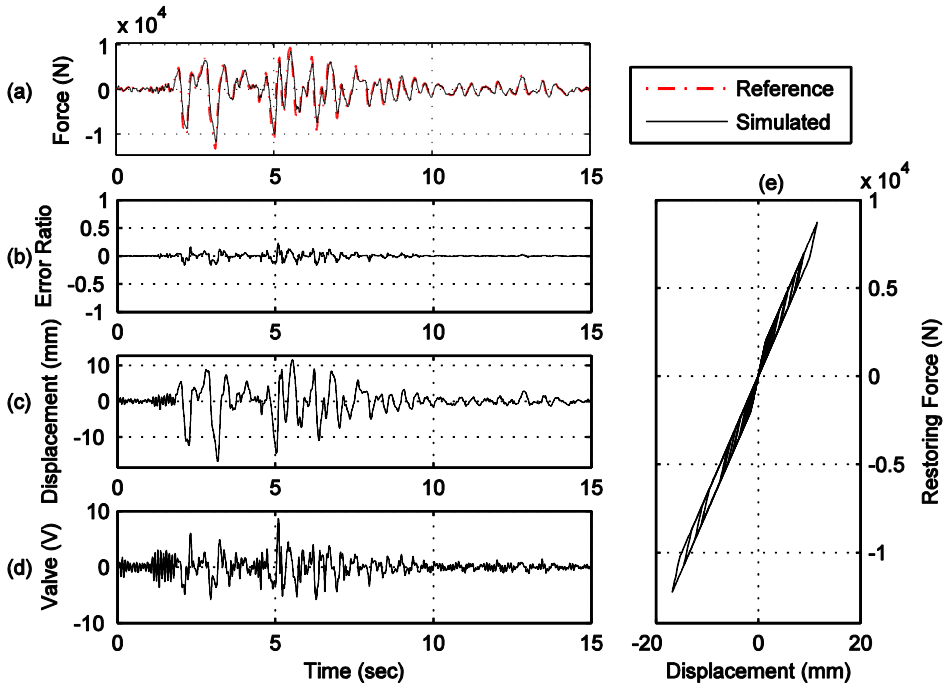

Figure C.5. Yield strength Y_y = 1,000 N, post-yield stiffness $k_1 = 0.5*k_0$.

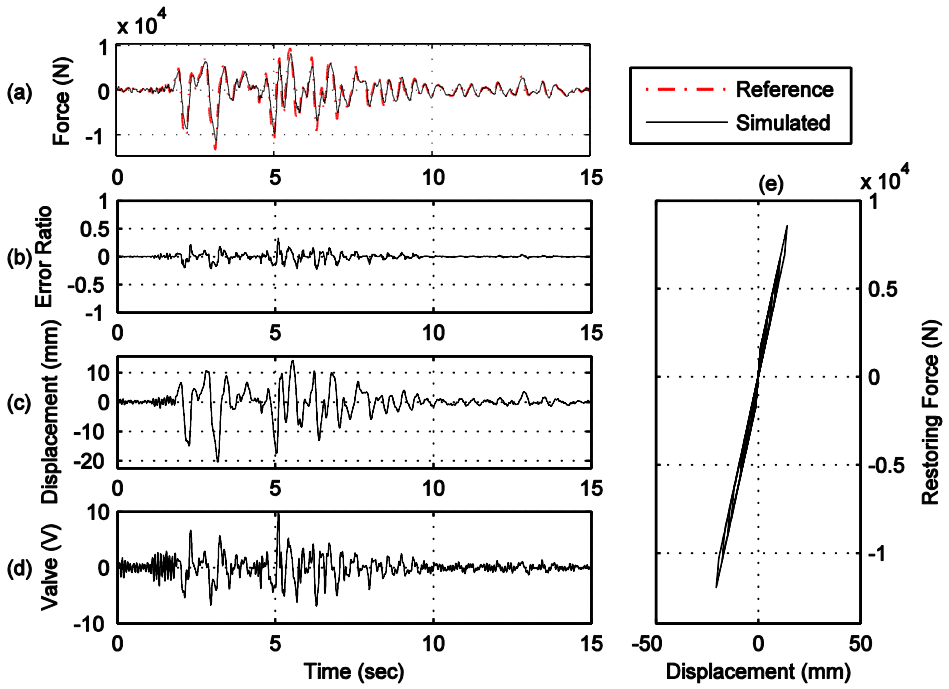

Figure C.6. Yield strength Y_y = 1,000 N, post-yield stiffness $k_1 = 0.4*k_0$.

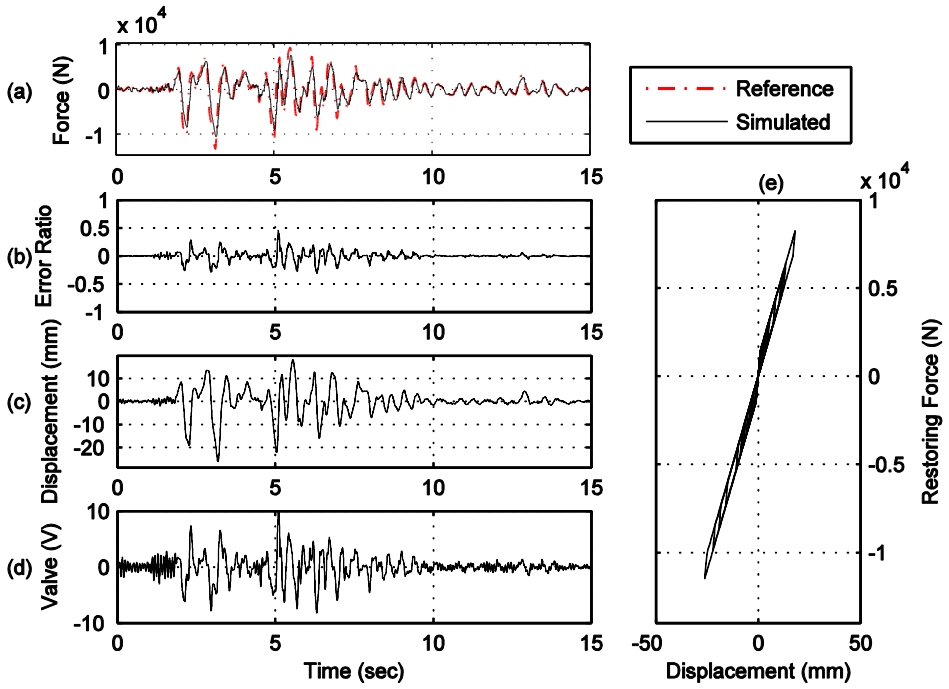

Figure C.7. Yield strength Y_y = 1,000 N, post-yield stiffness $k_1 = 0.3*k_0$.

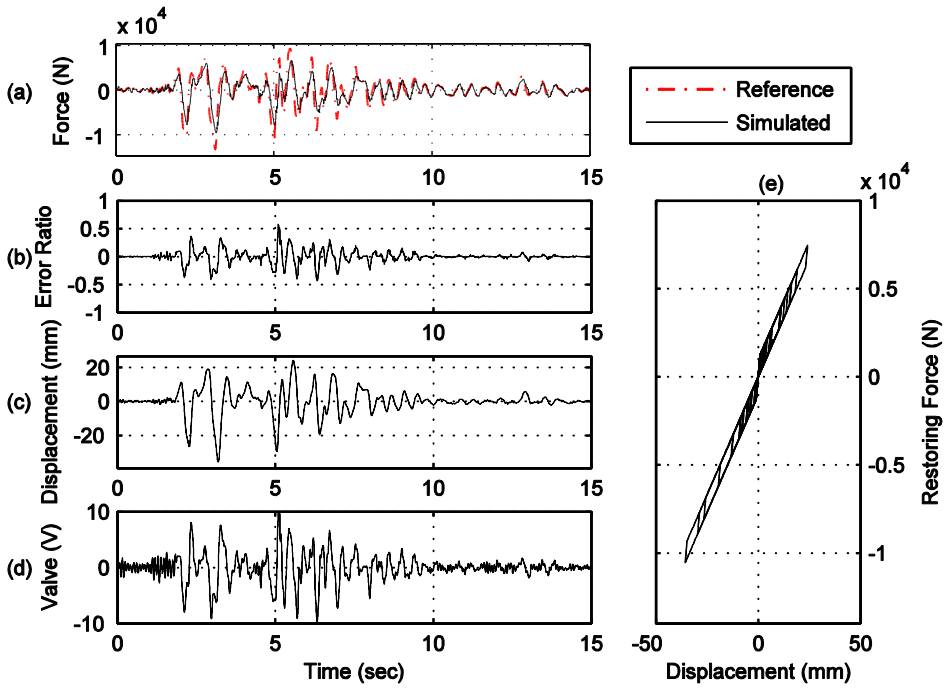

Figure C.8. Yield strength Y_y = 1,000 N, post-yield stiffness $k_1 = 0.2*k_0$.

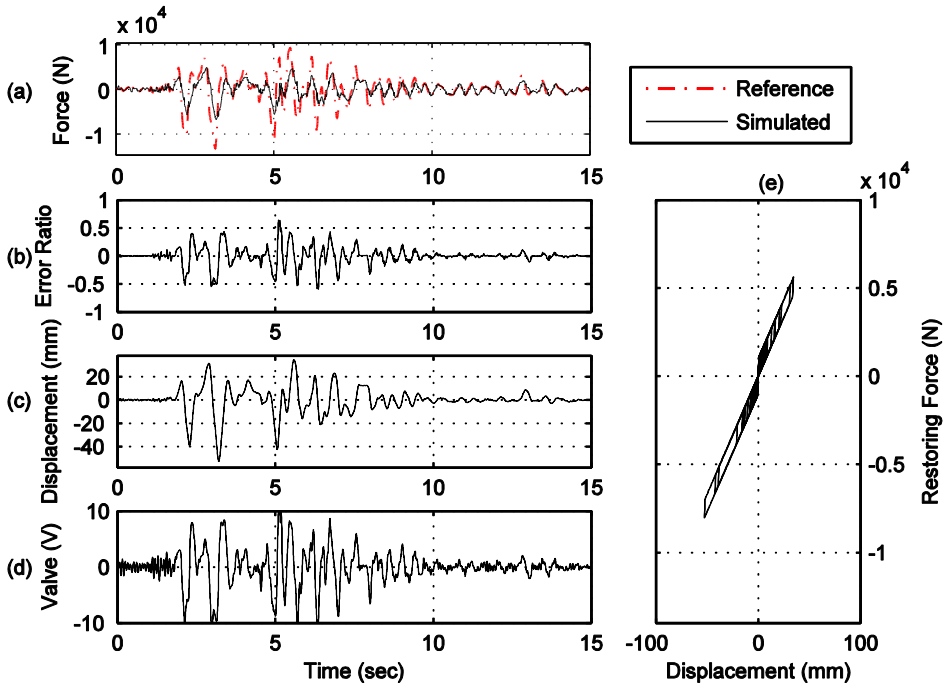

Figure C.9. Yield strength Y_y = 1,000 N, post-yield stiffness $k_1 = 0.1*k_0$.

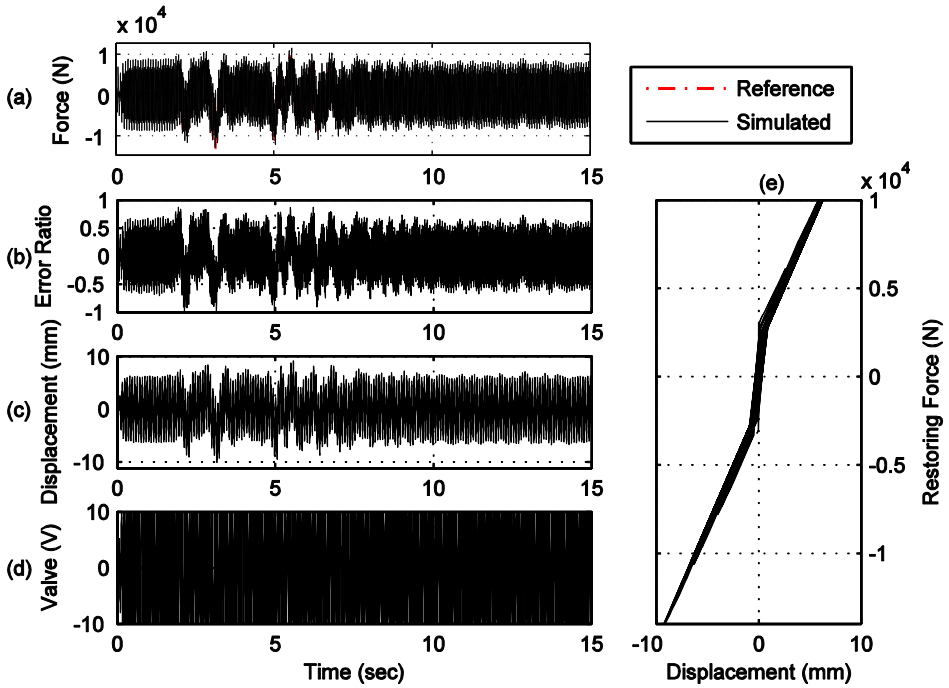

Figure C.10. Yield strength Y_y = 3,000 N, post-yield stiffness $k_1 = 0.9*k_0$.

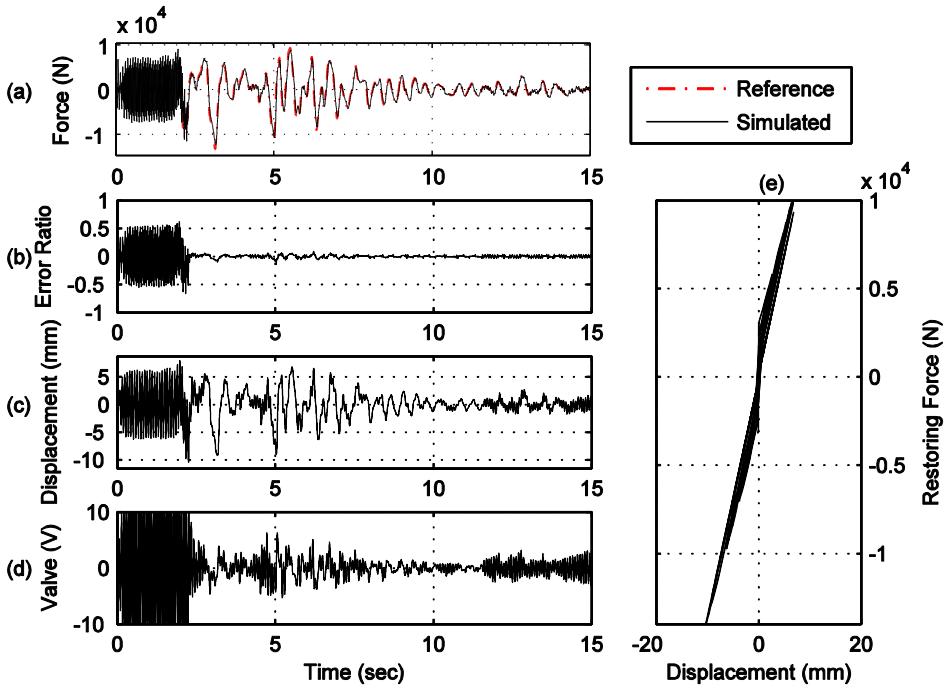

Figure C.11. Yield strength Y_y =3,000 N, post-yield stiffness $k_1 = 0.8*k_0$.

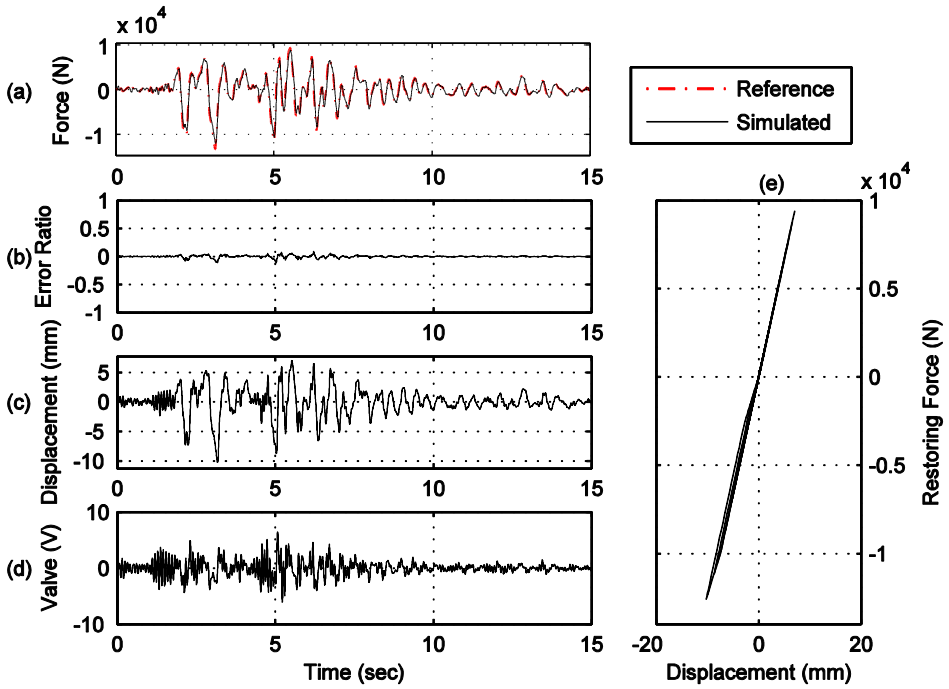

Figure C.12. Yield strength Y_y =3,000 N, post-yield stiffness $k_1 = 0.7*k_0$.

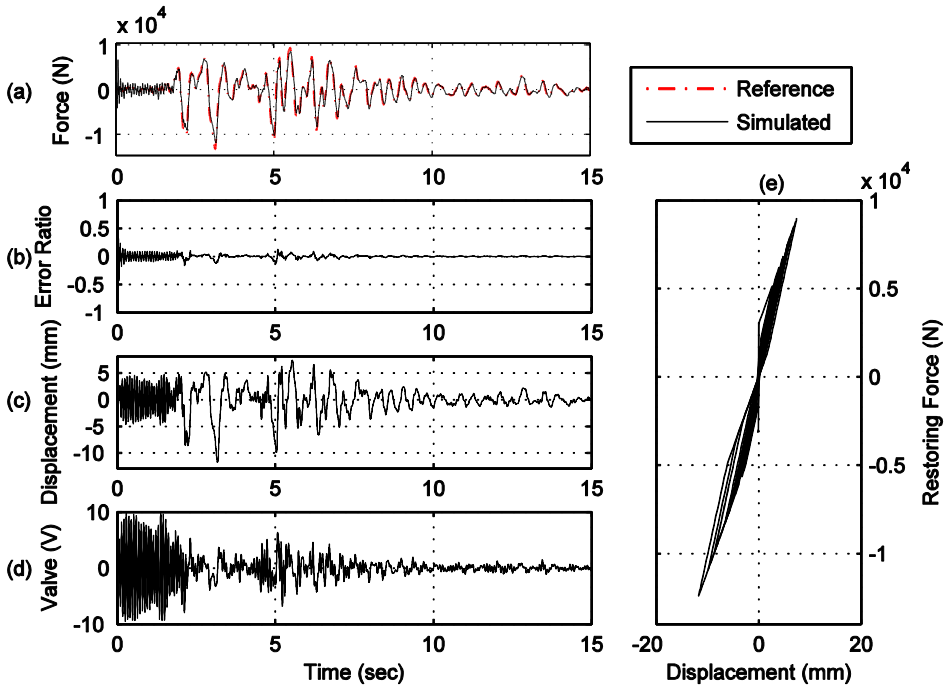

Figure C.13. Yield strength Y_y =3,000 N, post-yield stiffness $k_1 = 0.6*k_0$.

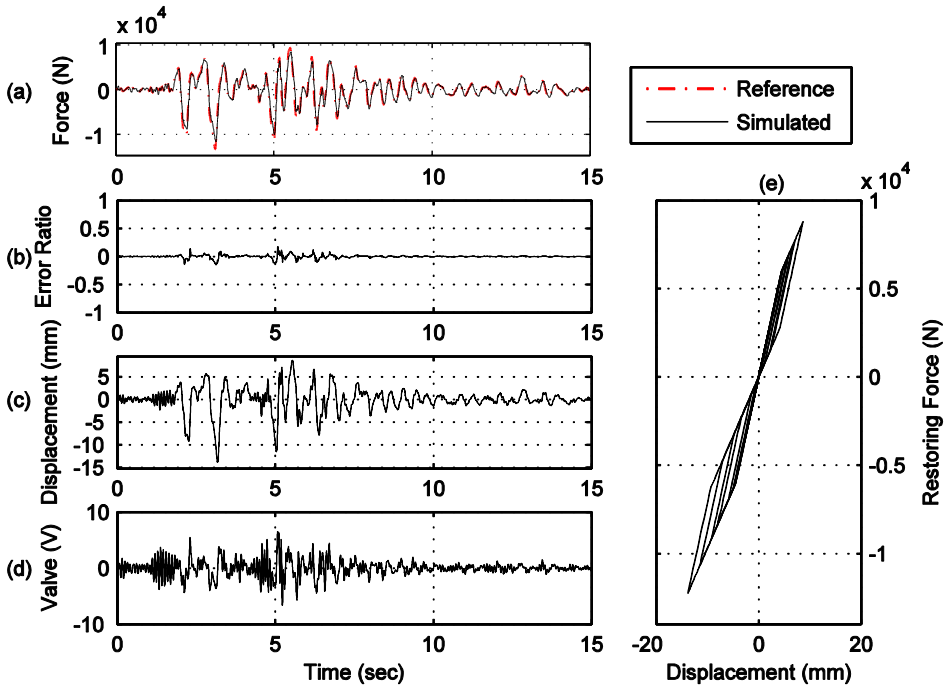

Figure C.14. Yield strength Y_y =3,000 N, post-yield stiffness $k_1 = 0.5*k_0$.

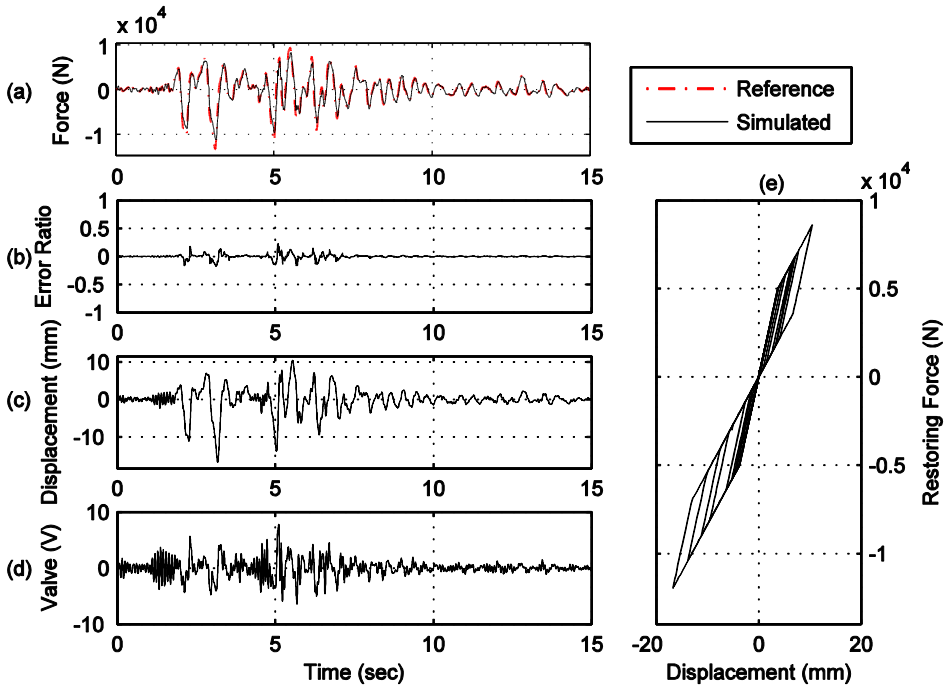

Figure C.15. Yield strength Y_y =3,000 N, post-yield stiffness $k_1 = 0.4*k_0$.

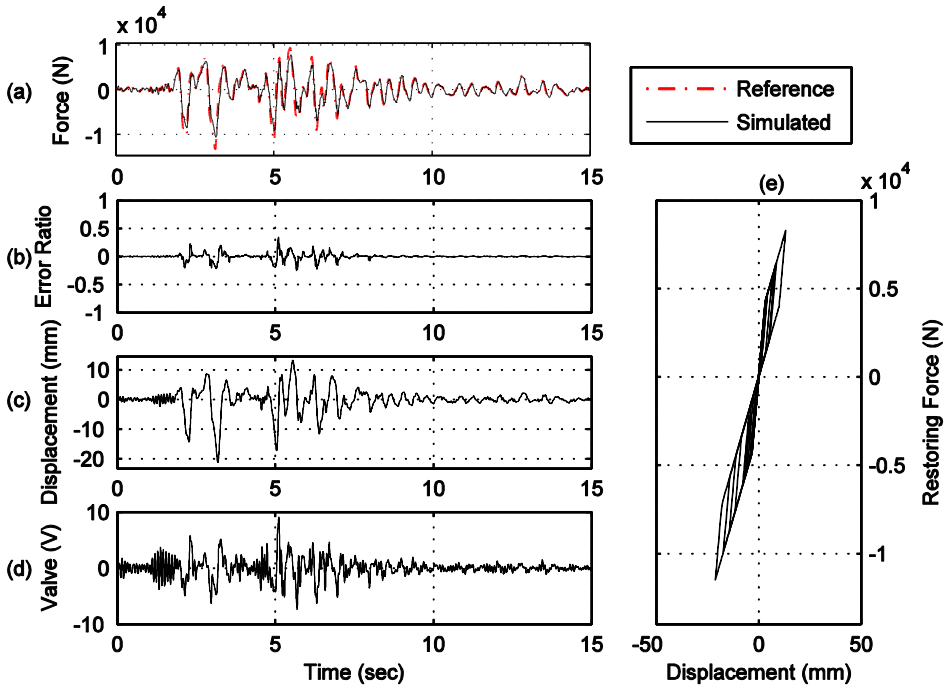

Figure C.16. Yield strength Y_y =3,000 N, post-yield stiffness $k_1 = 0.3*k_0$.

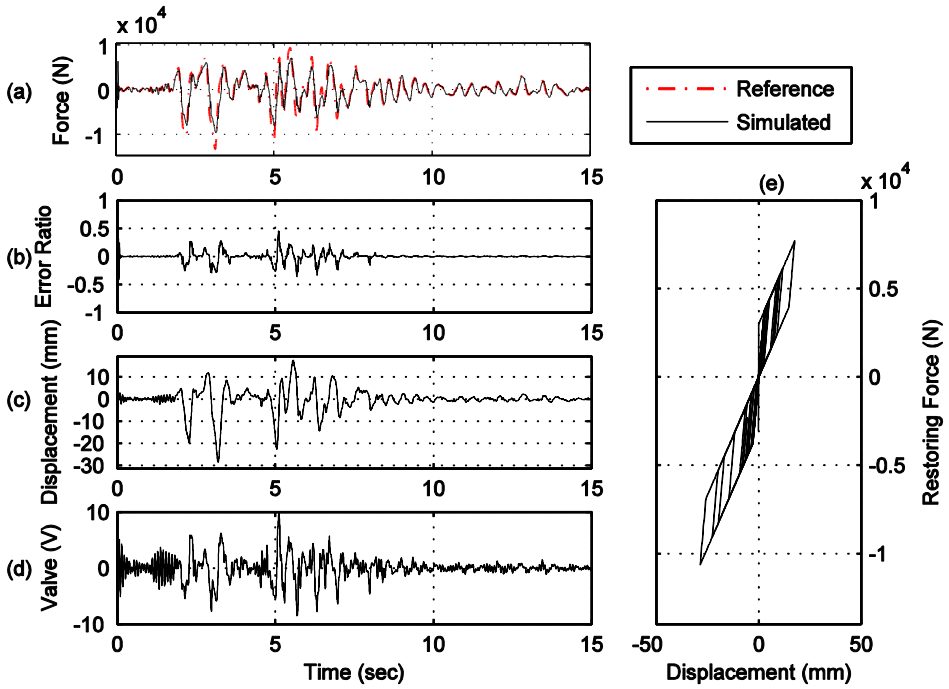

Figure C.17. Yield strength Y_y =3,000 N, post-yield stiffness $k_1 = 0.2*k_0$.

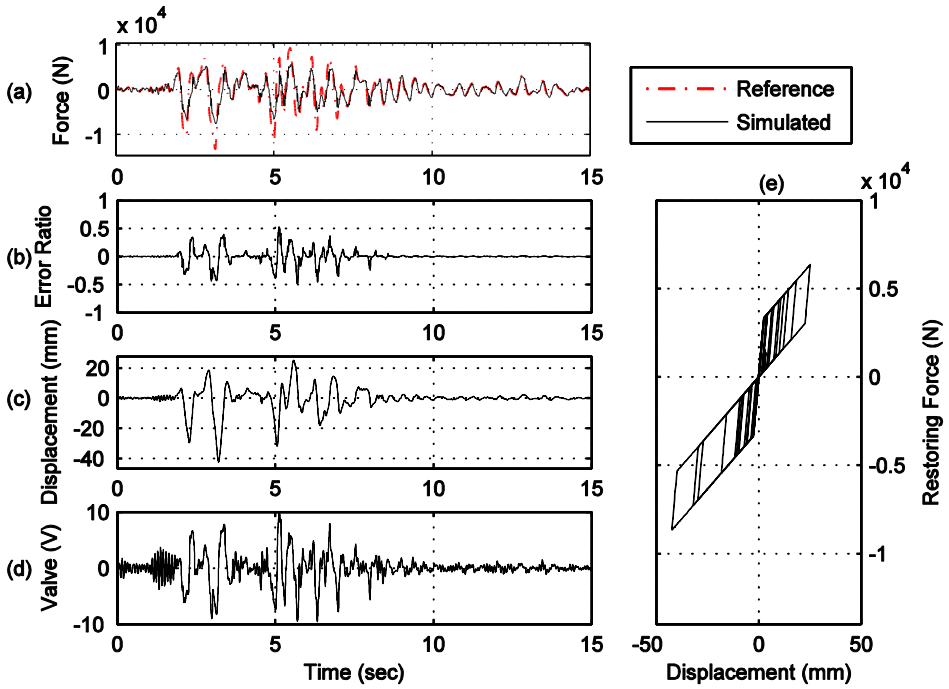

Figure C.18. Yield strength Y_y =3,000 N, post-yield stiffness $k_1 = 0.1*k_0$.

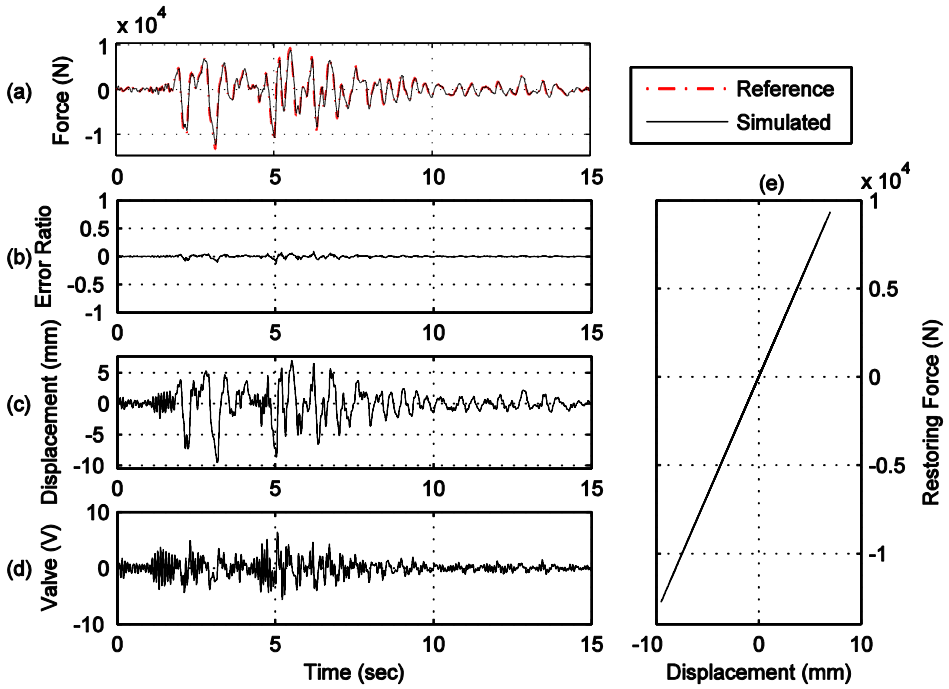

Figure C.19. Yield strength Y_y =5,000 N, post-yield stiffness $k_1 = 0.9*k_0$.

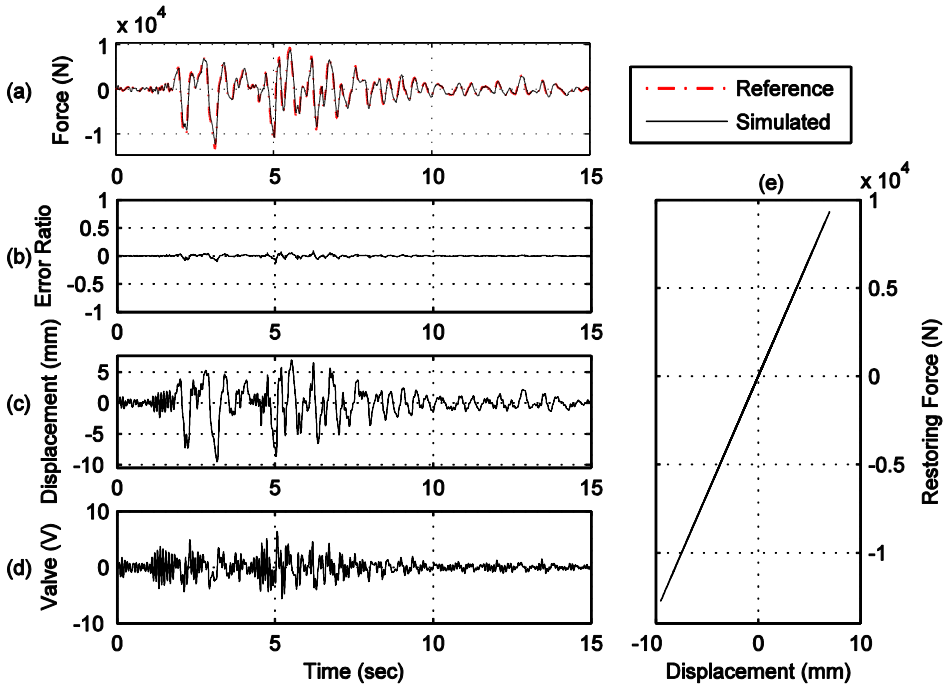

Figure C.20. Yield strength Y_y =5,000 N, post-yield stiffness $k_1 = 0.8*k_0$.

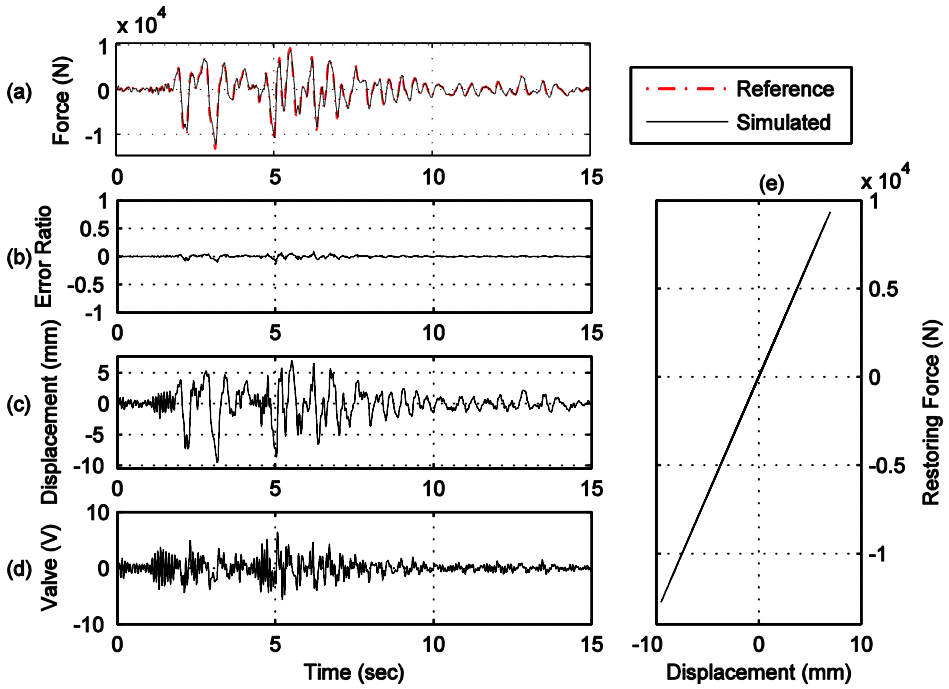

Figure C.21. Yield strength Y_y =5,000 N, post-yield stiffness $k_1 = 0.7*k_0$.

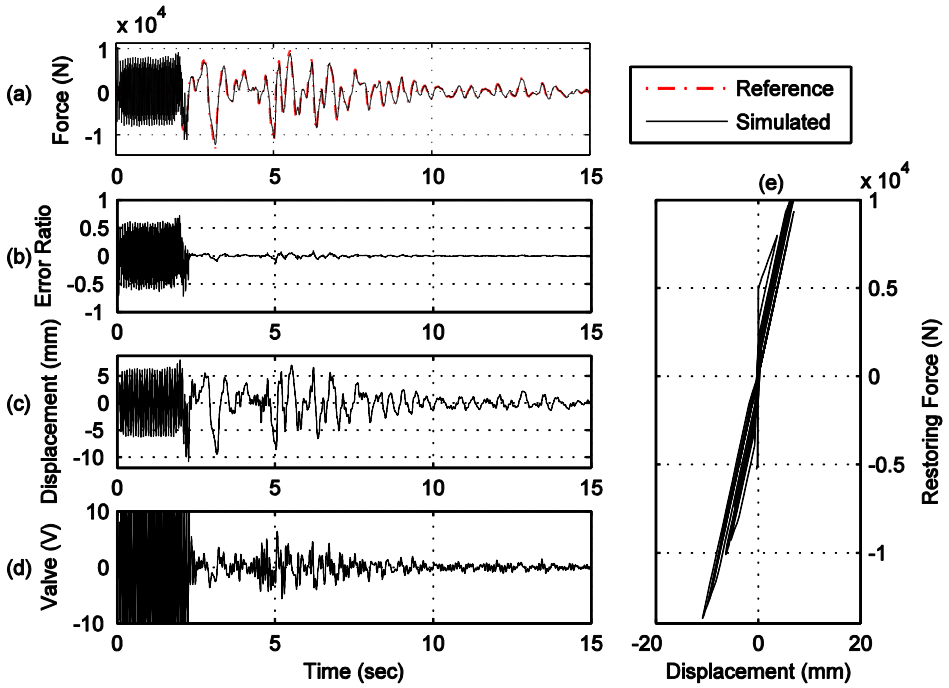

Figure C.22. Yield strength Y_y =5,000 N, post-yield stiffness $k_1 = 0.6*k_0$.

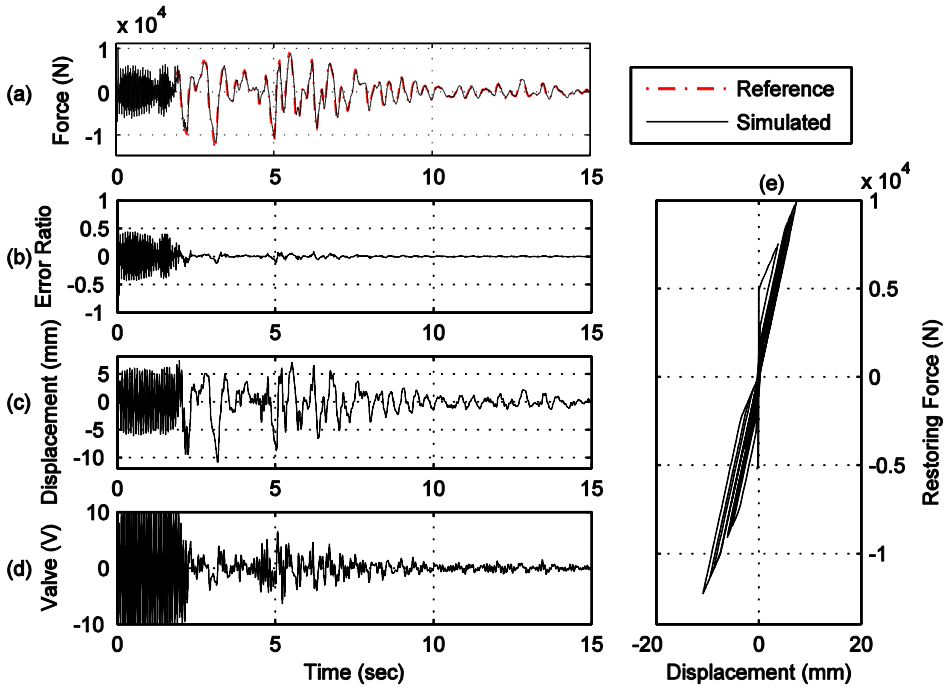

Figure C.23. Yield strength Y_y =5,000 N, post-yield stiffness $k_1 = 0.5*k_0$.

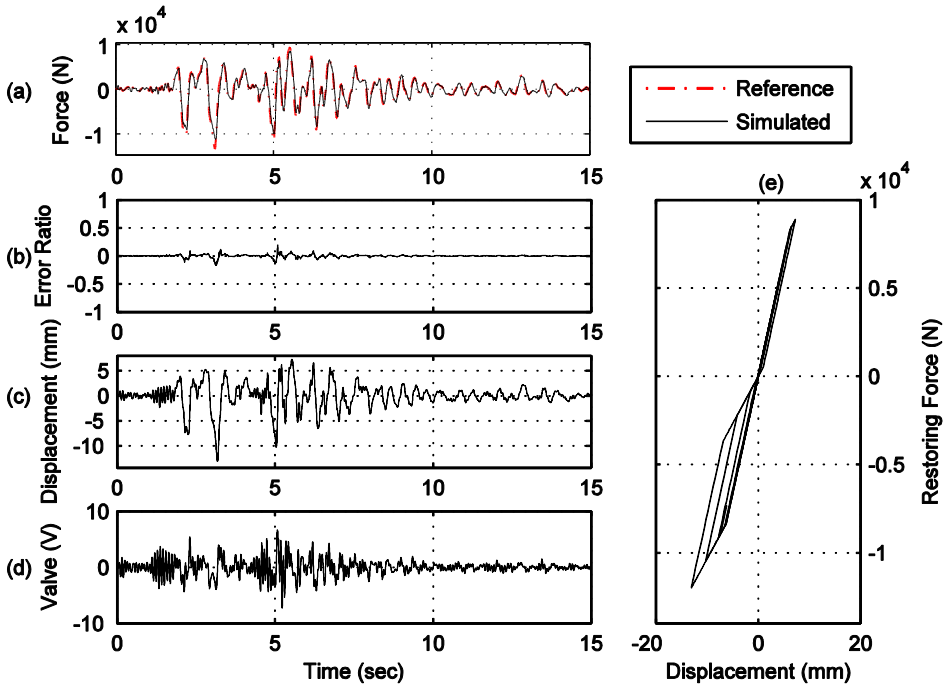

Figure C.24. Yield strength Y_y =5,000 N, post-yield stiffness $k_1 = 0.4*k_0$.

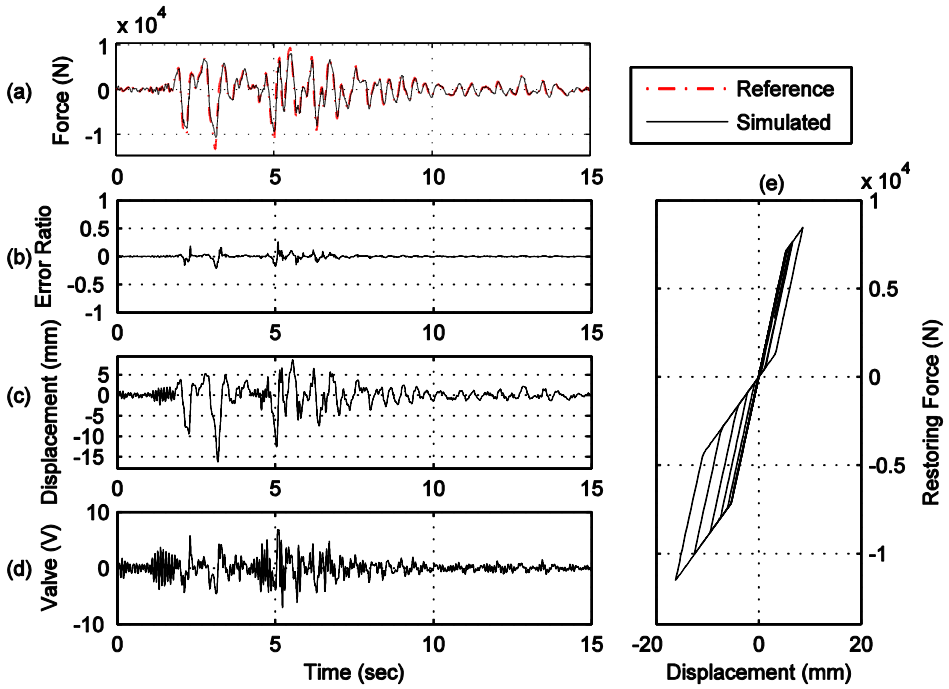

Figure C.25. Yield strength Y_y =5,000 N, post-yield stiffness $k_1 = 0.3*k_0$.

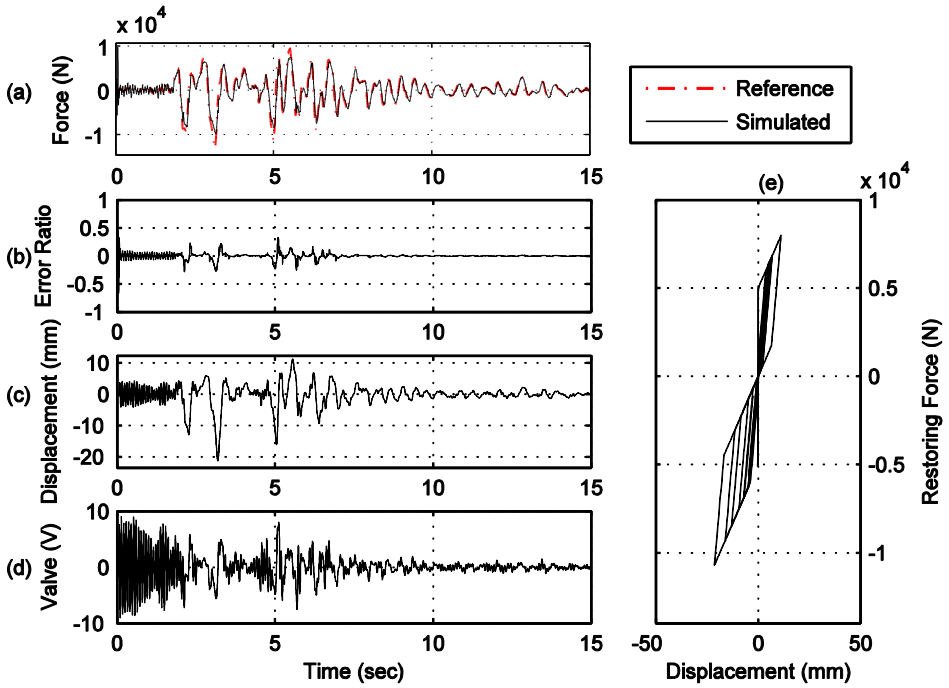

Figure C.26. Yield strength Y_y =5,000 N, post-yield stiffness $k_1 = 0.2*k_0$.

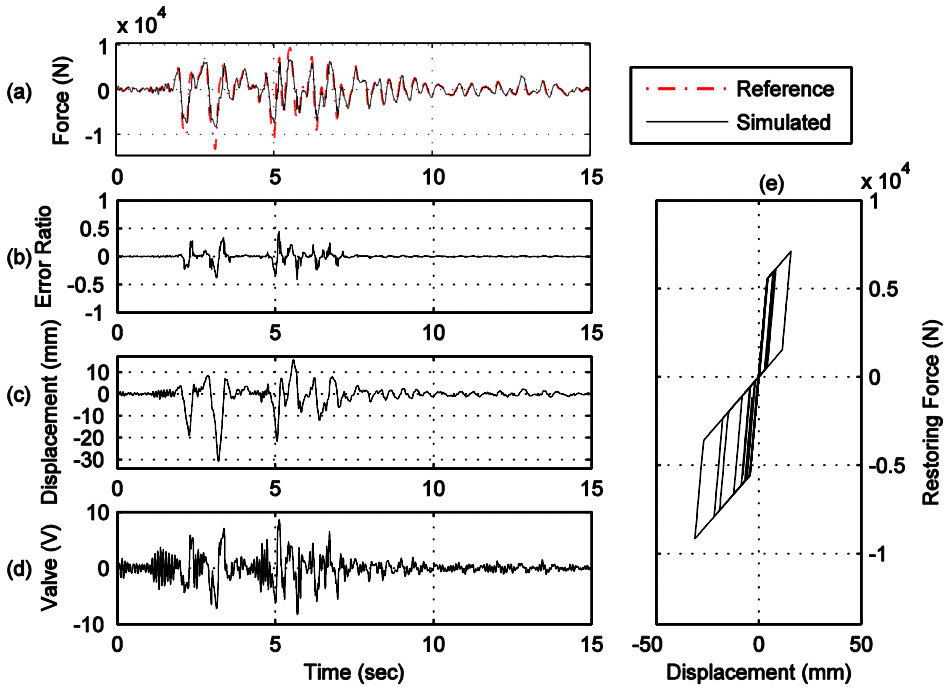

Figure C.27. Yield strength Y_y =5,000 N, post-yield stiffness $k_1 = 0.1*k_0$.

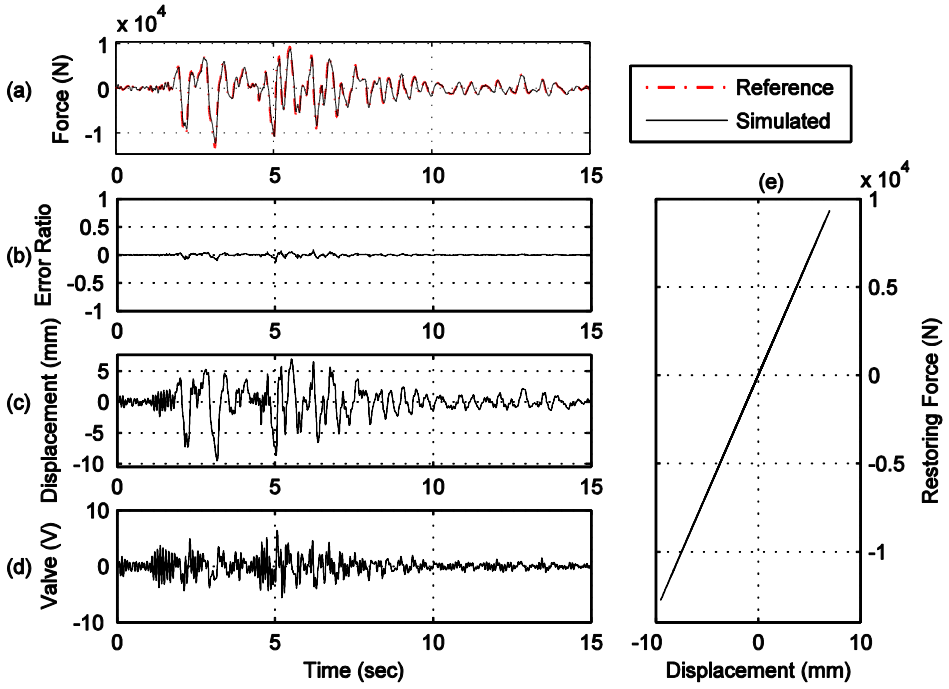

Figure C.28. Yield strength Y_y =7,000 N, post-yield stiffness $k_1 = 0.9*k_0$.

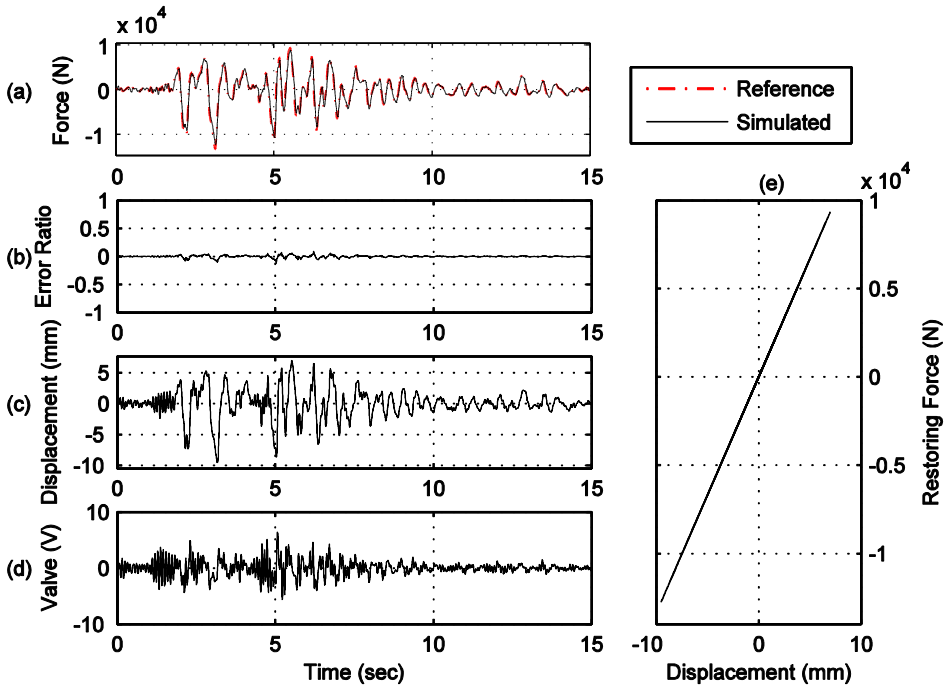

Figure C.29. Yield strength Y_y =7,000 N, post-yield stiffness $k_1 = 0.8*k_0$.

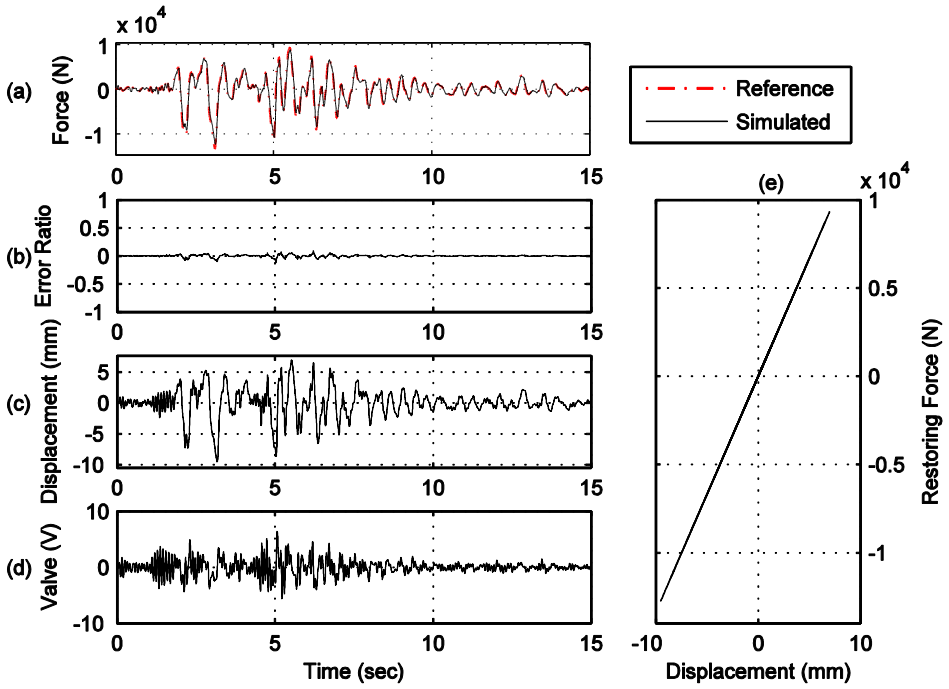

Figure C.30. Yield strength Y_y =7,000 N, post-yield stiffness $k_1 = 0.7*k_0$.

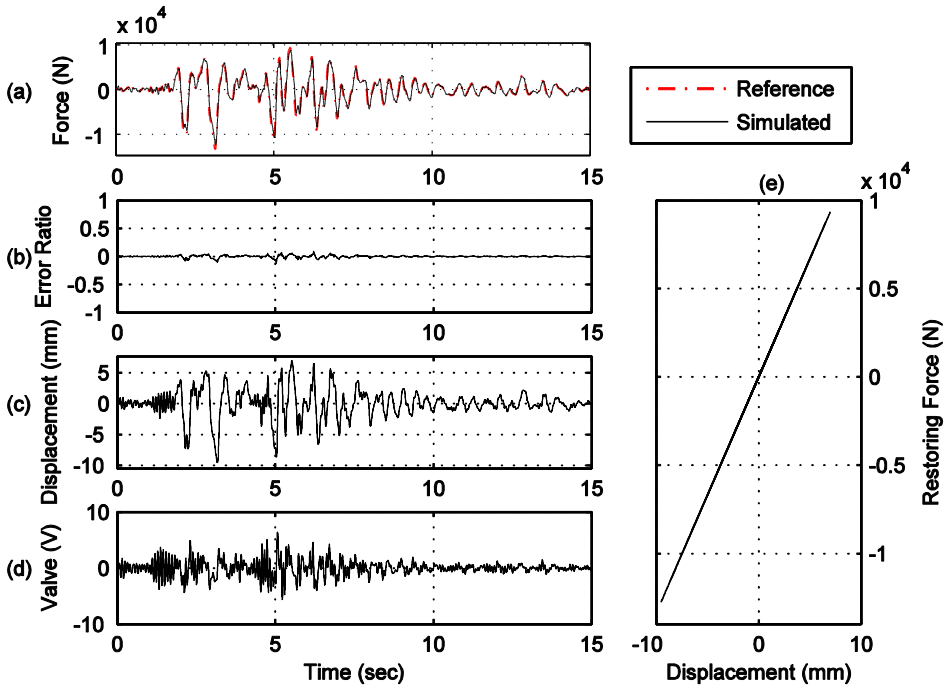

Figure C.31. Yield strength Y_y =7,000 N, post-yield stiffness $k_1 = 0.6*k_0$.

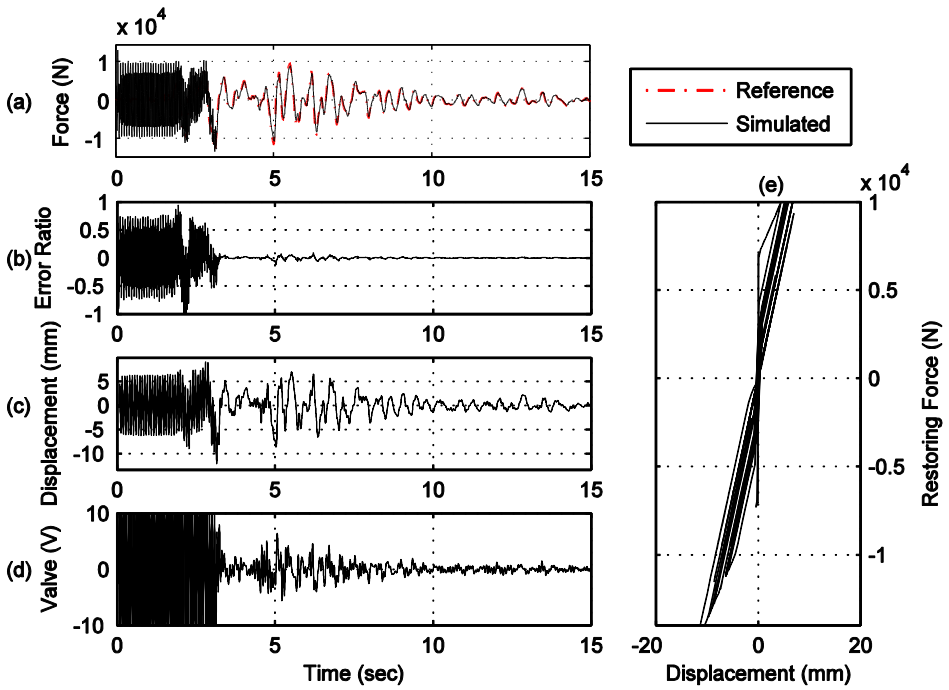

Figure C.32. Yield strength Y_y =7,000 N, post-yield stiffness $k_1 = 0.5*k_0$.

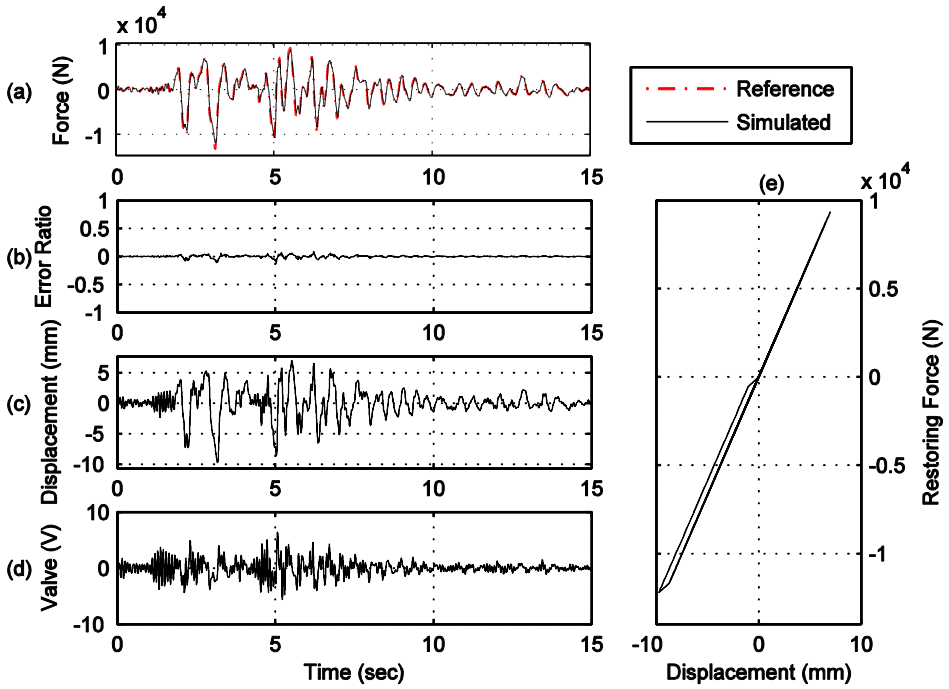

Figure C.33. Yield strength Y_y =7,000 N, post-yield stiffness $k_1 = 0.4*k_0$.

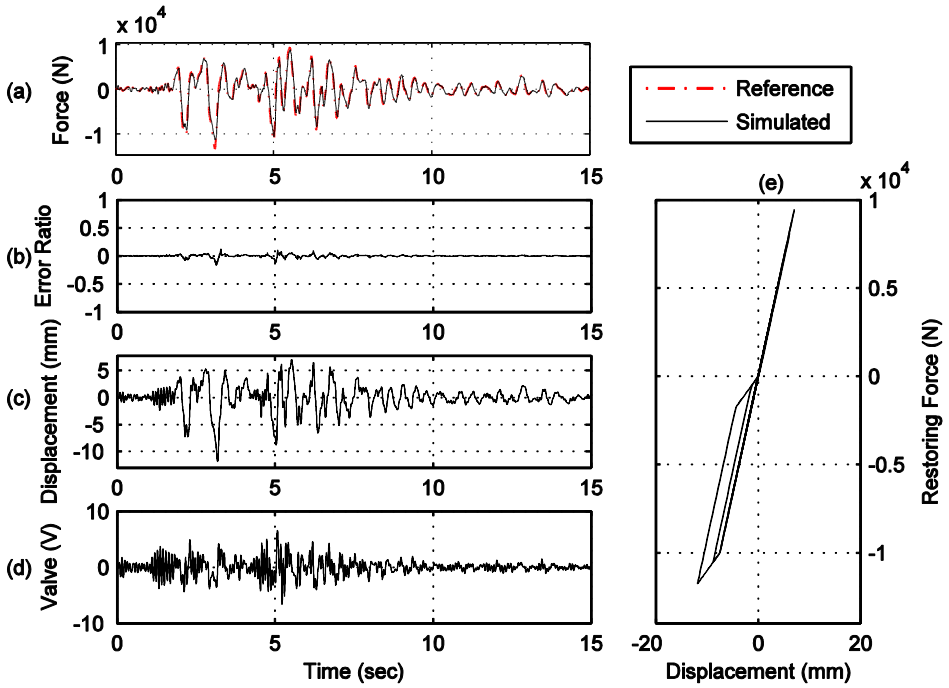

Figure C.34. Yield strength Y_y =7,000 N, post-yield stiffness $k_1 = 0.3*k_0$.

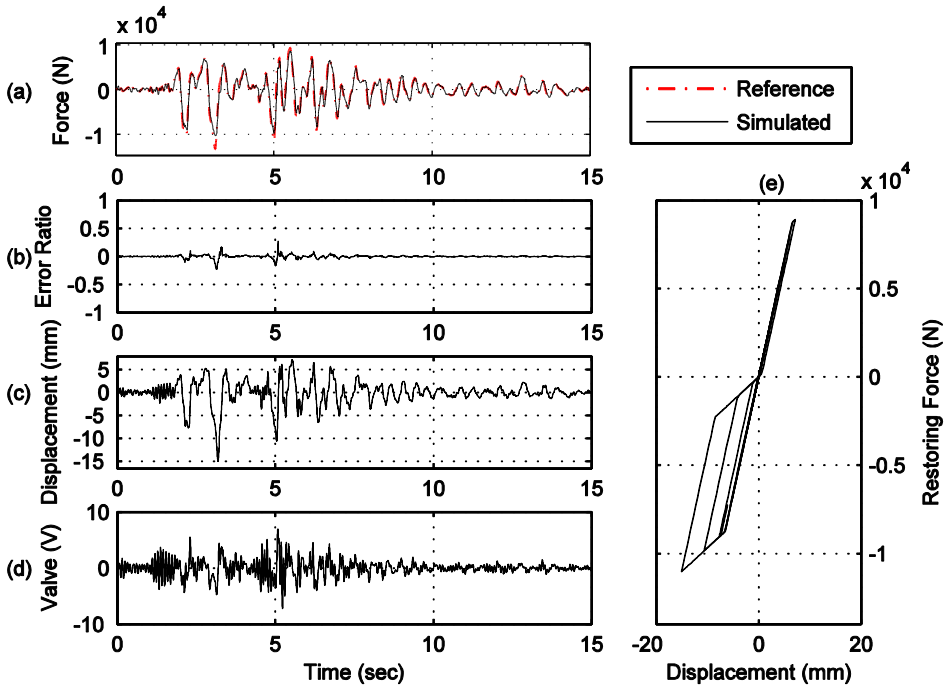

Figure C.35. Yield strength Y_y =7,000 N, post-yield stiffness $k_1 = 0.2*k_0$.

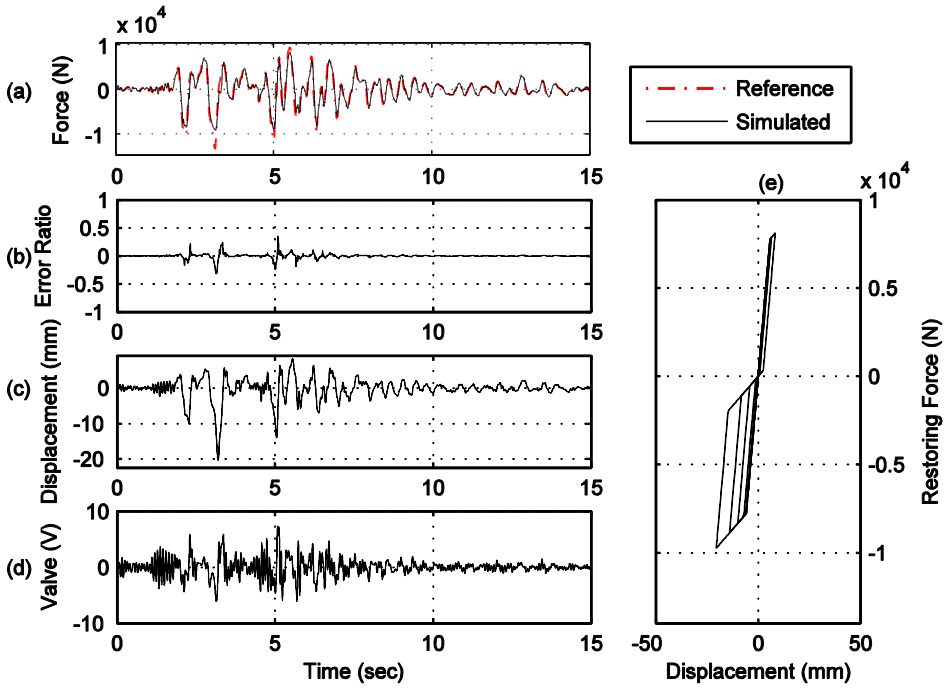

Figure C.36. Yield strength Y_y =7,000 N, post-yield stiffness $k_1 = 0.1*k_0$.

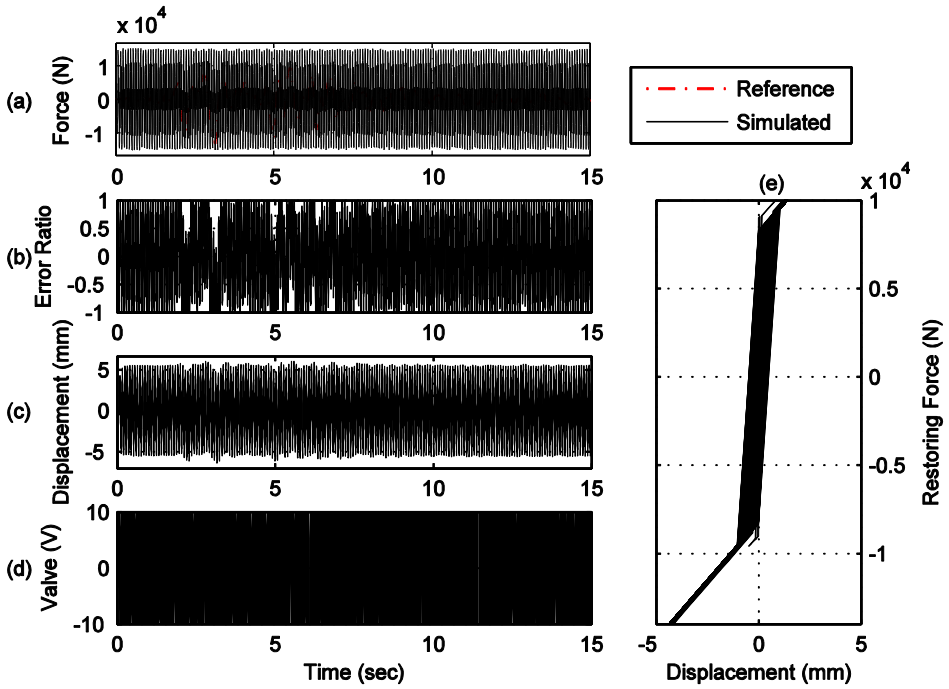

Figure C.37. Yield strength Y_y =9,000 N, post-yield stiffness $k_1 = 0.9*k_0$.

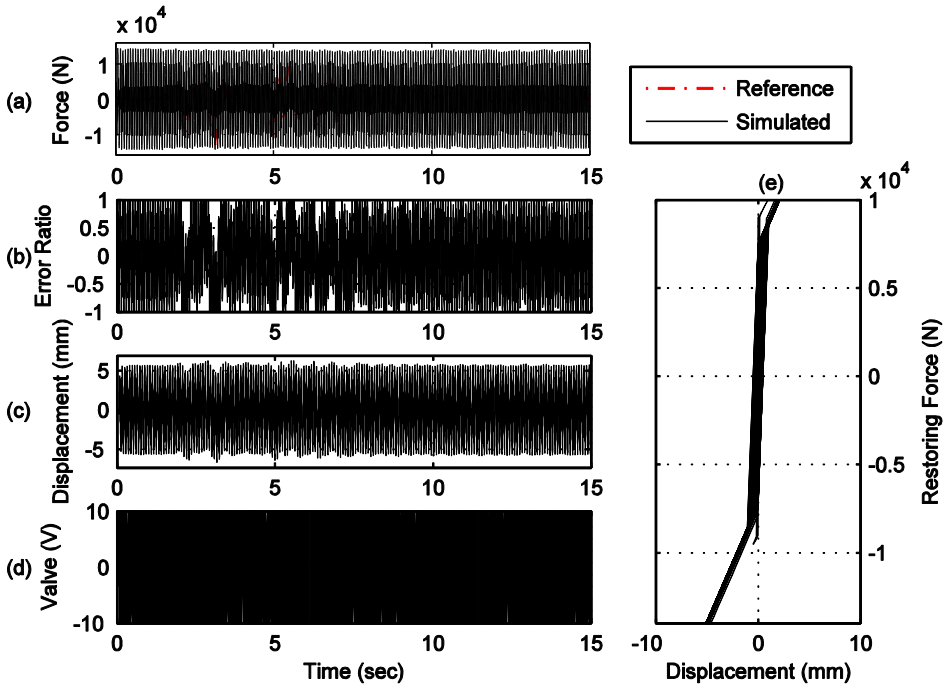

Figure C.38. Yield strength Y_y =9,000 N, post-yield stiffness $k_1 = 0.8*k_0$.

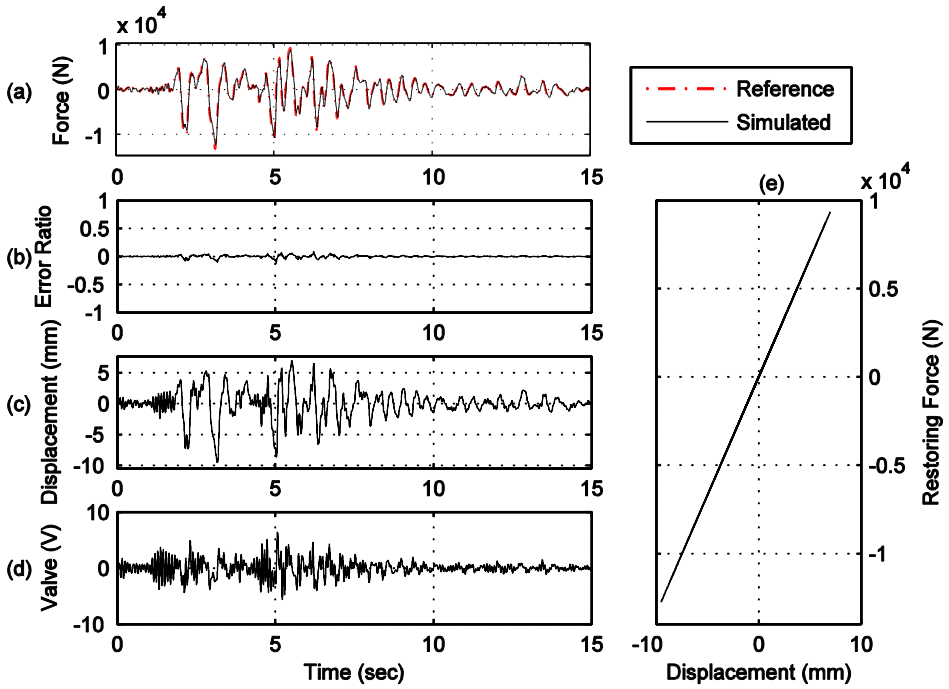

Figure C.39. Yield strength Y_y =9,000 N, post-yield stiffness $k_1 = 0.7*k_0$.

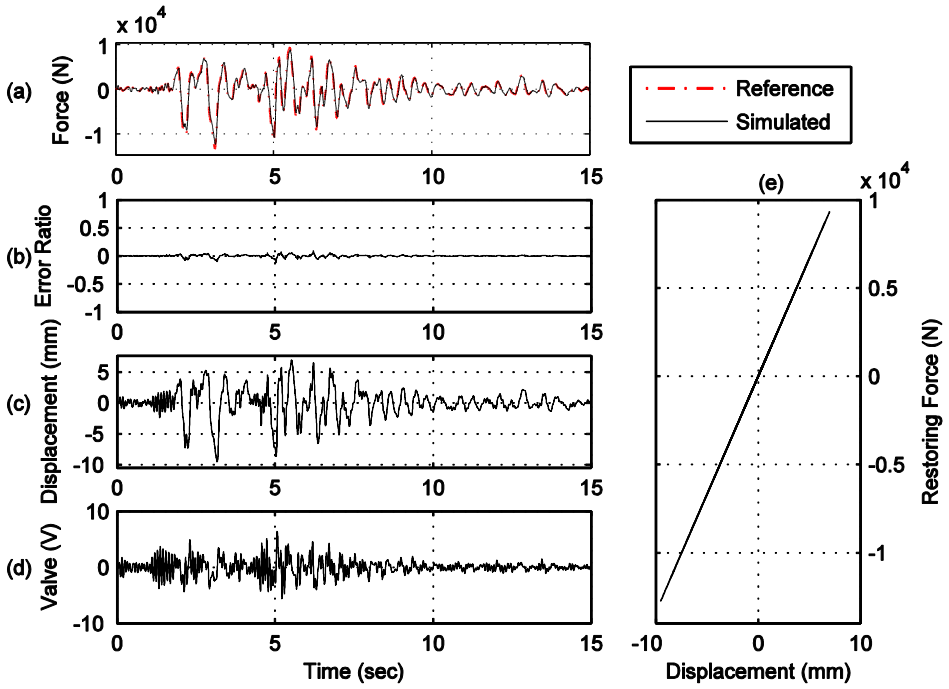

Figure C.40. Yield strength Y_y =9,000 N, post-yield stiffness $k_1 = 0.6*k_0$.

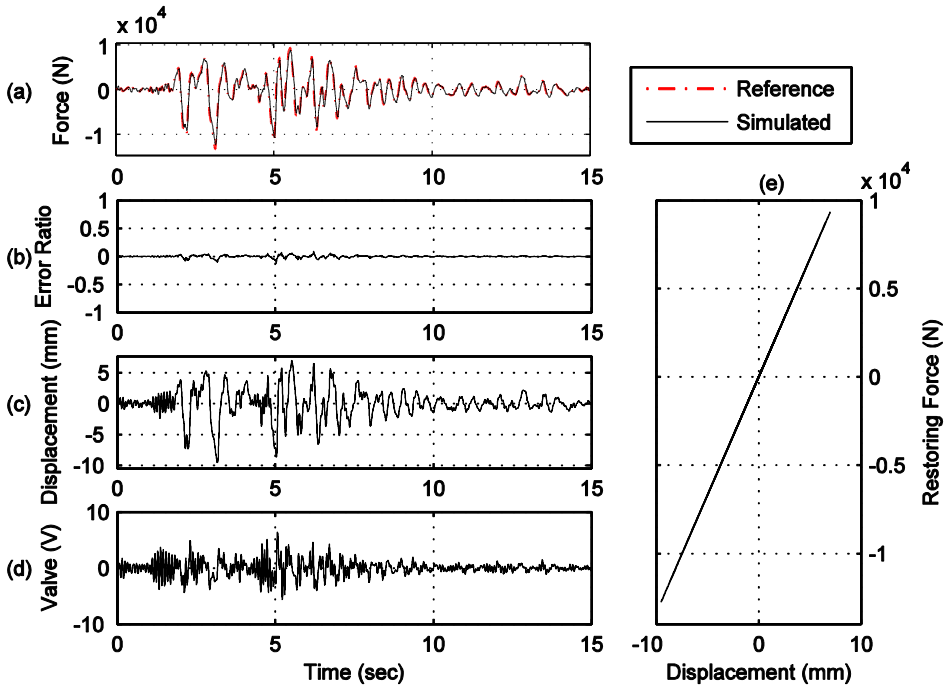

Figure C.41. Yield strength Y_y =9,000 N, post-yield stiffness $k_1 = 0.5*k_0$.

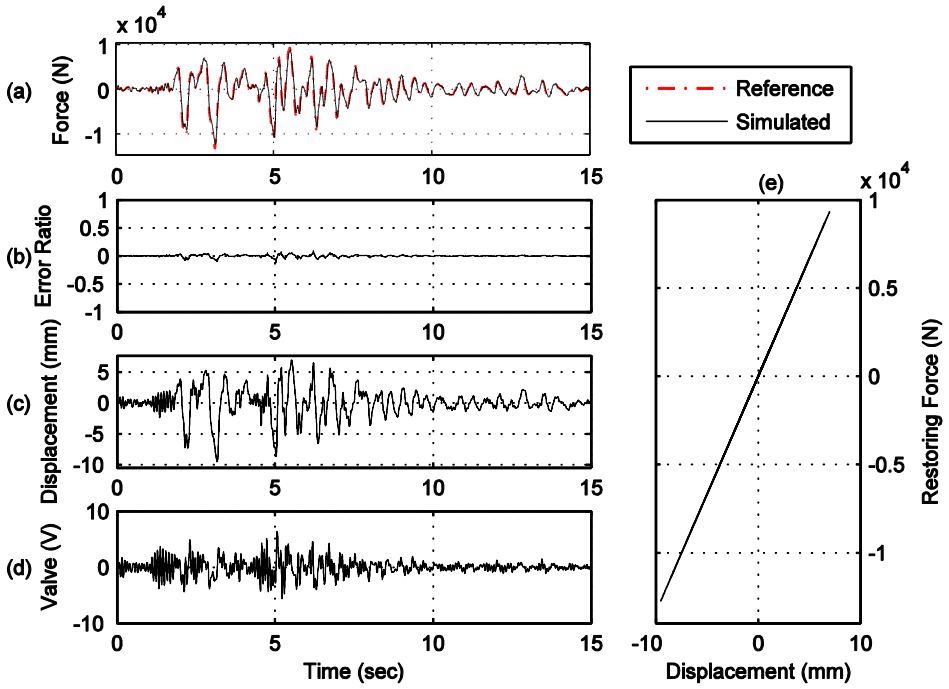

Figure C.42. Yield strength Y_y =9,000 N, post-yield stiffness $k_1 = 0.4*k_0$.

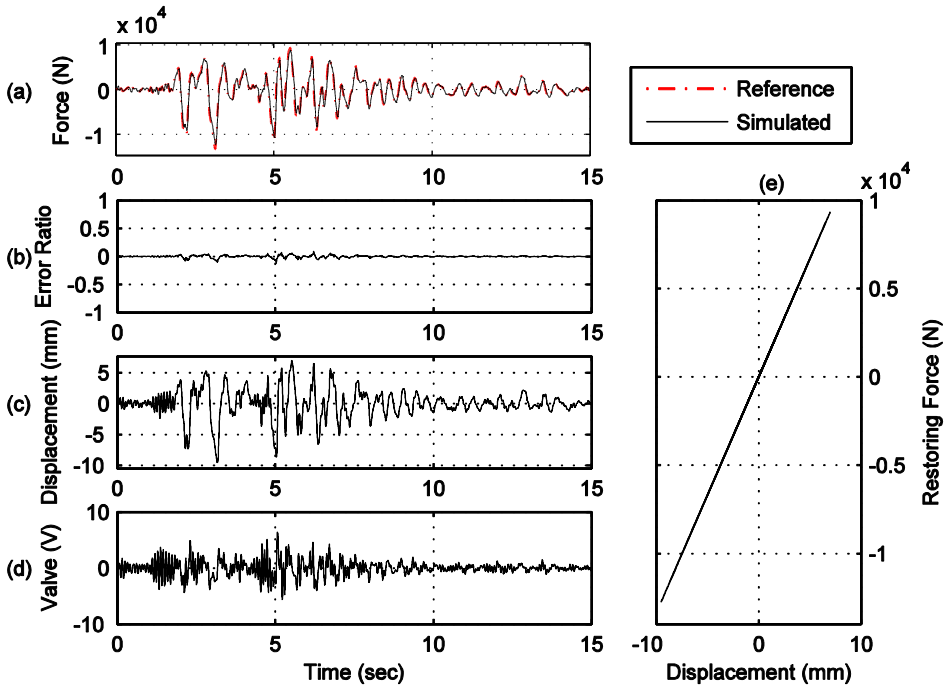

Figure C.43. Yield strength Y_y =9,000 N, post-yield stiffness $k_1 = 0.3*k_0$.

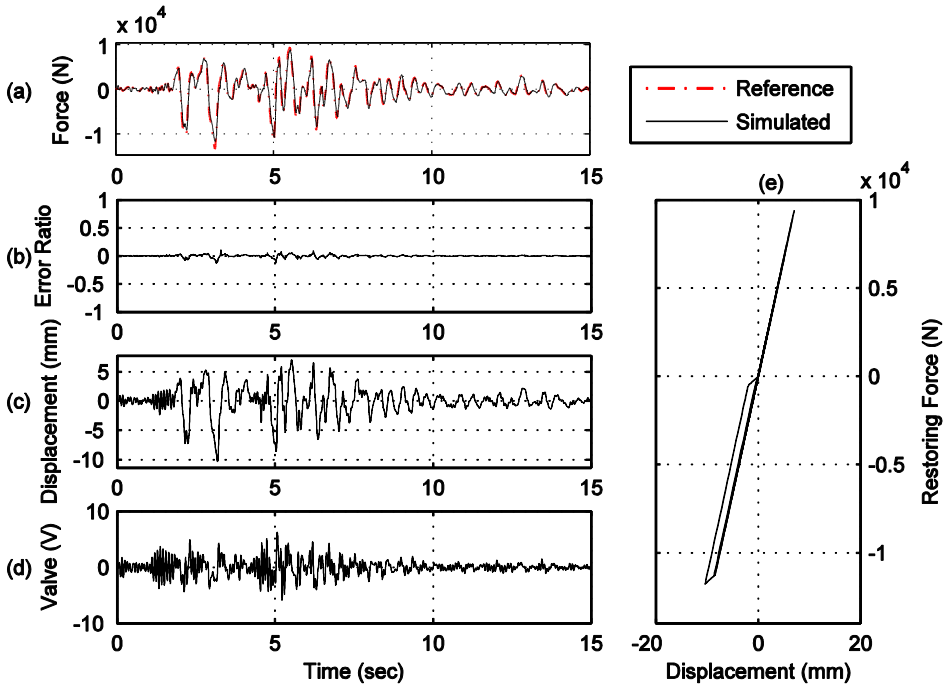

Figure C.44. Yield strength Y_y =9,000 N, post-yield stiffness $k_1 = 0.2*k_0$.

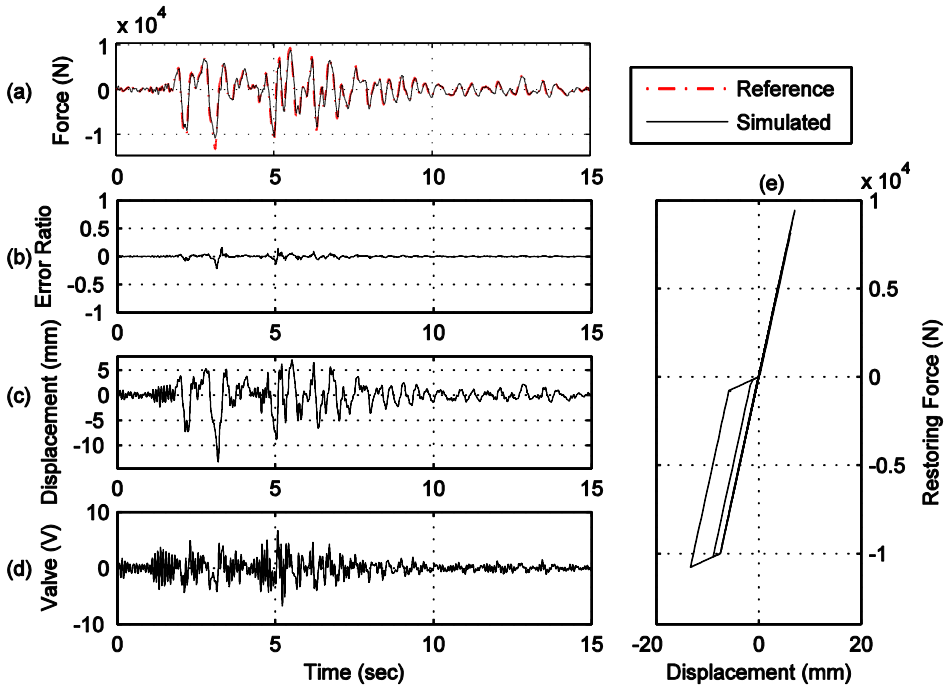

Figure C.45. Yield strength Y_y =9,000 N, post-yield stiffness $k_1 = 0.1*k_0$.

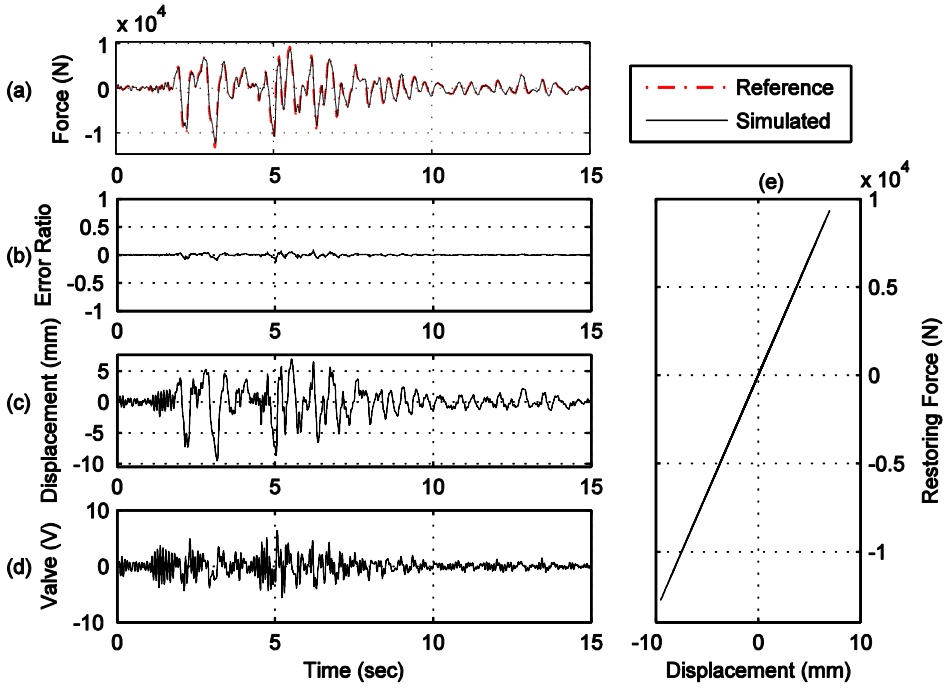

Figure C.46. Yield strength Y_y =11,000 N, post-yield stiffness $k_1 = 0.9*k_0$.

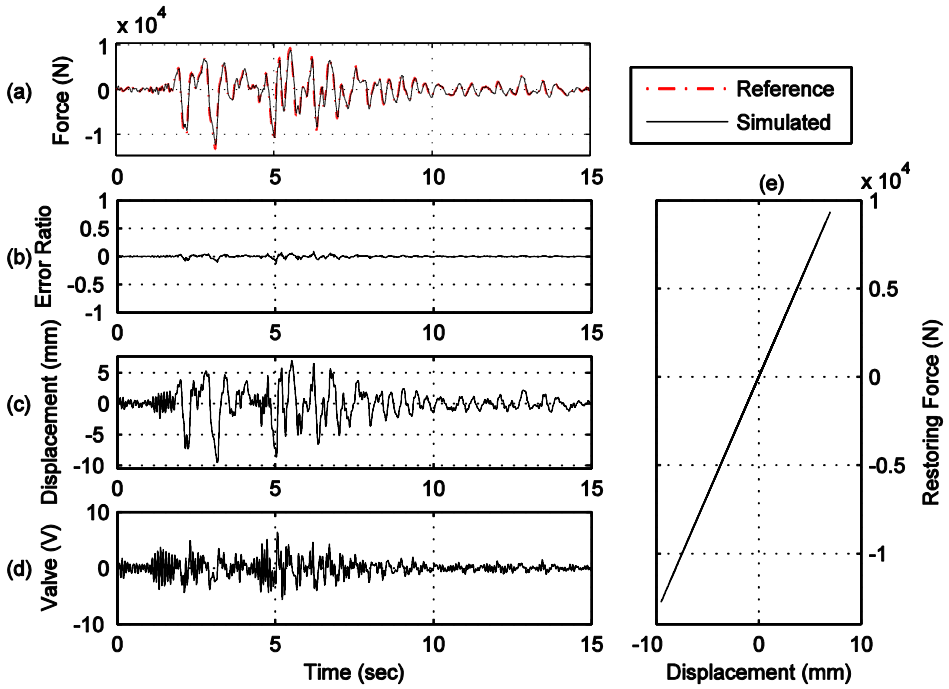

Figure C.47. Yield strength Y_y =11,000 N, post-yield stiffness $k_1 = 0.8*k_0$.

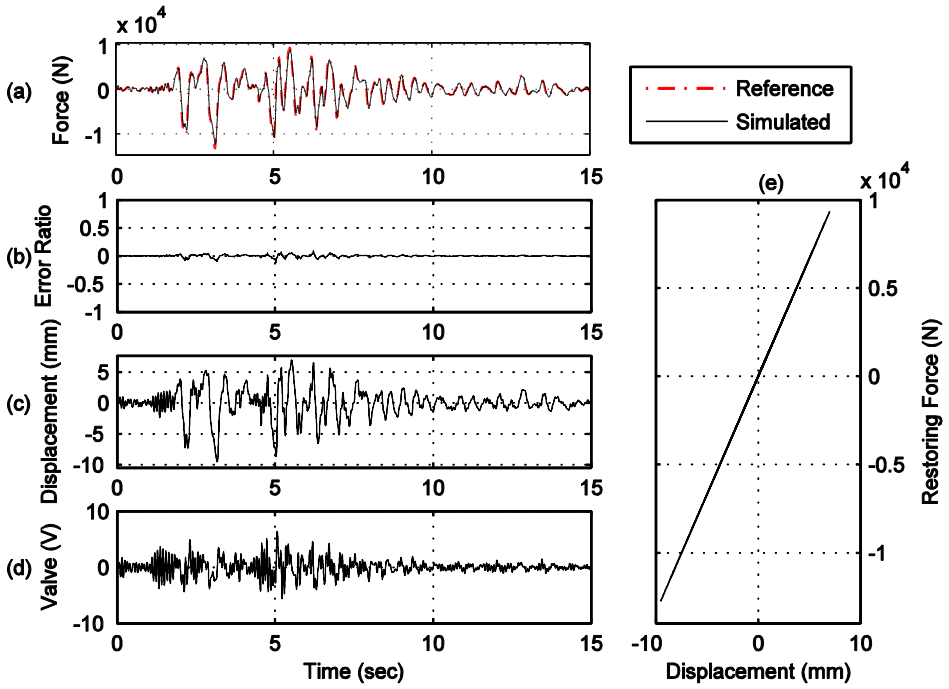

Figure C.48. Yield strength Y_y =11,000 N, post-yield stiffness $k_1 = 0.7*k_0$.

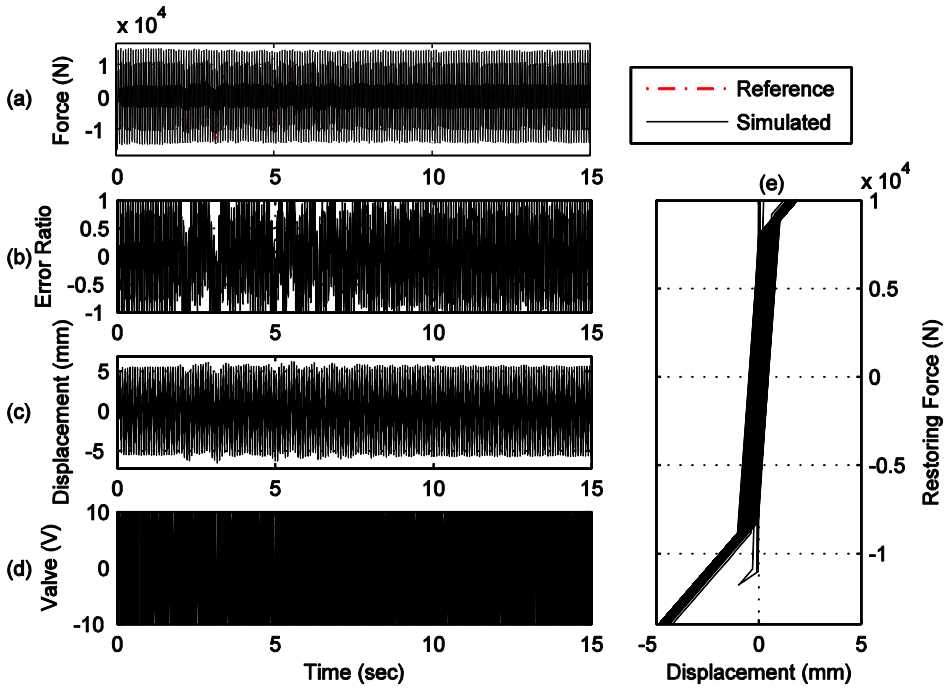

Figure C.49. Yield strength Y_y =11,000 N, post-yield stiffness $k_1 = 0.6*k_0$.

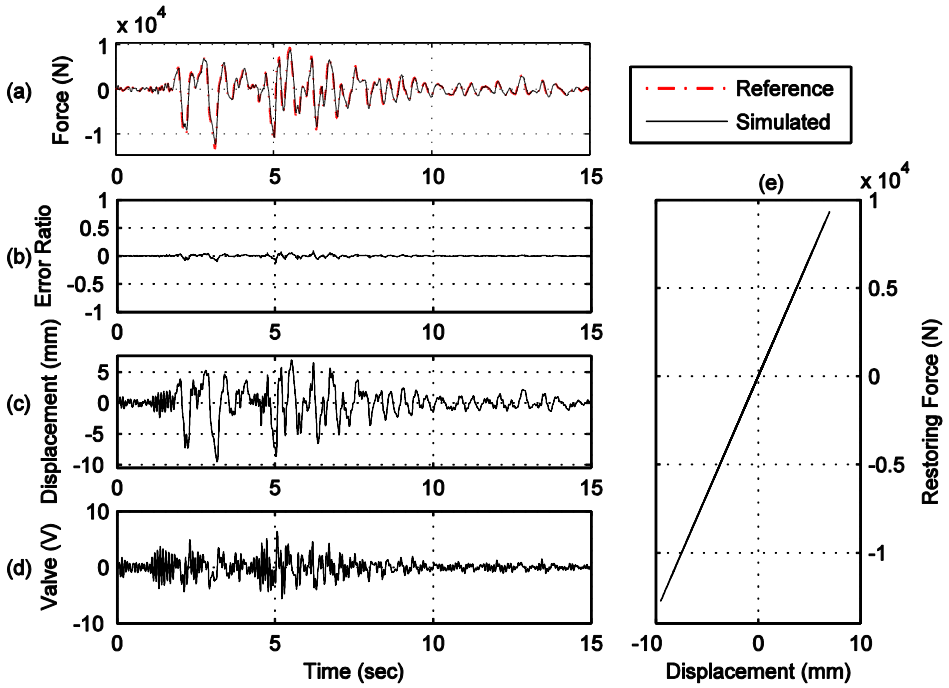

Figure C.50. Yield strength Y_y =11,000 N, post-yield stiffness $k_1 = 0.5*k_0$.

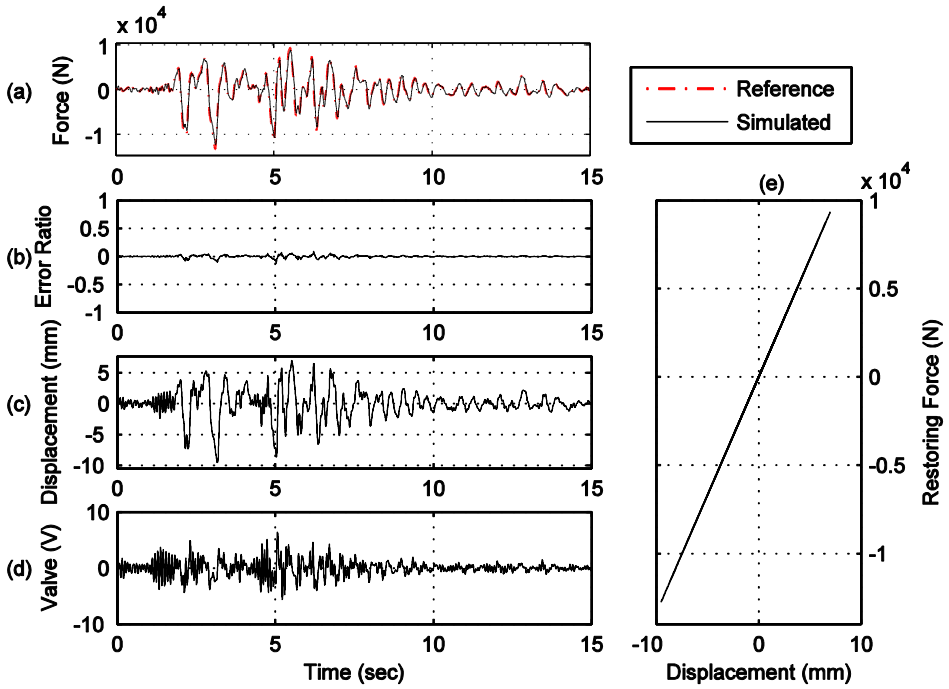

Figure C.51. Yield strength Y_y =11,000 N, post-yield stiffness $k_1 = 0.4*k_0$.

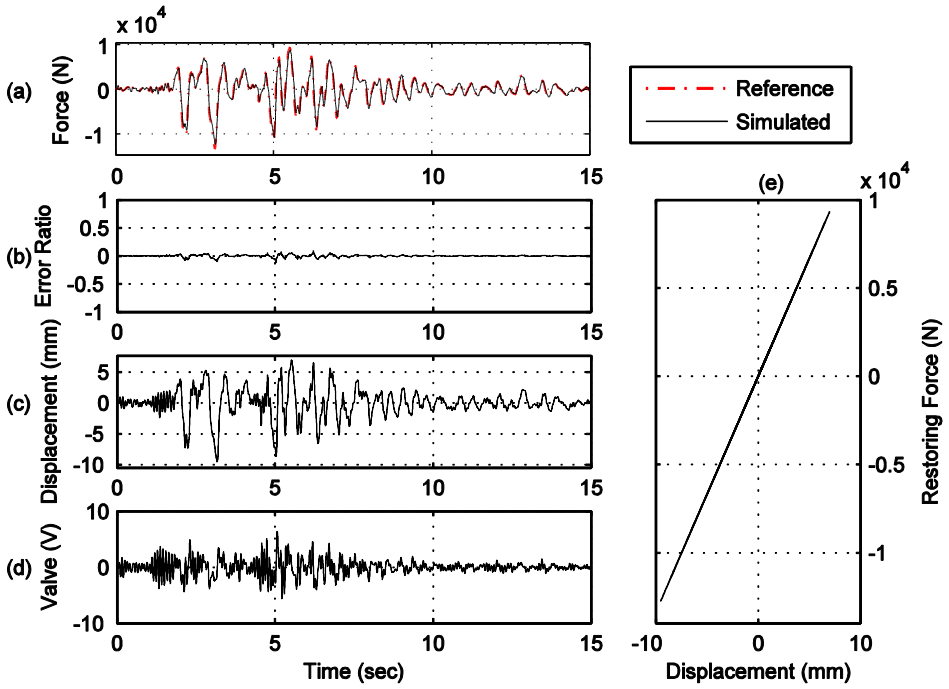

Figure C.52. Yield strength Y_y =11,000 N, post-yield stiffness $k_1 = 0.3*k_0$.

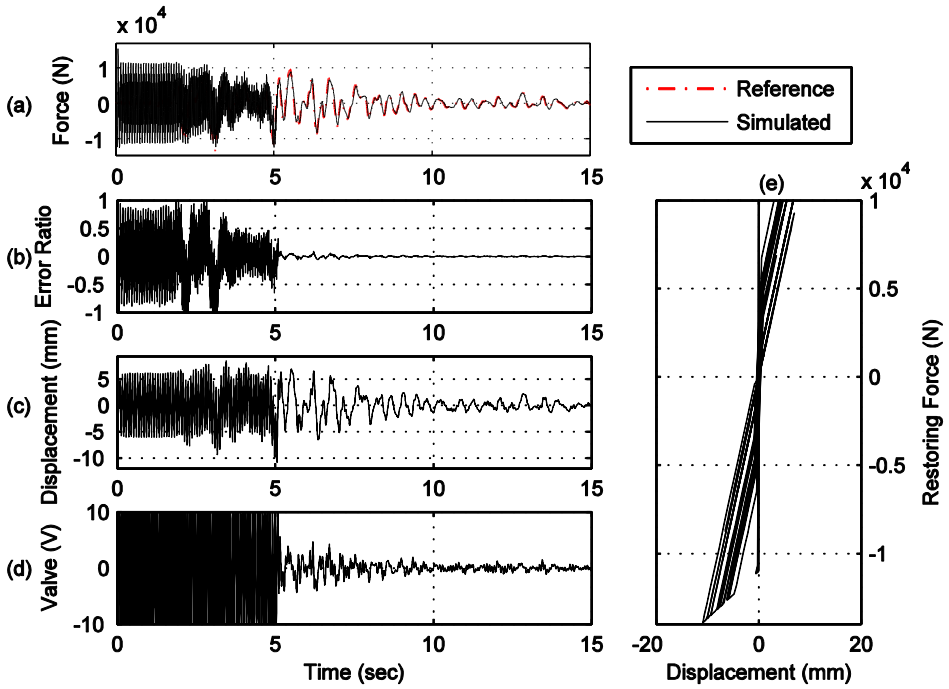

Figure C.53. Yield strength Y_y =11,000 N, post-yield stiffness $k_1 = 0.2*k_0$.

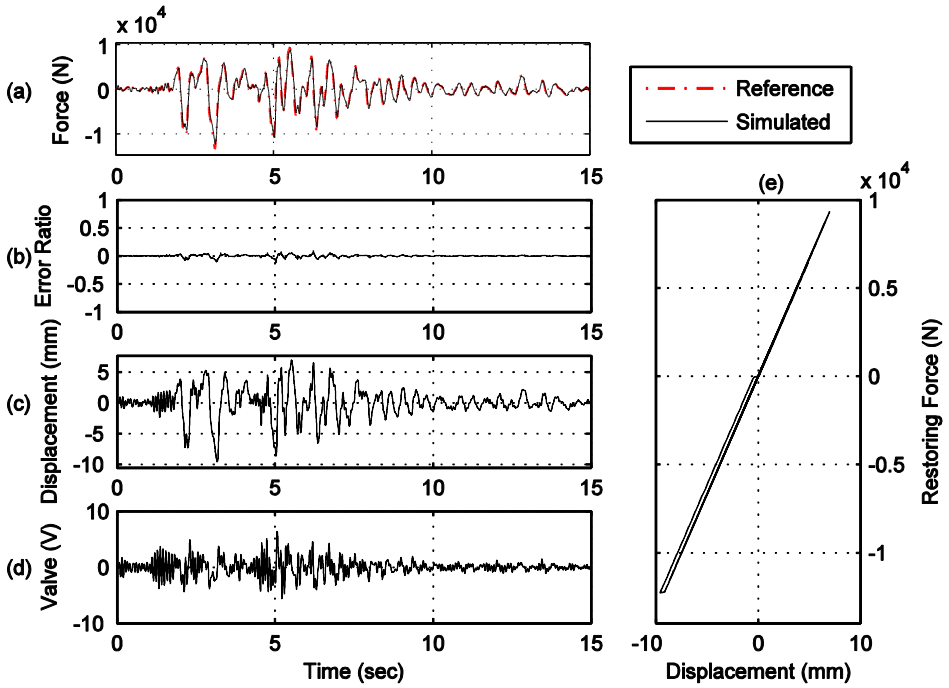

Figure C.54. Yield strength Y_y =11,000 N, post-yield stiffness $k_1 = 0.1*k_0$.

Pinned Base

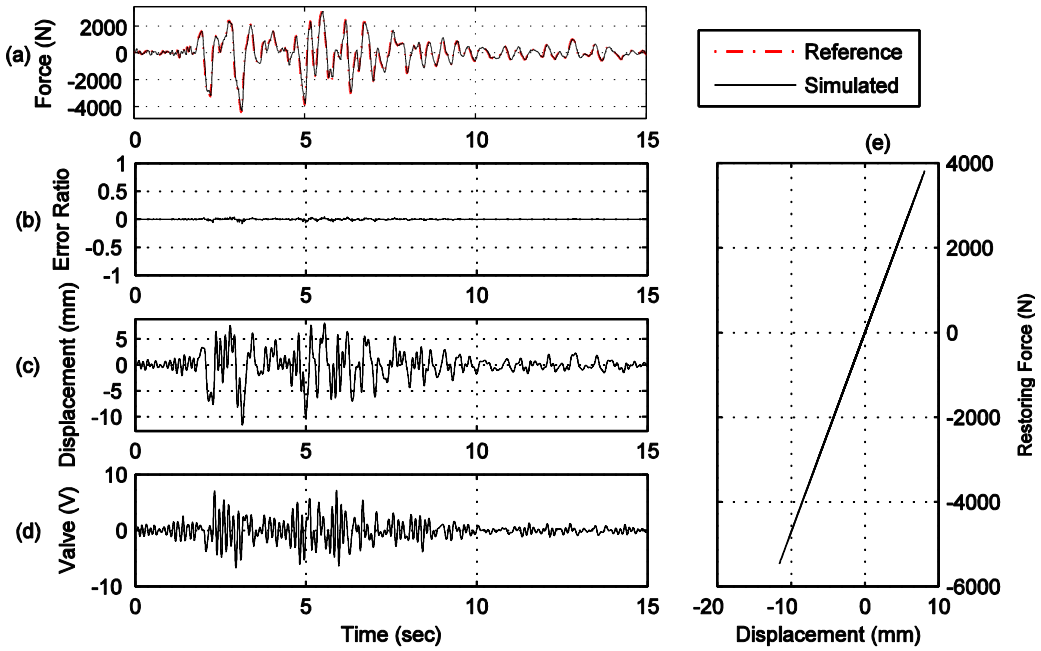

Figure C.55. Yield strength Y_y =1,000 N, post-yield stiffness $k_1 = 0.9*k_0$.

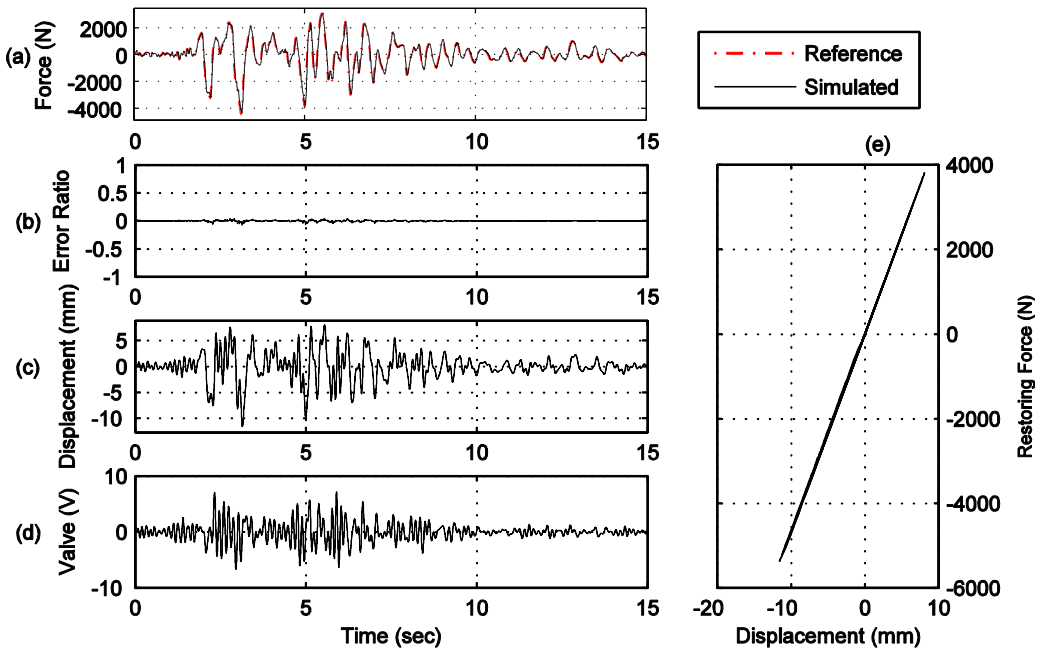

Figure C.56. Yield strength Y_y =1,000 N, post-yield stiffness $k_1 = 0.8*k_0$.

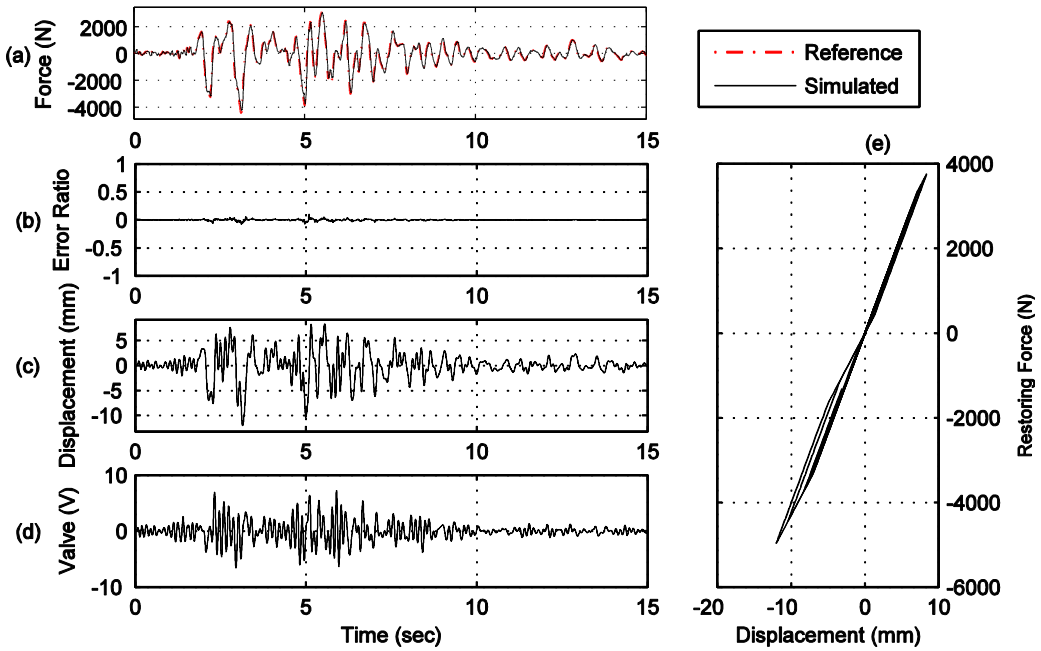

Figure C.57. Yield strength Y_y =1,000 N, post-yield stiffness $k_1 = 0.7*k_0$.

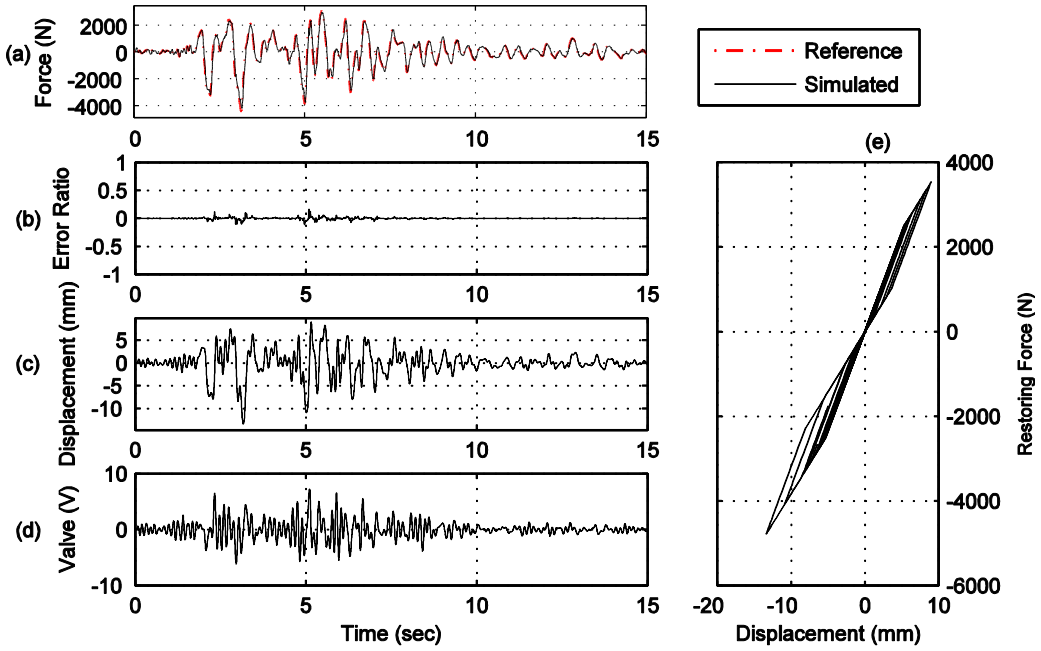

Figure C.58. Yield strength Y_y =1,000 N, post-yield stiffness $k_1 = 0.6*k_0$.

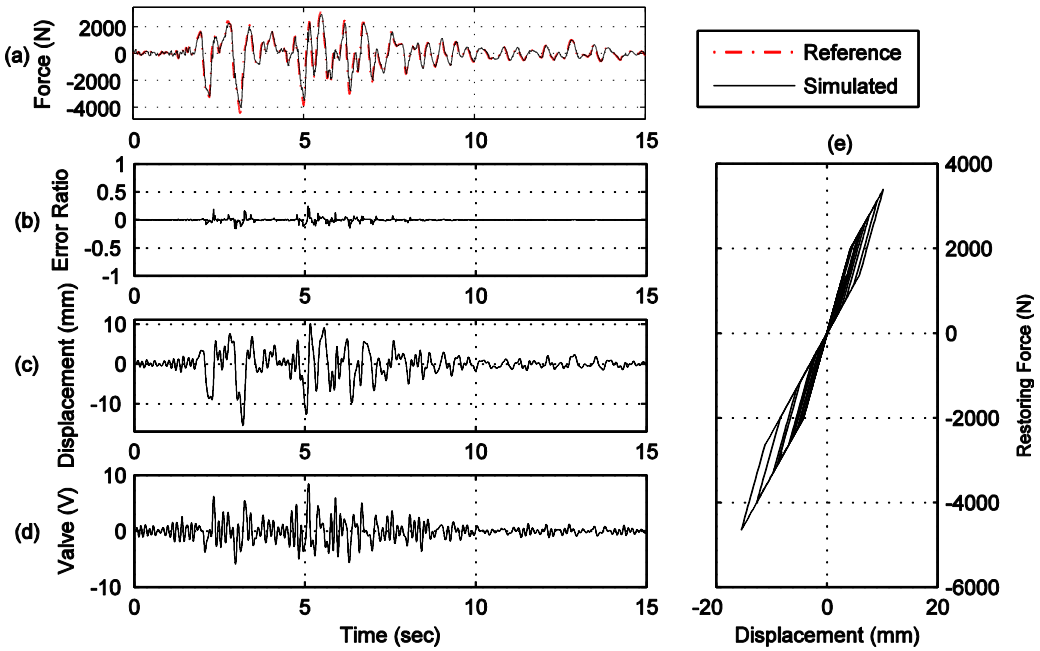

Figure C.59. Yield strength Y_y =1,000 N, post-yield stiffness $k_1 = 0.5*k_0$.

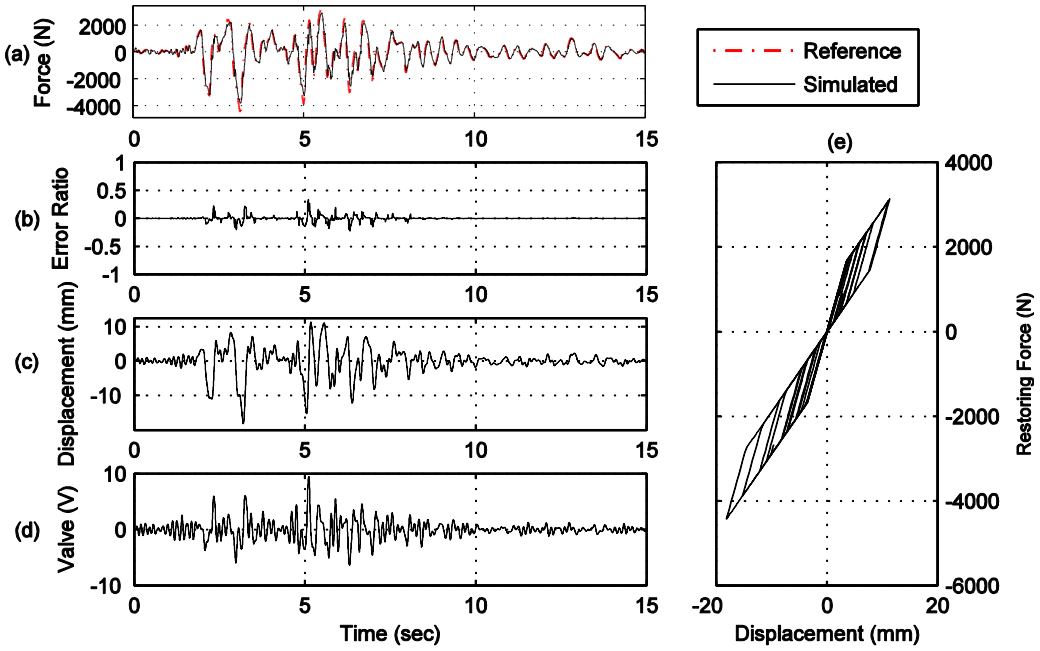

Figure C.60. Yield strength Y_y =1,000 N, post-yield stiffness $k_1 = 0.4*k_0$.

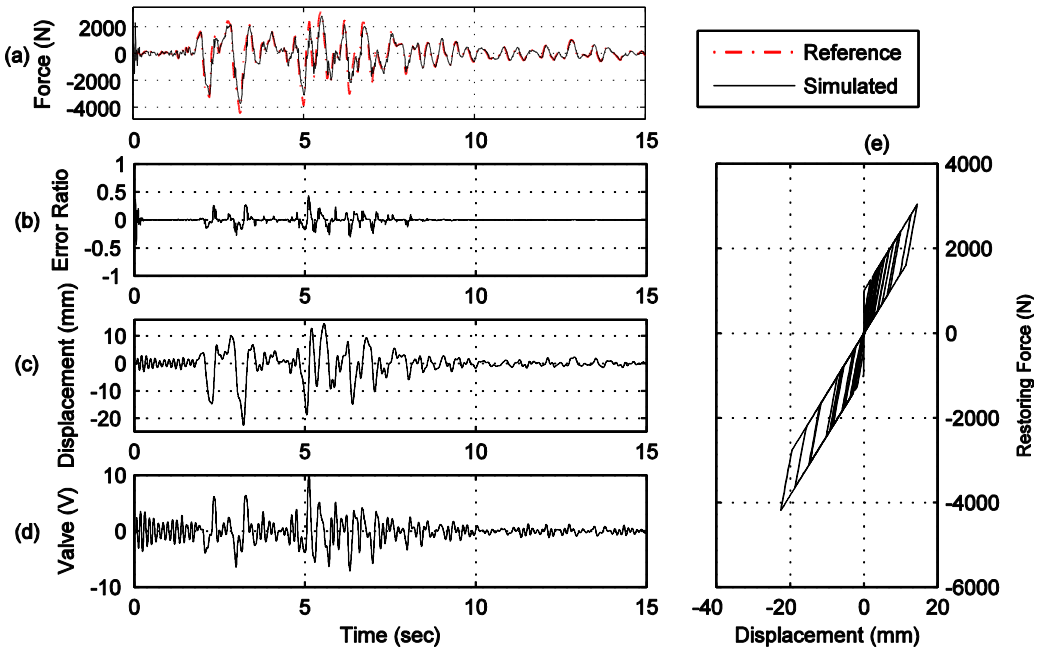

Figure C.61. Yield strength Y_y =1,000 N, post-yield stiffness $k_1 = 0.3*k_0$.

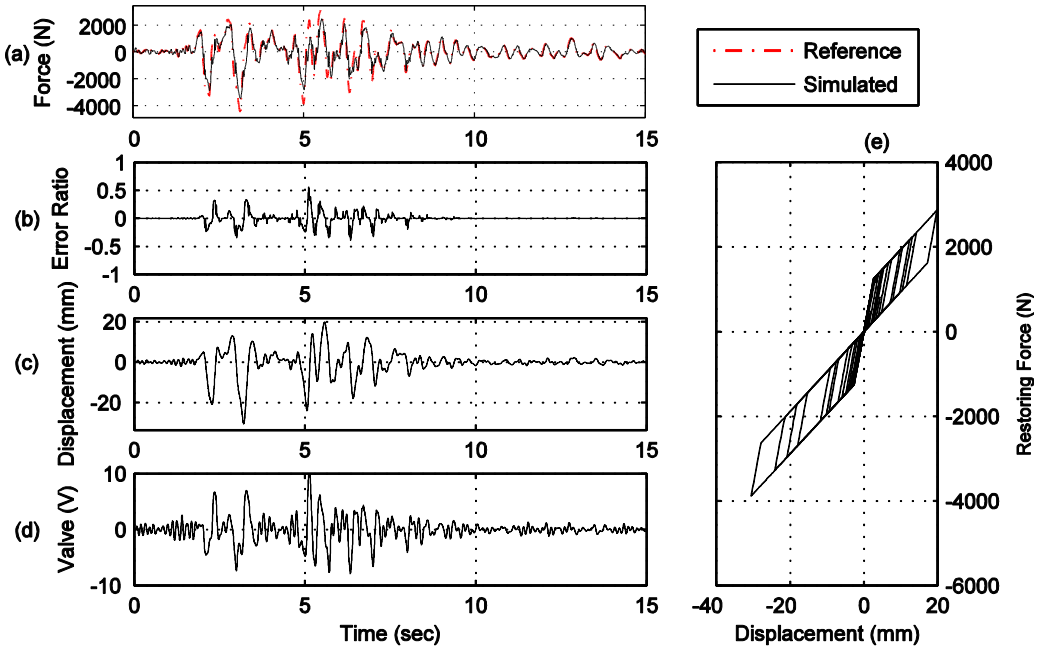

Figure C.62. Yield strength Y_y =1,000 N, post-yield stiffness $k_1 = 0.2*k_0$.

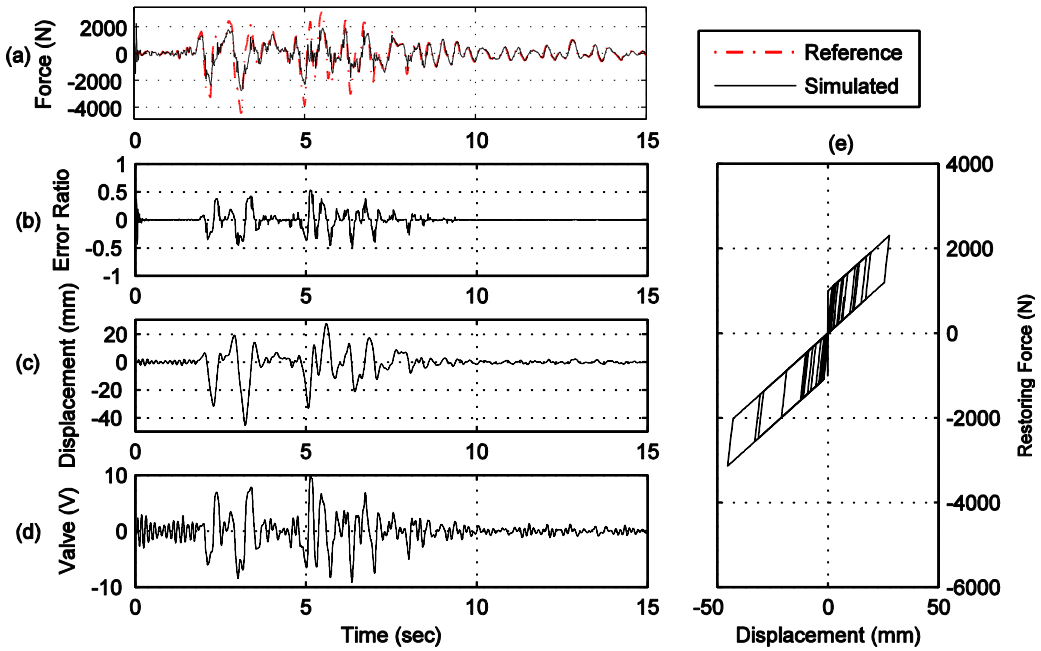

Figure C.63. Yield strength Y_y =1,000 N, post-yield stiffness $k_1 = 0.1*k_0$.

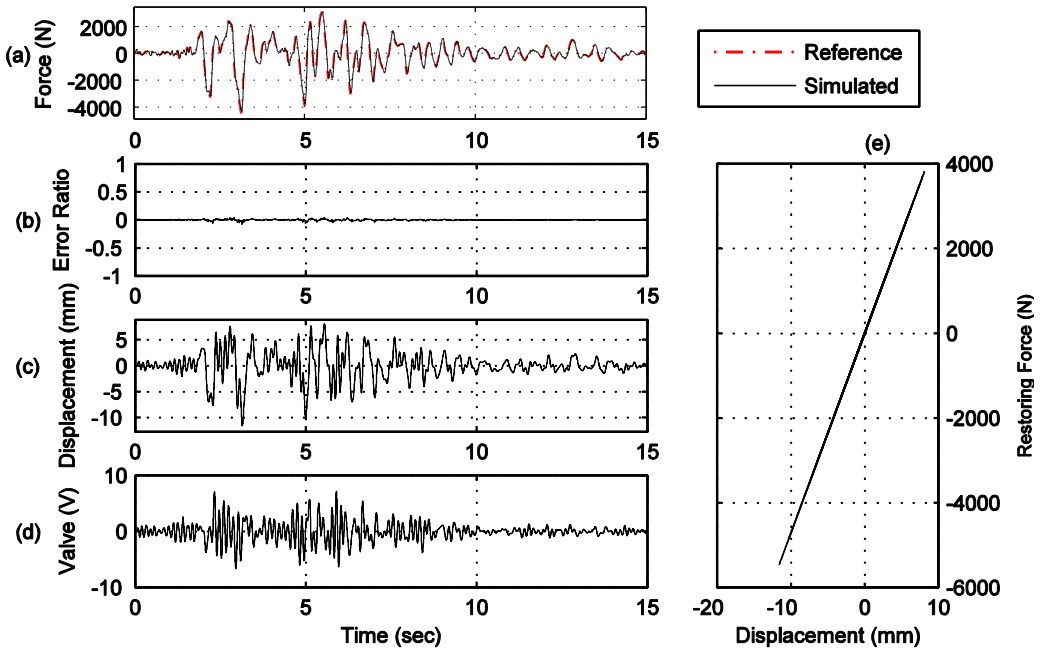

Figure C.64. Yield strength Y_y =1,500 N, post-yield stiffness $k_1 = 0.9*k_0$.

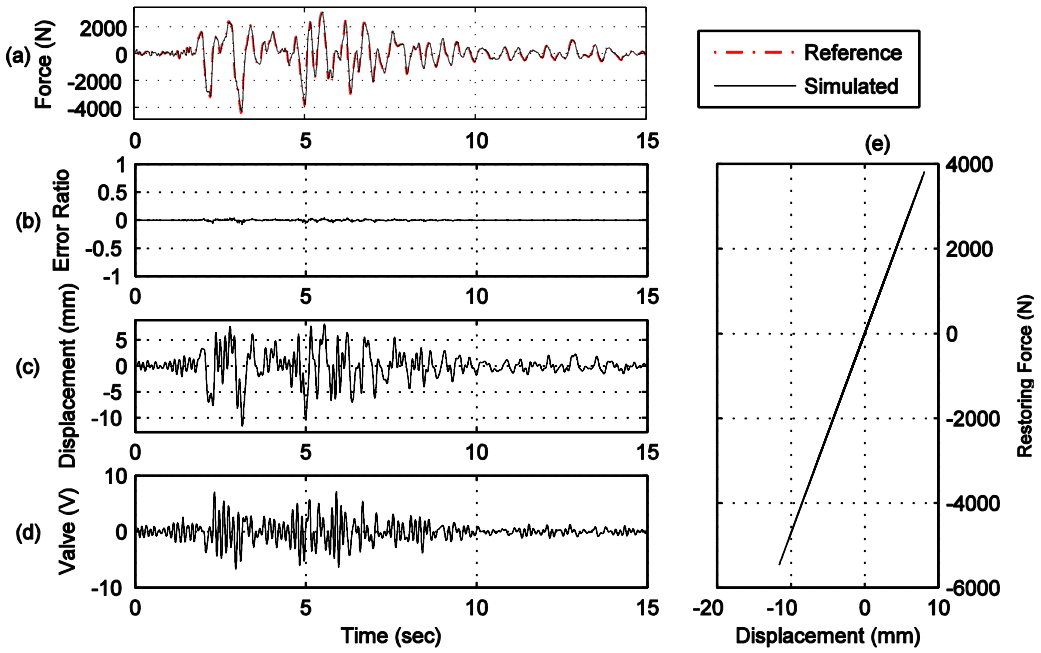

Figure C.65. Yield strength Y_y =1,500 N, post-yield stiffness $k_1 = 0.8*k_0$.

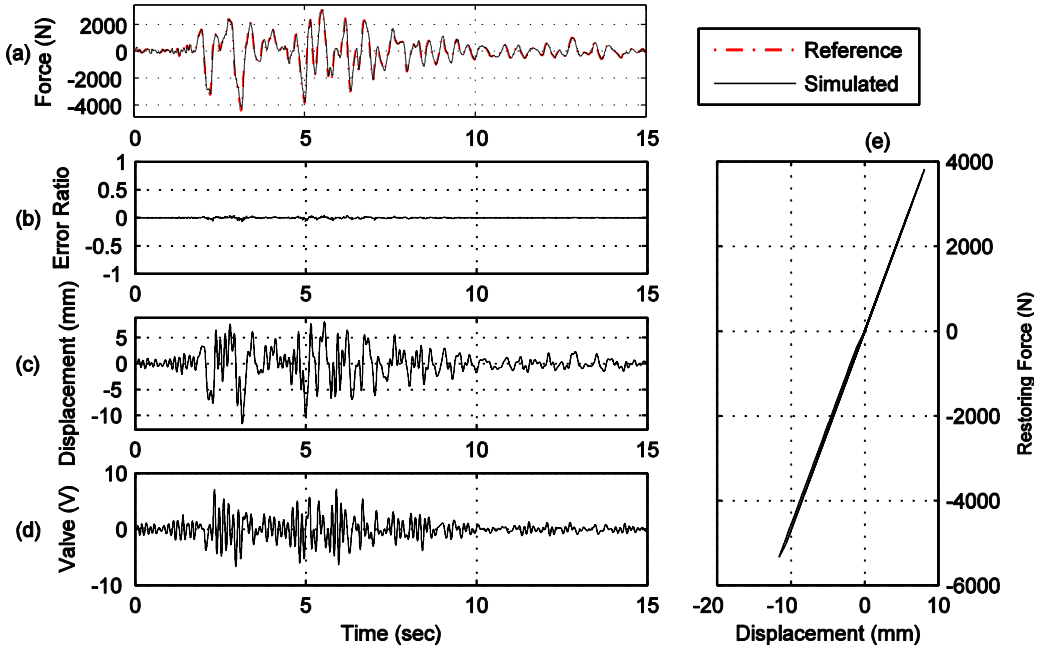

Figure C.66. Yield strength Y_y =1,500 N, post-yield stiffness $k_1 = 0.7*k_0$.

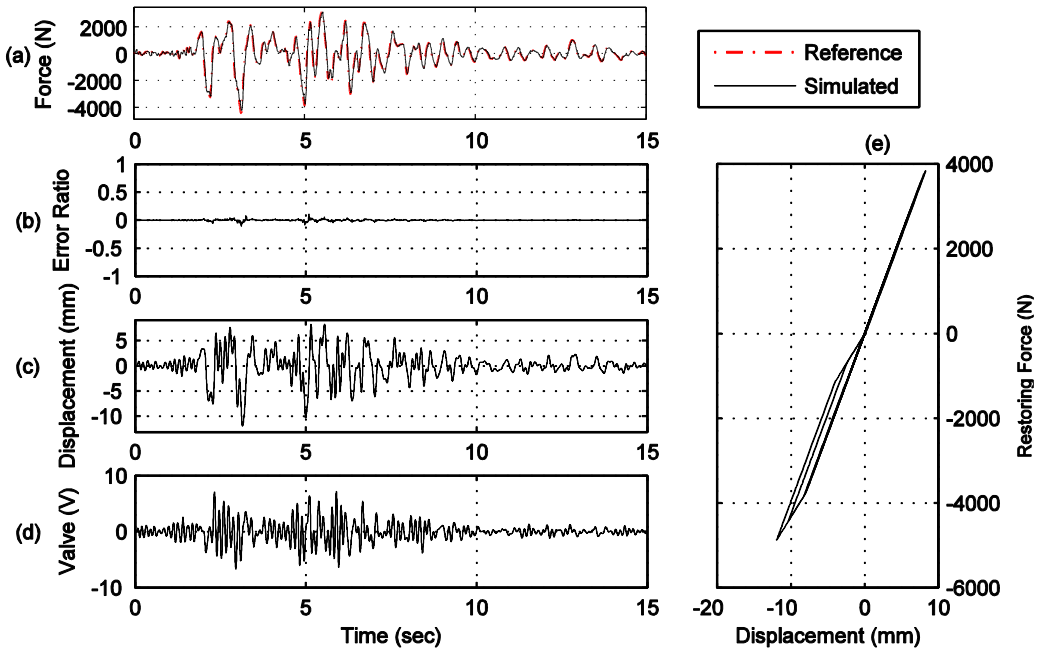

Figure C.67. Yield strength Y_y =1,500 N, post-yield stiffness $k_1 = 0.6*k_0$.

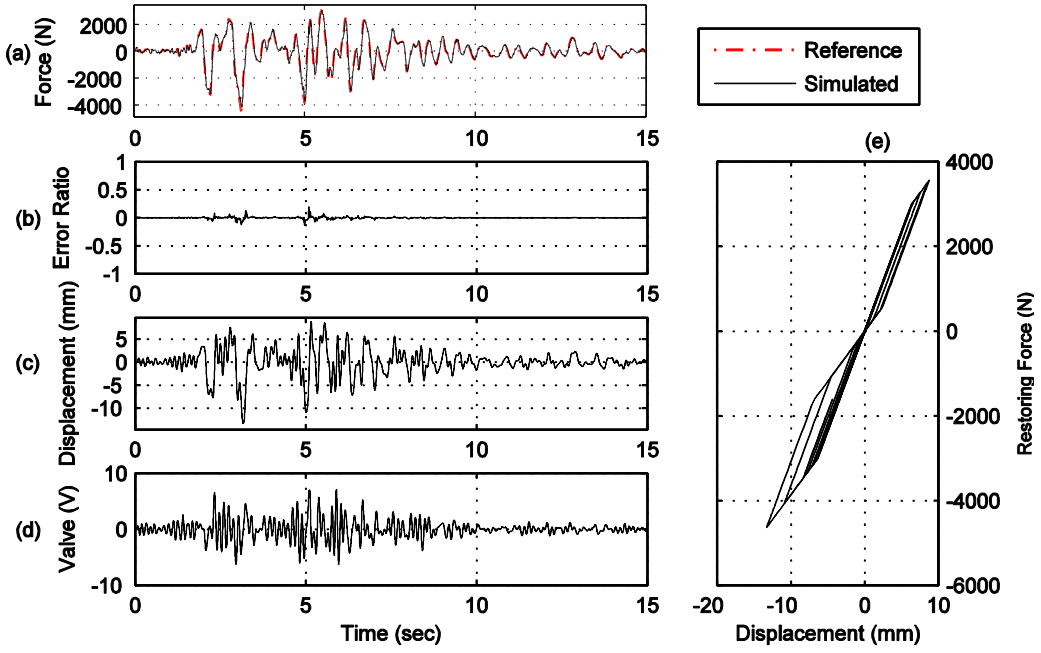

Figure C.68. Yield strength Y_y =1,500 N, post-yield stiffness $k_1 = 0.5*k_0$.

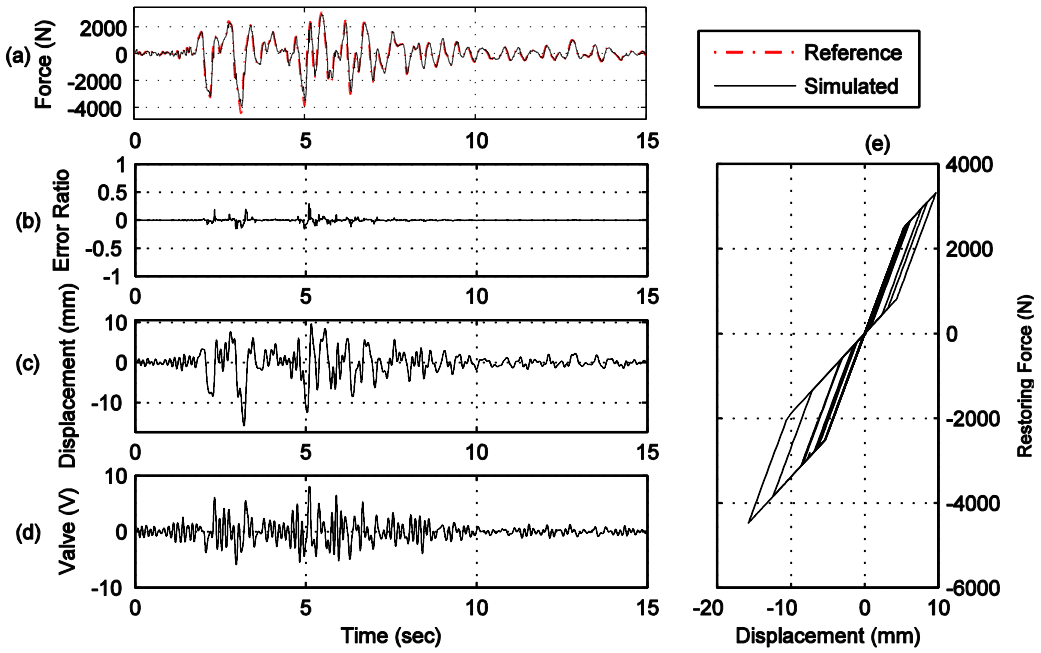

Figure C.69. Yield strength Y_y =1,500 N, post-yield stiffness $k_1 = 0.4*k_0$.

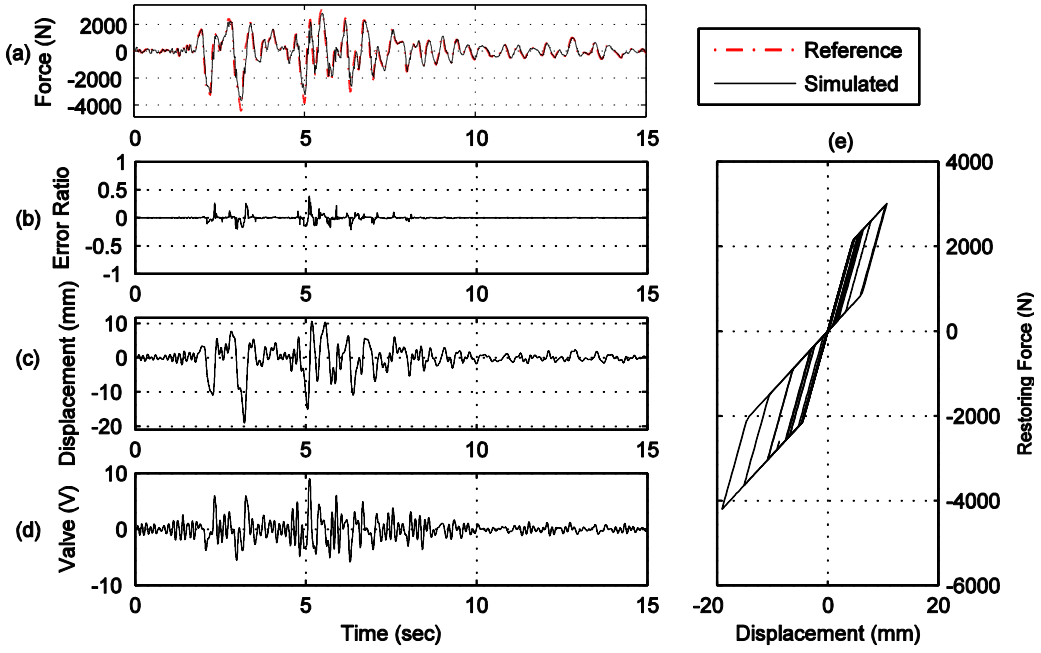

Figure C.70. Yield strength Y_y =1,500 N, post-yield stiffness $k_1 = 0.3*k_0$.

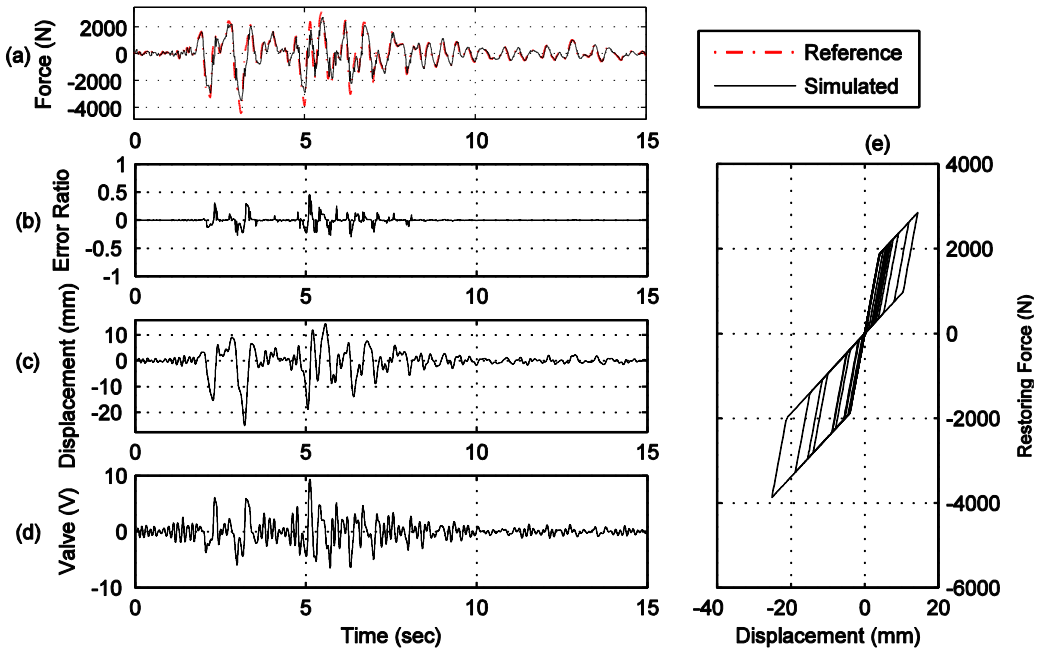

Figure C.71. Yield strength Y_y =1,500 N, post-yield stiffness $k_1 = 0.2*k_0$.

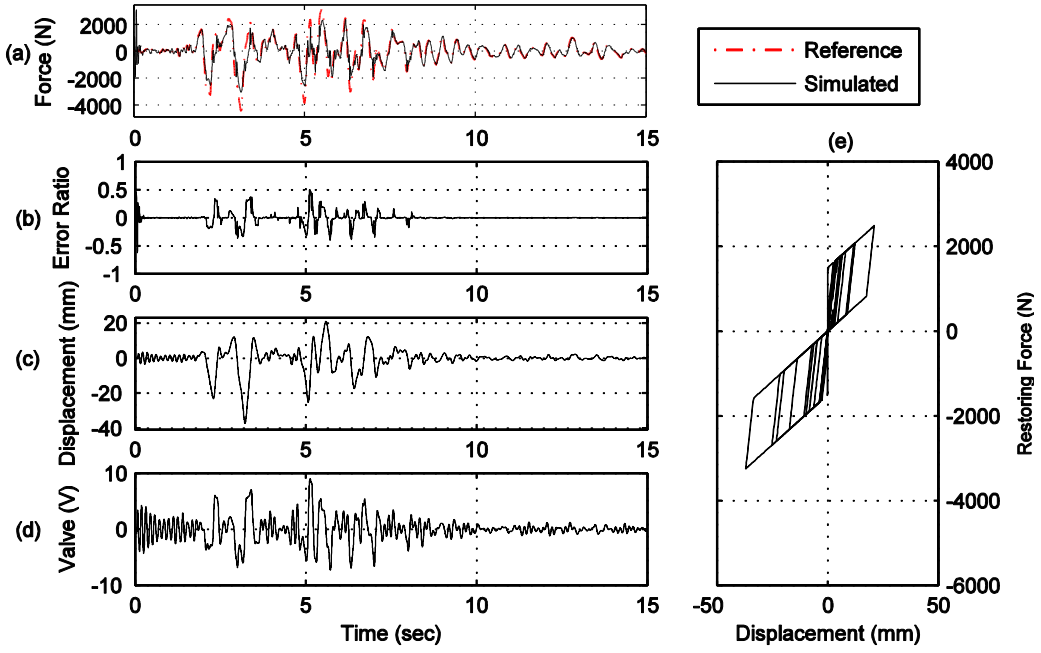

Figure C.72. Yield strength Y_y =1,500 N, post-yield stiffness $k_1 = 0.1*k_0$.

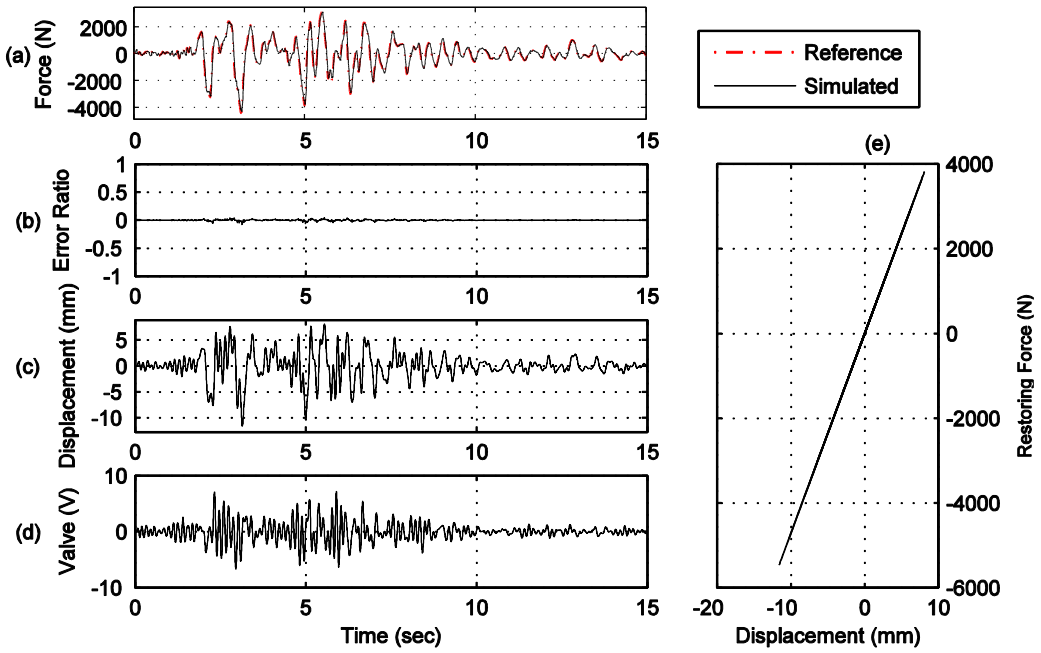

Figure C.73. Yield strength Y_y =2,000 N, post-yield stiffness $k_1 = 0.9*k_0$.

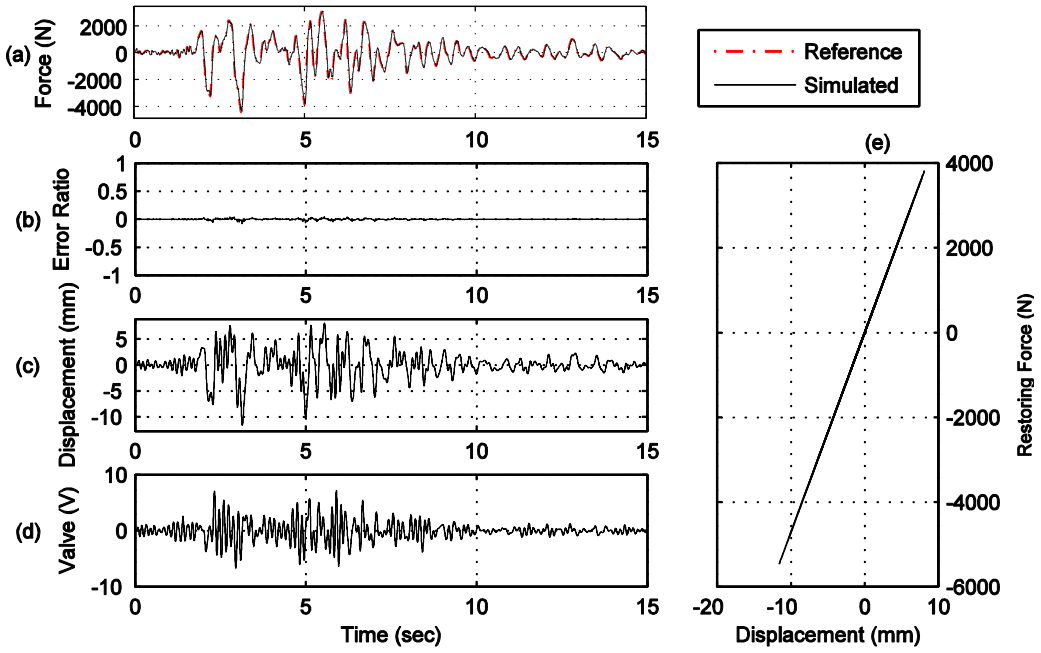

Figure C.74. Yield strength Y_y =2,000 N, post-yield stiffness $k_1 = 0.8*k_0$.

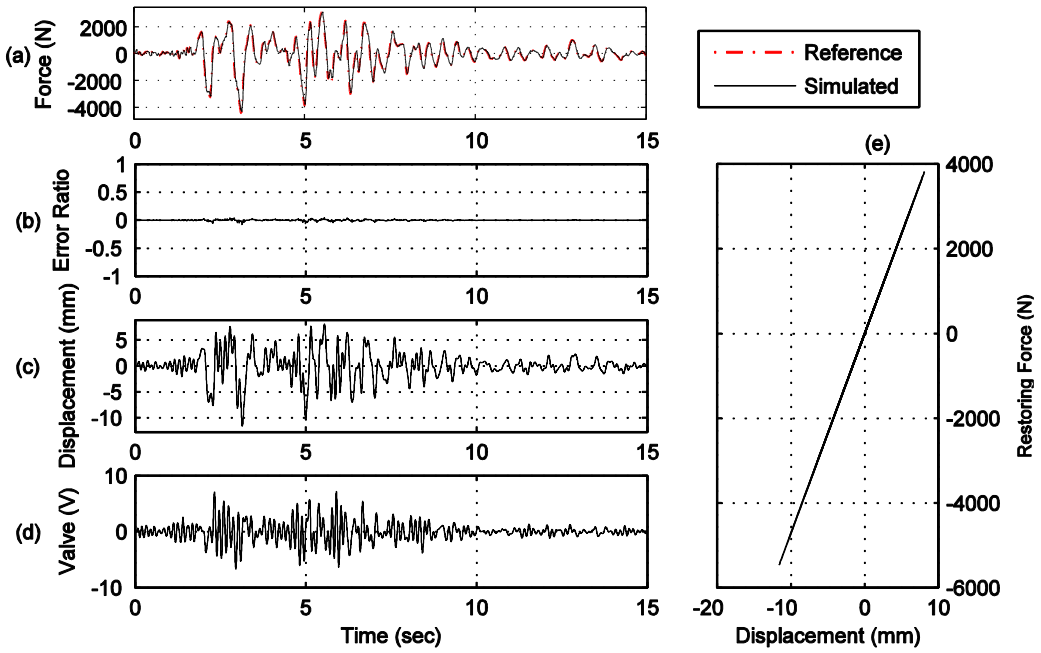

Figure C.75. Yield strength Y_y =2,000 N, post-yield stiffness $k_1 = 0.7*k_0$.

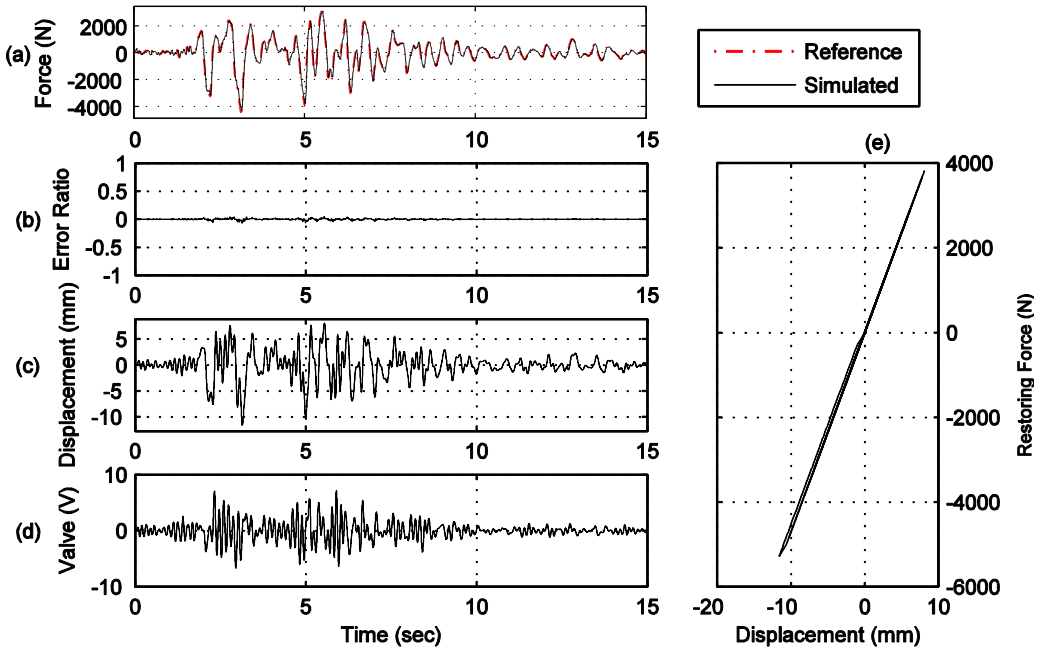

Figure C.76. Yield strength Y_y =2,000 N, post-yield stiffness $k_1 = 0.6*k_0$.

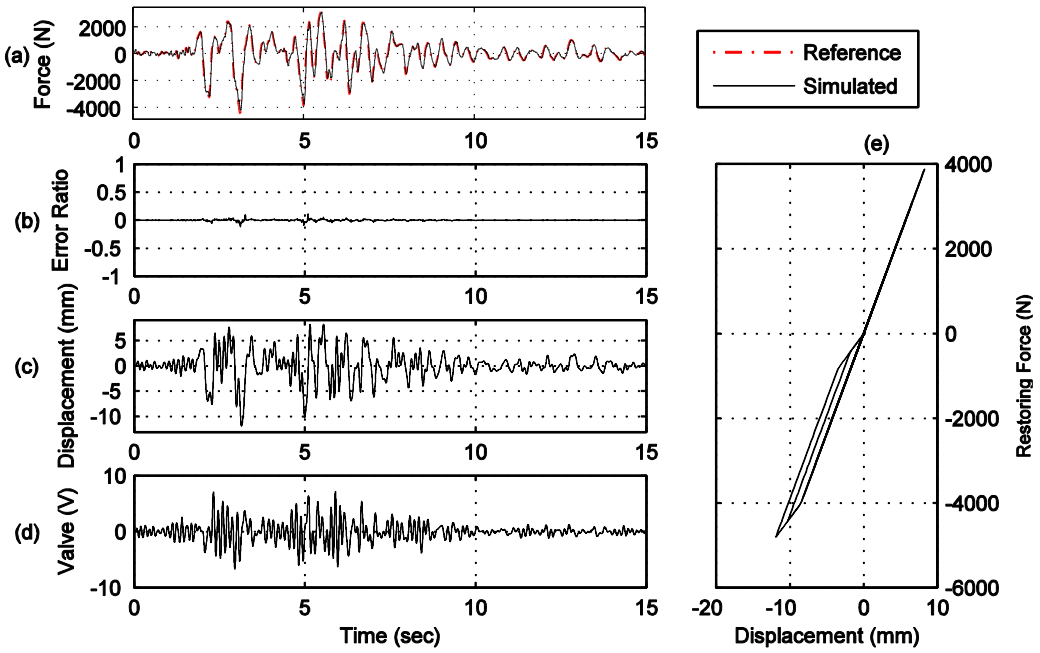

Figure C.77. Yield strength Y_y =2,000 N, post-yield stiffness $k_1 = 0.5*k_0$.

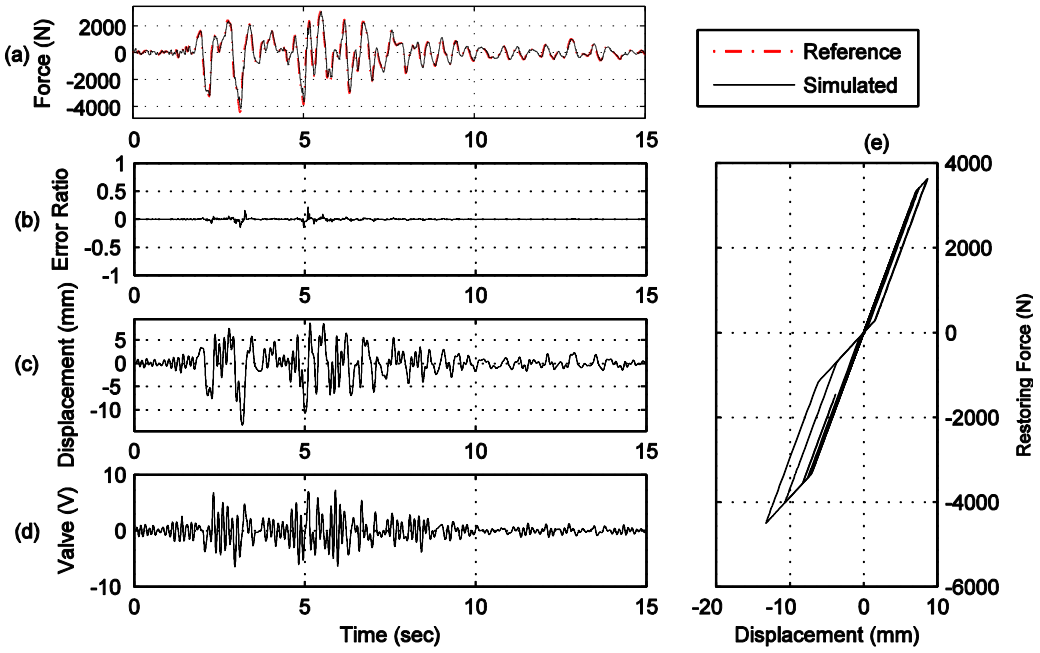

Figure C.78. Yield strength Y_y =2,000 N, post-yield stiffness $k_1 = 0.4*k_0$.

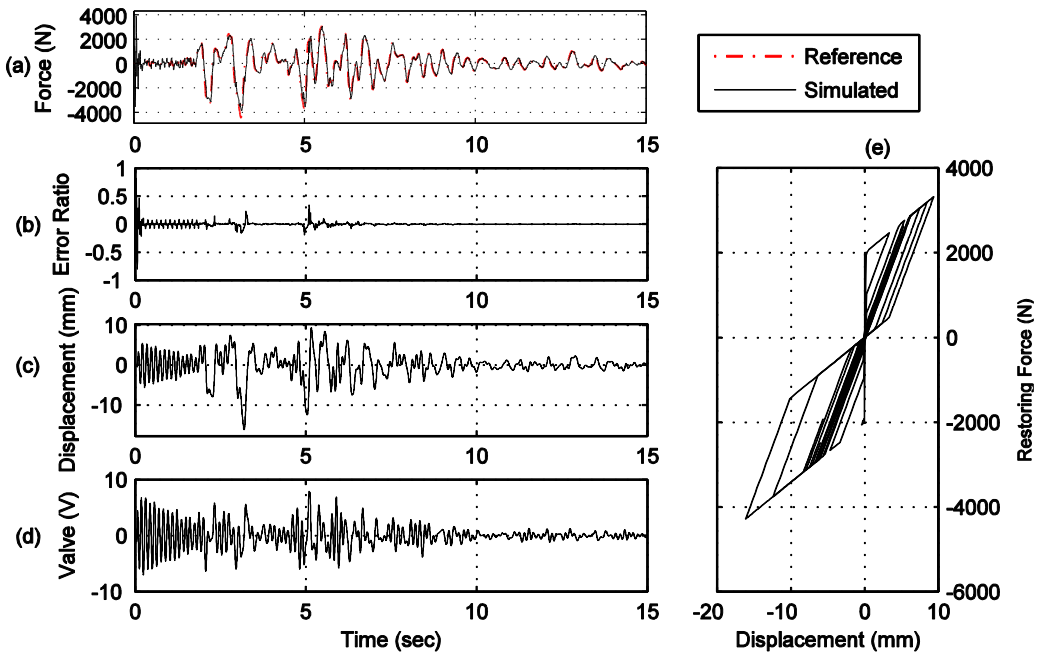

Figure C.79. Yield strength Y_y =2,000 N, post-yield stiffness $k_1 = 0.3*k_0$.

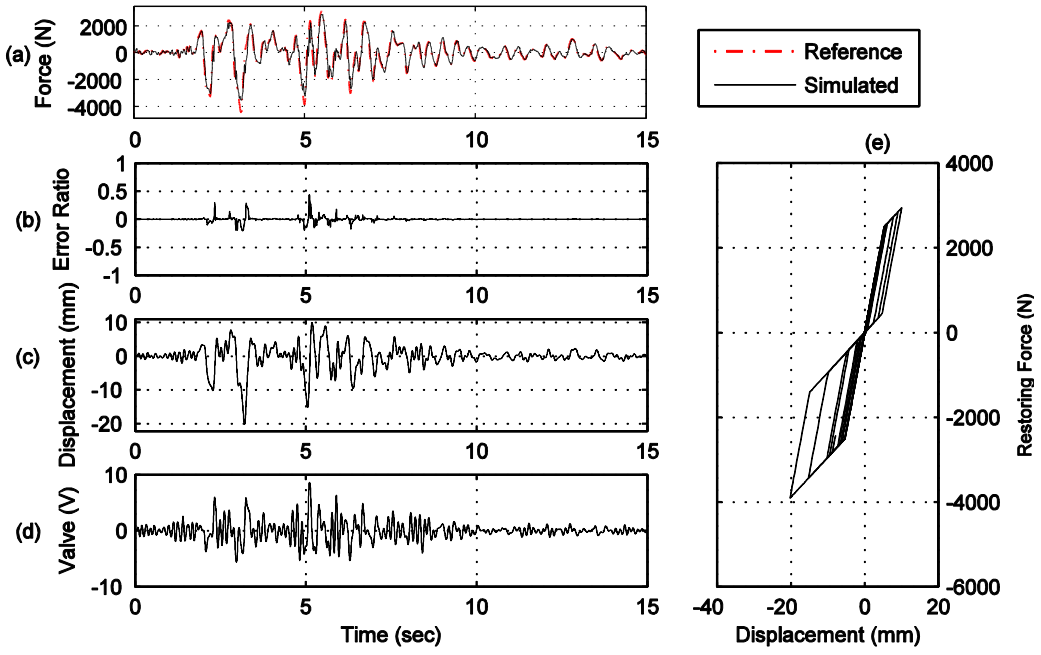

Figure C.80. Yield strength Y_y =2,000 N, post-yield stiffness $k_1 = 0.2*k_0$.

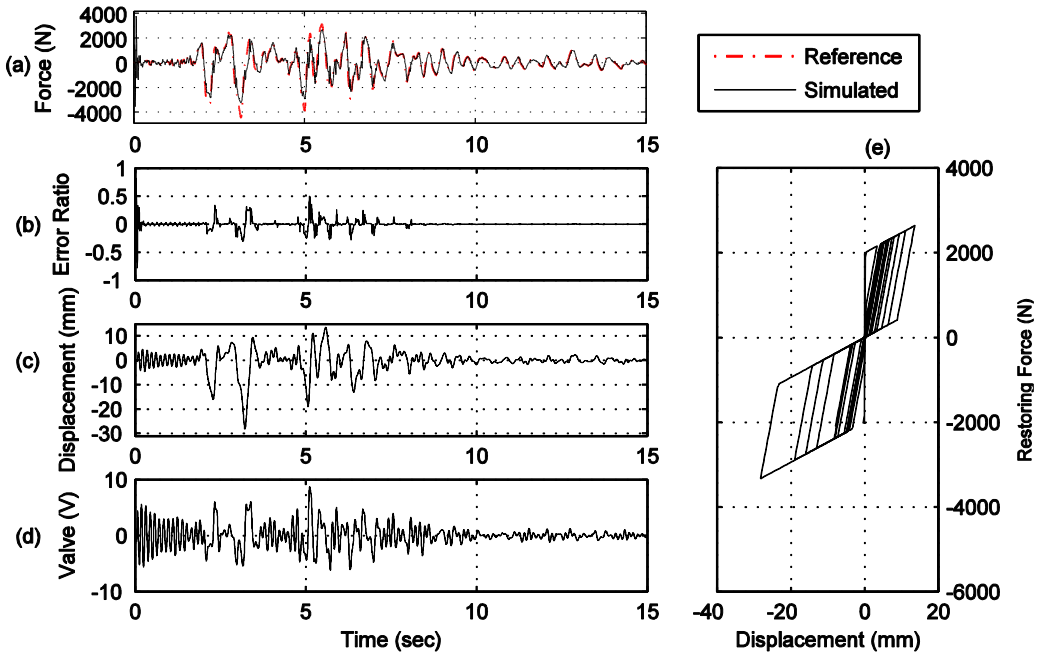

Figure C.81. Yield strength Y_y =2,000 N, post-yield stiffness $k_1 = 0.1*k_0$.

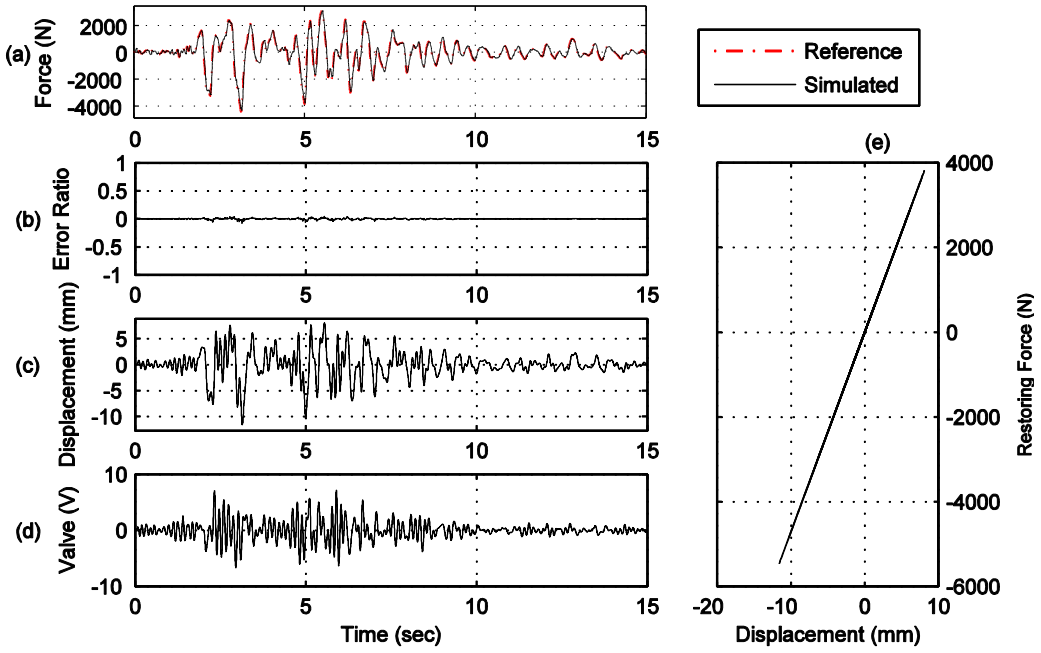

Figure C.82. Yield strength Y_y =2,500 N, post-yield stiffness $k_1 = 0.9*k_0$.

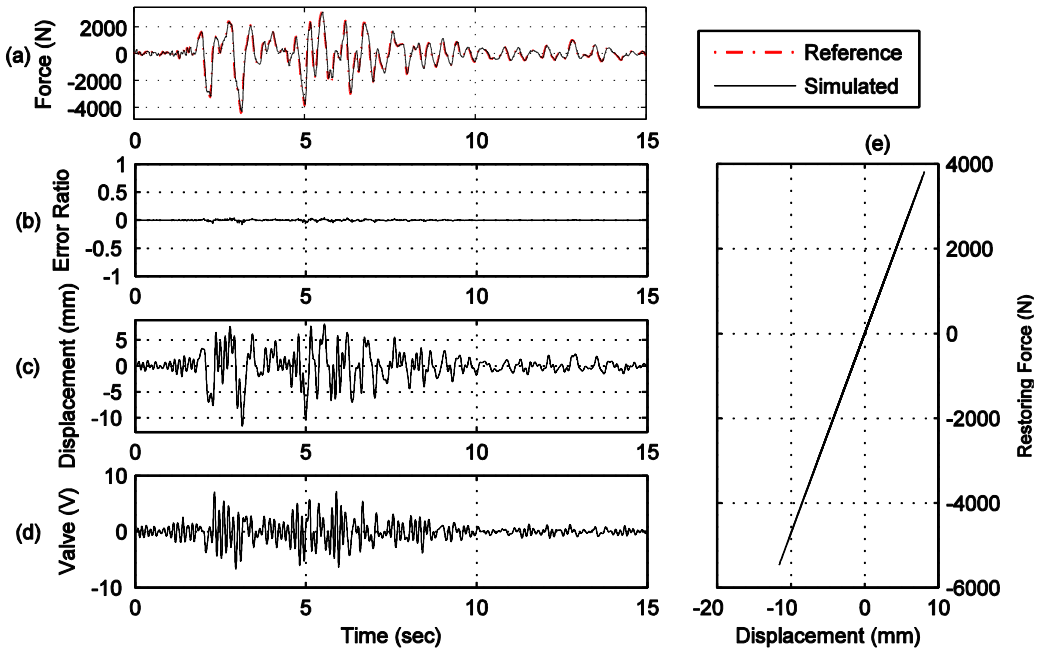

Figure C.83. Yield strength Y_y =2,500 N, post-yield stiffness $k_1 = 0.8*k_0$.

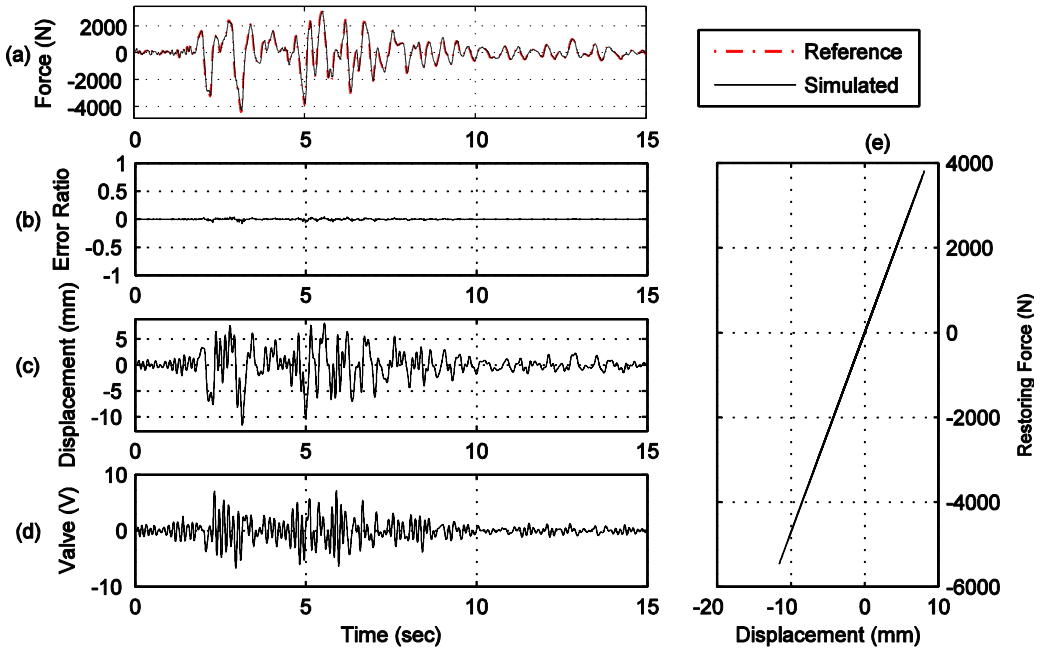

Figure C.84. Yield strength Y_y =2,500 N, post-yield stiffness $k_1 = 0.7*k_0$.

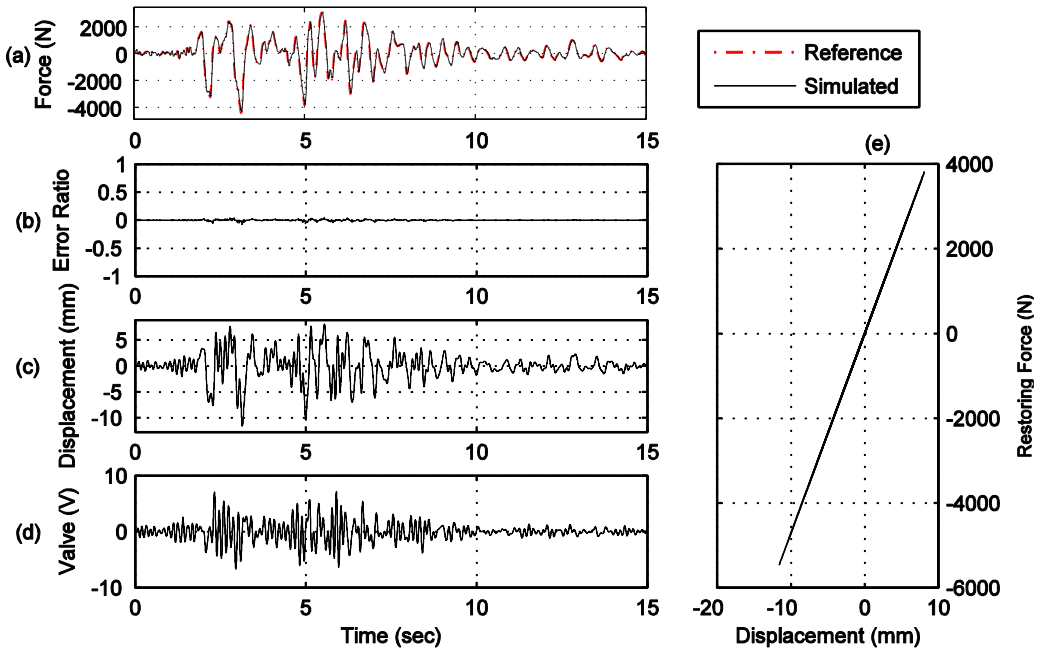

Figure C.85. Yield strength Y_y =2,500 N, post-yield stiffness $k_1 = 0.6*k_0$.

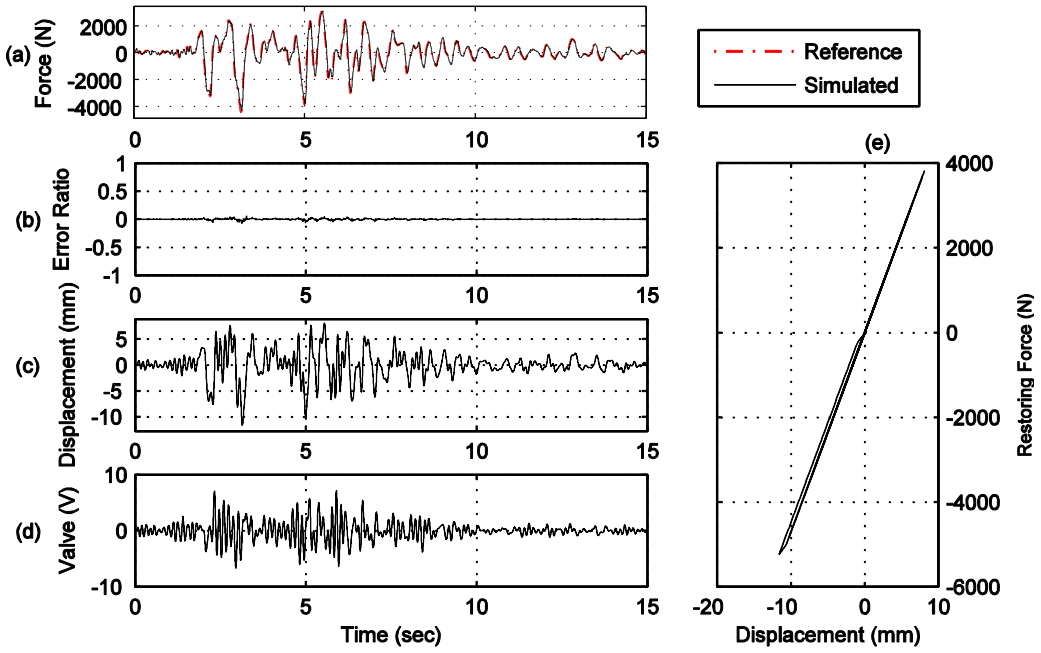

Figure C.86. Yield strength Y_y =2,500 N, post-yield stiffness $k_1 = 0.5*k_0$.

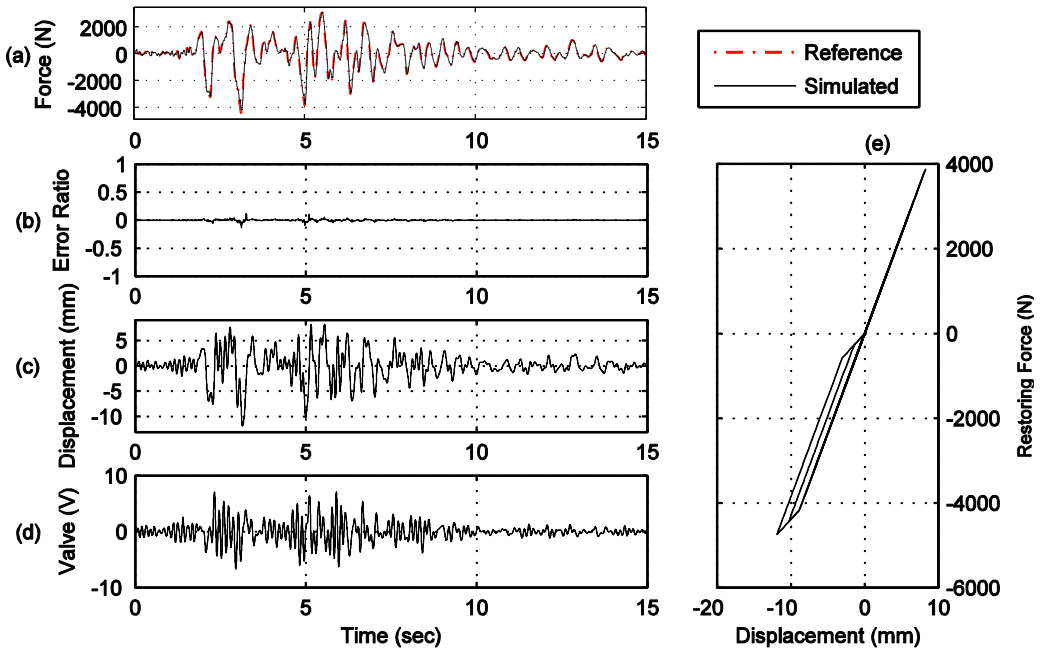

Figure C.87. Yield strength Y_y =2,500 N, post-yield stiffness $k_1 = 0.4*k_0$.

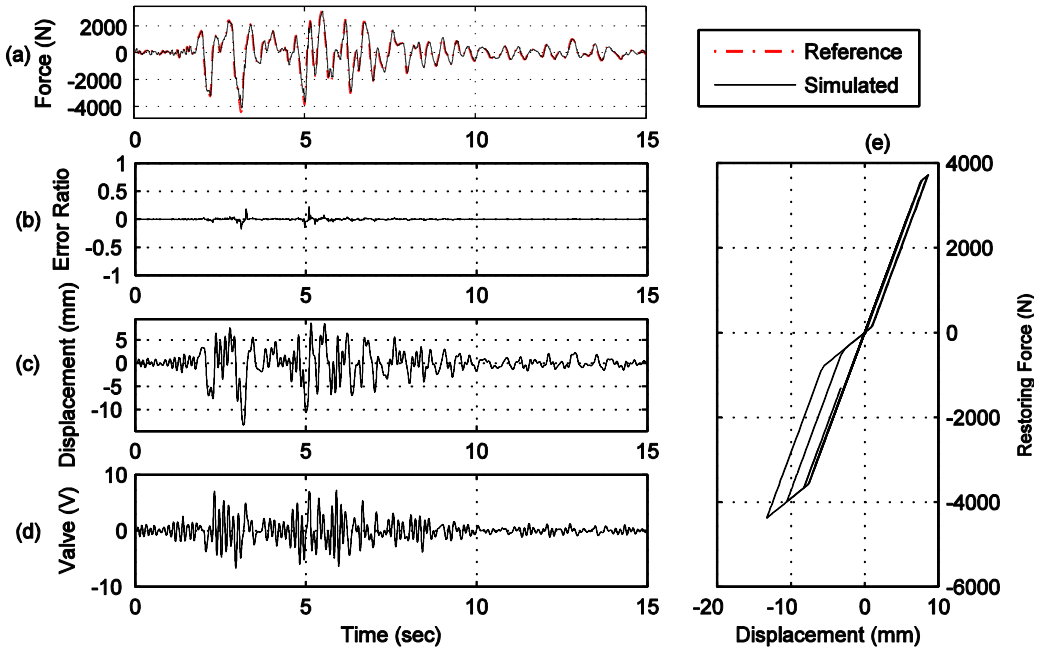

Figure C.88. Yield strength Y_y =2,500 N, post-yield stiffness $k_1 = 0.3*k_0$.

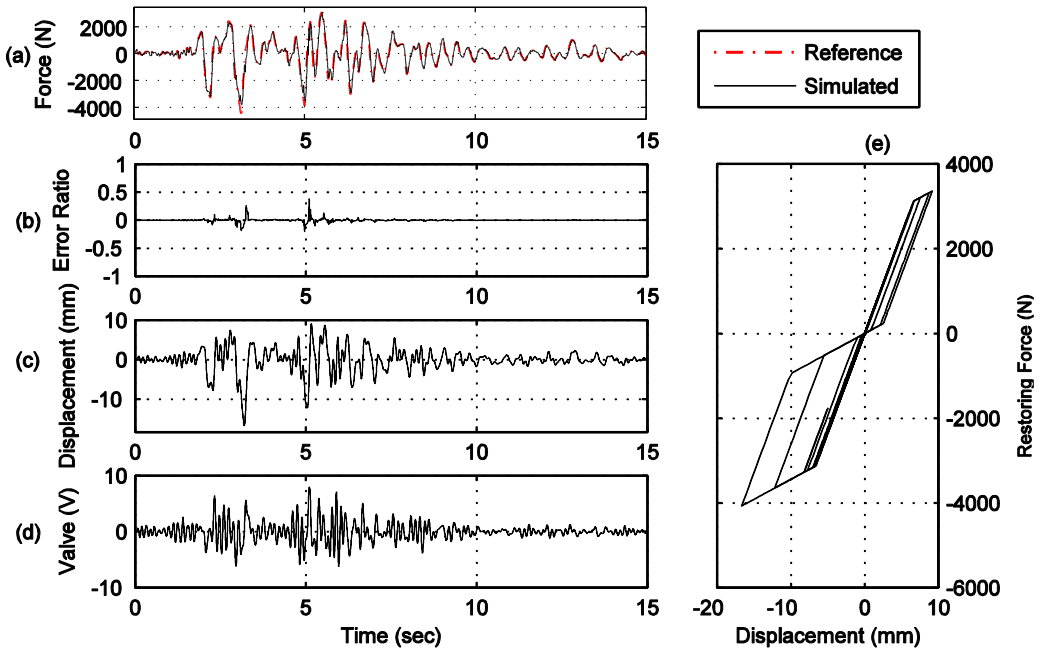

Figure C.89. Yield strength Y_y =2,500 N, post-yield stiffness $k_1 = 0.2*k_0$.

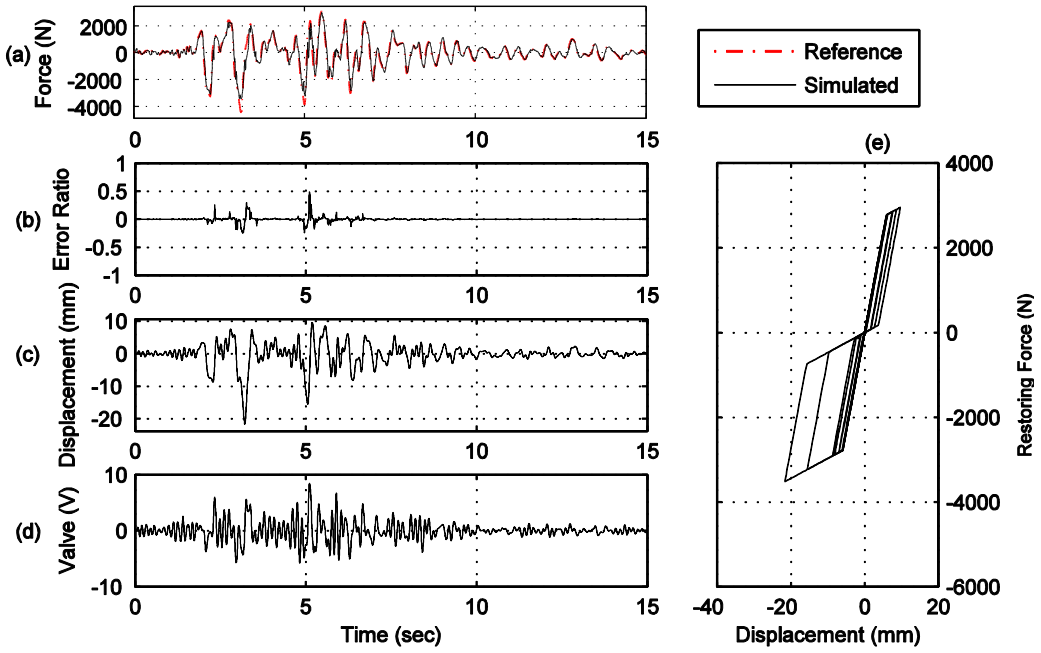

Figure C.90. Yield strength Y_y =2,500 N, post-yield stiffness $k_1 = 0.1*k_0$.

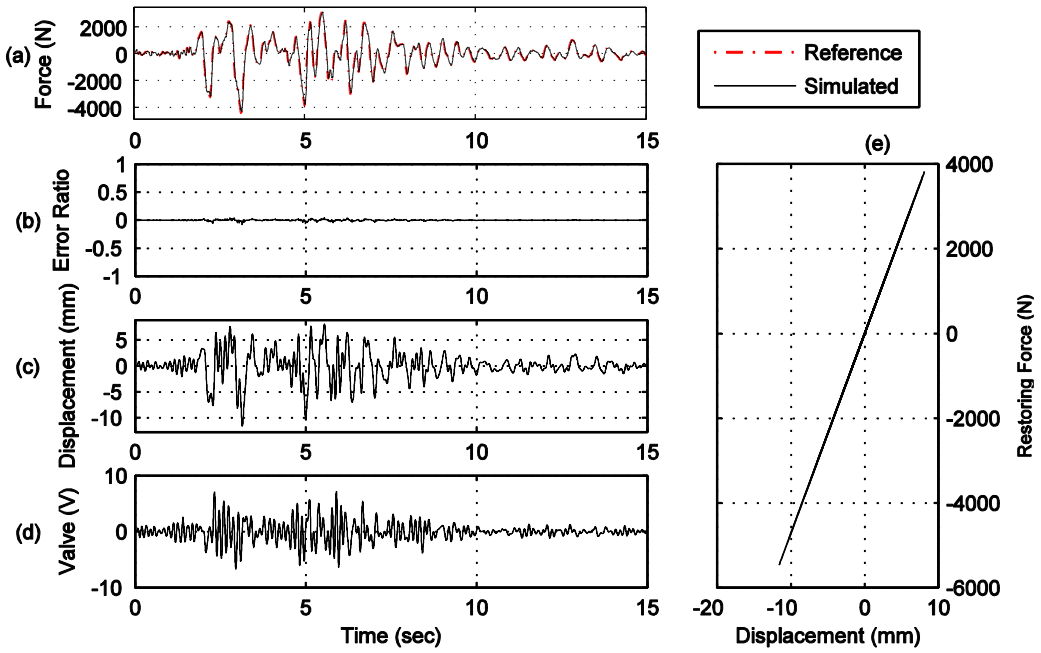

Figure C.91. Yield strength Y_y =3,000 N, post-yield stiffness $k_1 = 0.9*k_0$.

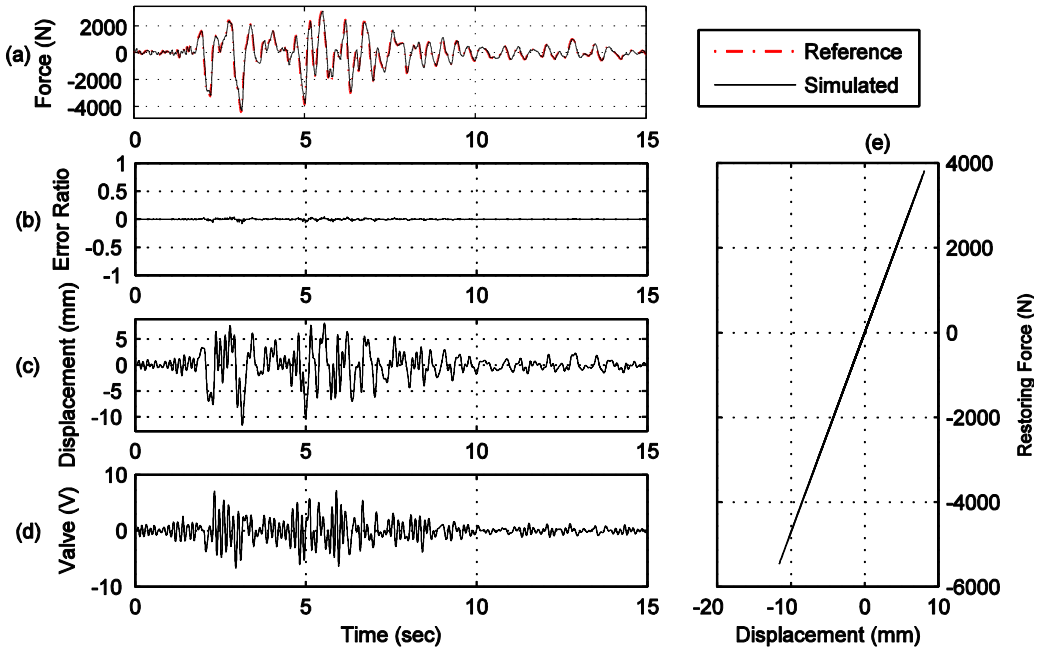

Figure C.92. Yield strength Y_y =3,000 N, post-yield stiffness $k_1 = 0.8*k_0$.

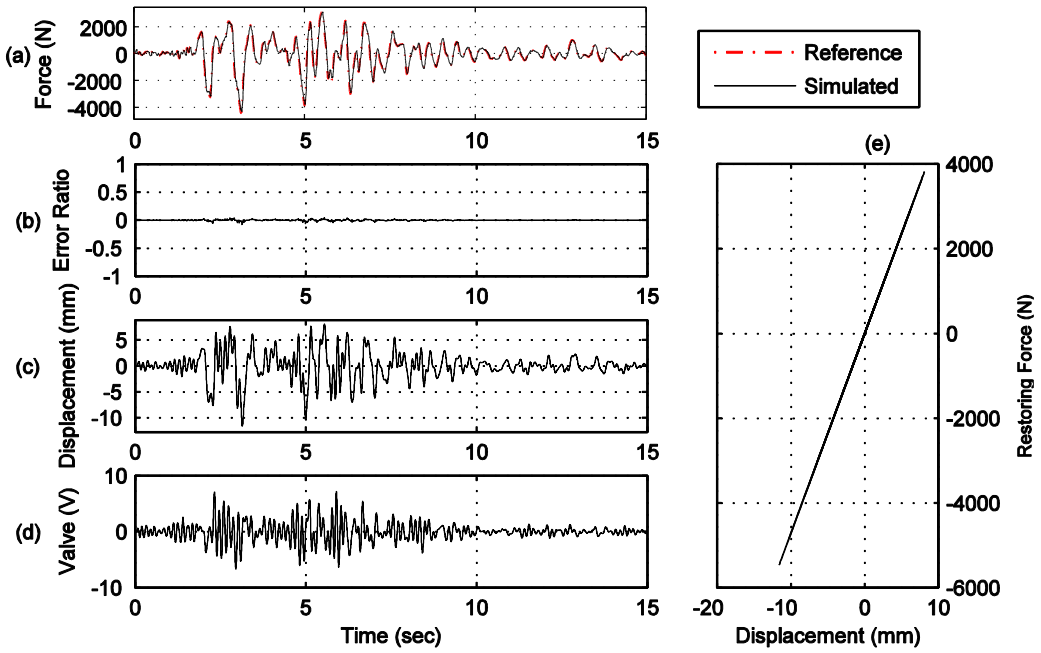

Figure C.93. Yield strength Y_y =3,000 N, post-yield stiffness $k_1 = 0.7*k_0$.

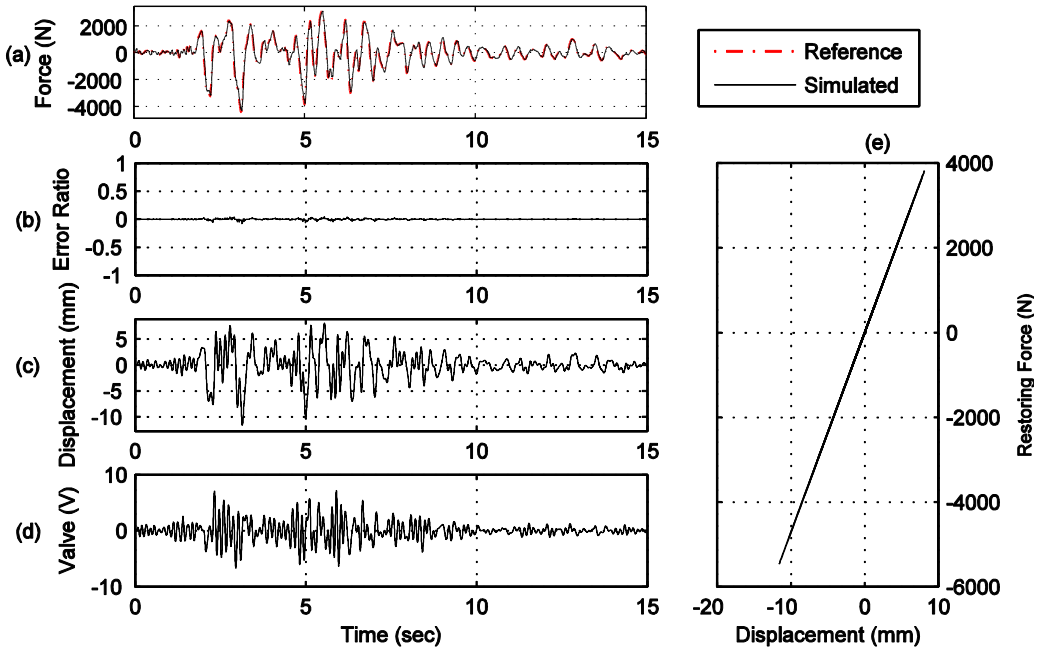

Figure C.94. Yield strength Y_y =3,000 N, post-yield stiffness $k_1 = 0.6*k_0$.

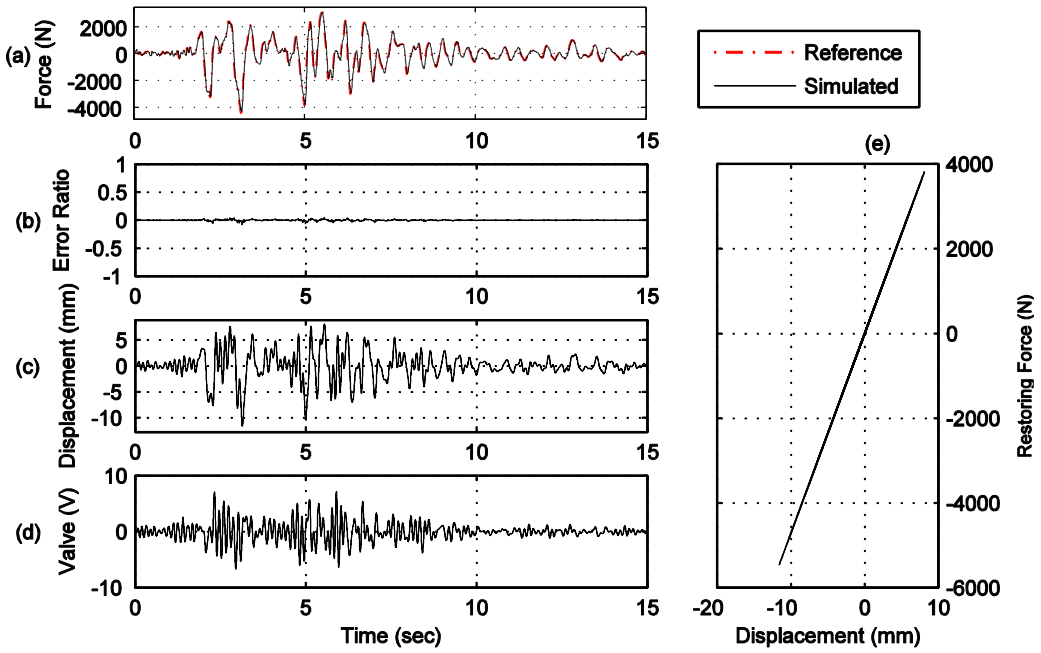

Figure C.95. Yield strength Y_y =3,000 N, post-yield stiffness $k_1 = 0.5*k_0$.

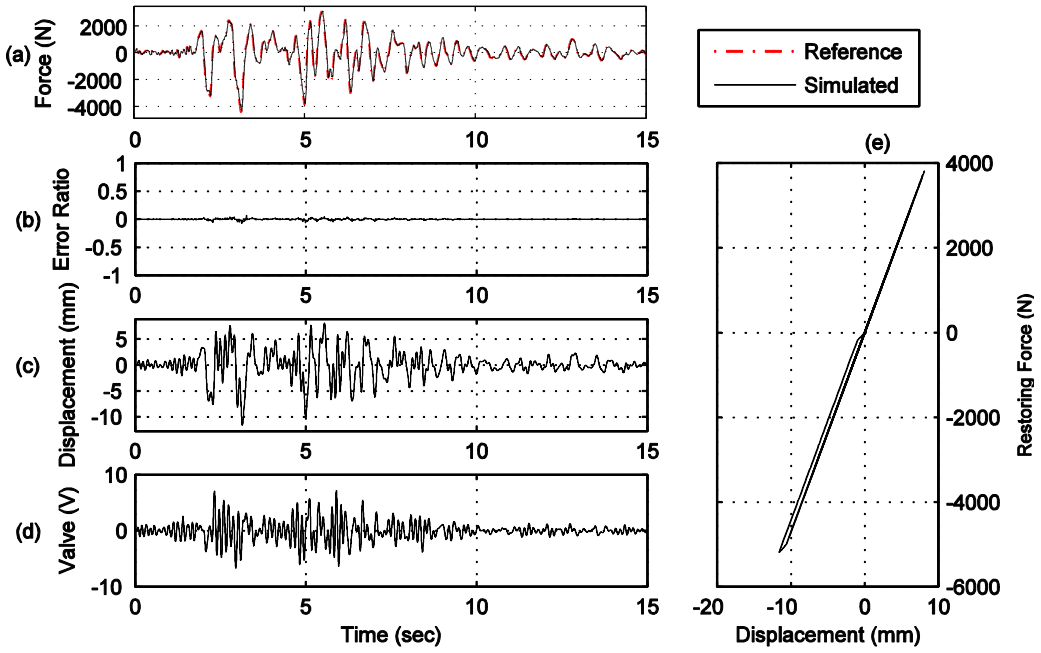

Figure C.96. Yield strength Y_y =3,000 N, post-yield stiffness $k_1 = 0.4*k_0$.

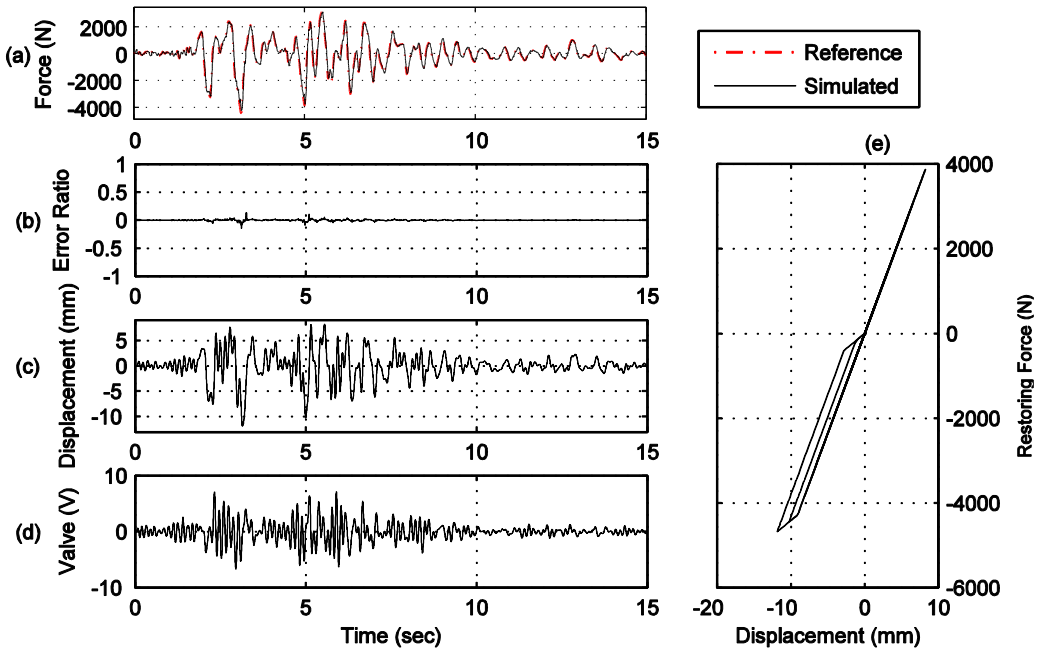

Figure C.97. Yield strength Y_y =3,000 N, post-yield stiffness $k_1 = 0.3*k_0$.

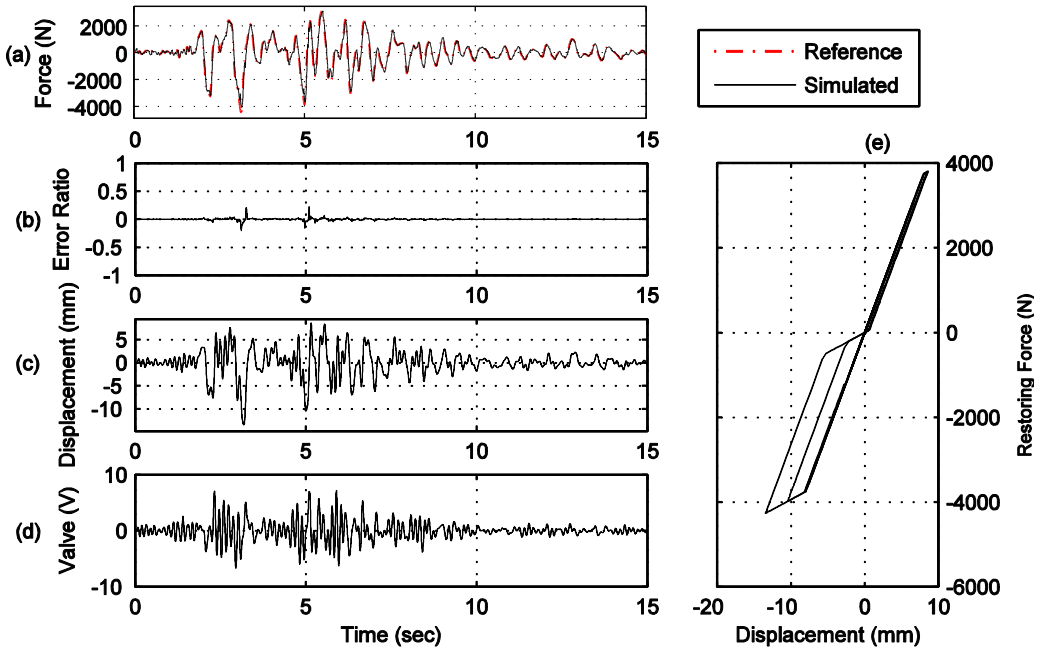

Figure C.98. Yield strength Y_y =3,000 N, post-yield stiffness $k_1 = 0.2*k_0$.

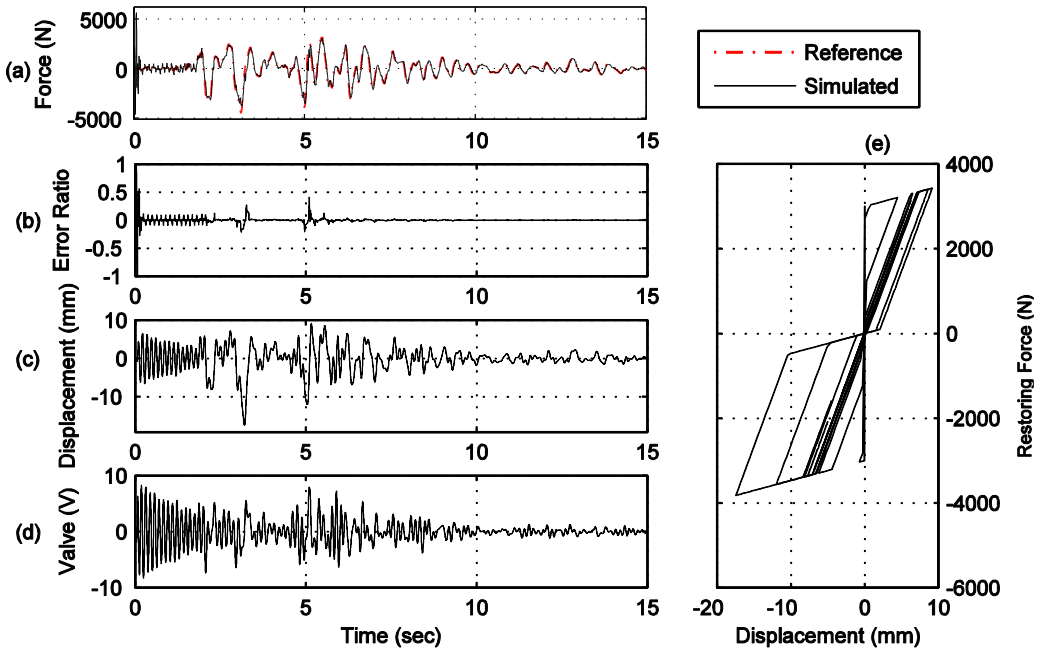

Figure C.99. Yield strength Y_y =3,000 N, post-yield stiffness $k_1 = 0.1*k_0$.

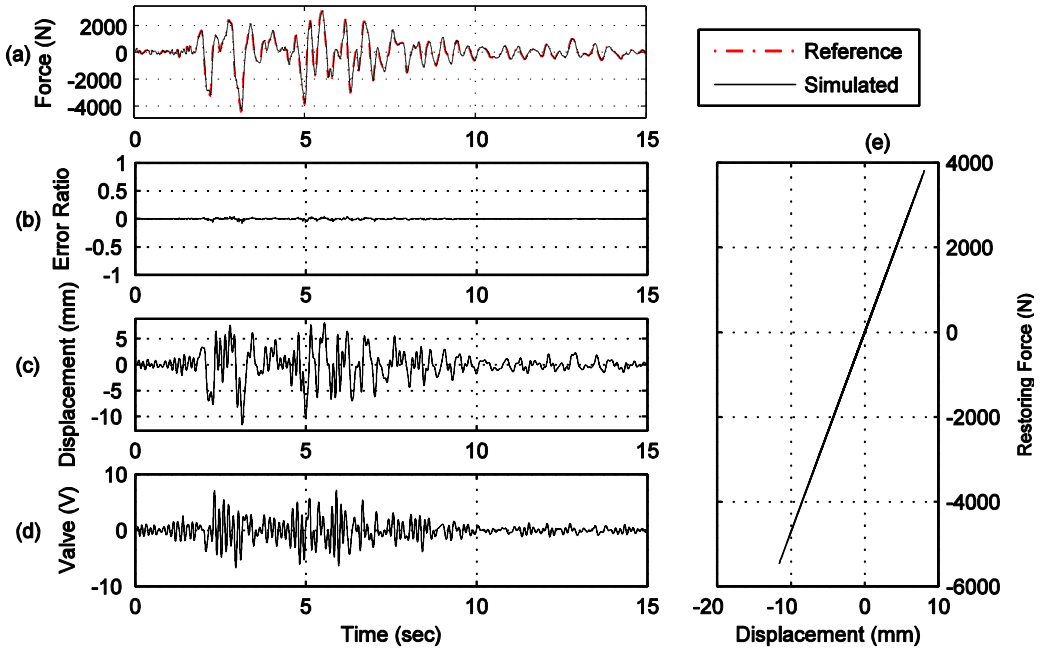

Figure C.100. Yield strength Y_y =3,500 N, post-yield stiffness $k_1 = 0.9*k_0$.

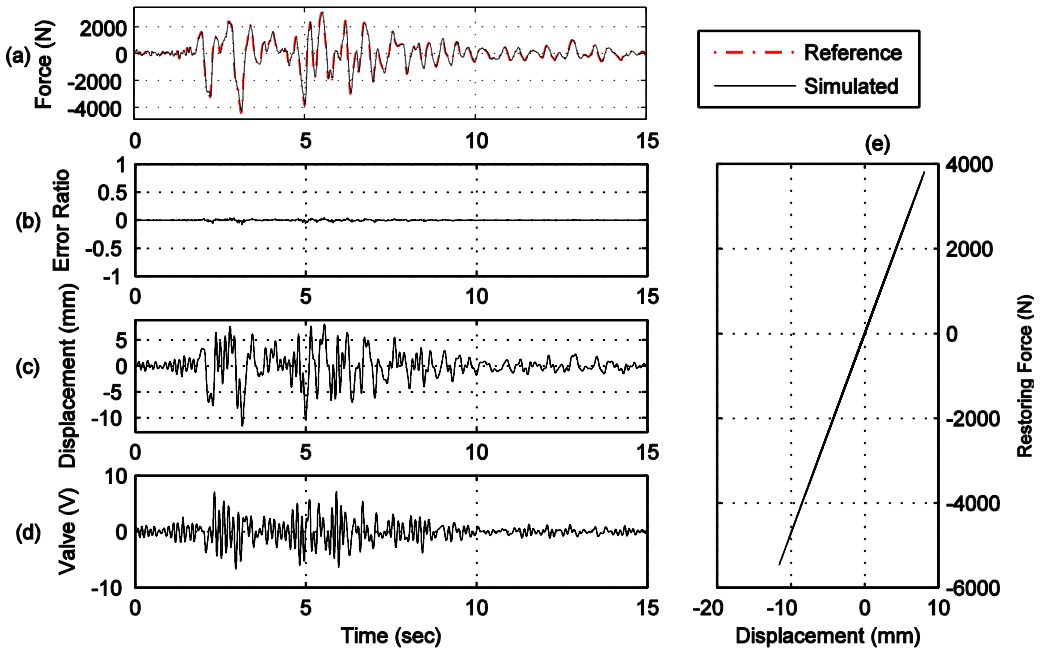

Figure C.101. Yield strength Y_y =3,500 N, post-yield stiffness $k_1 = 0.8*k_0$.

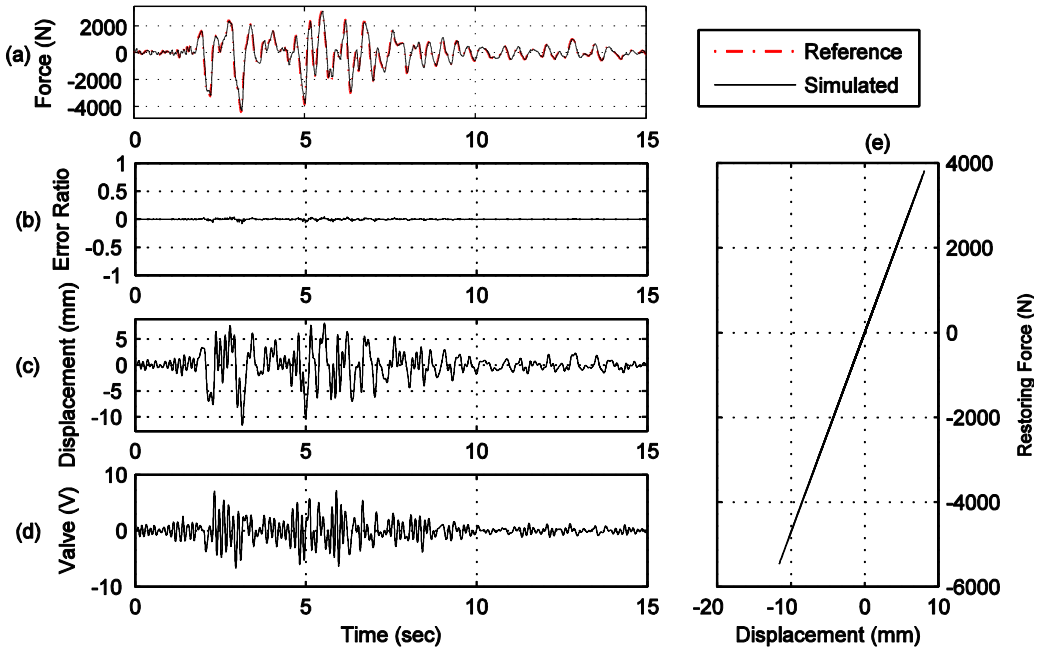

Figure C.102. Yield strength Y_y =3,500 N, post-yield stiffness $k_1 = 0.7*k_0$.

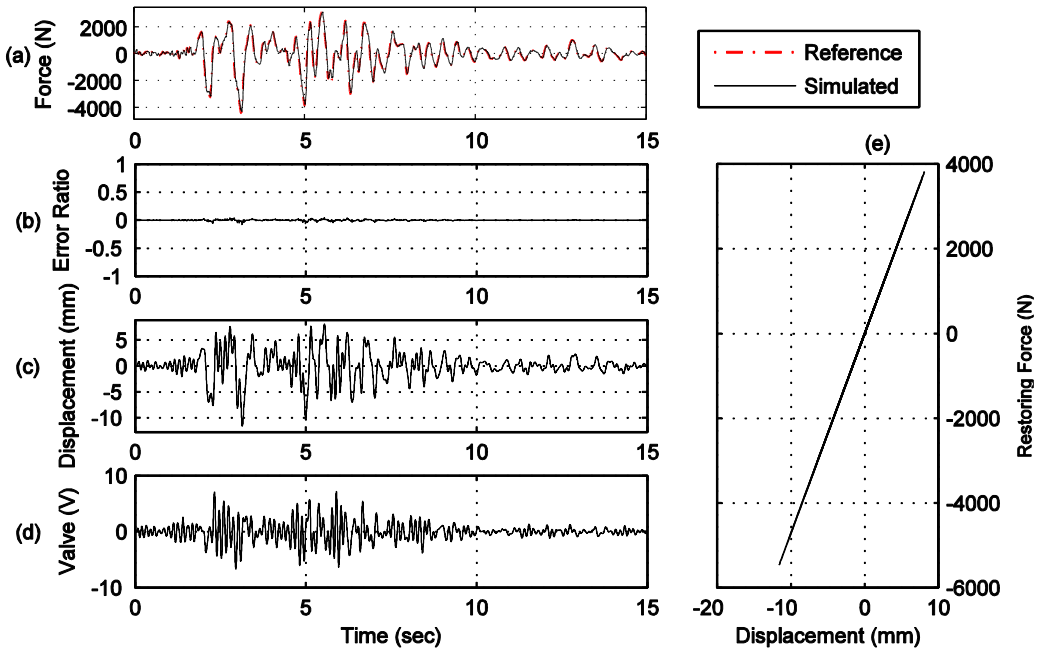

Figure C.103. Yield strength Y_y =3,500 N, post-yield stiffness $k_1 = 0.6*k_0$.

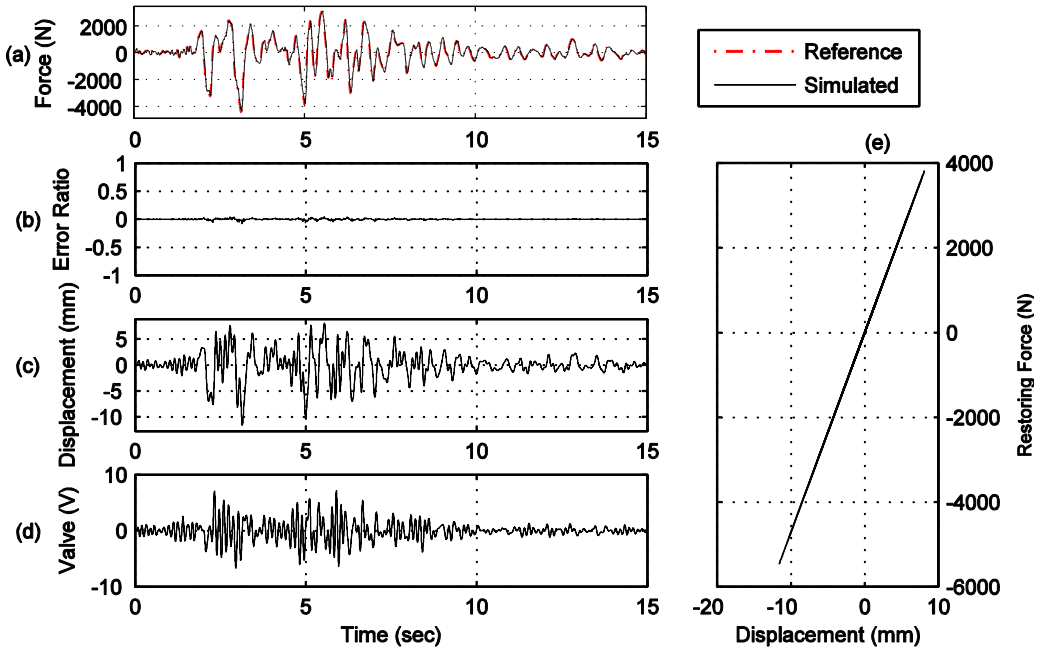

Figure C.104. Yield strength Y_y =3,500 N, post-yield stiffness $k_1 = 0.5*k_0$.

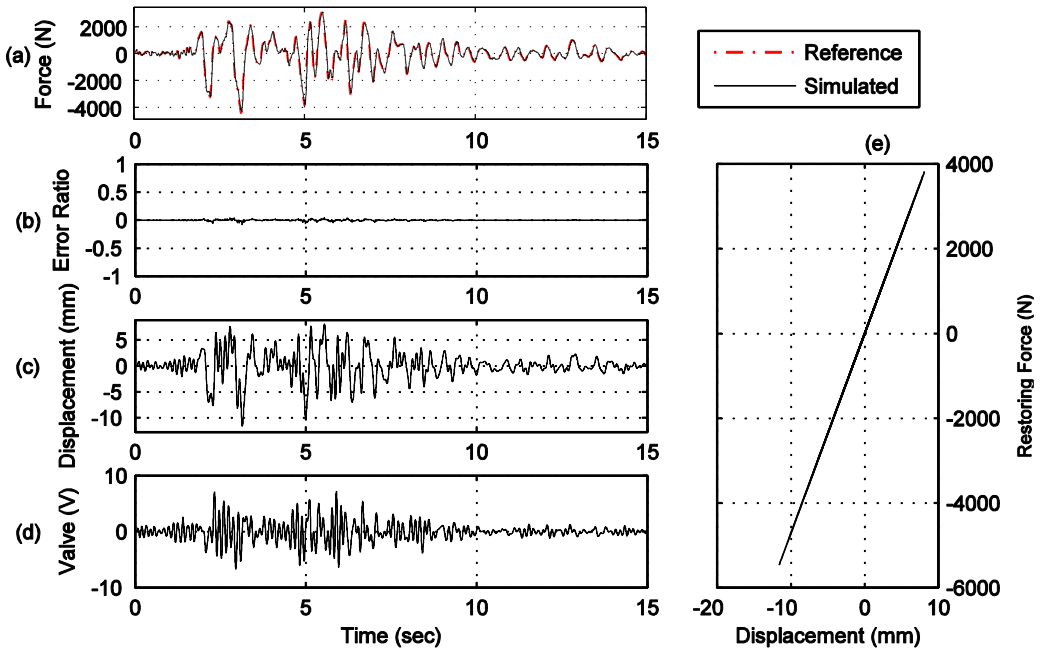

Figure C.105. Yield strength Y_y =3,500 N, post-yield stiffness $k_1 = 0.4*k_0$.

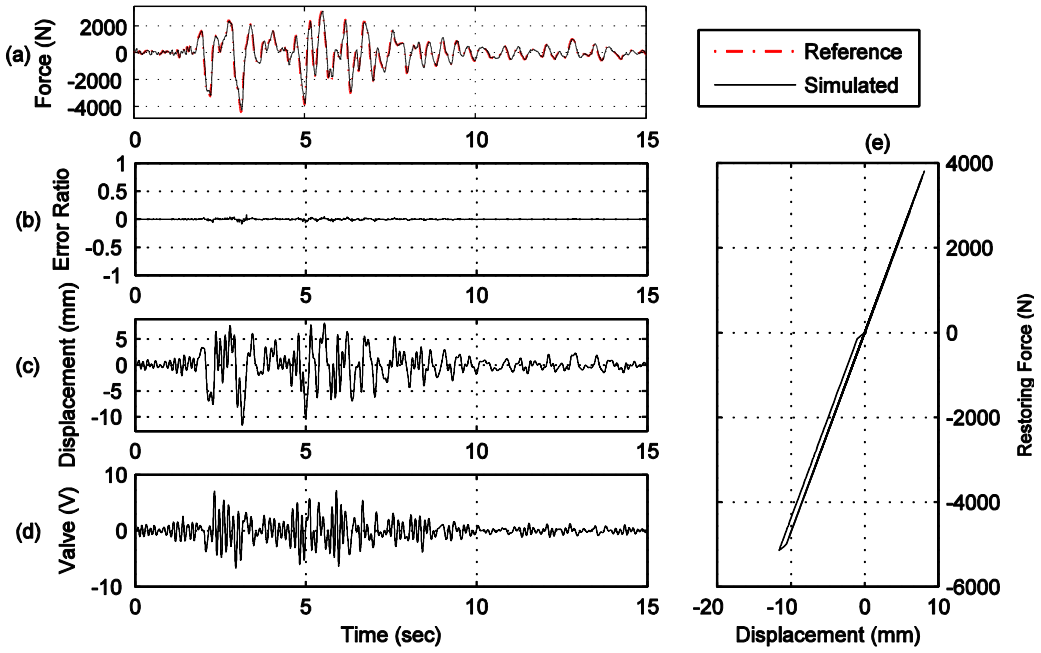

Figure C.106. Yield strength Y_y =3,500 N, post-yield stiffness $k_1 = 0.3*k_0$.

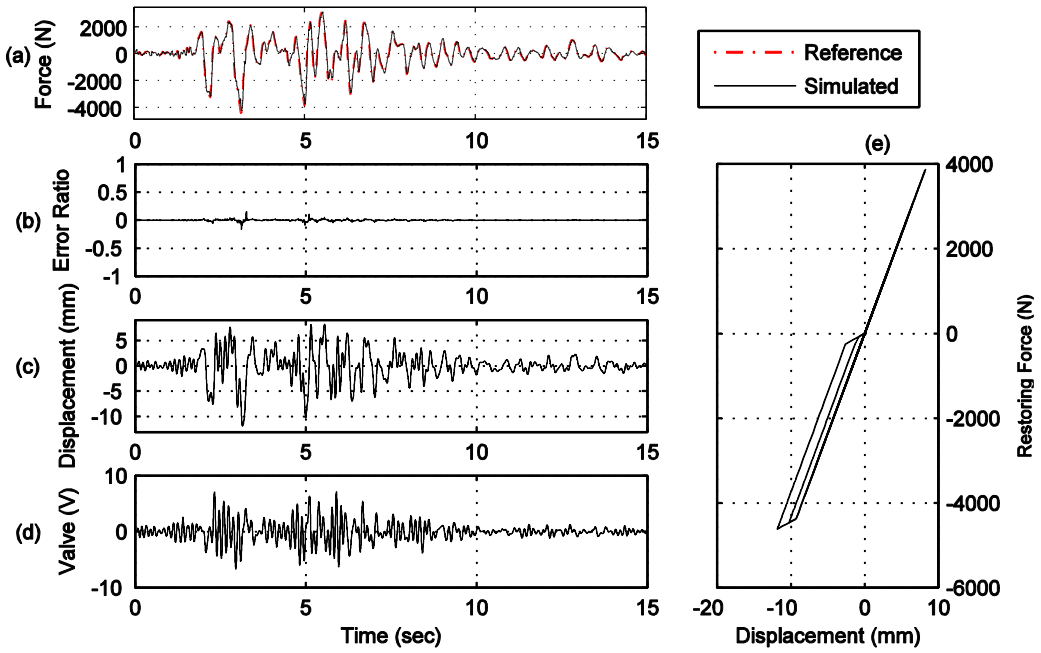

Figure C.107. Yield strength Y_y =3,500 N, post-yield stiffness $k_1 = 0.2*k_0$.

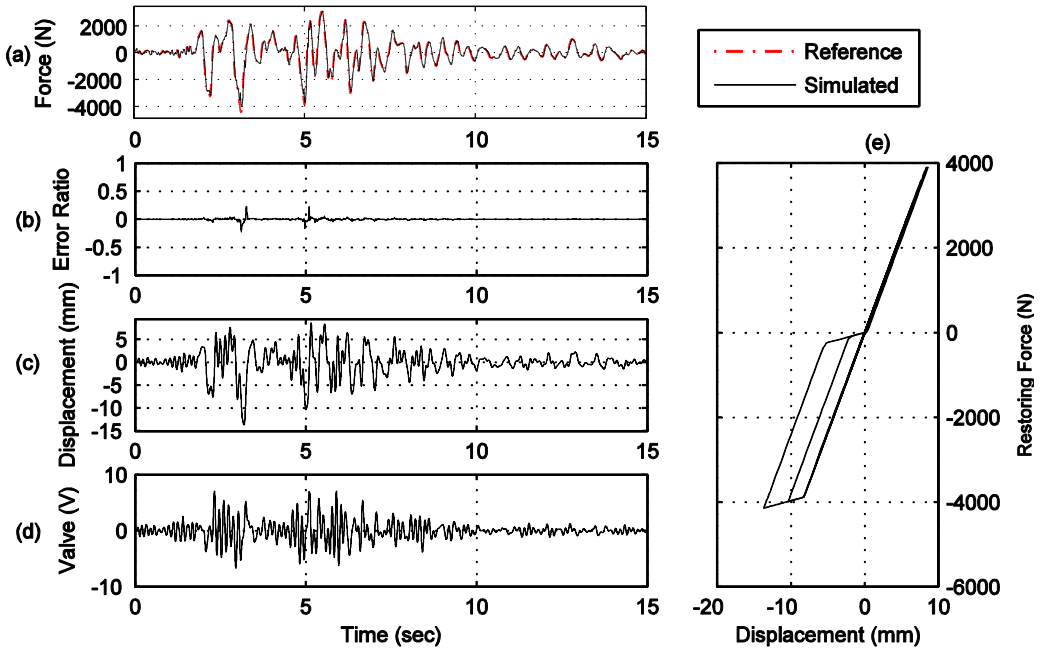

Figure C.108. Yield strength Y_y =3,500 N, post-yield stiffness $k_1 = 0.1*k_0$.

Bibliography

Alleyne A., and Liu, R. (1999). "Nonlinear Force/Pressure Tracking of an Electrohydraulic Actuator", Proceedings of 1999 IFAC World Congress, Beijing, China, B:469-474.

Astrom, K.J. and Murray, R.M. (2007). "Feedback Systems: An Introduction for Scientists and Engineers", California Institute of Technology.

Chopra, A.K. (2012). "Dynamics of Structures: Theory and Applications to Earthquake Engineering", Pearson: New Jersey, ISBN 10: 0-13-285803-7.

Conte, J.P., and Trombetti, T.L. (2000). "Linear Dynamic Modeling of a Uni-Axial Servo-Hydraulic Shaking Table System", *Earthquake Engineering and Structural Dynamics*, 29: 1375-1404.

Dimig, J., Shield, C., French, C., Bailey, F., and Clark, A. (1999). "Effective Force Testing: A Method of Seismic Simulation for Structural Testing", *Journal of Structural Engineering*, 125 (9): 1028-1037.

Dyke, S., Spencer, B., Quast, P., Sain, M. (1995). "Role of Control-Structure Interaction in Protective System Design", *Journal of Engineering Mechanics*, 121 (2): 322-338.

Erikson, R.K. (1997). "Fundamentals of Power Electronics", Chapman and Hall: New York, ISBN 0-412-08541-0.

Kopasakis, G. (2007). "Feedback Control Systems Loop Shaping Design with Practical Considerations", NASA/TM-2007-215007.

Merritt, H.E. (1967). "Hydraulic Control Systems", Wiley: New York, ISBN 10: 0471596175.

Nakata, N. (2013). "Effective Force Testing Using a Robust Loop Shaping Controller", *Earthquake Engineering and Structural Dynamics*, 42: 261-275.

Nakata, N., and Krug, E. (2013). "Computational Framework for Effective Force Testing and a Compensation Technique for Nonlinear Actuator Dynamics", *Structural Control and Health Monitoring*, DOI: 10.1002/stc.1599.

Nakata, N., and Krug, E. (2013). "Validation of Loop Shaping Force Feedback Controller for Nonlinear Effective Force Testing", *Journal of Vibration and Control*, DOI: 10.1177/1077546313517585.

Nakata, N., and Krug, E. (2013). "Multidegrees-of-Freedom Effective Force Testing: a Feasibility Study and Robust Stability Assessment", *Earthquake Engineering and Structural Dynamics*, 42: 1985-2002.

Nakata, N., and Krug, E. (2014). "Experimental Implementation and Verification of Multi-Degrees-of-Freedom Effective Force Testing", *Earthquake Engineering and Structural Dynamics*, 43:413-428.

Sivaselvan, M.V., Reinhorn, A.M., Shao, X., and Weinreber, S. (2008). “Dynamic Force Control with Hydraulic Actuators Using Added Compliance and Displacement Compensation”, *Earthquake Engineering and Structural Dynamics*, 37: 1785-1800.

Zhao, J., Shield, C., French, C., and Posbergh, T. (2005). “Nonlinear System Modeling and Velocity Feedback Compensation for Effective Force Testing”, *Journal of Engineering Mechanics*, 131 (3): 244-253.

Zhao, J., Shield, C., French, C., and Posbergh, T. (2006). “Comparison of Tests of a Nonlinear Structure Using a Shake Table and the EFT Method”, *Journal of Structural Engineering*, 132 (9): 1473-1481.

Vita

Matthew Dove was born in Baltimore, Maryland on May 22nd, 1990. He attended Archbishop Curley High School in Baltimore, Maryland. In May 2012, he received a Bachelor of Civil Engineering degree from the University of Delaware in Newark, Delaware. He pursued his graduate studies at the Johns Hopkins University and is a candidate for the degree of Master of Science in Engineering from the department of Civil Engineering in May 2014.